

Demonstrating Landsat's New Potential to Monitor
Coastal and Inland Waters

by

Aaron Gerace

B.S. Mathematics, Brockport College, 2000

M.A. Mathematics, Brockport College, 2002

A dissertation submitted in partial fulfillment of the
requirements for the degree of Doctor of Philosophy
in the Chester F. Carlson Center for Imaging Science
Rochester Institute of Technology

May 2010

Signature of the Author _____

Accepted by _____
Coordinator, Ph.D. Degree Program Date

CHESTER F. CARLSON CENTER FOR IMAGING SCIENCE
ROCHESTER INSTITUTE OF TECHNOLOGY
ROCHESTER, NEW YORK

CERTIFICATE OF APPROVAL

Ph.D. DEGREE DISSERTATION

The Ph.D. Degree Dissertation of Aaron Gerace
has been examined and approved by the
dissertation committee as satisfactory for the
dissertation required for the
Ph.D. degree in Imaging Science

Dr. John R. Schott, Dissertation Advisor	Date
--	------

Dr. David Messinger

Dr. Carl Salvaggio

Dr. Anthony Vodacek

Dr. Frank Sciremammano, Jr.

DISSERTATION RELEASE PERMISSION
ROCHESTER INSTITUTE OF TECHNOLOGY
CHESTER F. CARLSON CENTER FOR IMAGING SCIENCE

Title of Dissertation:

**Demonstrating Landsat's New Potential to Monitor
Coastal and Inland Waters**

I, Aaron Gerace, hereby grant permission to Wallace Memorial Library of R.I.T. to reproduce my thesis in whole or in part. Any reproduction will not be for commercial use or profit.

Signature _____ Date _____

Demonstrating Landsat's New Potential to Monitor Coastal and Inland Waters

by

Aaron Gerace

Submitted to the
Chester F. Carlson Center for Imaging Science
in partial fulfillment of the requirements
for the Doctor of Philosophy Degree
at the Rochester Institute of Technology

Abstract

The Operational Land Imager (OLI) is a new Landsat sensor being developed by the joint USGS-NASA Landsat Data Continuity Mission (LDCM) that exhibits the potential to be a state-of-the-art instrument for studying inland and coastal waters. With upgrades such as a new Coastal Aerosol band, 12 bit quantization, and improved signal-to-noise, OLI will be spectrally and radiometrically superior to its predecessors. When considering Landsat's already high 30 meter spatial resolution, coupled with the fact that its data is free to the community, the OLI sensor may prove to be more valuable than any other environmental imaging satellite to date. The first part of this research investigates the potential for the next Landsat instrument to be used to determine the major constituents contained in water. An OLI sensor model is designed and its ability to retrieve water constituents from space is compared to existing technologies. To support this effort, two over-water atmospheric compensation methods are developed which will enable OLI data to be used in this constituent retrieval process.

The ability to characterize material transport in coastal regions is an ongoing effort in the remote sensing community and is essential to determining the environmental processes taking place in, and ultimately the health of, the water. When moderate resolution thermal data is used in conjunction with high resolution reflective data, such as the 30 meter resolution data from OLI, a three dimensional characterization of the water can be developed. In the second part of this work, a model of the Genesee River plume in Rochester, NY is simulated and the ability to calibrate the model with remotely sensed thermal data is demonstrated.

Acknowledgements

I think it goes without saying that this has been a profound experience. As I finish writing, editing, and re-editing this document the reality of the last four years has not yet sunk in. Although the degree for this dissertation will be in my name, this work belongs to many others. I don't believe I can adequately put into words the contributions made by the following individuals but I feel compelled to try.

First, I would like to recognize the people of RIT. Thank you Dr. Schott for giving me the opportunity to work on this project. This has been a truly unique experience, one which I will never forget. Without your support, both intellectually and financially, this dissertation could not have been possible. You have made a positive contribution to my family's lives for years to come.

I would like to collectively recognize my committee members: Dr. David Messinger, Dr. Carl Salvaggio, Dr. Anthony Vodacek, and Dr. Frank Sciremammano, Jr. I believe that it is a selfless act to be a member of one's committee, especially when the subject matter does not relate directly to your own research. For this, I would like to thank each of you for enthusiastically contributing to my success. I would also like to recognize the DIRS staff. You are the medium for which success is possible and should be proud, not only of your research, but also of your positive influence on peoples lives. A special acknowledgement goes out to Cindy Schultz as she was a constant source of motivation (harassment). Thank you Cindy for dealing with us "kids" on a daily basis. I would finally like to thank all of Dr. Schotts students, both past and present. I feel that we are a fraternity of our own as we have experienced the hazing first hand. A special thanks goes out to Frank Padula and Brian Malone. As friends, you each made a unique contribution to my work.

Secondly, I would like to acknowledge the individuals who are close to me in my life. First, thank you Mom and Dad for the good genes. More importantly, thank you for providing Ron, Kenny, and I with a safe and nurturing environment growing up and instilling the value of education in our lives. Our success was dependent on your efforts. I have a better understanding of that now as a father and I am truly proud to have you both as my parents. I would also like to thank my in-laws: Susan and Gary Phillips, Kenneth and Mary Lindsay, and Dan Boprey. The many little things you all did to alleviate my stress made

this experience tolerable. Additionally, a special thanks goes out to my brothers Kenny Gerace, Ronald Gerace, and brother in-law Kevin Lindsay. Some of my fondest memories include the three of you. These memories helped pass the days when my research wasn't going according to plan (which was more often than not).

Next, I would like to acknowledge my classmates Prudhvi Gurram and Matt Montanaro. It's hard to summarize the contributions that you clowns made to my work and my life: Allowing my family to take over your apartments, driving up for my defense, listening to dry-runs of my talks, helping me solve pressing issues, studying for the comprehensive exam, listening to my day-to-day problems, yada-yada-yada. You guys are wise beyond your years. I'm proud and privileged to know each of you.

Finally, I would like to thank the individuals who were most affected by my decision to go back to school. I have known my wife, Trisha, for over 19 years and I am so grateful (and amazed) that she is a part of my life. Although I don't verbalize it every day, I am constantly thankful that you supported me in pursuing my dreams. You are my best friend and I couldn't have done any of this without you. Thank you for enduring this experience with me. This degree is as much yours as it is mine. I love you so much.

To my children: Adam, Madelyn, and baby. Although you won't understand this for many years, you are the three that motivated me to pursue this work. Not a day went by that each of you weren't on my mind. You have all made the last four years particularly interesting. I love you guys and I am a better person today because of you all.

Thank you everyone,

Aaron Gerace

Rochester, New York

May 2010

Contents

Abstract	I
List of Figures	X
List of Tables	XX
1 Introduction	1
2 Objectives	7
2.1 Problem Statement	7
2.2 Statement of Objectives	10
2.3 Description of Tasks	11
2.3.1 Primary Requirements	11
2.3.2 Future Objectives	14
2.4 Contribution to Field	15
3 Background and Theory	17
3.1 Sensor-Reaching Radiance	17
3.1.1 Exoatmospheric Irradiance	18
3.1.2 Solar Paths	19
3.1.3 Thermal Paths	20
3.1.4 Governing Equation	21
3.2 Constituent Retrieval	23
3.2.1 The Rochester Embayment	23
3.2.2 Paths Contributing to Constituent Retrieval	24

3.2.3	The Water Column	26
3.2.4	Sun Glint	31
3.2.5	The Atmosphere	32
3.2.6	The Sensor	35
3.2.7	Constituent Retrieval Algorithms	38
3.2.7.1	The Look-Up Table	39
3.2.7.2	Hydrolight	40
3.2.7.3	Amoeba	43
3.2.7.4	The Retrieval Process	44
3.3	Surface Temperature Retrieval	45
3.3.1	Blackbody Radiators and the Planck Equation	46
3.3.2	Fundamental Properties of Matter	46
3.3.3	The Retrieval Process	48
3.4	The ALGE Hydrodynamic Model	49
3.5	Concluding Remarks	51
4	Constituent Retrieval with the OLI Sensor: Methodology	53
4.1	The OLI Sensor	53
4.1.1	Sensor Response	54
4.1.2	Quantization	56
4.1.3	Signal-to-Noise	57
4.2	Over-Water Atmospheric Compensation	58
4.2.1	Solar-Glint Removal Algorithm	59
4.2.2	Atmospheric Compensation Algorithms	64
4.2.2.1	Spectral Shape Matching Method	65
4.2.2.2	SeaWiFS Algorithm for Case 1 Waters	67
4.2.2.3	SeaWiFS Algorithm for Case 2 Waters	69
4.2.2.4	OLI Algorithm for Case 2 Waters (Blue Band)	72
4.2.2.5	OLI Algorithm for Case 2 Waters (Band Ratios)	80
4.2.2.6	The Empirical Line Method	84
4.3	The Constituent Retrieval Algorithm	86

4.3.1	Look-up Table Development	86
4.3.1.1	Measuring IOP's	86
4.3.1.2	Other Inputs to Hydrolight	93
4.3.2	Running Amoeba	94
4.4	Concluding Remarks	96
5	Constituent Retrieval with the OLI Sensor: Results	99
5.1	Synthetic Data	99
5.1.1	Evaluation of the OLI Sensor	100
5.1.1.1	The Scene	100
5.1.1.2	Simulated Data	100
5.1.1.3	Results	105
5.1.2	Evaluation of the OLI Atmospheric Compensation Algorithm on Simulated Data	109
5.1.2.1	OLI Atmospheric Compensation Algorithm (Blue Band) .	110
5.1.2.2	OLI Atmospheric Compensation Algorithm (Band Ratios)	111
5.1.3	Evaluation of the OLI Atmospheric Compensation Algorithm on a Simulated Scene	113
5.1.3.1	Simulating A Scene	113
5.1.3.2	OLI's Blue Band Method	116
5.1.3.3	OLI's Band Ratio Method	119
5.2	Impact of Hydrolight Inputs on Constituent Retrieval	121
5.2.1	CDOM Absorption Coefficients	121
5.2.2	Chlorophyll Absorption Coefficients	123
5.2.3	Chlorophyll Phase Functions	125
5.2.4	Wind Speed and Solar Zenith Angle	127
5.3	Real Data	129
5.3.1	Constituent Retrieval Using ELM	130
5.3.2	Constituent Retrieval Using OLI's Blue Band Method	134
5.3.3	Constituent Retrieval Using OLI's Band Ratio Method	138
5.4	Concluding Remarks	143

6	Using Thermal Data to Calibrate a Hydrodynamic Model	145
6.1	Thermal Data	146
6.1.1	NPOESS/MODIS	146
6.1.2	Radiometric Sharpening	147
6.1.3	Surface Temperature Retrieval	150
6.1.3.1	Landsat Data	151
6.1.3.2	MODIS Data	153
6.2	The Hydrodynamic Model	154
6.2.1	ALGE Inputs	155
6.2.2	Calibrating the Hydrodynamic Model	160
6.2.2.1	Running ALGE	160
6.2.2.2	Developing the Calibration LUT	161
6.2.2.3	Calibrating ALGE Model Using Thermal Data	162
6.2.2.4	Results	162
6.3	Concluding Remarks	168
7	Summary and Recommendations	169
7.1	Summary	169
7.2	Future Work	170
A	Determining Exoatmospheric Irradiance	i
B	Development of Basics IOP's of Water	iii
C	Sensor Characteristics	vii
C.1	Spectral Response	vii
C.1.1	ETM+	vii
C.1.2	OLI	viii
C.1.3	AVIRIS	x
C.1.4	SeaWiFS	xi
C.1.5	MODIS	xii
C.2	SNR and Quantization Requirements	xiii
C.2.1	ETM+	xiii

C.2.2	OLI	xiv
C.2.3	Other Instruments	xv
C.3	OLI SNR Margins	xvi

List of Figures

2.1	<i>Flow chart illustrating how atmospherically compensated, registered thermal and reflective data can be used to calibrate a hydrodynamic model.</i>	8
3.1	<i>Exoatmospheric Irradiance($\frac{W}{m^2_{nm}}$) as a function of wavelength(nm).</i>	18
3.2	<i>Major solar paths contributing to sensor-reaching radiance.</i>	19
3.3	<i>Major self-emitted paths contributing to sensor-reaching radiance.</i>	21
3.4	<i>RGB image of the Rochester Embayment illustrating the various lakes and ponds in the area.</i>	24
3.5	<i>Contributions to sensor-reaching radiance from an imaged water pixel.</i>	25
3.6	<i>Spectral absorption coefficients for pure water (solid line) and pure seawater (dashed line). [Data taken from [Hale and Querry, 1973], [Jackson, 1975], [Smith and Baker, 1981], [Zoloratev and Demin, 1977] and compiled in [Mobley, 1994]]</i>	26
3.7	<i>Contributions to sensor-reaching radiance from the water column.</i>	29
3.8	<i>(a) shows the absorption coefficients for pure water as a function of wavelength as measured by [Pope and Fry, 1997] and (b) shows its corresponding scattering coefficients as derived by [Smith and Baker, 1981].</i>	31
3.9	<i>Sketch of solar and sky glint.</i>	32
3.10	<i>Plot of total transmission from 0 to 15 microns for a typical mid-latitude, summer scene containing rural aerosols. This plot was generated using the Moderate Resolution Atmospheric Transmittance Code (MODTRAN).</i>	35
3.11	<i>Illustration of light passing through a sensor.</i>	36

3.12	<i>Response vs. wavelength plots showing the degradation of a signal as it passes through a sensor.</i>	37
3.13	<i>Illustration of the constituent retrieval process using LUTs.</i>	39
3.14	<i>Three dimensional LUT. Water constituent concentrations make up the domain and reflectance spectra make up the range.</i>	40
3.15	<i>Figure illustrating how hydrolight uses plane-parallel geometry to compute the total upwelling radiance in the air just above the wind-blown sea surface. Water-leaving radiance is shown in path (1), reflected solar radiance in path (2), and reflected sky radiance in path (3).</i>	41
3.16	<i>Plot of the points in the LUT encountered as Amoeba finds the minimum. .</i>	44
3.17	<i>Planck curves for a 300 Kelvin and 5800 Kelvin Blackbody.</i>	47
3.18	<i>Sketch of a LUT resulting from various blackbody curves.</i>	49
4.1	<i>Reflective bands of OLI.</i>	55
4.2	<i>Example of water signal that has been spectrally sampled to OLI's sensor response.</i>	55
4.3	<i>Illustration of the response resolution associated with the 8-bit quantizer of ETM+ and the 12-bit quantizer of OLI. Reflectance range $[0 - 1]$ has been divided into 256 levels for ETM+ and 4096 levels for OLI.</i>	56
4.4	<i>Cartoon of a whiskbroom and a pushbroom sensor which can be found in ETM+ and OLI, respectively.</i>	58
4.5	<i>Figure showing how a linear relationship between the NIR band and visible band is determined.</i>	60
4.6	<i>Figure showing how linear regression can be used in glint removal to develop a more robust linear relationship between brightness values in the NIR band and visible band.</i>	61
4.7	<i>True color images showing the effects of the deglinting algorithm on Cranberry Pond in the Rochester Embayment. The left figure shows the original image and the right shows the glint removed image.</i>	63

4.8	<i>True color images showing the effects of the deglinting algorithm on Long Pond in the Rochester Embayment. The left figure shows the original image and the right shows the glint removed image.</i>	64
4.9	<i>Illustration of the complications associated with performing aerosol retrieval with a multispectral sensor. (Left) shows a LUT of various atmospheres that may be used in the aerosol retrieval process. (Middle) shows the result of spectrally sampling an arbitrary pixel with the AVIRIS sensor response function. (Right) shows the result of spectrally sampling an arbitrary pixel with the OLI sensor response function.</i>	66
4.10	<i>Two different water samples that have been imaged by the OLI sensor through two different atmospheres.</i>	67
4.11	<i>Sample scatterplot of Rayleigh-corrected reflectances used to determine the image parameters α and $\epsilon_m^{(7,8)}$ [Ruddick et al., 2000].</i>	71
4.12	<i>(Left) shows the TOA radiance for a random sample of water pixels that were created in Hydrolight and then passed through an atmosphere with a horizontal visibility of 23 kilometers. (Right) shows the signals after being spectrally sampled to the OLI reflective bands.</i>	73
4.13	<i>ROI chosen from Lake Ontario.</i>	74
4.14	<i>Histograms of the pixels from the ROI described in Figure 4.13. (a) shows the histogram of band 1 from OLI which is centered at 443 nanometers. (b) shows the histogram of band 3 from OLI which is centered at 563 nanometers.</i>	75
4.15	<i>Three dimensional LUT. Water constituent concentrations make up the domain and reflectance spectra make up the range.</i>	76
4.16	<i>Four dimensional LUT. Water constituent concentrations and atmospheric visibility make up the domain and radiance spectra make up the range.</i>	77
4.17	<i>Overlapping red and blue curves indicate issue associated with using band ratios to determine visibility with multispectral data. Red spectra show imaged values for a range of water constituents and a 25 kilometer visibility atmosphere. Blue values are for the same range of constituents and a 30 kilometer visibility.</i>	78

4.18	<i>(Left) TOA radiance for various water bodies (25 kilometer visibility atmosphere). (Right) Chosen water type based on spectral shape. The red curve is an imaged water pixel and the black curves represent the closest water type.</i>	79
4.19	<i>Figure showing OLI's band 5 (862 nanometers) and band 6 (1605 nanometers) radiance values for a subset of the 4-D LUT described in section 4.2.2.4. From the top family of curves to the bottom, visibility is [10,15,20,25] kilometers.</i>	81
4.20	<i>RGB image of the Rochester Embayment illustrating the various lakes and ponds in the area.</i>	83
4.21	<i>Example of the linear relationship that can be developed when the reflectances and their associated radiances are known for an imaged water pixel.</i>	85
4.22	<i>RGB image of the Rochester Embayment. Crosses represent locations where in situ observations were made.</i>	87
4.23	<i>(Left) The absorption coefficients for pure water as a function of wavelength as measured by [Pope and Fry, 1997]. (Right) The corresponding scattering coefficients as derived by [Smith and Baker, 1981].</i>	87
4.24	<i>CDOM absorption coefficients for the various ground truth locations shown in Figure 4.22. The solid black line represents the average of all coefficients.</i>	88
4.25	<i>CDOM Absorption coefficients as a function of wavelength.</i>	89
4.26	<i>(a) shows the absorption coefficients for Phytoplankton(Chlorophyll) as a function of wavelength. (b) shows its corresponding scattering coefficients.</i>	90
4.27	<i>(a) shows the absorption coefficients for suspended sediments as a function of wavelength and (b) shows its corresponding scattering coefficients.</i>	90
4.28	<i>Scattering phase function for pure water.</i>	91
4.29	<i>Scattering phase function for chlorophyll and suspended sediments with a backscatter fraction of 0.025 or 2.5%. Data was obtained from a Hydrolight supplied phase-function, [Mobley, 1994].</i>	92

4.30	<i>Illustration of the variability associated with spectra in the LUT. Green is spectrum associated with $(CHL, SM, CDOM) = (1, 1, 4)$. Blue is spectrum associated with $(CHL, SM, CDOM) = (3, 1, 4)$. Black is spectrum associated with $(CHL, SM, CDOM) = (46, 24, 14)$. Red is spectrum associated with $(CHL, SM, CDOM) = (68, 24, 14)$.</i>	95
4.31	<i>Two-dimensional representation of an optimization issue associated with Amoeba.</i>	96
5.1	<i>RGB image of the Rochester Embayment. AVIRIS data of Rochester, NY collected on May 20, 1999.</i>	101
5.2	<i>Illustration of the constituent retrieval process when assumption of perfect atmospheric compensation is made.</i>	102
5.3	<i>Black numbers show average RMS-error that we can expect to obtain from constituent retrieval process. Red numbers express these errors as a percent of the range of concentrations observed in the scene. The SNRs shown in Table C.7 are used for this experiment.</i>	106
5.4	<i>Comparison of RMS-errors that can be achieved from constituent retrieval process with required SNR, SNR at half margin, and SNR at full margin.</i>	108
5.5	<i>4 parameter LUT used to perform atmospheric compensation. Visibility ranged between 5 and 60 kilometers in 5 kilometer increments.</i>	110
5.6	<i>Results of the constituent retrieval process when performed on synthetic data with atmospheric effects included. OLI's Blue Band method was used to compensate for the atmosphere. SNR's at half the margins described in Appendix C.3 were used.</i>	111
5.7	<i>Results of the constituent retrieval process when performed on synthetic data with atmospheric effects included. OLI's Band Ratio method was used to compensate for the atmosphere. SNR's at half the margins described in Appendix C.3 were used.</i>	112
5.8	<i>RGB image of the Rochester Embayment. Data was collected by Landsat 7 on May 16, 1999.</i>	114

5.9	<i>Simulated image of Rochester Embayment. The constituent retrieval process was performed on 6 ROI's (each containing 36 pixels) using the OLI atmospheric compensation algorithms to account for the atmosphere.</i>	115
5.10	<i>Results of the constituent retrieval process when performed on synthetic image using all 6 ROI's in Figure 5.9.</i>	117
5.11	<i>Results of the constituent retrieval process when performed on a pond-by-pond basis. SNRs at half the margins shown in Figure C.8 were used. (***) Could not converge to a Pond Global solution).</i>	118
5.12	<i>Results of the constituent retrieval process when OLI's Band Ratio method is used to remove the atmosphere. SNRs at half the margins shown in Figure C.8 were used in this study.</i>	120
5.13	<i>CDOM absorption coefficients of nine water samples taken from ponds in the Rochester Embayment. The bold, black curve indicates the average absorption coefficients used to develop the LUT.</i>	122
5.14	<i>Results of CDOM absorption coefficient study. The full margin noise of Figure C.8 was used in this experiment.</i>	123
5.15	<i>Chlorophyll absorption coefficients of four water samples taken from ponds in the Rochester Embayment. The bold, black curve indicates the average absorption coefficients used to develop the LUT.</i>	124
5.16	<i>Results of Chlorophyll absorption coefficient study. The full margin noise of Figure C.8 was used in this experiment.</i>	125
5.17	<i>Scatterplot of backscatter fraction versus chlorophyll-a concentration for multiple water samples. Various models that attempt to fit the data are overlaid (a)[Whitmire et al., 2007], (b)[Sullivan et al., 2005].</i>	126
5.18	<i>Results of the chlorophyll phase function study. The full margin noise of Figure C.8 was used in this experiment.</i>	127
5.19	<i>Results of solar/zenith and wind speed study. The full margin noise of Figure C.8 was used in this experiment.</i>	128
5.20	<i>The locations of ground truth samples and ELM data points in the Rochester Embayment.</i>	130

5.21	<i>Results of the constituent retrieval process when ELM is used to compensate for the atmosphere. Long Pond is used as the bright region in the ELM. . .</i>	131
5.22	<i>Results of the constituent retrieval process when ELM is used to compensate for the atmosphere. Ontario Beach sand is used as the bright region in the ELM.</i>	132
5.23	<i>Results of the constituent retrieval process using the OLI atmospheric compensation algorithm (Blue Band).</i>	134
5.24	<i>NEΔL versus wavelength for the four imaging spectrometers of AVIRIS. . .</i>	135
5.25	<i>Spectral biases that are applied to data for both the ELM and OLI atmospheric compensation methods. Blue curves are biases associated with the OLI algorithm while the green and brown curves are the biases associated with the Long Pond ELM and Ontario Beach sand ELM, respectively. . . .</i>	136
5.26	<i>Spectral gains that are applied to data for the ELM and OLI atmospheric compensation methods. Blue curves are the gains associated with the OLI algorithm while the green and brown curves are the gains associated with the Long Pond ELM and Ontario Beach sand ELM, respectively.</i>	137
5.27	<i>Deglinted OLI data of Cranberry Pond and Long Pond in the Rochester Embayment. The ROIs were chosen to overlap CP1 and LP1 in Figure 5.20.</i>	139
5.28	<i>Results of the constituent retrieval process when the OLI Band Ratio method is used to compensate for the atmosphere.</i>	139
5.29	<i>(Left) Retrieved reflectances resulting from the atmospheric compensation of the red ROI pixels shown in Figure 5.27 (Cranberry Pond) when the OLI Band Ratio method is used. (Right) Modeled reflectances of ROI based on in situ measurements.</i>	140
5.30	<i>(Left) Retrieved reflectances resulting from the atmospheric compensation of the green ROI pixels shown in Figure 5.27 (Long Pond) when the OLI Band Ratio method is used. (Right) Modeled reflectances of ROI based on in situ measurements.</i>	140
5.31	<i>ROIs taken from AVIRIS data over both land and water pixels in an attempt to determine if a calibration error exists in the data.</i>	141

5.32	(a) Spectral slice for VNIR wavelengths of AVIRIS data for land ROI (blue) shown in Figure 5.31. (b) Spectral slice for VNIR wavelengths of AVIRIS data for water ROI (red) shown in Figure 5.31.	141
5.33	Results of the constituent retrieval process using OLI Band Ratio method to compensate for the atmosphere. (Top) Reflectances retrieved from Cranberry Pond before 9% bias correction, after 9% bias correction, and modeled expected reflectance based on in situ observations. (Bottom) Analogous curves for Long Pond.	142
5.34	Results of the constituent retrieval process using OLI Band Ratio method to compensate for the atmosphere after a 9% bias correction is applied to the first 3 bands of the OLI data.	143
6.1	Landsat 7 imagery illustrating a possible correlation between reflective data (Left) and thermal data (Right) in coastal waters.	148
6.2	(Left) Simulated MODIS thermal data of Rochester Embayment. (Right) Corresponding area as seen by the RGB reflective bands of Landsat 7.	149
6.3	1 kilometer MODIS thermal data that has been sharpened to 30 meter resolution using Landsat 7 reflective data.	150
6.4	Major self-emitted paths contributing to sensor reaching radiance.	152
6.5	Plot of apparent temperature versus radiance for the temperature range 270.0-300.0 Kelvin. Radiosonde data was used in MODTRAN to model the atmosphere.	153
6.6	Landsat 5 true color image of the Rochester Embayment, which includes the Genesee River plume.	155
6.7	Illustration of how bathymetry data can be used to generate the input files igrid.dat and idepth.dat for the ALGE Hydrodynamic model.	156
6.8	Schematic of major energy inputs for a typical lake.	157
6.9	Large-area simulation of Lake Ontario. The resulting surface currents can be used as nudging vectors for the small-area simulation.	158

6.10	<i>Comparison of the Genesee River's flow rate at two locations. The Charlotte Pump Station is within 1/2 mile of the river's mouth while the Ford Street sensor is six miles upstream.</i>	159
6.11	<i>ALGE surface temperature output of the Rochester Embayment after 212 simulation hours. Land pixels were fixed at 15°C to show the contrast in water.</i>	160
6.12	<i>Calibration LUT containing ALGE simulations.</i>	161
6.13	<i>(Left) Atmospherically compensated Landsat 5 thermal data which was collected on July 13, 2009. (Right) RGB subimage to be used in optimization process. Land pixels have been fixed at 16°C in the subimage to show the temperature contrast in the water pixels.</i>	164
6.14	<i>Real data (left) that is to be registered to modeled data (right).</i>	164
6.15	<i>Result of registering the two forms of data shown in Figure 6.14 and masking mixed pixels.</i>	165
6.16	<i>Modeled thermal data (Right) whose surface temperatures most closely resembled the Landsat 5, satellite data (Left). The model's corresponding parameter quadruplet is (wind speed, wind direction, flow speed, flow temperature) = (88.9, 6.1, 61.8, 19.5).</i>	166
6.17	<i>Modeled thermal data (Right) chosen from LUT using plume optimization and Landsat 5, satellite data (Left).</i>	167
B.1	<i>Geometry used to define inherent optical properties.</i>	iii
B.2	<i>Example of scattering phase function for pure water.</i>	vi
C.1	<i>ETM+ response function vs. wavelength(nm)</i>	viii
C.2	<i>OLI VNIR response function vs. wavelength(nm).</i>	ix
C.3	<i>OLI VNIR/SWIR response function vs. wavelength(nm).</i>	x
C.4	<i>AVIRIS VNIR response function vs. wavelength(nm).</i>	x
C.5	<i>SeaWiFS VNIR response function vs. wavelength (μm).</i>	xii
C.6	<i>MODIS bands with a description of their primary uses.</i>	xii
C.7	<i>MODIS bands with a description of their primary uses.</i>	xiii
C.8	<i>Potential SNR Margins for the OLI instrument.</i>	xvi

List of Tables

4.1	<i>Constituent concentrations used to develop triplets for input into Hydrolight.</i>	94
6.1	<i>ALGE input parameters; variation from observed, nominal value.</i>	163
C.1	<i>L7 ETM+ Salient Characteristics.</i>	viii
C.2	<i>OLI Spectral Bands.</i>	ix
C.3	<i>SeaWiFS Spectral Bands.</i>	xi
C.4	<i>Saturation radiances for the first five bands of ETM+ for both the low gain and high gain settings, [ETM Manual, 2003].</i>	xiv
C.5	<i>ETM+ Signal to noise ratios at L_{low} radiance levels for the first five bands, [ETM Manual, 2003].</i>	xiv
C.6	<i>Saturation radiances for the first six reflective bands of OLI, [LDCM Manual, 2006]</i>	xv
C.7	<i>OLI Signal to noise ratios for $L_{typical}$ radiance levels in the visible and near-infrared bands, [LDCM Manual, 2006].</i>	xv

Chapter 1

Introduction

The ability to achieve continuous monitoring of the global water supply from satellite imagery is an ongoing effort in the remote sensing community. Historically, water studies involving the use of satellite imagery have focused mainly on the open ocean. These case 1 waters are relatively easy to monitor as their optical properties are dominated by one constituent called phytoplankton, a microscopic free-floating organism. With the improvement of sensor technology, however, it has become possible to study more optically complex, case 2 waters. These types of waters, which are typically found in coastal regions or inland lakes and ponds, are classified as optically complex as they contain suspended materials and colored dissolved organic matter (CDOM), in addition to phytoplankton. Our improved ability to monitor case 2 waters has led to a desire to study issues that are more sophisticated in nature than those studied over traditional case 1 waters. As opposed to simply trying to characterize the concentration of phytoplankton in a water body, ongoing efforts include the monitoring of water quality, a desire to characterize sedimentation in coastal waters, and perhaps even the ability to predict beach closings. With this increased ability and interest in studying case 2 waters has come a significant increase in the complexity of the corresponding algorithms. Therefore, methods that once held for case 1 waters have to be modified, or in some cases reconstructed altogether. A major thrust of this research effort is the development of such algorithms.

In addition to the need for more sophisticated algorithms to study case 2 waters, is a demand for state-of-the-art sensor technology. Historically, instruments such as the Sea-viewing Wide Field-of-view Sensor (SeaWiFS) and the Moderate Resolution Imag-

ing Spectroradiometer (MODIS) have been used over the open ocean and along coastal regions to determine the constituents in a water body (chlorophyll, suspended material, colored-dissolved organic matter). Due to their 1 kilometer spatial resolution, however, these sensors are ineffective in independently monitoring many inland and turbid coastal waters whose constituents can have large spatial variability. Current Landsat instruments, on the other hand, have the spatial resolution required to effectively monitor complicated case 2 waters. However, with only four bands in the visible and near-infrared (VNIR), an 8-bit quantizer, and limited signal-to-noise, the Landsat Thematic Mapper sensors lack the radiometric fidelity that is necessary for studying case 2 waters where a significant change in coloring agents (constituents) often leads to only a small change in sensor-reaching radiance.

A new sensor being developed by the joint USGS-NASA Landsat Data Continuity Mission (LDCM) exhibits the potential to be both radiometrically and spatially sufficient for the monitoring of case 2 waters. With Landsat 5 and Landsat 7 expected to become inoperable in the next few years, efforts are being made to extend the collection of Landsat data. Consequently, NASA and the USGS are developing the Operational Land Imager (OLI) sensor which will image the Earth from the next Landsat satellite. Equipped with 5 VNIR bands that collect 30 meter pixels, this new Landsat instrument will have spectral and spatial coverage similar to that of the Enhanced Thematic Mapper Plus (ETM+) found onboard Landsat 7. With upgrades such as a 12-bit quantizer and improved signal-to-noise ratios (SNR), however, the OLI instrument will be radiometrically superior to its predecessor. This enhanced radiometric fidelity coupled with the existing spatial resolution will provide the community with a sensor that is potentially state-of-the-art for the monitoring of our global water supply. This study is aimed at evaluating this potential. When used in conjunction with a thermal sensor, the OLI instrument should prove to be a powerful tool for solving sophisticated case 2 water problems.

The mouth of a river is an interesting area for those studying case 2 waters as environmental concerns are common in these regions. Runoff from rain events contaminate local streams and rivers with anthropogenic contaminants such as petroleum, pesticides, and fertilizers. In a given watershed, these suspended or dissolved contaminants will ultimately get deposited into a common area such as a lake or ocean and can negatively impact the

ecosystem. Taking advantage of our proximity to Lake Ontario and the Rochester Embayment, this research effort uses hydrodynamic modeling to describe the sedimentation process taking place in and around the mouth of the Genesee River. Since models are seldom perfect, remotely sensed thermal and reflective data can be used to calibrate the model and ensure that it accurately describes the river's flow.

The initial step to be taken in this research is the identification of an appropriate reflective sensor to be used throughout the study. Since the Genesee River plume and the surrounding embayment can be characterized as optically complex, a sensor with high radiometric fidelity is required to observe these waters from space. Due to its improved spectral coverage and radiometric characteristics, Landsat's OLI instrument exhibits great potential for studying case 2 waters. Accordingly, much of this research is aimed at evaluating this potential and demonstrating that OLI is state-of-the-art for monitoring inland and coastal waters. By modeling its spectral coverage, improved SNR, and 12-bit quantization we show that the next Landsat sensor is unique in its ability to study optically complex waters making it an ideal choice for this research.

In choosing this new Landsat instrument, however, a few complications arise. Due to exhaustive efforts made by the LDCM science team, it appears that the Thermal InfraRed Sensor (TIRS) will be included onboard the next Landsat satellite. This is great news for the Landsat Data Continuity Mission as the applications that have been demonstrated with its thermal data are endless. The OLI instrument remains the main priority of this mission, however, so some risk does still exist for the TIRS instrument. As a result, accommodations have been made for this work in the event that instruments such as MODIS have to be used to obtain thermal data. MODIS has a spatial resolution of 1 kilometer for its thermal bands while Landsat has 30 meter resolution for its reflective bands. In order to calibrate the hydrodynamic model as described in this work, these two resolutions should be nearly equal. Therefore, a need to radiometrically sharpen the thermal data presents itself. Using a modified version of an algorithm by [Robinson et al., 2000], a technique that will radiometrically sharpen 1 kilometer thermal data down to 30 meters will be demonstrated, enabling the data to match spatially. This approach represents a fall back only in the event that TIRS data are not available.

Secondly, existing atmospheric compensation algorithms for multispectral sensors over

case 2 waters are designed for instruments containing two near-infrared (NIR) bands. The new OLI sensor, however, will not be equipped with the bands necessary to utilize these current methods. In an effort to overcome this obstacle, a major thrust of this work is aimed at the development of atmospheric compensation techniques that are appropriate for the new Landsat OLI instrument. As OLI is expected to be a boon to the water community, developing techniques to atmospherically compensate its data is critical. Two algorithms are presented in this work, each taking advantage of OLI's improved spectral coverage and radiometric fidelity to compensate its data.

Lastly, if TIRS data are not available there will be calibration issues associated with using two separate platforms to collect the data. The hydrodynamic model that we use in this research works by accepting environmental inputs such as wind speed, river flow rate, meteorological conditions, etc. These inputs are used to solve a standard set of hydrostatic equations which yield sea surface temperatures and sediment deposition as outputs. Any error in defining these environmental parameters will lead to an inaccurate representation of the sedimentation process. Therefore, there will be a need to calibrate our model using the two forms of satellite data. By comparing observed thermal data to modeled sea surface temperatures and observed reflective data to modeled reflectances, our model can be calibrated and the sedimentation process can be accurately described. If these two forms of data are collected on separate platforms, there will be a time delay between calibration steps that needs to be addressed. In this work, we postulate a two step calibration process in which thermal data can be used to calibrate the plume's shape while the reflective data can be used to calibrate the plume's color. When observed data adequately matches the predicted data, our model is considered calibrated and the sedimentation and materials transport process can be described. Note that although this approach is intended for data which is collected from two different platforms, it can be used if both sensors are on the same platform as expected with the OLI and TIRS instruments.

A significant amount of background material is required to develop an understanding of how to model sedimentation and materials transport in a river plume. Therefore, after defining the objectives of this research in Chapter 2, the science and theory required for a general understanding of how satellite imagery can be used to study case 2 waters is introduced. In doing so, Chapter 3 describes the governing equation for sensor reaching ra-

diance, illustrates how this equation can be applied specifically to the constituent retrieval and surface temperature retrieval problems, and gives an overview of the hydrodynamic model that will be used to fuse the two processes. In Chapters 4 and 5, we further expand on these concepts by focusing on two major thrusts of this work. First, the new features of the OLI instrument are described and results of an experiment designed to evaluate its potential to be used for the constituent retrieval process are presented. Next, two OLI-specific over-water atmospheric compensation algorithms are developed in support of this research effort. Using these algorithms to account for the atmosphere, the constituent retrieval process is performed on both synthetic and real data to evaluate their efficiency. Finally, Chapter 6 describes the methods that enable thermal data to be used as a calibration tool for the ALGE hydrodynamic model and demonstrates these methods for the Genesee River plume on July 13th, 2009. Chapter 7 discusses the future of this work and makes recommendations on how to expand on the methods described in this dissertation.

Chapter 2

Objectives

The fusion of thermal and reflective data through the use of a hydrodynamic model in an effort to describe the sedimentation process occurring within a water body is a complex problem. A comprehensive description of such an effort is cumbersome and confusing to those not intimately involved in the process. Therefore, it is useful to segment problems of this nature into a series of smaller, more manageable tasks. Doing so allows one to monitor the overall success of their methods while providing a clear description of the modeling process.

The purpose of this chapter is to provide the reader with a description of the tasks that will be achieved in this research effort. In Section 2.1, a description of the overall goal of this research is provided. As this goal represents present and future work, Section 2.2 lists the tasks necessary for completion of this dissertation as well as some future objectives. In Section 2.3, a brief description of these tasks is given along with details of how their successful completion will be measured. Finally, this chapter closes with a section that describes this work's original contribution to the field of remote sensing and imaging science.

2.1 Problem Statement

The comprehensive goal of this research, including present and future work, is to use two forms of satellite data in conjunction with a hydrodynamic model to describe the water quality and sedimentation process in coastal waters. Specifically, one can use thermal and reflective data to calibrate the surface temperature and sediment profile predictions of a

hydrodynamic model, respectively.

In order to discuss the details of the problem addressed in this thesis, one must understand the comprehensive goal of the project. That is, how can reflective and thermal data be used to calibrate a hydrodynamic model and ultimately describe a river's discharge? Assuming for a moment that data can be perfectly registered spatially and atmospherically compensated, the model's calibration process can be illustrated with a flow chart.

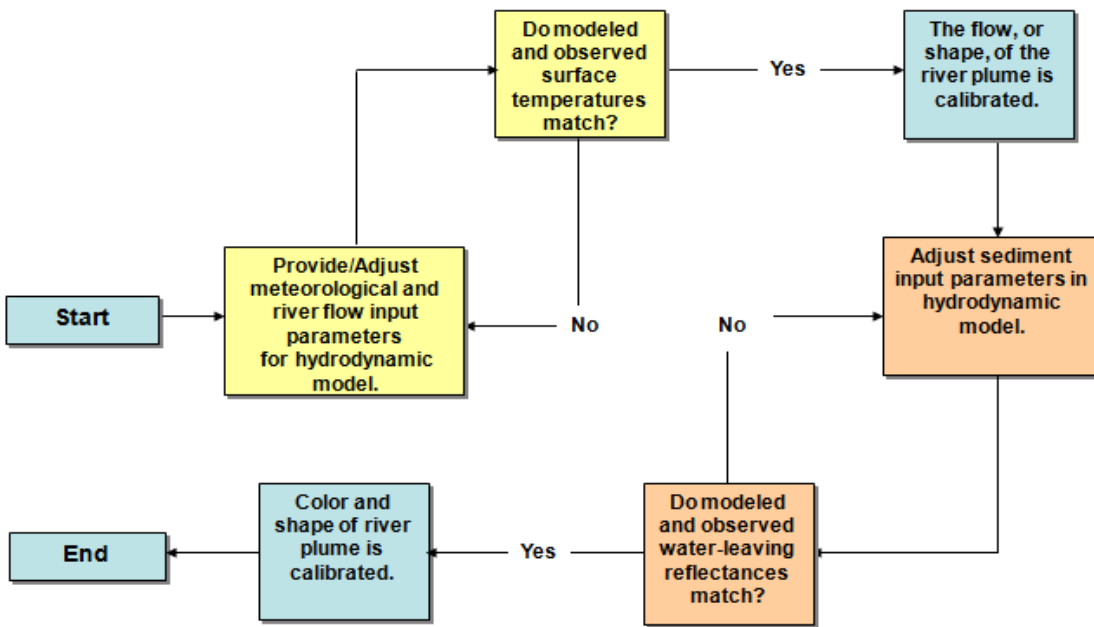


Figure 2.1: *Flow chart illustrating how atmospherically compensated, registered thermal and reflective data can be used to calibrate a hydrodynamic model.*

Starting from the left, Figure 2.1 shows the modeling process which begins with the user providing the hydrodynamic model with relevant environmental inputs from a scene. These inputs should accurately reflect the environmental conditions that encompass a scene of interest at the time of a collect. Once the model is applied, its predicted surface temperatures can be compared, in a least-squares sense, to the remotely sensed thermal data. In this thermal calibration loop, inputs that have a direct effect on the shape of a plume will be adjusted. If the modeled data does not match the observed data, inputs such as wind speed, wind direction, river temperature, and river flow rate can be adjusted until a

suitable match exists. Once a match is obtained, the input parameters that created the optimal model are fixed and the shape of the plume can be considered calibrated.

With fixed thermal calibration parameters in place, reflective data can now be used to calibrate the hydrodynamic model. Again, the model is applied and a comparison is made. This time, however, an emphasis is placed on adjusting the input parameters that will affect the plume's color. Inputs such as particle diameter, particle density, and river source concentration of particulates will be varied until the model's prediction of sediment load matches observed reflective data. Once a suitable match is obtained, both the shape and color of the river plume can be considered calibrated. To describe the sedimentation and materials transport process, the outputs of this optimized model can be observed.

The flow chart in Figure 2.1 depicts the hydrodynamic model's calibration process as being interactive in nature. It describes an iterative process in which inputs are adjusted based on the accuracy of outputs. Although this process does a nice job in illustrating what one hopes to accomplish when calibrating the model, it is not practical to perform this type of iterative method. To avoid extensive run times (hours or sometimes days) after a collection, multiple runs of the hydrodynamic model can be performed prior to a collect. This will eliminate the need to iterate by providing the user with a look-up table (LUT) of possible variations to the model. By identifying the parameters that will significantly affect the river plume, inputs to the model can be varied to obtain multiple simulations of the hydrodynamic process. Then, at the time of the collect, the observed data can be compared to the modeled data in the LUT to determine a suitable match.

Figure 2.1 also illustrates the calibration process under the assumptions that perfect atmospheric compensation can be performed and that the data are registered. Clearly, one's ability to characterize and accurately account for the atmosphere is essential to a well-calibrated model as poor atmospheric compensation will lead to a misrepresentation of observed surface temperatures and water reflectances. This misrepresentation will cause the hydrodynamic model to be poorly calibrated. The registration issues encountered in this work may be a little less obvious, however. Although it appears that TIRS will be included on the next Landsat satellite, there may still be some risk associated with this sensor. If the worst-case scenario occurs and TIRS data are not available for this work, the thermal and reflective data will need to be collected on two separate platforms. As

a result, not only will we need to register the two images spatially but we will need to account for the data temporally.

There are two major thrusts that this research will focus on, each of which will play an integral role in describing the sedimentation process. First, OLI's ability to retrieve water constituents will be rigorously tested and atmospheric compensation techniques designed specifically for this sensor will be created. Validating OLI and developing techniques to compensate its data is a critical first step toward calibrating a river plume's color. Secondly, this research will focus on using thermal data as a means to calibrate the shape of the Genesee River plume. By performing the thermal calibration, many of the techniques required by the overall calibration process (such as registration and radiometric sharpening) will be developed and demonstrated. With a comprehensive description of the process in place, the specific goals of this research effort can now be discussed.

2.2 Statement of Objectives

The successful completion of this research effort will be marked by the completion of the following primary requirements. Future objectives will be addressed if time permits.

Primary Requirements:

1. Evaluate the improved features of the OLI sensor and demonstrate its potential to be used in case 2 water quality studies.
2. Design an over-water, atmospheric compensation algorithm that is suitable for the OLI sensor and demonstrate its ability on synthetic and real data.
3. Demonstrate the ability to radiometrically sharpen moderate resolution thermal data with high resolution Landsat reflective data which will enable it to be used as a calibration tool for the hydrodynamic model. (Note that the method developed could be applied to TIRS data or MODIS data if TIRS data are not available.)
4. Develop a method that will enable Landsat-retrieved thermal data to be used as a calibration tool for a hydrodynamic model of the Genesee River plume.

Future Objectives:

5. Develop a method that will enable OLI reflective data to be used as a calibration tool for a hydrodynamic model of the Genesee River plume.
6. Develop a method that addresses the time issues associated with fusing both Landsat-retrieved thermal data and OLI reflective data, which will serve as calibration tools for a hydrodynamic model of the Genesee River plume.

2.3 Description of Tasks**2.3.1 Primary Requirements****1. Evaluate the improved features of the OLI sensor and demonstrate its potential to be used in case 2 water quality studies.**

The initial objective in this research is to identify a sensor that will be suitable for studying case 2 waters. An acceptable sensor must not only exhibit the spatial and radiometric fidelity that is necessary for monitoring optically complex waters but should also have global coverage and easily accessible data. To this end, OLI's potential to be used for water quality research will be evaluated. With a ground sample distance (GSD) of 30 meters, the OLI sensor is especially attractive as it has an adequate spatial resolution to monitor case 2 waters whose constituents vary on the order of tens of meters. Also, like its predecessors, its data will be free to the community. Historically, Landsat instruments have not been used for water research due to their inferior radiometric fidelity. Therefore, the first goal of this work is to demonstrate that the OLI instrument is spectrally and radiometrically sufficient to be used for the constituent retrieval process.

To perform this task, a model that incorporates the sensor's spectral responsivity, 12-bit quantization, and signal-to-noise ratios will be developed. This model will be used to evaluate OLI's ability to perform the constituent retrieval process by comparing it to the ability of its predecessor, the Enhanced Thematic Mapper Plus (ETM+). This multispectral sensor, which is currently onboard Landsat 7, has the necessary spatial resolution for monitoring case 2 waters but has insufficient spectral resolution and radiometric fidelity. Therefore, ETM+ will serve as a baseline to measure OLI's success against. Also included in this study is the Airborne Visible/Infrared Imaging Spectrometer (AVIRIS). With over

sixty bands in the VNIR, 12-bit quantization, and high signal-to-noise ratios, AVIRIS serves as a “best-case scenario” for the constituent retrieval process. Although we hope to achieve retrieval errors with OLI that are in-line with AVIRIS, the sensor will be accepted if it can obtain retrieval errors of under 10% of the range of the observed constituents in the scene.

The constituent retrieval process for the three sensors will be initially performed under the assumption that the atmosphere can be perfectly accounted for. Making this type of restriction enables us to measure the degradation to the water signal that results from just the sensor. If OLI cannot adequately retrieve water constituents under perfect atmospheric conditions then it has no hope of doing so under realistic conditions. Performing constituent retrieval in the presence of an atmosphere is an issue to be resolved in the next task.

2. Design an over-water, atmospheric compensation algorithm that is suitable for the OLI sensor and demonstrate its ability on synthetic and real data.

The second stage of the OLI sensor evaluation involves retrieving water constituents when atmospheric effects are included. Therefore, we wish to measure OLI’s ability to perform constituent retrieval in the presence of an atmosphere. Current atmospheric compensation algorithms that are designed for multispectral sensors typically involve employing a band ratio technique that makes use of two NIR bands. OLI, however, will only be equipped with one NIR band so this research focuses heavily on developing atmospheric compensation techniques that makes use of its unique “Aerosol Blue” band, its NIR band, and its shortwave infrared (SWIR) band.

Successful completion of this task can be measured by our ability to adequately remove the atmosphere in an effort to retrieve a water’s constituents. Retrieval errors of less than 15% of the range of observed constituents will be considered a success in this stage, [Raqueno et al., 2000].

3. Demonstrate the ability to radiometrically sharpen moderate resolution thermal data with high resolution Landsat reflective data which will enable it to be used as a calibration tool for the hydrodynamic model.

The next major objective that will be accomplished in this research is to develop a method that will use the reflective bands of Landsat to radiometrically sharpen lower resolution thermal data. This is a necessary step as the new Landsat satellite will either not be equipped with a thermal band or it will have a thermal instrument with reduced spatial resolution. High resolution surface temperatures still need to be obtained, however, in order to calibrate the hydrodynamic model. Sensors such as MODIS or NPOESS (National Polar-orbiting Operational Environmental Satellite System) contain the thermal bands necessary for temperature retrieval and adequate temporal coverage but lack the appropriate spatial resolution for coastal and inland water studies. Simulated data will be used in this work to demonstrate how the reflective bands of Landsat can be used to radiometrically sharpen the thermal bands of MODIS as a fall back if TIRS data are not available. If TIRS data are available, the same method will be applicable with better results because of the reduced difference in resolution and contemporaneous acquisition.

This demonstration will be performed by simulating 1 kilometer MODIS thermal data from 60 meter Landsat thermal data. The reflective bands of Landsat can then be used to sharpen the simulated imagery and the sharpened data compared to the original data to measure the success of the method. If time permits, 120 meter thermal data will be simulated and sharpened to 30 meters to show what we can expect if TIRS data are available.

4. Develop a method that will enable Landsat-retrieved thermal data to be used as a calibration tool for a hydrodynamic model of the Genesee River plume.

The final objectives addressed in this research are threefold and focus on the issue of calibrating the hydrodynamic model. The first involves the calibration of the modeled thermal data with Landsat-retrieved thermal data. This should be a straight forward task since the modeled data and observed data can be registered with a simple affine transform.

The thermal stage of the calibration process focuses on accurately modeling the shape of the Genesee River plume. Relevant input parameters to the hydrodynamic model will

be varied until the modeled data matches the observed data. This variation process will be captured in the form of a LUT and performed prior to a collect. Then, as thermal data become available, a nonlinear optimization routine can be used to search the LUT for the model whose output most suitably matches the observed thermal data. Once a model is chosen, the inputs are considered fixed and the plume’s motion is deemed calibrated. Success in this stage will be measured by our ability to accurately predict the plume’s shape as measured by temperature differences between modeled and measured surface temperature “images”.

2.3.2 Future Objectives

5. Develop a method that will enable OLI reflective data to be used as a calibration tool for a hydrodynamic model of the Genesee River plume.

This stage of the calibration process should prove to be a bit more difficult than the previous. In this task, the goal is to develop a method that will enable OLI’s reflective data to be used as a calibration tool for the hydrodynamic model. This reflective stage of the calibration process will focus on refining the “color” of the plume. In other words, the hydrodynamic model’s sediment input parameters will be varied until the modeled reflectance data matches the observed reflectance data. As in the thermal step, this variation process can be captured in the form of a LUT and performed prior to the collect. Additionally, an optimization routine can be used to search the LUT for a model that is most similar to the observed data.

Success in this stage will be measured by our ability to accurately calibrate the plume’s “color”. What makes this stage particularly difficult, however, is the form in which the model outputs the relevant data. The hydrodynamic model used in this research gives constituent profiles (concentrations as a function of depth) as one of its outputs. Developing a method to convert these profiles to water-leaving reflectances is imperative to enable the reflective calibration process. Therefore, success in this stage can only be achieved through a well developed conversion algorithm.

6. Develop a method that addresses the time issues associated with fusing both Landsat-retrieved thermal data and OLI reflective data, which serve as calibration tools for a hydrodynamic model of the Genesee River plume.

Steps 4 and 5 of this research effort focus on the calibration of the hydrodynamic model using thermal and reflective data, respectively. If TIRS data are not available for this research, a time-difference issue will arise from the utilization of two different platforms. A method to temporally fuse the two forms of data must be developed to enable a comprehensive calibration of the river plume model. The goal of this stage is to address these time-difference issues in an effort to develop a fully functional plume model that describes material transport in the Genesee River.

Success in this stage will be measured by our ability to effectively deal with the time issues associated with the imaging process and our ability to accurately characterize the sedimentation process occurring within the Genesee River plume.

2.4 Contribution to Field

The research described in this document will contribute to the field of remote sensing in several ways. Due to the spatial and radiometric limitations of current Earth-observing satellites, previous studies of water quality and material transport in coastal regions have used data assimilation with reflective satellite imagery in order to calibrate a hydrodynamic model [Li, 2007]. With the advent of the OLI sensor, the spatial and radiometric resolution required to characterize smaller river plumes has become available.

This work first contributes to the field of remote sensing by developing a method to evaluate a sensor's potential to be used for case 2 water quality studies. Specifically, we evaluate how OLI's addition of an aerosol blue band, a 12-bit quantizer, and improved signal-to-noise ratios affect its ability to perform constituent retrieval in the absence of atmospheric effects.

Secondly, an unforeseen side effect arises from our desire to utilize OLI data. Traditional algorithms designed to atmospherically compensate multispectral data collected over case 2 waters implement a two NIR band ratio method. As OLI will not be equipped with the

appropriate bands necessary to utilize such techniques, this research develops an OLI-specific, over-water atmospheric compensation algorithm. Insofar as the data from OLI are expected to improve case 2 water studies, a compensation algorithm to support such a sensor is imperative.

Finally, due to the improved technology of the new Landsat satellite, by fusing thermal and reflective data in an effort to calibrate a hydrodynamic model we can characterize the entire three-dimensional structure of a river plume. Although this work does not address the complete calibration process, the thermal portion which predicts a plume's shape is demonstrated. Additionally, a radiometric sharpening technique which uses high resolution reflectance data to sharpen moderate resolution thermal data is proposed which will enable the success of the thermal calibration process. The following chapter gives an overview of the background materials that are necessary to achieve such goals.

Chapter 3

Background and Theory

The science of remote sensing can be broadly described as the collection of light from a remote location to obtain information about a target. Specifically, when remotely imaging the Earth, photons are collected by placing a sensor on an airborne instrument or satellite and flying over an area of interest. This research focuses on fusing thermal and reflective satellite imagery in an effort to describe the processes occurring within a water body. The goal of this chapter is to develop the necessary concepts for an understanding of the science behind such a problem. We begin with a section that describes the paths light may encounter as it travels from the Sun to the sensor. Next, a discussion of how these various light paths can be separated to obtain useful information about a water body is presented. Lastly, a hydrodynamic model is introduced that can be used in conjunction with satellite imagery to describe the processes occurring at depth within the water.

3.1 Sensor-Reaching Radiance

Loosely defined, *sensor-reaching radiance* is the accumulation of photons at the front of a sensor that one wishes to collect in an effort to obtain information about a target. Photons can travel many different paths before reaching the front of a sensor. The origin of most of the light that will be collected in this context can be traced back to the Sun. Therefore, we will begin our development in this section by observing how energy is transported from the Sun to the Earth. The paths that these photons may encounter once they enter the Earth's atmosphere and how they may ultimately end up at the front of a sensor are detailed.

3.1.1 Exoatmospheric Irradiance

At the core of the Sun, the proton-proton cycle is an exothermic process that produces a tremendous amount of energy in the form of photons. These high-energy photons have a tendency to interact strongly with matter so they are repeatedly scattered, absorbed, and reemitted by the dense solar mass. As a result of these continuous interactions, longer wavelength photons eventually make their way to the surface of the Sun. These photons, whose wavelengths are primarily in the visible and near-infrared portion of the spectrum, are emitted from the Sun in all directions. Only a small fraction of this energy ever reaches the Earth and it is this fraction that we wish to study.

[Schott, 1997] shows that the total energy per unit area just outside the Earth's atmosphere originating from the Sun is approximately $1390 \frac{W}{m^2}$, (see Appendix A for a summary of the derivation). This energy is known as the *exoatmospheric irradiance* (E'_s) and is an integrated value that is typically described at the mean Earth-Sun distance. Sometimes it is useful to describe this irradiance spectrally (as a function of wavelength). Particularly, when working with sensors, one may only wish to detect light over a certain bandpass. When this is the case, we must account for the wavelength-dependent nature of exoatmospheric irradiance.

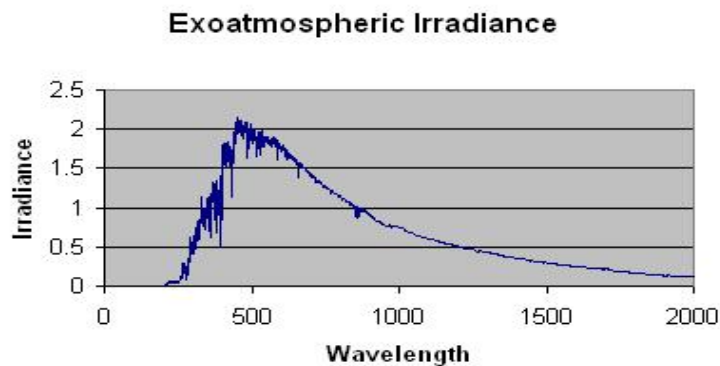


Figure 3.1: *Exoatmospheric Irradiance* ($\frac{W}{m^2_{nm}}$) as a function of wavelength (nm).

Figure 3.1 shows the magnitude of exoatmospheric irradiance per nanometer over a small window of the EM-spectrum. Representing irradiance in this fashion allows us to work over a desired wavelength interval. Therefore, we are not restricted to simply de-

scribing the total exoatmospheric energy but rather, we can describe the energy at desired wavelengths. With an understanding of exoatmospheric irradiance, we can discuss what may happen to photons as they enter the Earth's atmosphere.

3.1.2 Solar Paths

The phrase *solar paths* refers to the paths that photons originating from the Sun may take as they enter the Earth's atmosphere and ultimately end up at the front of the sensor. Not all photons that reach a sensor interact with the target of interest so a major goal of remote sensing is to isolate these photons from the total sensor-reaching radiance in an effort to describe the target. Therefore, a comprehensive knowledge of the possible solar paths is imperative. Figure 3.2 shows the major solar contributions to sensor-reaching radiance.

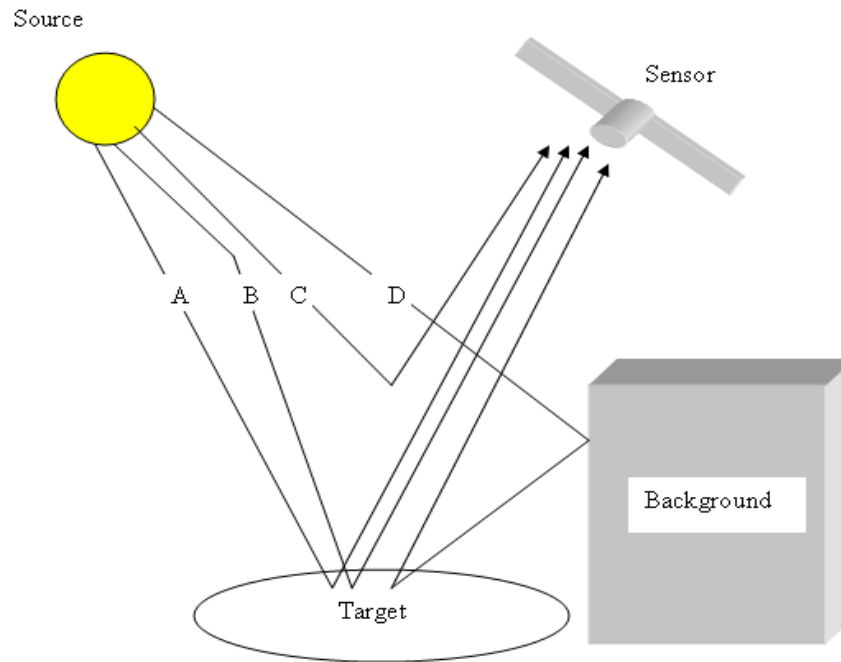


Figure 3.2: *Major solar paths contributing to sensor-reaching radiance.*

Path A can simply be described as photons from the Sun that pass through the Earth's atmosphere, reflect off a target, and again pass through the atmosphere on their way to the sensor. Path B, which is sometimes referred to as skylight, represent photons that are

scattered by the Earth’s atmosphere before reflecting off the target in the direction of the sensor. It is this path of light that allows us to see objects which are shadowed from direct solar photons. Path C shows light that originates from the Sun and gets scattered by the atmosphere in the direction of the sensor without any contact with the target. These photons offer no information about the target we are trying to observe. Lastly, light from path D represents photons from the Sun that travel through the atmosphere, reflect off some background object, and reflect off the target in the direction of the sensor.

All the solar paths discussed above contribute to the total sensor-reaching radiance. By isolating the photons that have interacted with a target, we can begin to describe its reflective properties. Knowledge of the reflective properties of an object is an important first step to determining its composition.

3.1.3 Thermal Paths

The paths described in Section 3.1.2 represent the major contributions to sensor-reaching radiance from light that originates from the Sun. Photons can also originate from the objects within a scene. These photons are known as *self-emitted* or *thermal* photons as they offer insight into the temperature of objects (similar to the way solar photons describe the reflective properties of objects). Figure 3.3 illustrates the self-emitted components of sensor-reaching radiance.

Path E can be described as photons that are self-emitted from the atmosphere, reflect off the target, and propagate to the front of the sensor. Path F also shows photons that are self-emitted from the atmosphere. However, they differ from those in path E in that they have no interaction with the target on their way to the sensor. Path G shows photons reaching the sensor that are self-emitted from the target. This path carries the dominant signal necessary to describe a target’s thermal properties. Lastly, objects in the background of a scene can self-emit photons that may reflect off the target on their way to the sensor. These photons are described by path H.

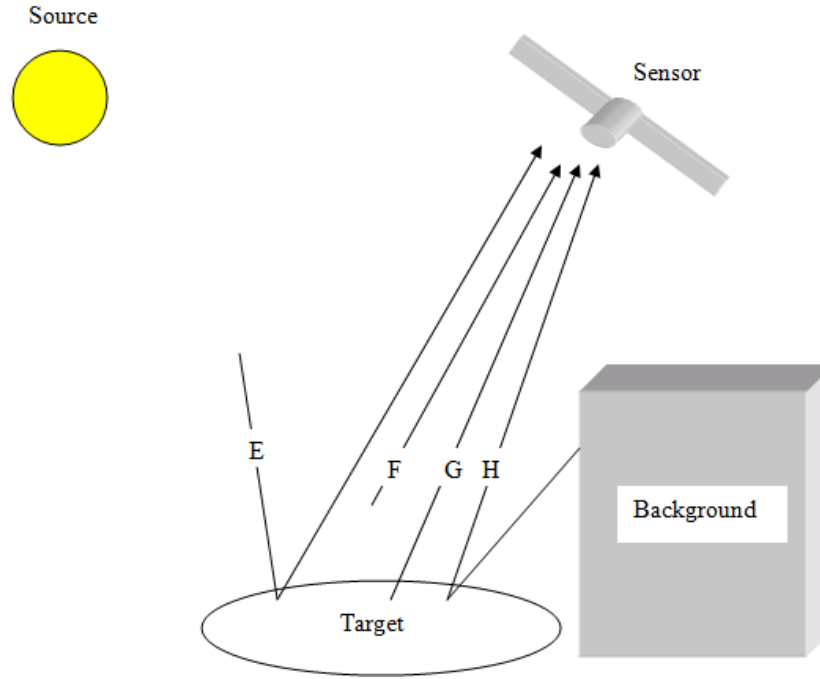


Figure 3.3: *Major self-emitted paths contributing to sensor-reaching radiance.*

As with solar paths, all the thermal paths discussed above contribute to sensor-reaching radiance. To determine the temperature of objects from photons in the thermal spectrum, we must isolate only the photons that interact with the target. Knowing the temperature of objects is another useful step towards describing the target.

3.1.4 Governing Equation

The previous sections describe the major contributions of radiance reaching the front of a sensor in a qualitative fashion. In order to process data received by a sensor, however, we must develop a quantitative description of this radiance. Conveniently, the total sensor-reaching radiance can be described as simply the sum of the radiances due to the individual solar and thermal paths,

$$L_T = L_A + L_B + L_C + L_D + L_E + L_F + L_G + L_H. \quad (3.1)$$

Since the water bodies that we are interested in imaging are typically several kilometers wide, we can assume that radiance from the background (L_D and L_H) does not contribute to total sensor-reaching radiance. Additionally, by making a simplifying assumption that the target we are imaging is approximately Lambertian (radiance is equal in all directions), [Schott, 1997] describes Equation 3.1 as

$$L(\lambda) = \frac{E'_s(\lambda) \cos \sigma' r(\lambda) \tau_1(\lambda) \tau_2(\lambda)}{\pi} + \frac{E_{ds}(\lambda) r(\lambda) \tau_2(\lambda)}{\pi} + L_{us}(\lambda) \quad (3.2)$$

for the solar terms and

$$L(\lambda) = \frac{E_{d\epsilon}(\lambda) r(\lambda) \tau_2(\lambda)}{\pi} + L_{u\epsilon}(\lambda) + \epsilon(\lambda) L_T(\lambda) \tau_2(\lambda) \quad (3.3)$$

for the self-emitted terms, where:

$L(\lambda)$	total sensor-reaching radiance
$E'_s(\lambda)$	exoatmospheric spectral irradiance
σ'	solar-zenith angle
$r(\lambda)$	spectral reflectance of target
$\tau_1(\lambda)$	Sun-target path transmission of atmosphere
$\tau_2(\lambda)$	target-sensor path transmission of atmosphere
$E_d(\lambda)$	downwelling irradiance
$L_u(\lambda)$	upwelling radiance
$\epsilon(\lambda)$	emissivity of target
$L_T(\lambda)$	radiance emitted from target

Notice that to distinguish between components in Equations 3.2 and 3.3, the subscript (s) is used for the solar (reflective) terms and (ϵ) is used for the emissive (thermal) terms. [Schott, 1997] shows that in the reflective wavelength region of the EM spectrum (approximately 0.3 – 2.5 microns) the terms in Equation 3.2 will be so many orders of magnitude larger than those in Equation 3.3 that the thermal terms can be dropped from the analysis over these wavelengths. Similarly, in the thermal region (approximately 8 – 14 microns) the terms in Equation 3.3 will be so many orders of magnitude larger than those in Equation 3.2 that the reflective terms can be dropped from the analysis over these wavelengths.

It should also be emphasized that Equations 3.2 and 3.3 hold only in the special case where we can assume that our target is approximately Lambertian. If this is not a valid assumption, then a target's bidirectional reflectance distribution function (BRDF) must be considered to account for the angular distribution of its reflectance. This can be a complicated implementation so whenever possible, the Lambertian assumption is desirable.

3.2 Constituent Retrieval

So far the paths contributing to sensor-reaching radiance have been described in a generic fashion that is applicable to most problems in remote sensing. In the special case where remotely sensed reflective data is used to determine the constituents in a water body, a new set of paths must be described. In this section, the constituent retrieval process is introduced and the paths of light that contribute to sensor-reaching radiance from a water body are described in detail.

3.2.1 The Rochester Embayment

As mentioned in Chapter 1, the ability to achieve a continuous monitoring of the Earth's fresh water supply is an ongoing effort in the remote sensing community. Satellite data can be used to determine the constituents contained in a water body. By determining the levels of biological activity occurring in a lake or pond, the condition of the water body can be characterized.

Figure 3.4 shows an RGB image of the embayment located just north of Rochester, NY which was obtained from the AVIRIS hyperspectral sensor on May 20, 1999. This data set is particularly useful due to the wide range of water bodies contained in the scene. For example, Lake Ontario can be classified as oligotrophic due to its low levels of biological activity. Long Pond, on the other hand, is in a eutrophic state due to the high levels of chlorophyll observed in the water body. The other ponds across this scene reflect a variety of trophic states that can occur in water, making this scene especially useful for validating our constituent retrieval methods.



Figure 3.4: *RGB image of the Rochester Embayment illustrating the various lakes and ponds in the area.*

3.2.2 Paths Contributing to Constituent Retrieval

In remote sensing, the imaging of water is unique in that the medium is transparent over a small window of the EM-spectrum. Therefore, light can actually penetrate the water and interact with its constituents. This interaction offers insight into what is contained in a water body. Specifically, the nature of how photons are absorbed or scattered in the medium allows us to determine its optical properties. Once the optical properties of a water body are known, the constituents that it contains can be determined. Therefore, collecting the light that is scattered out of a water body is a necessary first step in determining what is in the medium.

Analyzing this water-leaving signal is a formidable task. First, the instrument that we use to collect light is typically 700 kilometers away from our target. Secondly, recalling Equation 3.1, the radiance a sensor receives is the sum of many contributors. Therefore, to determine the constituents in a water body we must separate the signal just above its surface from the total signal received by the sensor. This process of isolating the water-leaving signal in an effort to determine the concentrations of a water body's constituents is

known as *constituent retrieval*. Figure 3.5 shows the five paths of light that will be relevant in performing the constituent retrieval process on an imaged water pixel.

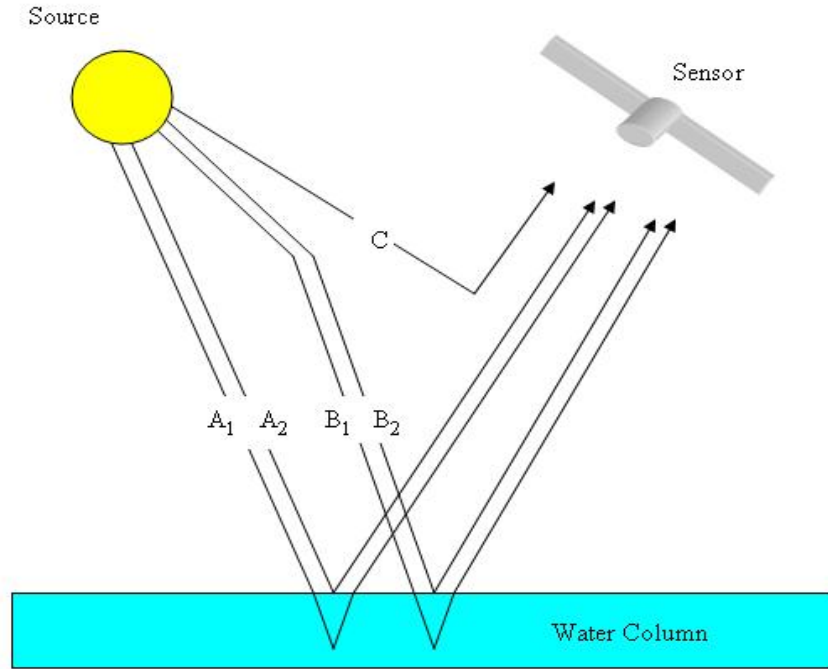


Figure 3.5: *Contributions to sensor-reaching radiance from an imaged water pixel.*

Paths A_1 and B_1 contain the photons that we wish to isolate from the total signal received by a sensor as only these paths interact with the water at depth. Path A_1 shows the direct solar light that enters the water column while path B_1 illustrates the corresponding skylight contributor. Light reaching the sensor along paths A_2 and B_2 represent signal due to solar and sky glint, respectively, which results from the Fresnel reflection of light off the water's surface. This undesirable signal is typically subtracted from the total radiance at the front of the sensor with the use of a glint removal algorithm. Finally, path C represents light that reaches the sensor after it is scattered by the atmosphere. This signal must also be subtracted from the total sensor-reaching radiance as it offers no information about the water body. A variety of atmospheric compensation algorithms exist to perform this task.

One should notice that all five paths described thus far are solar contributors, i.e., thermal paths do not carry any information about the nature of a water body's constituents. This stems from the fact that water is a strong absorber of light except in the visible and

near-infrared (VNIR), which makes up a very small portion of the EM-spectrum. Therefore, photons whose wavelengths differ from those contained in this window can only penetrate water up to a couple of millimeters. Accordingly, these photons offer no information about the constituents contained at depth in the water body. Figure 3.6 shows a plot of spectral absorption for pure water and pure seawater. This figure illustrates the window where absorption is at a minimum. Due to this absorptive nature of water, we are confined to using light in the VNIR to perform constituent retrieval.

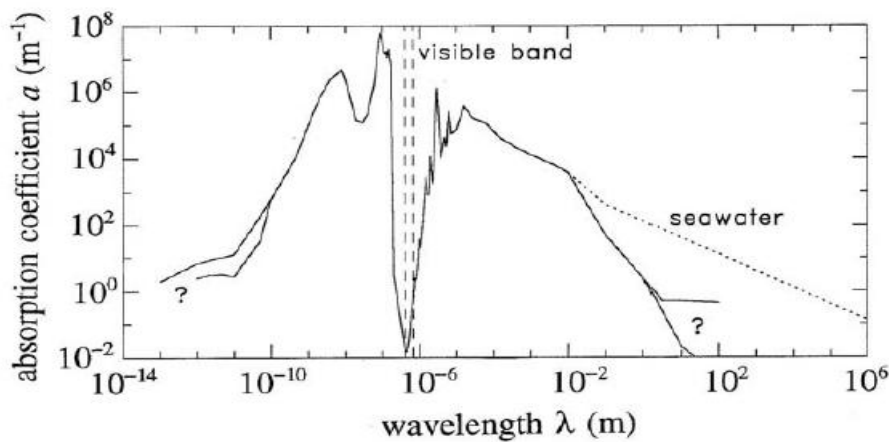


Figure 3.6: *Spectral absorption coefficients for pure water (solid line) and pure seawater (dashed line). [Data taken from [Hale and Querry, 1973], [Jackson, 1975], [Smith and Baker, 1981], [Zoloratev and Demin, 1977] and compiled in [Mobley, 1994]]*

The fact that we can only use a small window of the EM-spectrum to perform constituent retrieval makes this process somewhat daunting. We are further hindered by the fact that paths A_1 and B_1 , the desired signals, make up only a small fraction of the total sensor-reaching radiance. Therefore, to accurately perform constituent retrieval we must efficiently preserve these signals. To do so, a comprehensive knowledge of the five paths in Figure 3.5 is required.

3.2.3 The Water Column

Path A_1 from Figure 3.5 describes light originating from the Sun that enters the Earth's atmosphere, interacts with the water, and reaches the front of the sensor. It is this path of

light that we will initially investigate as we are particularly interested in how the light is attenuated as it enters the *water column*, a conceptual volume just below the sea surface which contains the materials we wish to study. Knowledge of this attenuation is the crux behind the constituent retrieval process. (A similar discussion can be held for path B_1 in Figure 3.5, or skylight, as it also interacts with the water column.)

We will begin our analysis of path A_1 from within the water. As light passes through the air-water interface and enters a water column it encounters a variety of particles. Water molecules, suspended sediments, bacteria, viruses, phytoplankton are just a few examples of the particles found in a water column. These constituents can affect the optical properties of the media, which determines how incident light will be attenuated. Specifically, [Mobley, 1994] describes the attenuation of water with its complex index of refraction, $m = n - ik$. The real part, n , governs scattering within the medium, which is caused by thermal, salinity, or other fluctuations of n . The imaginary part, k , governs absorption in the medium as [Kerker, 1969] relates them by

$$a(\lambda) = \frac{4\pi k(\lambda)}{\lambda}. \quad (3.4)$$

Describing the attenuation of light at such a microscopic level is not fruitful, however. To perform constituent retrieval, we must obtain all of the light that is scattered from a water column. Therefore, we tend to view light on a macro scale. Accordingly, there are large-scale properties associated with a body of water that will affect its interaction with light.

Inherent optical properties (IOPs) are those properties that depend only upon the medium, and therefore are independent of the ambient light field within the medium. The *absorption* and *scattering coefficients* are major IOPs that are used to characterize a water column. These values describe the magnitude of light that will be absorbed or scattered in an arbitrarily small volume of water. The *volume scattering phase function* is another important IOP that accounts for the angular distribution of the scattering. See Appendix B for a partial treatment or [Mobley, 1994] for a full treatment on these IOPs.

Apparent optical properties (AOPs) are properties that also depend on the nature of the constituents found in the medium. They differ from IOPs, however, in that they

account for the angular distribution of the ambient light field. This is a somewhat intuitive characteristic since a water body's appearance can vary throughout the day. The remote-sensing reflectance, shown in Equation 3.5, is an example of an AOP as this useful measure describes how much of the total incident downwelling irradiance is ultimately returned from a water column in a given viewing direction.

$$R_{RS}(\theta, \phi, \lambda, z = a) = \frac{L(\theta, \phi, \lambda, z = a)}{E_d(\lambda, z = a)} \left[\frac{1}{sr} \right] \quad (3.5)$$

where:

θ	sensor-zenith angle
ϕ	sensor-azimuth angle
L	water-leaving radiance
E_d	total downwelling irradiance
λ	wavelength dependent
a	height just above the water's surface.

It is this signal, which can be measured just above the water's surface ($z = a$), that we look to isolate from the total sensor-reaching radiance when performing the constituent retrieval process. By making the simplifying assumption that the water bodies studied in this research are approximately Lambertian for near nadir viewing, Equation 3.5 can be multiplied by π to obtain an irradiance reflectance. This allows us to use Equation 3.2 to determine the sensor-reaching radiance due to the water column.

Describing a water body according to its bulk optical properties implies that we have to make some generalizations about its constituents. For example, two species of bacteria with equal concentrations within a water body may scatter and absorb light identically. As a result, we can not distinguish between the two from a satellite. Therefore, a mutually exclusive partitioning of optical properties is needed to perform constituent retrieval. Contained within each subset of this partitioning are particles with similar optical properties. Figure 3.7 illustrates a common grouping of optical properties by showing each subset's interaction with incident light.

Path *I* shows the influence of bottom effects on the signal. Depending on the depth and

clarity of the water, the bottom can have a varying effect on the water's color. The nature of the floor's coverage will also influence the water-leaving signal. As this work only investigates river plumes where the water is assumed to be significantly deep, bottom reflectance does not contribute to sensor-reaching radiance. The interested reader can incorporate bottom effects by referring to [Gordon and Brown, 1974], [Leathers and McCormick, 1999], [S. Maritorena and Gentili, 1994], or [Wilson, 2000].

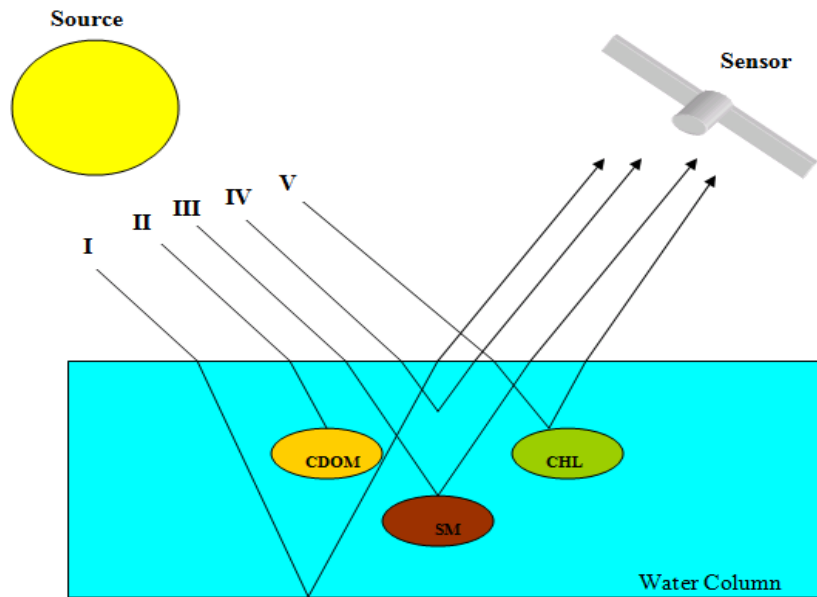


Figure 3.7: *Contributions to sensor-reaching radiance from the water column.*

Path *II* illustrates the influence of colored-dissolved organic matter (CDOM) on the remote-sensing reflectance. CDOM is made up of organic, dissolved substances originating from the degradation of phytoplankton or from distant sources such as runoff from organic rich soils. The optical properties of this water constituent are dominated by its absorption characteristics so to detect CDOM, we actually look for a “lack-of-signal” above the water’s surface. If its absorption is known for a reference wavelength λ_o then CDOM’s absorption is spectrally well-defined according to

$$a_y(\lambda) = a_y(\lambda_o)e^{[-0.014(\lambda-\lambda_o)]}, \quad (3.6)$$

over the interval [350nm,700nm], where $a_y(\lambda_o)$ is the absorption due to yellow matter at the reference wavelength [Bricaud et al., 1981].

Path *III* shows the case where light entering the column is scattered and absorbed by inorganic suspended materials. This category is somewhat loosely defined since the materials it includes can vary significantly. For example, sands can have a much different effect on the remote-sensing reflectance than soil. Also, the particle size can influence the optical properties of the water. The nature of suspended materials reflect the surrounding environment and is, therefore, scene dependent. Typically, to measure the scattering due to particles in natural water, any undissolved material is treated as a particle. The particle scattering function, $\beta_p(\psi; \lambda)$, is determined by subtracting the function due to pure water from the measured function from a sample and is summarized by

$$\beta_p(\psi; \lambda) \equiv \beta(\psi; \lambda) - \beta_w(\psi; \lambda), \quad (3.7)$$

where $\beta(\psi; \lambda)$ is the observed scattering function of a sample and $\beta_w(\psi; \lambda)$ is the scattering function due to pure water. Determining $\beta_p(\psi; \lambda)$ can be a daunting task, however, due to difficulties in accurately calculating $\beta(\psi; \lambda)$ when suspended particles are present.

Path *IV* represents the scattering and absorption of light by “pure water”. This theoretical medium represents water which is free from particles other than the water molecules. Since case 2 waters can range from inland lakes to the coastal region of oceans, the nature of pure water can vary slightly. Therefore, one must distinguish between pure water of inland lakes and pure *seawater* of the oceans to allow for varying IOPs due to dissolved salts. The most recent absorption coefficients for pure water were measured using an integrating cavity by [Pope and Fry, 1997] and are shown Figure 3.8(a). The scattering coefficients for pure water as derived by [Smith and Baker, 1981] are shown in Figure 3.8(b).

Lastly, path *V* shows the case where light entering the column is scattered and absorbed by phytoplankton. Phytoplankton are microscopic organisms found in the illuminated portions of water and can dramatically affect its optical properties. Since thousands of different species of phytoplankton can be found in natural water, they will invariably be referred to as chlorophyll throughout this work (named after their main pigment chlorophyll-a). Phytoplankton cells tend to be strong absorbers of visible light

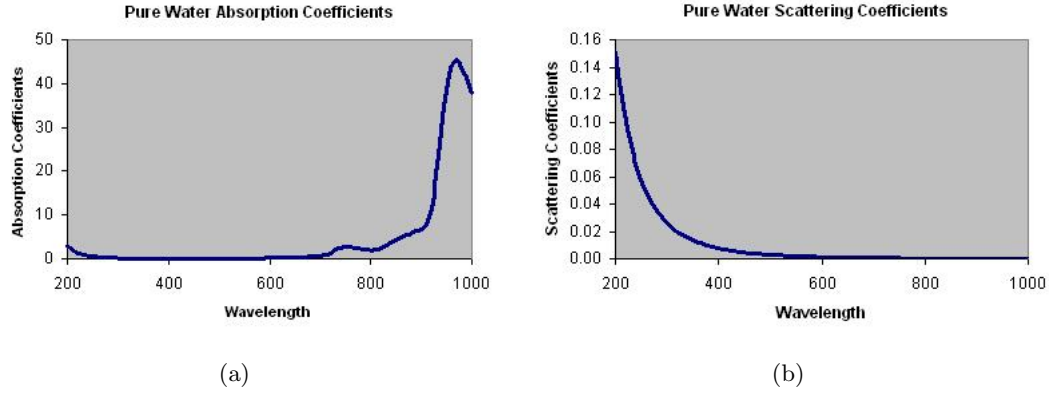


Figure 3.8: (a) shows the absorption coefficients for pure water as a function of wavelength as measured by [Pope and Fry, 1997] and (b) shows its corresponding scattering coefficients as derived by [Smith and Baker, 1981].

[Mobley, 1994], particularly at the blue and red ends of the visible spectrum (chlorophyll-a has peak absorption bands at 430nm and 665nm).

With all the paths of Figure 3.7 defined, the total absorption and scattering coefficients for a water body can be described by the equations

$$a(\lambda) = a_{H_2O} + C_{CHL} a_{CHL}^*(\lambda) + C_{SM} a_{SM}^*(\lambda) + C_{CDOM} a_{CDOM}^*(\lambda) \quad (3.8)$$

$$b(\lambda) = b_{H_2O} + C_{CHL} b_{CHL}^*(\lambda) + C_{SM} b_{SM}^*(\lambda), \quad (3.9)$$

respectively, where C_i describes a constituent's concentration, $a_i^*(\lambda)$ describes a constituent's spectral absorption cross section, and $b_i^*(\lambda)$ describes a constituent's spectral scattering cross section. Recall that CDOM will be treated as only an absorber in this work.

3.2.4 Sun Glint

Referring again to Figure 3.5, path A_2 shows direct solar photons that reflect off the surface of the water in the direction of the sensor and path B_2 shows an analogous surface reflection due to skylight. This phenomenon, known as glint, is an unwelcome signal that results from the Fresnel reflection of light at the air-water interface. Since this light reflects off the surface of the water, it does not provide any information about the constituents contained within a water column. Instead, it can flood a detector ruining any signal received by the

sensor. For this reason, many instruments are designed with the ability to tilt away from the incident angle, avoiding unwanted glint.

Water is a dynamic body, however, whose surface can change shape as a result of a change in variables such as wind speed or tidal forces. Therefore, it helps to conceptually think of a water's surface as being made up of thousands of little facets. Only those facets which are oriented at the appropriate angle will illuminate the sensor with solar glint. On the other hand, sky glint is always present in an image as every facet of water reflects some portion of the sky. Figure 3.9 illustrates the two types of glint that may be received by a sensor.

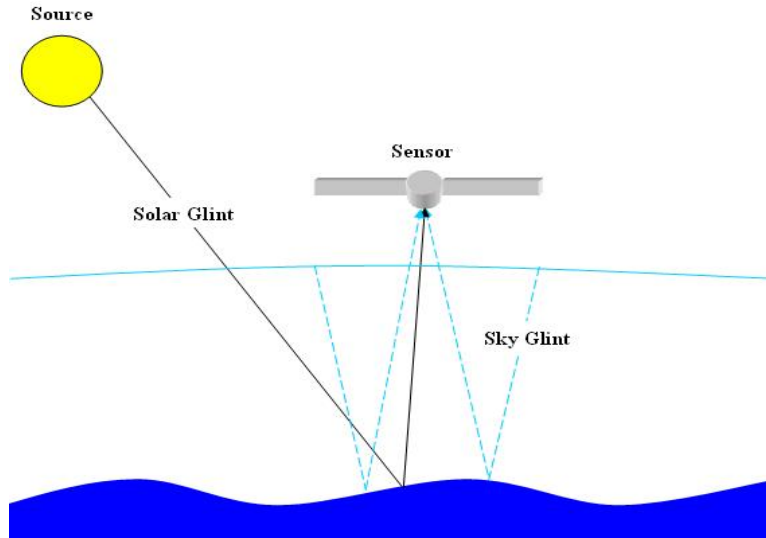


Figure 3.9: *Sketch of solar and sky glint.*

Glint removal algorithms can be used to account for the solar glint in an image (one such method is described in Section 4.2.1). When imaging from nadir, traditional atmospheric compensation algorithms (e.g., [Gordon and Wang, 1994], [Ruddick et al., 2000]) treat sky glint as an insignificant contributor to sensor-reaching radiance. Therefore, the contribution of sky glint to the total sensor-reaching signal will be treated as negligible in this research.

3.2.5 The Atmosphere

Section 3.2.3 describes how light encountering the constituents of a water column can undergo either scattering or absorption processes. Similarly, as light travels through the

atmosphere, reflects off a target and ultimately reaches the front of a sensor, these same interactions can occur. The atmosphere is itself a medium with a variety of constituents such as gas molecules and aerosols. The optical properties of these constituents will determine how light is attenuated by the atmosphere. This section briefly describes the absorption and scattering of light by atmospheric constituents and introduces a measure to describe the attenuation of light.

Atmospheric absorption is defined as the removal of electromagnetic energy from a beam by converting it to another form of energy, usually thermal [Schott, 1997]. This occurs when an incident photon induces a molecular vibration, rotation, or electron orbital transition to an excited energy state in the constituent molecules of the atmosphere. In ordinary gases this excitation energy will rapidly be transferred to a lower energy state, via collisions, before a lower energy photon is emitted [Hecht, 1990]. Absorption events are discrete in nature so only photons of select wavelengths will be absorbed by the atmosphere's constituent molecules. However, interactions between gas molecules will cause perturbations in their energy states which results in a broadening of the absorption features. When these broadened lines are close enough to each other, they combine to form an *absorption continuum* [Schott, 1997].

Sometimes it is the case that incident light gets absorbed by a molecule and is immediately re-emitted at the same wavelength. This re-emission can occur in any direction and is known as *scattering*. In a given volume of air, a variety of particle shapes and sizes may exist. Therefore, to precisely characterize the scattering processes that will occur in the volume is impossible. Gustav Mie, however, developed a complete analytical solution to describe the scattering of light by spherical particles in a medium. The Mie solution, referred to as *Mie scattering*, is valid for particles of any size.

Scattering involving particles that are much smaller than the incident wavelength are said to undergo *Rayleigh scattering*, whose intensity was determined by Lord Rayleigh to be dependent on wavelength according to

$$I \propto \frac{1}{\lambda^4}. \quad (3.10)$$

The Mie solution for particles that are much smaller than the incident wavelength are in good agreement with Rayleigh's determination.

The atmosphere also contains particles, such as aerosols or water droplets, whose size is equal to or greater than the wavelength of incident light. Particles whose size is similar to the wavelength of the incident light are said to undergo the process of *Mie scattering*, as the Mie solution describes this process well. The scattering due to particles whose size is much greater than the wavelength of incident light can be described with geometrical optics and is said to undergo *nonselective scattering*, which indicates how the scattering is independent of wavelength for such large particles.

Most of the scattering in the atmosphere results from the molecules and aerosols in the lower atmosphere, or boundary layer. This is due to the density of the constituents in this layer compared to the rest of the atmosphere. Therefore, multiple-scatter effects in this lower kilometer of the atmosphere can greatly influence the amount of light received at the sensor.

Atmospheric transmission is a measure that describes the ability of light to travel through the medium. This term incorporates both absorption and scattering into atmospheric attenuation by

$$\tau = e^{-(\beta_\alpha + \beta_r + \beta_a + \beta_{ns})z} \quad (3.11)$$

where:

τ is total transmission along a homogeneous path

β_α is the fractional amount of flux absorbed per unit length

β_r is the fractional amount of flux lost due to Rayleigh scatter per unit length

β_a is the fractional amount of flux lost due to Mie scatter per unit length

β_{ns} is the fractional amount of flux lost due to nonselective scatter per unit length

Figure 3.10 shows the total transmission of Earth's atmosphere over a typical scene in the summer for the mid-latitudes.

With the previous discussion in mind, path C in Figure 3.5 shows the upwelling radiance received at the front of the sensor. This signal contains photons originating from the Sun that get scattered in the direction of the sensor by the atmosphere before ever reaching the

water. Obviously, when studying water constituents, this is an undesired contribution to the sensor-reaching radiance and must be removed through a process called atmospheric correction, or compensation. We will investigate a variety of compensation algorithms in this work but only report results for the most effective.

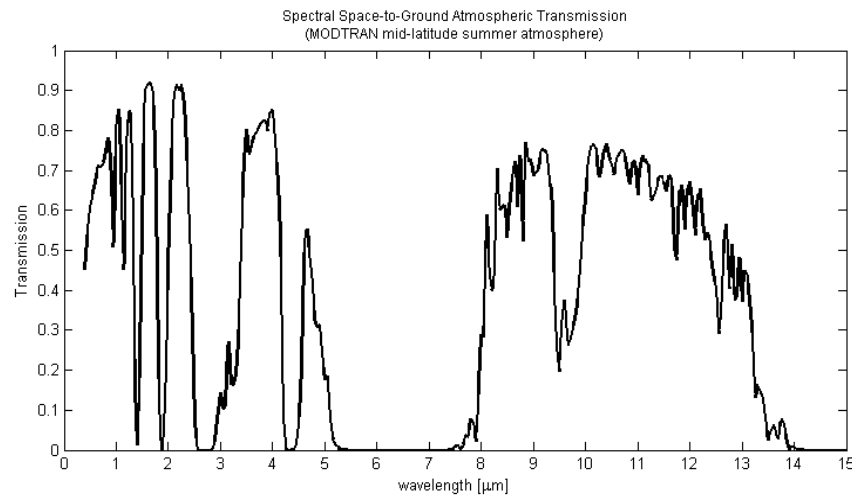


Figure 3.10: *Plot of total transmission from 0 to 15 microns for a typical mid-latitude, summer scene containing rural aerosols. This plot was generated using the Moderate Resolution Atmospheric Transmittance Code (MODTRAN).*

3.2.6 The Sensor

The previous sections describe the various paths that light may follow on its journey from the Sun, to the target, and ultimately to the front of the sensor. In order to utilize sensor-reaching radiance, however, we must pass the light through an instrument in an effort to record the energy. Therefore, we can sample light by passing it through optics, filtering out the desired wavelengths, submitting it to a quantization process, the entire time subjecting it to system noise. Figure 3.11 shows a generic illustration of the process involved in passing a signal through a sensor.

The ability to capture this sensor-reaching radiance comes at a cost. The sensor's interpretation of a signal is a degenerated version of the original signal at the front of the sensor. If we assume the ideal scenario where we have diffraction limited optics, the first major degradation of light comes from our desire to selectively choose specific wavelengths. This selection process is typically performed with filters or diffraction gratings placed in

front of the detector elements. Filters act by allowing only specific wavelengths of light to pass while a diffraction grating disperses the light into its spectrum enabling us to capture desired wavelengths with appropriately placed detectors. Since the inherent purpose of these instruments is to allow the user to selectively choose wavelengths from the original beam, the number of photons received by each detector is reduced. Therefore our signal-to-noise will be lowered through this process.

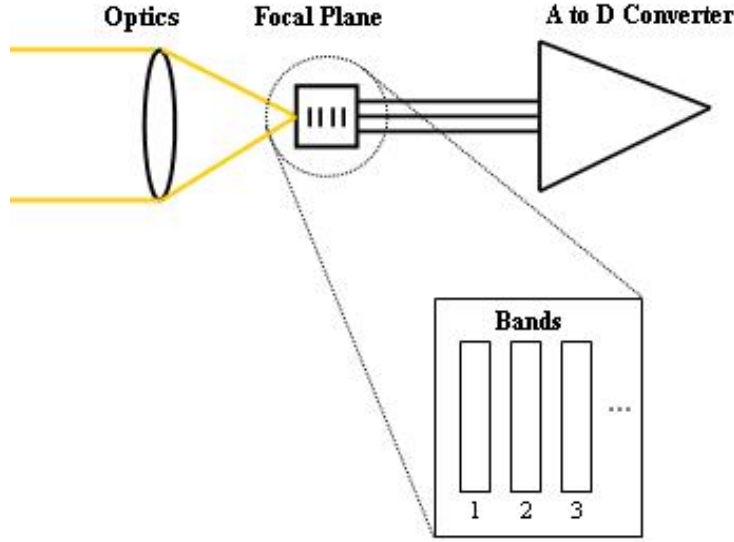


Figure 3.11: *Illustration of light passing through a sensor.*

At the detector, the signal is further degraded as a result of a spectral sampling process. This is where the signal is sampled based on the spectral response of the detector. Sampling is performed on a band-by-band basis according to

$$L_i = \frac{\int L(\theta, \phi, \lambda) R_i(\lambda) d\lambda}{\int R_i(\lambda) d\lambda}, \quad (3.12)$$

where:

- L_i is the effective radiance in band i
- $L(\theta, \phi, \lambda)$ is sensor-reaching radiance in (θ, ϕ) viewing direction
- $R_i(\lambda)$ is the spectral response function for band i (usually incorporating both the filter effects and the detector spectral response).

Therefore, the spectral sampling process converts the original, spectrally continuous signal to a single effective radiance value for each band. This is why the many bands of a hyperspectral sensor are preferred to the few bands of a multispectral sensor. The more bands we use to sample a signal the better we are able to preserve the signal's spectral shape.

It should be noted that a finite detector array will degrade the sensor-reaching signal spatially as well as spectrally. In this research, since our target of interest is water, the local spatial variability of the brightness values in a given water body is assumed to be negligible. This stems from the fact that water constituents have a small horizontal variability for most lakes and ponds. Even in the Genesee River plume where there is a high spatial variability of suspended sediments, the resulting variability in sensor-reaching radiance is quite small (as we'll see in later chapters). Therefore, in this research we will ignore spatial blurring effects that are due to the sensor other than the effect of detector size.

The last stage of degradation a signal will encounter as it is read in by a sensor comes in the form of quantization. The result of the spectral sampling process yields a vector of continuous signal values. We can use an analog-to-digital converter to digitize the signal, enabling us to utilize computers for processing. In doing so, however, the continuous response values are discretized causing a loss of information. Therefore, the quantization process further degrades our signal due to our need for digitization.

The three aforementioned processes will be revisited again in Chapter 4 for the sensors used in this study. An illustration at this point, however, will be useful. Figure 3.12 shows the degradation encountered by an arbitrary signal as it passes through the ETM+ sensor. Notice, from left to right, that the signal at the front of the sensor is continuous

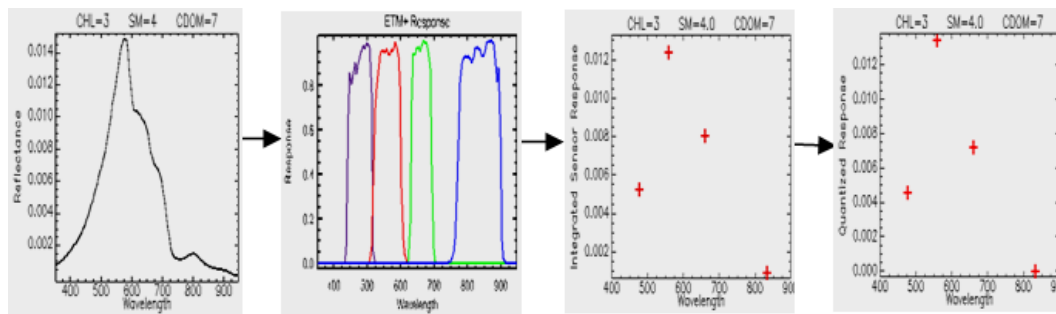


Figure 3.12: *Response vs. wavelength plots showing the degradation of a signal as it passes through a sensor.*

until it is spectrally sampled to the detectors response functions. Once sampled, the signal is spectrally discrete but can take on a continuous range of response values. Upon quantization in the last stage, however, the signal's response is also discretized causing further loss of information. Recall from Section 3.2.3 that when imaging water, only a small percentage of the signal received at the front of the sensor comes from the water column. Therefore, it is imperative that the sensor is designed in such a way that the degradation it imposes on a signal is minimized.

3.2.7 Constituent Retrieval Algorithms

There are a variety of constituent retrieval algorithms for case 2 waters that work to determine the concentrations of chlorophyll-a(CHL), suspended materials(SM), and colored-dissolved organic matter(CDOM) from an imaged water pixel. These methods rely on the assumption that adequate atmospheric compensation and glint removal can be performed leaving only the pixel's water-leaving reflectance. Once this water-leaving signal is isolated, the constituent retrieval algorithm can be applied to determine the constituents in the water column.

In this research, we use a constituent retrieval algorithm that uses look-up tables (LUTs) to determine a water's constituents from its reflectance [Raqueno et al., 2000]. LUTs can be thought of as a library of varying water types. Associated with each water type is its water-leaving spectra. When imaging a scene, we can compare observed water pixels to elements of the LUT to determine a water's constituents. Figure 3.13 shows the iterative process involved in using a LUT for constituent retrieval.

On a pixel-by-pixel basis, we perform atmospheric compensation and glint removal to obtain the water-leaving signal. This signal can be compared to the elements of the look-up table. If a match is found to within a predetermined threshold then we can determine the water constituents in the imaged pixel. If not, we iterate until a suitable match is found. This process is repeated for all pixels of interest in the scene. At this point, we have only described the constituent retrieval process in a generic fashion. Let's further investigate the details of the look-up table and the optimization routine Amoeba [Nelder and Mead, 1965], which will enable us to adequately describe the retrieval process.

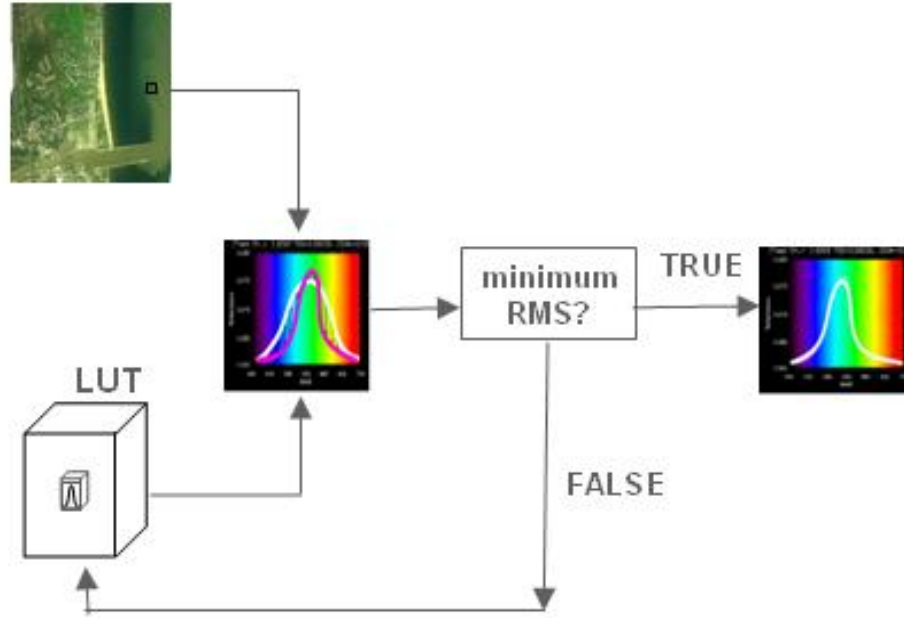


Figure 3.13: *Illustration of the constituent retrieval process using LUTs.*

3.2.7.1 The Look-Up Table

The purpose of a look-up table is to provide the user with a measure of “ground truth” for a scene of interest. Learning the details to its construction is essential to understanding the constituent retrieval process. The look-up table in this study can be thought of as a cube-like three-dimensional structure, see Figure 3.14. Just as in all 3-D spaces, we can describe any point in the LUT with an ordered triplet, i.e. (x,y,z) . However, associated with each ordered triplet is a water-leaving spectrum. So how is this LUT populated?

Recall that when we perform constituent retrieval, we are trying to determine the concentrations of the three major constituents in a body of water (Chlorophyll, Suspended Materials, and CDOM). We can use the range of concentrations of these constituents that we might expect to observe in a scene as the axes of the look-up table. In other words, instead of an x-axis we might have a chlorophyll concentration axis that ranges from 0 to 100 units because these are the concentrations measured from in situ observations. Similarly, instead of a y- and z-axis we will have a suspended material and CDOM axis, also with

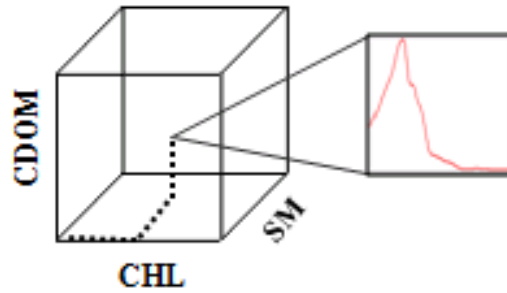


Figure 3.14: *Three dimensional LUT. Water constituent concentrations make up the domain and reflectance spectra make up the range.*

an appropriate range of concentrations. Now when we describe an ordered triplet, we are not just describing a point in space (x,y,z) but rather the concentrations of the three constituents (CHL,SM,CDOM). Associated with each ordered triplet is a water-leaving spectrum, see Figure 3.14. Now, with the axes labeled we must find an efficient way to determine the water-leaving spectrum associated with each coordinate.

3.2.7.2 Hydrolight

In the remote sensing of “ocean” color, a general knowledge of the water-leaving radiance distribution is essential to determining its constituents. As we just described, a LUT can serve as a means to compile water-leaving radiances that we may expect to observe in a scene. One way to populate such a LUT is through the painstaking process of collecting in situ observations. This procedure involves driving or rowing a boat out onto a water body, measuring the water-leaving signal with a spectrometer, taking a water sample and determining its constituents through a filtering process performed in the lab. This must be done multiple times to obtain a LUT that is representative of all the water types in a scene. Clearly, this is a daunting and unrealistic task. Alternatively, the in-water radiative transfer code Hydrolight [Mobley, 1994] can quickly compute the desired radiance distributions for natural waters.

Before describing what Hydrolight includes in its computations and how its outputs can be implemented, the user of this code should be wary of the fact that a couple of

simplifying assumptions are made for efficiency purposes. Hydrolight is solved using time-independent radiative transfer theory for plane-parallel geometries. The first assumption of time-independence is valid when the time scales for changes in environmental conditions (typically seconds to seasons) is much greater than the time it takes a light field to assume a steady state in the water (milliseconds) once the optical properties or boundary conditions are changed [Mobley, 1994]. Furthermore, although water bodies vary optically in both the horizontal and vertical directions, Hydrolight uses a plane-parallel geometry which assumes that the water column is horizontally homogeneous. This is a valid assumption if the horizontal homogeneity is at least several photon mean free paths, which is often the case in case 2 waters [Mobley, 1994]. Making these assumptions avoids the need to solve a computationally large time-dependent, three-dimensional problem.

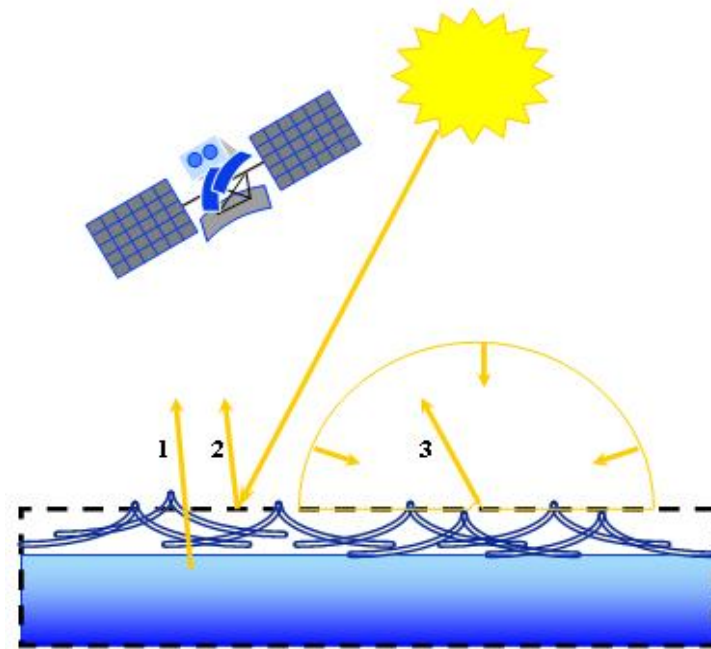


Figure 3.15: *Figure illustrating how hydrolight uses plane-parallel geometry to compute the total upwelling radiance in the air just above the wind-blown sea surface. Water-leaving radiance is shown in path (1), reflected solar radiance in path (2), and reflected sky radiance in path (3).*

A variety of inputs must be defined by the user to yield the desired outputs of Hydrolight. Particularly, the IOPs of the water column, the state of the wind blown surface, and the spectral radiance distribution of the sky must be provided as inputs to the model.

Figure 3.15 illustrates the nature in which Hydrolight computes the total upwelling radiance in the air just above the water, which is the output of interest for the determination of “ocean” color. The state of the sea surface is modeled using Cox-Munk wave slope statistics [Cox and W.Munk, 1954a][Cox and W.Munk, 1954b], which effectively describe the optical reflection and transmission properties of the surface for moderate wind speeds and solar angles away from the horizon [Mobley, 1994]. Once the transmission and reflection properties are determined, the plane-parallel geometry is enforced as indicated by the dashed patch of water in Figure 3.15. This allows Hydrolight to calculate the angle and power of the transmitted/reflected fractions of radiance using the familiar Snell’s law,

$$n_1 \sin \theta_1 = n_2 \sin \theta_2 \quad (3.13)$$

and Fresnel’s formula respectively,

$$r(\theta') = \frac{1}{2} \left(\left(\frac{\sin(\theta' - \theta_t)}{\sin(\theta' + \theta_t)} \right)^2 + \left(\frac{\tan(\theta' - \theta_t)}{\tan(\theta' + \theta_t)} \right)^2 \right) \quad (3.14)$$

where θ' represents the angle of incidence for either the air-incident or water-incident case [Sears, 1949].

Next, Hydrolight solves the “...integro-differential radiative transfer equation (RTE)...”, based on the water’s user-defined inherent optical properties, to determine the spectral radiance due to the transmitted fraction of light at any depth [Mobley, 1994]. The depth of interest in this research is $z = a$, which is just above the surface of the water. Therefore, as indicated in Figure 3.15, the total upwelling spectral radiance just above the sea surface, $L(z = a, \theta, \phi, \lambda)$, which is reported by Hydrolight for any arbitrary viewing-angle is comprised of (1) a water-leaving component, (2) a reflected component due to the Fresnel reflectance of solar radiance, and (3) a reflected component due to the Fresnel reflectance of sky radiance. Conveniently, Hydrolight outputs component (1) separately from components (2) and (3) to accommodate those studying ocean color from space. It is this water-leaving radiance, component (1), that we will incorporate into our LUT.

With a basic understanding of how Hydrolight works, we can divert our attention to its utility. Recall that we want to avoid having to collect in situ observations in order to

populate our LUT. Rather, we would prefer to use Hydrolight to generate water-leaving reflectances that are representative of the scene. To achieve this, we must provide the IOPs of the water column, the state of the wind blown surface, and the spectral radiance distribution of the sky as inputs to the model. Additionally, Hydrolight can be set for a specific illumination angle and nadir viewing to match Landsat acquisition conditions on the day of interest. Finally, by providing Hydrolight with varying constituent concentrations, we can determine the water-leaving spectrum associated with any ordered triplet in the LUT, Figure 3.14. The end result of this process should be a LUT which contains a representative sampling of the possible water types in a scene of interest. The constituents define the axes and a Hydrolight-generated water-leaving reflectance spectrum is associated with each sample point.

It should be noted that since we are dealing with concentrations of water constituents, the axes of the LUT are made up of continuous values. Therefore, it is inevitable that when we try to match an imaged water pixel to an element of the LUT an appropriate match will not be found. This arises from the fact that the aforementioned Hydrolight process only finitely populates the LUT. Hence, there is a large amount of open space where we do not have spectral information. Since we desire the spectra associated with all regions of the LUT, the need for an interpolator clearly presents itself.

3.2.7.3 Amoeba

Amoeba is a function that performs minimization in multidimensional spaces using the down-hill simplex method developed by [Nelder and Mead, 1965]. Through an iterative process it is able to find the minima of an n-dimensional function, which is ideal for searching the three-dimensional LUT in our work. As seen in Figure 3.16, Amoeba derives its name from the nature in which it closes in on a minimum as if it were surrounding its prey. The function smartly chooses points in the space to perform the minimization test until ultimately, it closes in on the proper minimum.

Maybe of equal importance to Amoeba's ability to find minima, however, is its interpolating capability as developed by [Raqu  o et al., 2000]. As discussed in Section 3.2.7.1, the number of potential concentration triplets contained within our LUT is infinite. To describe the spectra associated with all these points would be impossible. Through the use

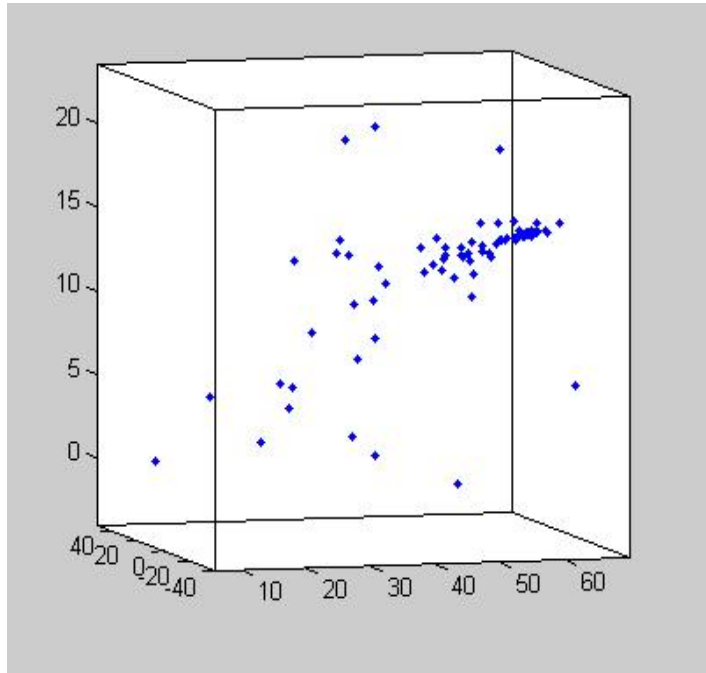


Figure 3.16: *Plot of the points in the LUT encountered as Amoeba finds the minimum.*

of a three dimensional piecewise linear interpolator, however, we can determine the spectra associated with an infinite number of concentration triplets by interpolating across the LUT’s finite number of known concentration triplets, and their corresponding Hydrolight-generated spectra. This characterization of Amoeba as being a dual purposed tool allows us to explicitly describe the process it follows in determining a minimum and, consequently, the constituents contained in a water pixel.

3.2.7.4 The Retrieval Process

The constituent retrieval process begins by the user providing Amoeba with a retrieved water-leaving spectral curve from an image. Recall that this curve is obtained by performing atmospheric compensation and glint removal on an imaged water pixel. Once provided with a spectral curve, the optimizer initiates a search of the LUT for a matching curve, see Figure 3.13.

Amoeba performs this search by choosing an “arbitrary” point in the LUT, as shown in Figure 3.16. The spectrum associated with this point, which is determined through the interpolation process, is compared to the spectrum provided by the user. If the RMS-error

between the two curves is greater than a predetermined threshold, then another point in the LUT is chosen. This process continues until the RMS-error between the two spectral curves is less than a predetermined threshold. Once a match of the spectrum of the imaged water pixel is found in the LUT, the coordinates associated with this optimal curve are determined. These coordinates represent the water pixel's constituent concentrations, which is the desired result. This process is repeated for all pixels in the image.

The retrieval process described above is our proposed approach for this research and has been demonstrated on several efforts [Raqueno et al., 2000]. The capabilities of this method are limited by one's ability to perform adequate atmospheric compensation and glint removal. Techniques that will allow us to compensate for the atmosphere and remove glint from an image are discussed in Section 4.2.2. The utility of this method also depends on our ability to create a LUT that is representative of the scene of interest. As solar location, wind speed and sky conditions vary, new LUT's may need to be constructed. In Chapter 4, a study is introduced that investigates our ability to retrieve water constituents for a particular scene as the solar-zenith angle and wind speeds of our LUT are adjusted.

3.3 Surface Temperature Retrieval

When performing constituent retrieval as discussed in Section 3.2, the goal of the process is to determine the reflective properties of the medium from the radiance received by the sensor. *Surface temperature retrieval* is analogous to constituent retrieval but for the thermal portion of the electro-magnetic spectrum. Recall from Equation 3.3 that there are three major self-emitted contributors to radiance reaching the sensor.

$$L(\lambda) = \frac{E_{de}(\lambda)r(\lambda)\tau_2(\lambda)}{\pi} + L_{ue}(\lambda) + \epsilon(\lambda)L_T(\lambda)\tau_2(\lambda). \quad (3.15)$$

Only the path $\epsilon(\lambda)L_T\tau_2(\lambda)$ gives us any useful information about the temperature of the target, however. Therefore, it is this path that we look to isolate when we perform temperature retrieval. Before describing the retrieval process, we must first discuss the meaning of $\epsilon(\lambda)$ and how to calculate $L_T(\lambda)$. This section develops the necessary background for performing surface temperature retrieval in the thermal portion of the EM-spectrum.

3.3.1 Blackbody Radiators and the Planck Equation

In physics, a *blackbody* is a theoretical surface that perfectly absorbs and re-emits all incident electromagnetic radiation. Max Planck first derived an expression for the spectral radiant exitance of a blackbody in 1901, [Planck, 1901]. The *Planck equation*, is given by

$$M(\lambda) = \frac{2\pi hc^2}{\lambda^5} \frac{1}{e^{\frac{hc}{\lambda kT}} - 1}, \quad (3.16)$$

where:

h	Planck constant	$6.6256 \cdot 10^{-34} [J \cdot s]$
c	speed of light in vacuum	$2.9979 \cdot 10^8 [m/s]$
k	Boltzmann constant	$1.3807 \cdot 10^{-23} [J/K]$
λ	wavelength of emission	$[m]$
T	absolute temperature	$[K]$.

One should notice from observing Planck's equation that the exitance from a blackbody is temperature and wavelength dependent. Therefore, if we know the temperature of a blackbody, we can find its exitance spectrum. Furthermore, if we assume that our target is Lambertian (which is a good assumption for water in the longwave infrared (LWIR) when viewed near nadir) then

$$L_T(\lambda) = \frac{M(\lambda)}{\pi}. \quad (3.17)$$

Figure 3.17 illustrates how the Planck equation can be used to generate a family of blackbody curves. Each curve represents a blackbody at a certain temperature and is plotted as radiance versus wavelength. However, objects in nature are never perfect emitters. Therefore, we need to define a metric that describes how "blackbody-like" an object is.

3.3.2 Fundamental Properties of Matter

Emissivity is a metric that defines how well an object radiates energy compared to that of a perfect blackbody and is given by

$$\epsilon(\lambda) = \frac{M_\lambda(T)}{M_{\lambda BB}(T)}, \quad (3.18)$$

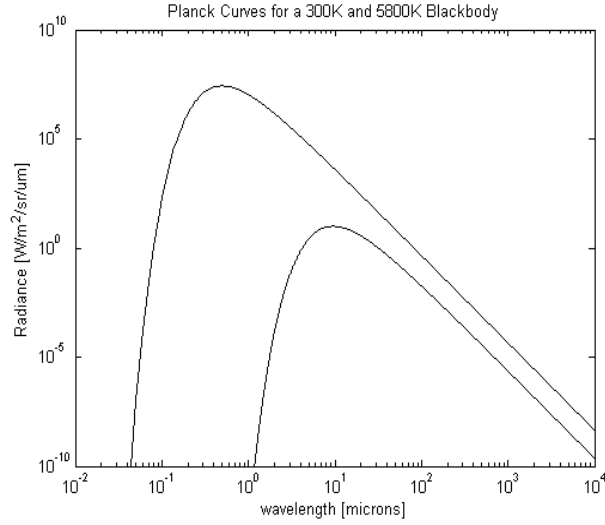


Figure 3.17: *Planck curves for a 300 Kelvin and 5800 Kelvin Blackbody.*

where $M_\lambda(T)$ is the radiant exitance, defined as the power per unit area emitted from a surface. Notice that since a blackbody is the perfect emitter, emissivity is always between 0 and 1. It is useful to know how emissivity relates to reflectivity. Therefore, we will take a moment to develop this relationship.

We begin by describing some fundamental properties of matter. The *transmissivity* of a material can be thought of as its ability to allow incident flux, or light, to propagate through it and is given by

$$\tau(\lambda) = \frac{M_\tau}{E_i}, \quad (3.19)$$

where E_i is the incident irradiance and M_τ is the transmitted exitance. The *reflectivity* of a material describes its ability to redirect incident flux, back into the incident hemisphere

$$r(\lambda) = \frac{M_r}{E_i}, \quad (3.20)$$

where E_i is the incident irradiance and M_r is the reflected exitance. The *absorptivity* of a material is its ability to remove incident light by converting it to another form of energy and is given by

$$\alpha(\lambda) = \frac{M_\alpha}{E_i}, \quad (3.21)$$

where E_i is the incident irradiance and M_α is the flux per unit area converted to another form of energy. These three definitions should be intuitive to the reader from life experience. If we draw from one of the fundamental laws of physics, conservation of energy allows us to conclude

$$\alpha + \tau + r = 1. \quad (3.22)$$

Furthermore, if we are working with materials where transmission is negligible,

$$\alpha + r = 1. \quad (3.23)$$

Kirchhoff's law provides a relationship between emissivity and absorptivity by noting that they are equal for objects in thermal equilibrium. Using this law, Equation 3.22 becomes

$$\epsilon + \tau + r = 1, \quad (3.24)$$

and if we again assume that the object is opaque, then

$$\epsilon + r = 1. \quad (3.25)$$

Equation 3.25 gives us a nice relationship between reflectance and emissivity for opaque targets, such as water in the thermal infrared.

3.3.3 The Retrieval Process

Recall that when we perform surface temperature retrieval, we are interested in determining the surface temperature of a water pixel based on the total sensor-reaching radiance. Therefore, our goal is to model

$$L(\lambda) = \frac{E_{de}(\lambda)r(\lambda)\tau_2(\lambda)}{\pi} + L_{ue}(\lambda) + \epsilon(\lambda)L_T(\lambda)\tau_2(\lambda), \quad (3.26)$$

so that the modeled radiance equals the observed radiance from a water pixel. This can be performed with the use of LUTs as summarized below.

We start the surface temperature retrieval process with the generation of multiple blackbody curves using Planck's equation to solve for $L_T(\lambda)$ in $\epsilon(\lambda)L_T(\lambda)\tau_2(\lambda)$ for a range

of temperatures. The emissivity of water is spectrally flat in the thermal with a value of 0.986 [Padula, 2008] so assuming one can obtain knowledge of the atmospheric parameters, Equation 3.26 can be solved to acquire sensor-reaching radiance for all blackbody curves. Finally, we spectrally sample the sensor-reaching radiances to the spectral response of our sensor using Equation 3.12, i.e., what would our sensor see if it was observing these various radiances. The result of this sampling process will be a look-up table of integrated radiance values instead of the original blackbody curves. Figure 3.18 illustrates this for a thermal sensor with only one band (attenuation due to the atmosphere has been ignored).

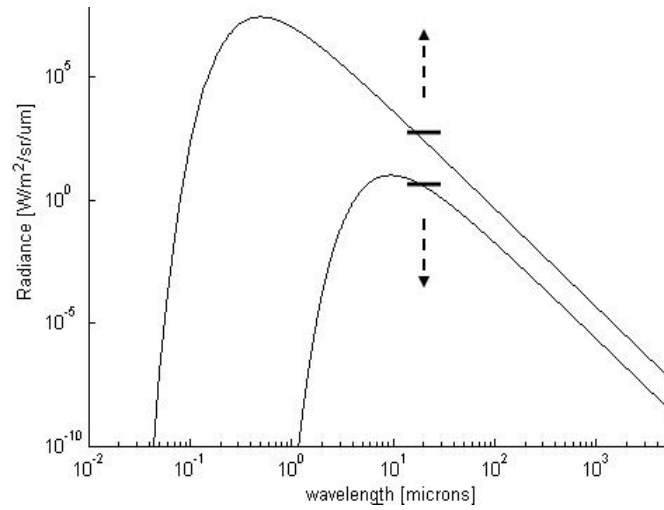


Figure 3.18: *Sketch of a LUT resulting from various blackbody curves.*

Notice that the x-axis is wavelength, the y-axis is radiance and associated with each value of the newly created LUT is a temperature. Now, the sensor-reaching radiance of an imaged water pixel can be compared to the elements of the LUT to determine its apparent temperature. As with the constituent retrieval process, our ability to perform temperature retrieval efficiently hinges on our abilities to adequately model the atmosphere. The thermal atmospheric compensation method used in this work is detailed in Section 6.1.3.

3.4 The ALGE Hydrodynamic Model

Sections 3.2 and 3.3 introduce the background materials necessary for an understanding of how remotely sensed reflective and thermal data can be used to determine water constituents and surface temperatures, respectively. These two forms of data are useful for

describing a water body at the time the data is collected. Hydrodynamic models, on the other hand, are designed to describe the movement of water over time. By accurately determining the input parameters for a scene of interest, a robust model will correctly output the flow of a water body. The ALGE hydrodynamic model developed by [Garrett, 1997] is one such model that is especially useful for remote sensing applications. In addition to predicting water flow, ALGE outputs sediment profiles and surface temperatures. Therefore, the model is designed for applications where satellite based reflective and thermal imagery are available to serve as calibration tools.

A major goal of this research is to describe the sedimentation and materials transport in a river plume. Recalling Figure 3.4, this work seeks to develop a three dimensional simulation of the Genesee River plume located in the Rochester Embayment. The ALGE hydrodynamic model can be used to develop this simulation and the methods of Sections 3.2 and 3.3 can be used in an effort to calibrate the model.

The ALGE code works by the user first defining a variety of input parameters for the model. Variables such as the geometry of the water body, voxel (3-D pixel) size, Sun angle, surface roughness, inflow temperature, outflow temperature and water velocity are commonly defined. The user may also wish to describe the nature of the particles in the water, i.e., particle density, particle diameter, and river source concentration of particulates. Additionally, ALGE requires a time history of the meteorological inputs for the scene of interest. Barometric pressure, wind speed, wind direction, precipitable water, etc., will all have an effect on a water's movement. The model uses these inputs to solve a standard set of hydrostatic equations and yield the desired outputs,

$$\frac{\partial u}{\partial t} = -\frac{\partial uu}{\partial x} - \frac{\partial vu}{\partial y} - \frac{\partial wu}{\partial z} - \frac{1}{\rho} \frac{\partial p}{\partial x} + fv + \frac{\partial}{\partial x} \left(K_H \frac{\partial u}{\partial x} \right) + \frac{\partial}{\partial y} \left(K_H \frac{\partial u}{\partial y} \right) + \frac{\partial}{\partial z} \left(K_z \frac{\partial u}{\partial z} \right) \quad (3.27)$$

$$\frac{\partial v}{\partial t} = -\frac{\partial uv}{\partial x} - \frac{\partial vv}{\partial y} - \frac{\partial wv}{\partial z} - \frac{1}{\rho} \frac{\partial p}{\partial y} - fu + \frac{\partial}{\partial x} \left(K_H \frac{\partial v}{\partial x} \right) + \frac{\partial}{\partial y} \left(K_H \frac{\partial v}{\partial y} \right) + \frac{\partial}{\partial z} \left(K_z \frac{\partial v}{\partial z} \right) \quad (3.28)$$

$$\frac{\partial T}{\partial t} = -\frac{\partial uT}{\partial x} - \frac{\partial vT}{\partial y} - \frac{\partial wT}{\partial z} - \frac{1}{\rho} \frac{\partial p}{\partial x} + \frac{\partial}{\partial x} \left(K_H \frac{\partial T}{\partial x} \right) + \frac{\partial}{\partial y} \left(K_H \frac{\partial T}{\partial y} \right) + \frac{\partial}{\partial z} \left(K_z \frac{\partial T}{\partial z} \right) \quad (3.29)$$

$$\frac{\partial w}{\partial z} = -\frac{\partial u}{\partial x} - \frac{\partial v}{\partial y} \quad (3.30)$$

$$\frac{\partial p}{\partial z} = -\rho g \quad (3.31)$$

where u , v , and w are velocity components, T is temperature, K_H/K_z are horizontal and vertical diffusion coefficients, f is the Coriolis parameter, g is acceleration due to gravity, p is hydrostatic pressure and ρ is water density. From the user's standpoint, ALGE outputs 3-D maps of temperature, the u , v , and w velocity components, and the C_{CHL} , C_{SM} , and C_{CDOM} constituent concentrations.

As alluded to, ALGE is particularly useful for those studying water bodies from space. This utility arises from the nature of its outputs. Using ALGE, one can generate a surface temperature map and the concentration of the constituents in each water voxel. By comparing the modeled data to observed data, remotely sensed imagery can be used to calibrate the model's predictions. This works by adjusting the model's input parameters until its output suitably matches the remotely sensed data. Once a match is determined, the input parameters are used to describe the state of the environment at the time of the collect. Chapter 6 specifically describes how thermal data can be used to calibrate ALGE's prediction of the flow of the Genesee River.

3.5 Concluding Remarks

This chapter has provided an overview of the theory that is necessary for a basic understanding of how to study river plumes from space. We began the discussion by describing the various paths that light may traverse as it travels from the Sun to the sensor. Next, we described how these paths could be separated to obtain useful information about a water body. Finally, we briefly introduced a hydrodynamic model and discussed how satellite data can be used to calibrate the model. With a basic understanding of the necessary background material, we are now ready to introduce the specific approach that we will follow to solve our problem; modeling the Genesee River plume and using satellite data to calibrate the model.

In Chapters 4 through 6, we will take a detailed look at the methods used in this research. A variety of studies will be introduced that test the validity of our methods. The completion of each is necessary for one to successfully model and calibrate the river plume. Particularly, we will evaluate OLI's potential to be used in water quality research. Having a sensor with the appropriate radiometric fidelity is imperative for studying case 2

waters from space. If OLI meets the necessary requirements we can take advantage of its superior spatial resolution throughout this work. Secondly, we will introduce two new atmospheric compensation algorithms that were developed specifically for the OLI sensor. Next, a study that evaluates our ability to perform the constituent retrieval process using one LUT for a variety of water types and illumination conditions will be discussed. Lastly, we will elaborate on the temperature retrieval process, which is necessary for the calibration of the hydrodynamic model. Chapter 6 will provide the reader with the tools necessary for modeling and calibrating a hydrodynamic model.

Chapter 4

Constituent Retrieval with the OLI Sensor: Methodology

The purpose of this chapter is to introduce the OLI-specific methods that will be used for the constituent retrieval process. We will begin with a discussion of the improved features of the OLI instrument and describe how these features adequately preserve the sensor-reaching signal to enable the constituent retrieval process. Secondly, two over-water atmospheric compensation algorithms are introduced which have been developed specifically for the OLI sensor. Finally, we conclude this chapter with a description of the constituent retrieval algorithm that will be used in this research to invert water-leaving reflectances to water constituents. Results of experiments that were designed to evaluate the performance of these methods will be presented in Chapter 5.

4.1 The OLI Sensor

Performing water quality studies from satellite imagery is a unique problem as most of the signal that we receive at a sensor comes from sources other than the water. Because this water-leaving radiance is extremely low, the quality of the sensor that we use in detecting it is paramount. Logically, a hyperspectral sensor with low noise and little loss of information due to quantization is desired. Often, budget restrictions and data accessibility limit our use of such instruments. On the other hand, sensors such as Landsat's Enhanced Thematic Mapper Plus (ETM+) or Sea-viewing Wide Field-of-view Sensor (SeaWiFS) are desirable

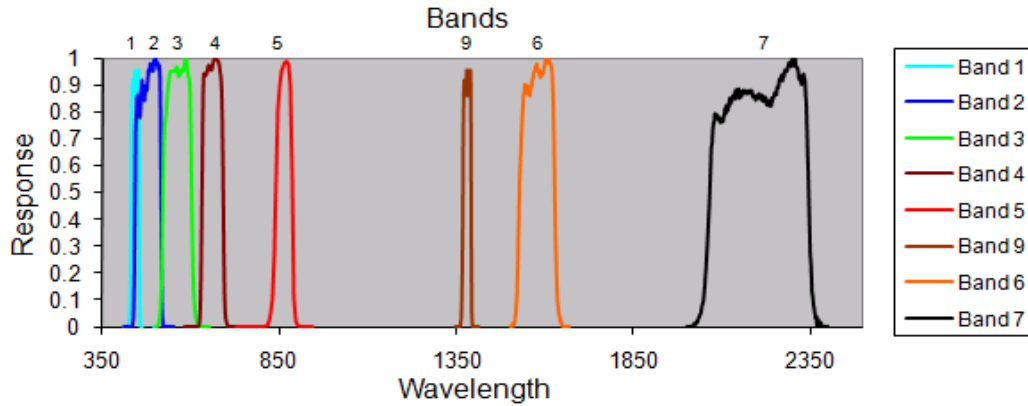
for water quality studies as their data is readily available to the community. Limitations in the characteristics of these instruments, however, restrict our use of such sensors. With pixels that are 30 meters on a side, ETM+ has ideal spatial resolution for studying case 2 waters, particularly river plumes. Modest spectral resolution, limited signal-to-noise ratios, and 8-bit quantization precludes this sensor from suiting our needs. Conversely, SeaWiFS has sufficient spectral resolution, high signal-to-noise, and a 10-bit quantizer but poor spatial resolution with 1 kilometer pixels. Therefore, neither sensor is appropriate for studying spatially diverse coastal or inland waters.

The Landsat Data Continuity Mission (LDCM) is developing a new multispectral sensor that captures the desired characteristics of the two sensors and will provide data that is equally accessible. Similar to ETM+, it will have sufficient spatial resolution for plume studies with 30 meter GSD's. Minding the shortcomings of ETM+ however, LDCM's Operational Land Imager (OLI) will have higher signal-to-noise ratios and an improved 12-bit quantizer. Additionally, OLI will have 5 bands in the VNIR compared to the 4 bands of ETM+ and the 8 bands of SeaWiFS. Discussing these features in detail will offer us insight into how the precious water-leaving signal will be attenuated as it is read in by the OLI sensor.

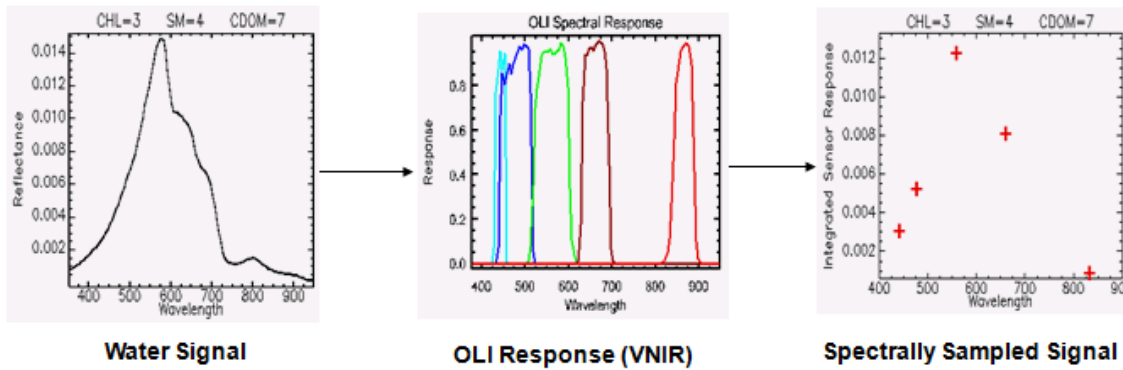
4.1.1 Sensor Response

Figure 4.1 shows the spectral response of OLI's detectors in the reflective portion of the EM spectrum. OLI's response differs from that of ETM+ as it is equipped with a "Coastal Aerosol" band centered at 440 nanometers (band 1) and a "Cirrus" band centered at 1375 nanometers (band 9). Band 1 has a narrow 20 nanometer bandwidth and will prove to be useful for atmospheric compensation while band 9 will enable the detection of cirrus clouds in an image. Additionally, OLI's band 5 is superior to the NIR band of ETM+ as it exhibits a bandwidth of only 40 nanometers (compared to the 120 nanometer bandwidth of ETM+).

If we consider the spectral response of the OLI sensor within the context of the constituent retrieval process, one should recall that only VNIR light can interact with water at depth. Therefore, in the area of water quality research, bands 6, 7, and 9 of the OLI sensor are ignored as they lend no information to the nature of a water's constituents.

Figure 4.1: *Reflective bands of OLI.*

However, as we will see later, band 6 may contribute to the atmospheric compensation process. Figure 4.2 illustrates the spectral sampling process a signal will experience as it is read in by the OLI sensor.

Figure 4.2: *Example of water signal that has been spectrally sampled to OLI's sensor response.*

Notice that since OLI has five bands in the VNIR, the end result of spectrally sampling an arbitrary water-leaving signal is five discrete values. Therefore, in place of the once continuous signal, a discrete vector with five values remains.

4.1.2 Quantization

Quantization refers to the discretization of the continuous response (amplitude) of a signal. Referring again to Figure 4.2, we see that the process of spectrally sampling a signal to the reflective bands of OLI causes a spectrally continuous signal to become spectrally discrete. The response values of this spectrally discrete signal, however, are still continuous. For a sensor to be able to read out the signal, the response values must be digitized through a quantization process.

OLI will be equipped with a 12-bit quantizer, as opposed to the 8-bit quantizer of ETM+. As a result, the continuous range of response values in a scene can be partitioned into 4096 (2^{12}) values for OLI while ETM+ allows for only 256 (2^8) such partitions. The result of this improved response resolution will be an increased ability to preserve the original signal. Figure 4.3 illustrates OLI's enhanced radiometric fidelity, where the entire reflectance range $[0 - 1]$ has been divided into 256 levels for ETM+ and 4096 levels for OLI.

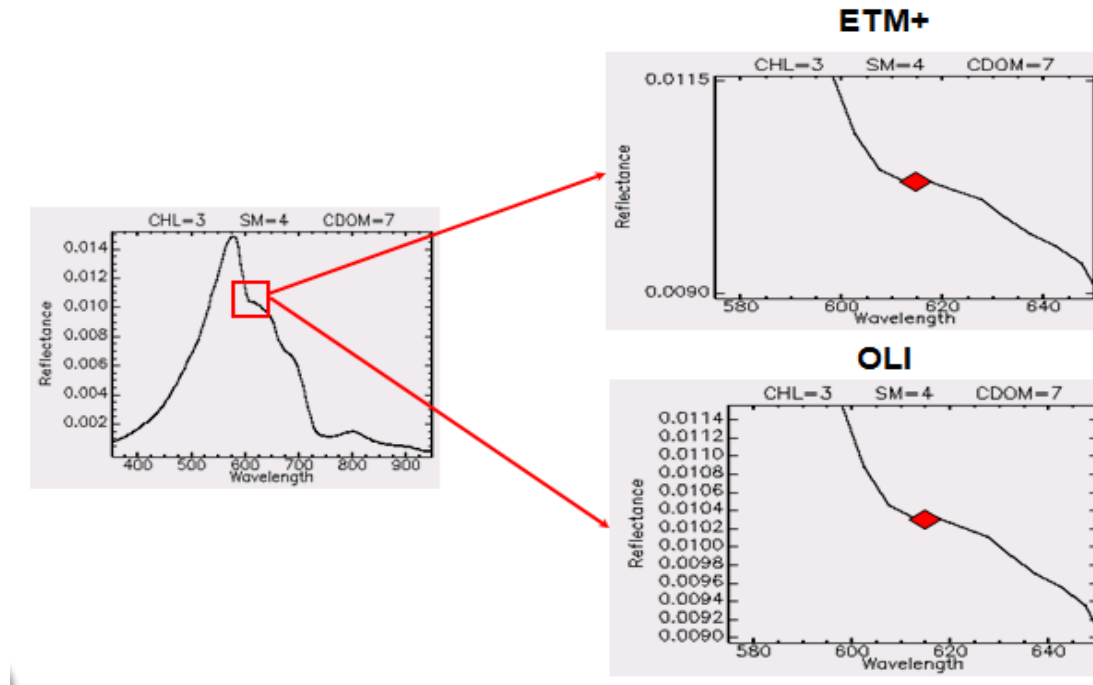


Figure 4.3: *Illustration of the response resolution associated with the 8-bit quantizer of ETM+ and the 12-bit quantizer of OLI. Reflectance range $[0 - 1]$ has been divided into 256 levels for ETM+ and 4096 levels for OLI.*

The signal on the left hand side of Figure 4.3 represents the water-leaving reflectance associated with an arbitrary water pixel. If we spectrally sample this signal with the red band of ETM+ (band 3) and OLI (band 4), we obtain the red values on the right hand side. These values now need to be quantized (digitized) for the signal to be read out. To simulate the quantization process, the spectrally sampled reflectance values can be rounded to the nearest quantization level. On the right hand side of Figure 4.3 we see that for every 1 quantization level that ETM+ has to place the spectrally sampled signal, OLI has 16 quantization levels. As a result, the 12-bit quantizer is better able to preserve the original signal. We will show later the importance of quantization in terms of the constituent retrieval process.

4.1.3 Signal-to-Noise

In an effort to achieve higher signal-to-noise ratios, the OLI instrument will be equipped with a pushbroom sensor as opposed to the whiskbroom technology of ETM+. Both types of instruments use linear array detectors to collect the data, but the whiskbroom sweeps the data in the across-track direction as the satellite passes overhead in the along-track direction. Alternatively, the pushbroom sensor pushes the data in the along-track direction only, which eliminates unnecessary movement. Figure 4.4 illustrates the ground path for both types of sensors.

The pushbroom sensor has an advantage over the whiskbroom as it can collect the same swath of data without any across-track movement. By eliminating this sweeping motion, a pushbroom sensor avoids the need to employ a bow-tie scan line corrector. The end result is an instrument that has increased signal-to-noise ratios due to longer dwell times and fewer moving parts.

To quantify the improved signal-to-noise ratios of the pushbroom instrument, Table C.7 of Appendix C show the SNR requirements for the reflective bands of OLI. When compared to the signal-to-noise ratios for the reflective bands of the ETM+ sensor (Table C.5), the pushbroom technology of OLI is clearly superior.

Improved spectral resolution, signal-to-noise ratios, and response resolution through the use of a 12-bit quantizer should enable the OLI instrument to be a useful tool for water quality research. In Chapter 5, results of an experiment designed to quantify the effects

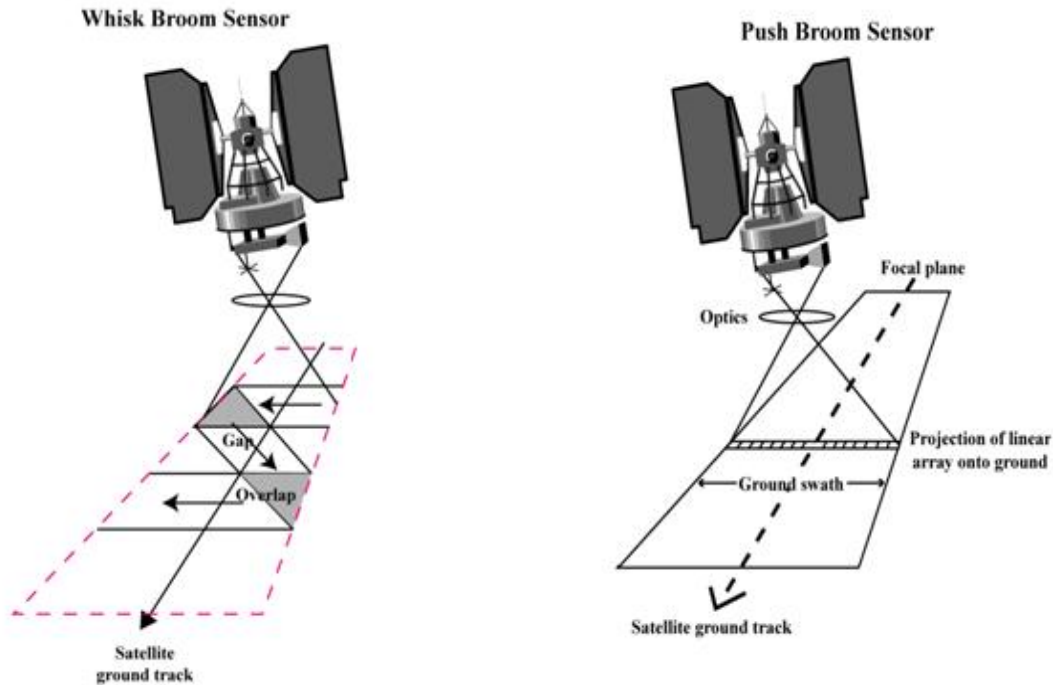


Figure 4.4: *Cartoon of a whiskbroom and a pushbroom sensor which can be found in ETM+ and OLI, respectively.*

of these improved features and evaluate the efficiency of the OLI sensor in performing the constituent retrieval process are presented.

4.2 Over-Water Atmospheric Compensation

To determine the constituents contained in a body of water from satellite imagery, recall that one must initially isolate the water-leaving signal from the total sensor-reaching radiance. To do this, effects due to the atmosphere must be removed from the data. In this section, we describe the tools that are necessary to perform solar glint removal and atmospheric compensation using a multispectral instrument. Since it is natural to describe the water-leaving signal in terms of its reflectance, some of the algorithms that we will introduce in this section adopt the notation of [Gordon and Wang, 1994] who define apparent reflectance as

$$\rho = \frac{\pi L}{F_o \cos \theta}, \quad (4.1)$$

where L is upward radiance in the given viewing direction, F_o is exoatmospheric irradiance, and θ is the solar-zenith angle. Using this terminology, we can define a governing equation for sensor-reaching reflectance as

$$\rho_t(\lambda) = \rho_r(\lambda) + \rho_a(\lambda) + \rho_{ra}(\lambda) + T_v(\lambda)[\rho_w(\lambda) + \rho_g(\lambda)], \quad (4.2)$$

where:

$\rho_t(\lambda)$ is the reflectance at the top of the atmosphere

$\rho_r(\lambda)$ is the reflectance due to multiple scatter by air molecules only (Rayleigh scatter)

$\rho_a(\lambda)$ is the reflectance due to multiple scatter by aerosols only

$\rho_{ra}(\lambda)$ is the reflectance due to the interaction between Rayleigh and aerosol scattering

$T_v(\lambda)$ is the diffuse atmospheric transmittance from the water to the sensor

$\rho_g(\lambda)$ is the reflectance due to solar photons reflecting off the air-water interface (glint)

$\rho_w(\lambda)$ is the desired water-leaving reflectance.

To perform the constituent retrieval process we must solve for $\rho_w(\lambda)$ in Equation 4.2, which is a basic algebra task if all the terms are known. When imaging a scene, however, the sensor only obtains the left side of the equation. This section describes the methods that are used in this research for determining the right side of the governing equation.

4.2.1 Solar-Glint Removal Algorithm

Glint removal is a necessary first step in isolating $\rho_w(\lambda)$ from Equation 4.2 as the atmospheric compensation routine developed for this research relies on band ratio techniques. If glint is not initially removed from the image, the ratios can be compromised causing the algorithm to fail. This section describes an easy, yet efficient algorithm to remove solar glint from an image.

The origin of the glint removal method that has been chosen for this research can be traced back to the work done by [Hochberg et al., 2003] which relies on two basic assumptions: (1) Signal in the NIR is comprised only of sun glint and a “spatially ambient NIR

component” and (2) There is a linear relationship between sun glint in the visible bands and the signal in the NIR. The first assumption is valid when the water-leaving signal and the signal due to the atmosphere is spatially homogeneous. This is true for case 1 waters or case 2 waters whose constituent concentrations do not vary much spatially, assuming that the atmospheric conditions are adequate for remote sensing. The second assumption of a linear relationship between sun glint in the visible bands and the signal in the NIR is also valid due to the nature of water’s index of refraction. According to [Mobley, 1994], the real index of refraction for water (which governs reflection at the air-water interface) is nearly equal for all wavelengths in the VNIR. Therefore, the amount of glint in the NIR lends insight into the amount of glint in the visible and a linear relationship exists between the two.

To develop this linear relationship, [Hochberg et al., 2003] suggests locating both the darkest and brightest pixel in the image (or a subset region of homogeneous water containing glint). The assumption is that these pixels would have the same spectral signature were it not for the glint. Then for each visible band, the values for the two pixels can be plotted on a visible band vs. NIR band axis. This allows one to find a linear relationship between brightness values in the NIR and their corresponding brightness values in each visible band, see Figure 4.5. These relationships can then be used to remove glint from any arbitrary water pixel in the scene.

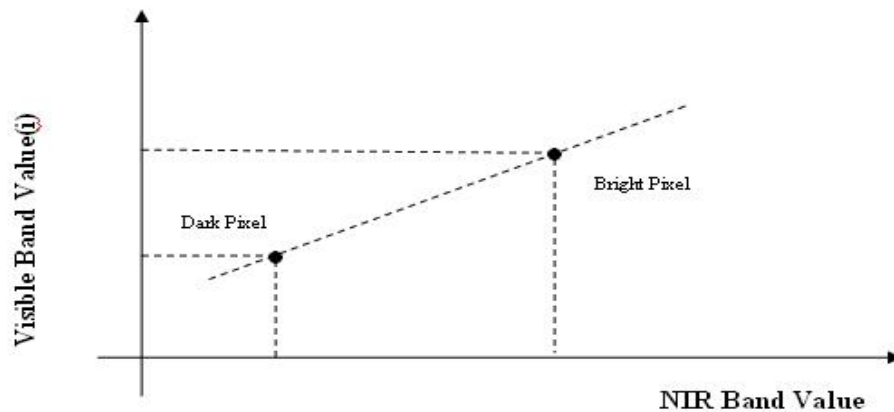


Figure 4.5: *Figure showing how a linear relationship between the NIR band and visible band is determined.*

This method is attractive due to its simplicity but is ultimately flawed as errors may be introduced by outliers in the scene. For example, boats or other foreign objects can appear as the brightest NIR pixel in the image which will result in the creation of incorrect linear relationships. Although the method is not robust for all scenes, its concepts are instructive for understanding a more efficient method developed by [Hedley et al., 2005].

[Hedley et al., 2005] suggest a version of Hochberg’s method which establishes the linear relationship between bands using linear regression on a sample of pixels rather than just a brightest and darkest pixel. The method works by the user initially defining a region of interest (ROI) in the scene that contains glint but would otherwise have a spectrally homogeneous brightness. Next, for each band a scatter plot is made which includes all the pixels in the ROI, Figure 4.6. The x-value of the ordered pair will contain the pixel’s NIR brightness and the y-value will include the pixel’s visible band brightness. Then, linear regression can be implemented to determine the best-fit line for each scatter plot.

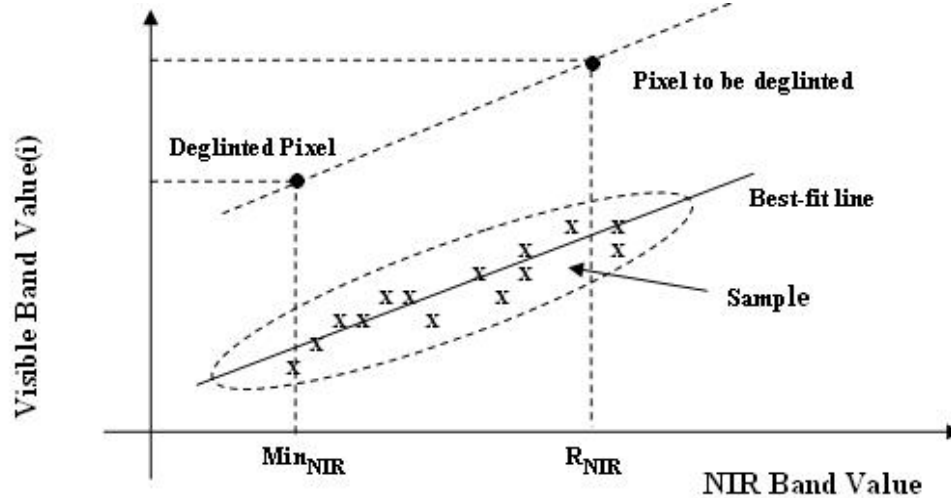


Figure 4.6: Figure showing how linear regression can be used in glint removal to develop a more robust linear relationship between brightness values in the NIR band and visible band.

With the equation of the line defined, we now have developed a relationship between the NIR band and the visible band. Therefore, if we know the amount of signal due to glint that we need to remove in the NIR (Δx) then we know how much glint to remove in

the visible band (Δy) simply by recalling the slope equation, $m = \frac{\Delta y}{\Delta x}$ (i.e., $\Delta y = m\Delta x$). Figure 4.6 illustrates the deglinting process for a single pixel, where the pixel's brightness in the visible band has been offset for clarity. This method is performed for all pixels in the scene on a band-by-band basis. [Hedley et al., 2005] summarizes the algorithm as follows.

Solar-Deglinting Algorithm Summary

Step 1: Select a region of interest in the image that contains sun glint. The ROI should include one or more regions containing pixels that would be spectrally homogeneous in the absence of glint. Deep water is recommended but not required.

Step 2: Perform linear regression on all the pixels gathered in step 1, on a band-by-band basis. The x-axis of the scatterplot used for the regression should contain the NIR brightness values while the y-axis should contain the visible brightness values. The goal of this step is to determine the slope, denoted b_i , of the best-fit line. Hedley suggests performing this step for each band that requires glint removal. In practice, however, it is efficient to simply implement this step for all visible bands. Therefore, if an image contains 5 bands (4 visible and a NIR) this step will be performed 4 times.

Step 3: Deglint all pixels in the image with the equation,

$$R'_i = R_i - b_i(R_{NIR} - Min_{NIR}) \quad (4.3)$$

where:

- R'_i is the solar-glint corrected pixel brightness in band i,
- R_i is the brightness in band i of the pixel to be deglinted,
- b_i is the regression slope in band i,
- R_{NIR} is the brightness in the NIR band of the pixel to be deglinted,
- Min_{NIR} represents the brightness of a pixel with no glint in the NIR.

There is a minor side-effect associated with using this algorithm. Recall from elementary statistics that the equation resulting from the regression process is a valid predictor for those test pixels whose brightness values lie within the domain of brightness values defined

by the ROI. Therefore, if a test pixel is too bright in the NIR, negative values may result from the deglinting process in the visible bands. Since water has a negligible return in the NIR for case 1 waters and an extremely small return in case 2 waters, this issue will only apply to non-submerged objects: land, buoys, boats, etc. Accordingly, these pixels should be masked during the deglinting process to preserve their original values.

Additionally, this method is only ideal for removing solar glint over water that contains a uniform signal in the NIR. There will be issues associated with extending this algorithm to case 2 waters whose NIR signal is not constant. River plumes and turbid ponds or bays will contain a varying signal in the NIR which violates this algorithm's first assumption. To help alleviate this issue, we will use OLI's SWIR band (band 6) to determine the glint in an image since the water-leaving signal is negligible at 1600 nanometers (i.e., any sensor-reaching radiance in band 6 will be comprised of glint and atmospheric effects only). This is a viable option since the real part of water's refractive index is still nearly equal for all wavelengths in the VNIR/SWIR.

To illustrate the deglinting process, two ponds from Figure 3.4 which contain glint were submitted to the glint removal algorithm. The AVIRIS data were spectrally sampled using OLI's reflective bands for both Cranberry Pond and Long Pond and band 6 was used to remove glint from the corresponding VNIR bands. Figure 4.7 shows the effects of the deglinting algorithm on Cranberry Pond while Figure 4.8 shows the effects of the deglinting algorithm on Long Pond. Notice that in both cases the variability due to glint is removed.

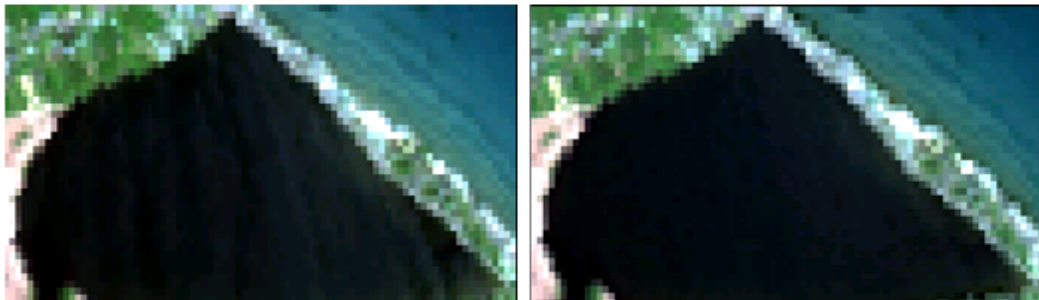


Figure 4.7: *True color images showing the effects of the deglinting algorithm on Cranberry Pond in the Rochester Embayment. The left figure shows the original image and the right shows the glint removed image.*



Figure 4.8: *True color images showing the effects of the deglinting algorithm on Long Pond in the Rochester Embayment. The left figure shows the original image and the right shows the glint removed image.*

In terms of our quest for the isolation of $\rho_w(\lambda)$ in Equation 4.2, this deglinting process effectively subtracts the $T_v(\lambda)\rho_g(\lambda)$ term from both sides of the equation,

$$\rho_t(\lambda) - T_v(\lambda)\rho_g(\lambda) = \rho_r(\lambda) + \rho_a(\lambda) + \rho_{ra}(\lambda) + T_v(\lambda)\rho_w(\lambda). \quad (4.4)$$

It is with Equation 4.4 that we can enter into the atmospheric compensation algorithm.

4.2.2 Atmospheric Compensation Algorithms

As discussed in Section 3.2.5, the purpose of atmospheric compensation is to determine the key atmospheric parameters that lead to the modification of a signal as it passes from the target to the sensor. By determining the transmission ($T_v(\lambda)$) and upwelling ($\rho_r(\lambda) + \rho_a(\lambda) + \rho_{ra}(\lambda)$) reflectance due to the atmosphere, the water-leaving reflectance ($\rho_w(\lambda)$) can be determined in an effort to solve for the water constituents contained in a water body. The level of sophistication of algorithms used to perform this task depends on both the type of sensor used in the study and the nature of the targets that we wish to observe. In most applications a hyperspectral sensor is preferred as the more bands a sensor has, the more information it can retain about a signal. Are these types of sensors necessary, however, or could we perform adequate atmospheric compensation with just a few bands?

The sensor that we wish to use in this research can be described as a limiting case for water quality studies. With just five bands in the VNIR and one in the SWIR, only a handful

of techniques are suitable to perform atmospheric compensation with the OLI instrument. Ideally, we would prefer to use some sort of spectral matching method since algorithms of this nature tend to be highly accurate [Green et al., 1998]. While these techniques have proven to be effective for hyperspectral sensors, they tend to fail for multispectral sensors which significantly degrade the spectral nature of a signal. Alternatively, many over-water atmospheric compensation algorithms designed for multispectral sensors use a band ratio technique in which the ratio of two NIR bands is computed to determine the atmosphere in a scene. These methods are easy to implement and are faster than the spectral matching algorithms but do not perform as well. Additionally, an algorithm of this nature would have to be modified for the OLI sensor as it does not contain 2 NIR bands. The focus of this section is to provide a sampling of techniques that can be used to compensate for the atmosphere in an image over water. These methods are introduced in a fashion that mirror the development of the OLI-specific atmospheric compensation algorithms.

4.2.2.1 Spectral Shape Matching Method

The *Spectral Shape Matching Method* is a common technique used to perform atmospheric compensation with hyperspectral data [Green et al., 1998]. The algorithm uses forward modeling in which known water-leaving spectra are propagated through modeled atmospheres, spectrally sampled to a sensor's response, and placed into a LUT. Then, by comparing the spectral shape of an imaged water pixel to the spectral shapes contained in the LUT, we can determine the most likely atmosphere associated with the pixel by simply finding an adequate match.

Figure 4.9 illustrates how the Spectral Shape Matching Method can be implemented. For simplicity, the left figure shows the TOA radiances for a fixed water type and various atmospheres which were modeled using MODTRAN. In the ideal case where a hyperspectral sensor is available, it is easy to envision how we might use a retrieved signal (middle) to choose an atmosphere from the LUT. The right figure, on the other hand, shows the same signal after it is spectrally sampled to the five VNIR bands of OLI. Clearly, the difficulty of our problem has increased due to the limited number of data values. In fact, spectral matching techniques fail for multispectral sensors as the occurrence of unique solutions diminishes.

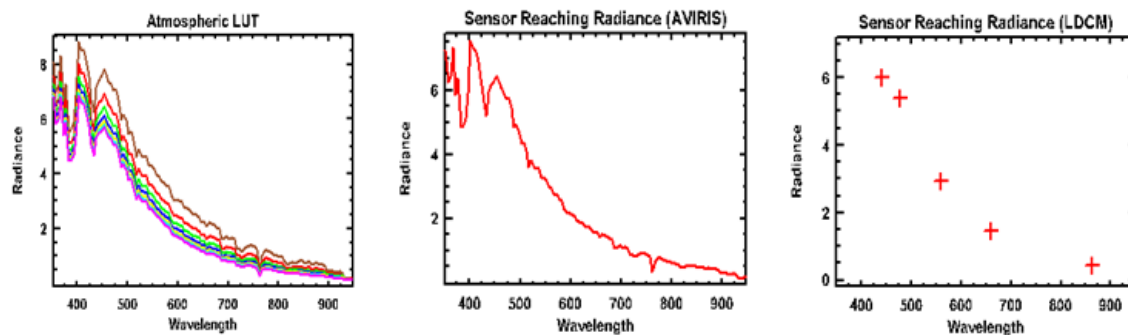


Figure 4.9: *Illustration of the complications associated with performing aerosol retrieval with a multispectral sensor. (Left) shows a LUT of various atmospheres that may be used in the aerosol retrieval process. (Middle) shows the result of spectrally sampling an arbitrary pixel with the AVIRIS sensor response function. (Right) shows the result of spectrally sampling an arbitrary pixel with the OLI sensor response function.*

Figure 4.10 further illustrates the issue that one encounters when trying to use a spectral matching technique with a multispectral sensor. The red values represent a water body with the concentration triplet ($CHL = 12[\frac{\mu g}{L}]$, $SM = 8[\frac{mg}{L}]$, $CDOM = 4$) that has been propagated through an atmosphere with a visibility of 30 kilometers and imaged with the OLI sensor. The blue values, on the other hand, represent a water body with the concentration triplet ($CHL = 46[\frac{\mu g}{L}]$, $SM = 0.25[\frac{mg}{L}]$, $CDOM = 10$) that has been propagated through an atmosphere with a visibility of 25 kilometers and imaged with the OLI sensor. Notice that these very different water types appear the same when imaged through two different atmospheres. If the Spectral Matching method is used to determine the constituent concentrations associated with these two pixels, there will most certainly be an error in the process.

Although this example illustrates why spectral matching techniques cannot be used directly to perform constituent retrieval with multispectral sensors, perhaps the concept can be used in conjunction with other methods to perform an adequate atmospheric compensation. We will investigate this thought further after a discussion of how band ratios can be used to account for the atmosphere.

The next two algorithms presented in this section are for the eight band sensor, SeaWiFS. This multispectral instrument has narrow bands in the VNIR centered at wavelengths 412, 443, 490, 510, 555, 670, 765, and 865 nanometers, see Appendix C. With 1 kilo-

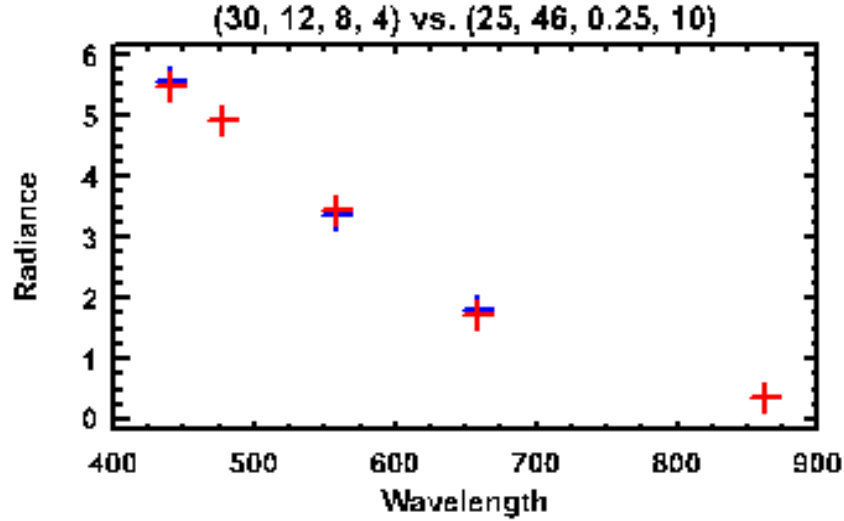


Figure 4.10: *Two different water samples that have been imaged by the OLI sensor through two different atmospheres.*

meter spatial resolution, SeaWiFS is ideal for studying large bodies of water. Although the data from this sensor cannot be used in this study, we introduce these SeaWiFS algorithms to provide a background for an atmospheric compensation technique that has been developed for this research. The first, by [Gordon and Wang, 1994], was designed for compensating data which has been collected over case 1 waters while the second, developed by [Ruddick et al., 2000], was designed for compensating data which has been collected over case 2 waters.

4.2.2.2 SeaWiFS Algorithm for Case 1 Waters

This algorithm developed by [Gordon and Wang, 1994] is based on the assumption that case 1 waters have negligible return in the NIR. Therefore, any signal received by a sensor's NIR bands is due solely to the atmosphere. It accounts for the multiple scattering that may occur as light encounters a dense atmosphere and uses the notation for top-of-the-atmosphere (TOA) reflectance as described in Equation 4.2. The following is performed on a pixel-by-pixel basis with solar-glint corrected data.

This algorithm begins with the user performing a Rayleigh correction, or subtracting the reflectance due to Rayleigh scatter from the total TOA reflectance. Recall that this

type of scattering occurs with particles that are smaller than the wavelength of incident light. Therefore, Rayleigh correction is the removal of light that is scattered in the direction of the sensor by just the air molecules. This reflectance can be found by running MODTRAN with the appropriate Sun-sensor geometry, in multiple-scatter mode, and in the absence of aerosols. With data that is glint and Rayleigh corrected, Equation 4.2 becomes

$$\rho_c(\lambda) = \rho_t(\lambda) - \rho_r(\lambda) - T_v(\lambda)\rho_{g_{solar}}(\lambda) = \rho_a(\lambda) + \rho_{ra}(\lambda) + T_v(\lambda)\rho_w(\lambda). \quad (4.5)$$

If we now invoke the assumption for case 1 waters that the water-leaving reflectance for bands 7 and 8 is negligible, we can conclude that $\rho_c(\lambda) = \rho_a(\lambda) + \rho_{ra}(\lambda)$ for these two bands. Therefore, the Rayleigh corrected reflectance is equal to the reflectance due to just aerosol and aerosol-Rayleigh scattering in the atmosphere for bands 7 and 8. Our goal, however, is to determine these atmospheric reflectances for all bands.

We continue the compensation algorithm by taking the observed ratio of Rayleigh corrected reflectances in bands 7 and 8, $\epsilon^{(7,8)} = \frac{\rho_c^7}{\rho_c^8}$, and comparing it to a LUT of theoretical ratios which are found from MODTRAN generated atmospheres. In other words, the user varies key atmospheric input parameters such as aerosols, visibility, and water vapor to simulate a variety of atmospheres that they may expect to encounter in a scene. Then, by spectrally sampling the Rayleigh removed upwelling component for all of the simulated atmospheres to the sensor's response function, $\epsilon^{(7,8)}$ can be determined for each atmosphere and archived in the form of a LUT.

Two theoretical ratios from the LUT will naturally surround the observed ratio and an interpolation factor can be determined. This factor tells us how far the observed ratio falls from the two closest surrounding ratios (atmospheres). We can then use this interpolation factor to extrapolate to the lower wavelengths. The idea is, if we find a pixel to have an atmosphere that falls half-way between two atmospheres in our LUT for its NIR wavelengths, then it should fall half-way between the two atmospheres for its shorter wavelengths as well.

Once an atmosphere is determined for all wavelengths, its effective reflectance can be subtracted from Equation 4.5 and the associated transmission divided out. This leaves the desired water-leaving spectrum,

$$\rho_w(\lambda) = \frac{\rho_t(\lambda) - T_v(\lambda)\rho_{g_{solar}}(\lambda) - \rho_r(\lambda) - \rho_a(\lambda) - \rho_{ra}(\lambda)}{T_v(\lambda)}. \quad (4.6)$$

The process is summarized as follows:

Summary:

Entering the algorithm with solar glint-removed data:

Step 1: On a pixel-by-pixel basis, Rayleigh correct data and determine ρ_c^7 and ρ_c^8 .

Step 2: Assuming water-leaving reflectances for bands 7 and 8 are equal to zero, set $\rho_c^7 = \rho_a^7 + \rho_{ra}^7 = \rho_{am}^7$ and $\rho_c^8 = \rho_a^8 + \rho_{ra}^8 = \rho_{am}^8$.

Step 3: Determine $\epsilon^{(7,8)} = \frac{\rho_{am}^7}{\rho_{am}^8}$ for the observed test pixel and for all candidate models which are obtained by varying key atmospheric input parameters (aerosol, visibility, water vapor) to MODTRAN.

Step 4: For a fixed aerosol type, search LUT for two closest models and determine interpolation ratio.

Step 5: Extrapolate the chosen model out to all wavelengths using interpolation ratio determined from two closest models.

Step 6: Subtract ρ_{am}^λ from both sides of Equation 4.5 and divide by the associated spectral transmission.

4.2.2.3 SeaWiFS Algorithm for Case 2 Waters

The previous method developed by [Gordon and Wang, 1994] is useful for performing atmospheric compensation of SeaWiFS imagery over case 1 waters. Due to its assumption of a zero water-leaving radiance in the NIR, however, it ultimately fails over case 2 waters. Signal due to backscatter from suspended materials may occur in these waters, causing the user to over-estimate the aerosols or optical thickness of the atmosphere. This leads to negative water-leaving reflectances in the visible, which is not possible. For this reason,

[Ruddick et al., 2000] make their own two assumptions to avoid this incorrect premise.

The first assumption requires that the ratio of multiple-scattering aerosols and aerosol-Rayleigh reflectances at 765 nanometers and 865 nanometers is spatially homogeneous over the subscene of interest

$$\epsilon_m^{(7,8)} = \frac{\rho_{am}^{(7)}}{\rho_{am}^{(8)}}. \quad (4.7)$$

In other words, it is sensible to avoid weather fronts, wind-blown dust events, etc., over the region of interest as they will cause spatial inhomogeneity in the NIR. Since the remote sensing of water bodies for the purpose of constituent retrieval must be performed on the clearest of days, this assumption will almost certainly be met.

Secondly, the ratio of water-leaving reflectances normalized by the Sun-sea transmittance in the NIR is assumed to be spatially homogeneous,

$$\alpha \equiv \frac{\rho_w^{(7)}/T_o^{(7)}}{\rho_w^{(8)}/T_o^{(8)}}. \quad (4.8)$$

By making these two assumptions, [Ruddick et al., 2000] are able to derive the multiple-scattering aerosol and aerosol-Rayleigh reflectances for bands 7 and 8,

$$\rho_{am}^{(8)} = \frac{\alpha \rho_c^{(8)} - \rho_c^{(7)}}{\alpha - \epsilon_m^{(7,8)}}, \quad (4.9)$$

and

$$\rho_{am}^{(7)} = \epsilon_m^{(7,8)} \left[\frac{\alpha \rho_c^{(8)} - \rho_c^{(7)}}{\alpha - \epsilon_m^{(7,8)}} \right], \quad (4.10)$$

where $\epsilon_m^{(7,8)}$ and α are fixed calibration parameters that are scene dependent. Therefore, if we know $\epsilon_m^{(7,8)}$ and α for a region of interest, we can determine $\rho_{am}^{(7)}$ and $\rho_{am}^{(8)}$. Once $\rho_{am}^{(7)}$ and $\rho_{am}^{(8)}$ are determined, the steps outlined in [Gordon and Wang, 1994] can be implemented to retrieve the water-leaving spectrum. Note that for these case 2 waters, $\rho_{am}^{(7)} \neq \rho_c^{(7)}$ and $\rho_{am}^{(8)}$ may not equal $\rho_c^{(7)}$.

To determine $\epsilon_m^{(7,8)}$ and α for a given scene, Ruddick suggests making a scatterplot of Rayleigh corrected reflectances, $\rho_c^{(8)}$ vs. $\rho_c^{(7)}$ as shown in Figure 4.11. This enables one to find $\epsilon_m^{(7,8)}$ and α by observing $\rho_c^{(7)}/\rho_c^{(8)}$ in the appropriate regions of the plot. The circled region to the left represents aerosol-dominated pixels that have little reflectance in the NIR

due to water. The ratio $\rho_c^{(7)}/\rho_c^{(8)}$ is taken in this region to define $\epsilon_m^{(7,8)}$ as long as the ratio is fairly constant in the scatterplot (recall the first assumption in Equation 4.7 requires this ratio to be spatially homogeneous).

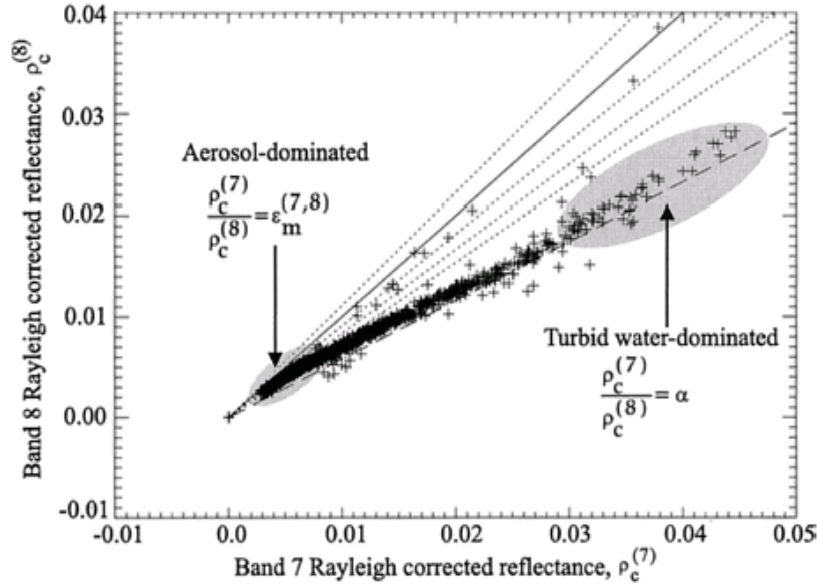


Figure 4.11: *Sample scatterplot of Rayleigh-corrected reflectances used to determine the image parameters α and $\epsilon_m^{(7,8)}$ [Ruddick et al., 2000].*

The circled region to the right represents turbid water pixels. In a similar fashion, we can take the ratio $\rho_c^{(7)}/\rho_c^{(8)}$ in this region to define α , assuming the ratio is fairly constant (recall the second assumption in Equation 4.8). Once these two calibration parameters have been calculated, they can be used in Equations 4.9 and 4.10 to find $\rho_{am}^{(7)}$ and $\rho_{am}^{(8)}$ and ultimately ρ_{am}^λ . The steps are summarized as follows:

Summary:

Entering the algorithm with solar glint-removed data:

Step 1: Plot band 8 vs. band 7 of Rayleigh corrected reflectance data. Use plot to determine calibration parameters $\epsilon_m^{(7,8)}$ and α .

Step 2: Use $\epsilon_m^{(7,8)}$ and α to determine $\rho_{am}^{(7)}$ and $\rho_{am}^{(8)}$ from Equations 4.9 and 4.10.

Step 3: Follow steps 3-6 for algorithm in the previous section.

This algorithm was developed for the eight-band SeaWiFS sensor, as it contains two NIR bands that are centered at 765 nanometers and 865 nanometers. It can be used with other sensors, however, given that they are equipped with similar bands. Unfortunately, this method cannot be used directly with OLI as it contains only one NIR band centered at 865 nanometers. With a basic understanding of both band ratio and spectral matching techniques, however, we are ready to discuss two atmospheric compensation algorithms which were conceived to support this research effort.

4.2.2.4 OLI Algorithm for Case 2 Waters (Blue Band)

The primary goal in developing an over-water atmospheric compensation algorithm for the OLI sensor was to create an accurate method that could be performed on a pixel-by-pixel basis. A limited number of bands precludes us from using spectral matching to atmospherically compensate OLI data while the lack of two NIR bands prevents us from using traditional band ratio techniques.

The following atmospheric compensation method is a hybrid that uses both spectral matching and band ratio techniques. Although the method has been developed for the OLI sensor it can be used for other sensors that meet some minimum requirements. In the following discussion we will first describe the empirical observation that lays the foundation for this algorithm. Next, we will discuss how this algorithm may be utilized with other sensors by defining a methodology for choosing suitable bands. Finally, we will describe the details of the algorithm. The results of several experiments designed to test the algorithm's efficiency are reported in Chapter 5.

The Empirical Observation

We begin the development of this algorithm by referring to Figure 4.12. This figure shows a random sample of Hydrolight-generated water pixels that has been propagated through an atmosphere with a horizontal visibility of 23 kilometers. Figure 4.12(a) shows the signals in terms of their radiance at the front of the sensor, which is 703 kilometers above the ground. Figure 4.12(b) shows the same pixels after being spectrally sampled to OLI's sensor response. What is interesting about these figures is how the signals appear to converge at certain wavelengths. For example, we have mentioned ad infinitum how water is a major

absorber of light in the infrared. Therefore, we can expect all signals in the NIR to appear the same at the sensor since water does not contribute much at these wavelengths, i.e., the atmosphere causes most of the NIR variability in the sensor-reaching signals (except for the most turbid cases). This phenomenon can be confirmed by observing the radiance values in Figure 4.12(a) for light whose wavelengths are greater than 750 nanometers.

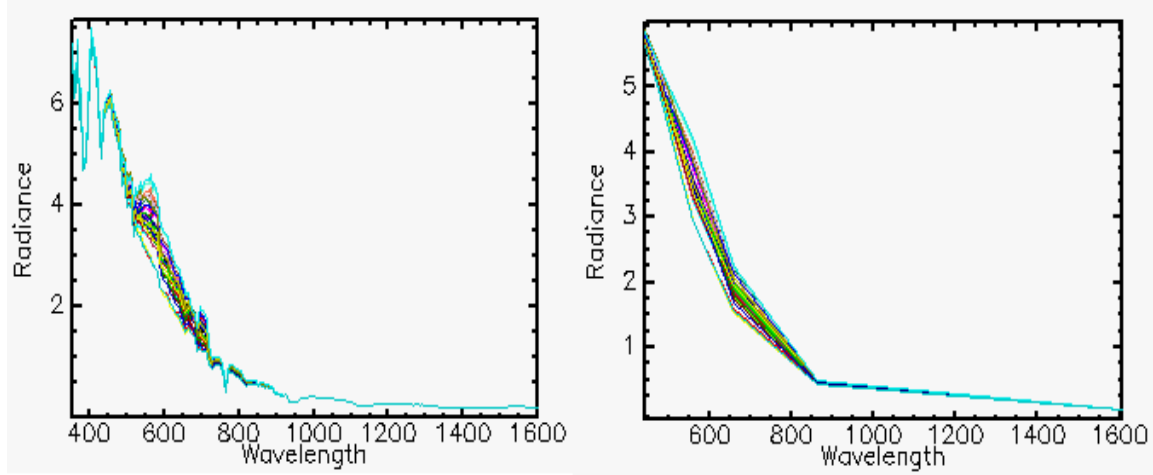


Figure 4.12: (Left) shows the TOA radiance for a random sample of water pixels that were created in Hydrolight and then passed through an atmosphere with a horizontal visibility of 23 kilometers. (Right) shows the signals after being spectrally sampled to the OLI reflective bands.

Interestingly, a similar trend occurs as we observe light whose wavelengths are shorter than 450 nanometers. Although there appears to be some spread in the data at these shorter wavelengths, it is much less than the variability encountered between 450 nanometers and 750 nanometers. To use band ratios directly to perform atmospheric compensation would require that

$$\epsilon^{(1,6)} = \frac{\rho_c^1}{\rho_c^6} = \frac{\rho_a^1 + \rho_{ra}^1 + T_v^1 \rho_w^1}{\rho_a^6 + \rho_{ra}^6 + T_v^6 \rho_w^6} \cong \text{constant}, \quad (4.11)$$

where $\rho_c^i = \rho_t^i - \rho_r^i - \rho_{g_{solar}}^i$ is Rayleigh corrected and solar glint-removed data for band i . In other words, for a fixed atmosphere, the ratio of band 1 to band 6 of OLI data should be approximately constant for all water pixels in the region of interest.

Although Equation 4.11 is true for certain water types, this research has determined that it will not hold under most circumstances due to the variability in band 1. Therefore,

to develop a functional compensation algorithm that uses band ratios we will *assume* that there is some variability in $\epsilon^{(1,6)}$ for OLI data but we look to account for this variability using spectral matching.

Other Sensors

Histograms can assist in determining which bands are suitable for use in this algorithm. An example of this can be seen by noticing Figure 4.13. This RGB image shows data of the Rochester Embayment, which was collected by the AVIRIS sensor and spectrally sampled to the reflective bands of OLI. If we take a region of interest (shown in red) from the image and create histograms of the radiance values occurring within each band, an interesting observation can be made. Certain bands seem to receive a predictable, somewhat constant signal.

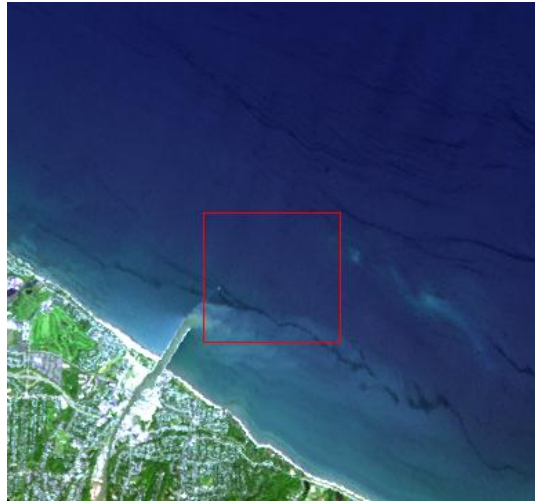


Figure 4.13: *ROI chosen from Lake Ontario.*

Figure 4.14 shows two such histograms from the ROI. Notice in Figure 4.14(a) that the histogram for band 1 has little spread and resembles a normal distribution. This implies that the variability in the sensor-reaching signal is not heavily influenced by the variability in the water's reflectivity. A band of this nature is a desirable choice for use in our algorithm. Alternatively, Figure 4.14(b) shows the histogram for band 3 of OLI. The radiance values occurring in this band clearly have more variability as its spread is larger than that of band 1. Furthermore, its distribution is not as well defined as the one shown in

Figure 4.14(a). Therefore, the variability in the signal at the sensor is due not only to the atmosphere but to the water as well. As our algorithm only looks to detect the atmosphere, a band of this nature would be undesirable.

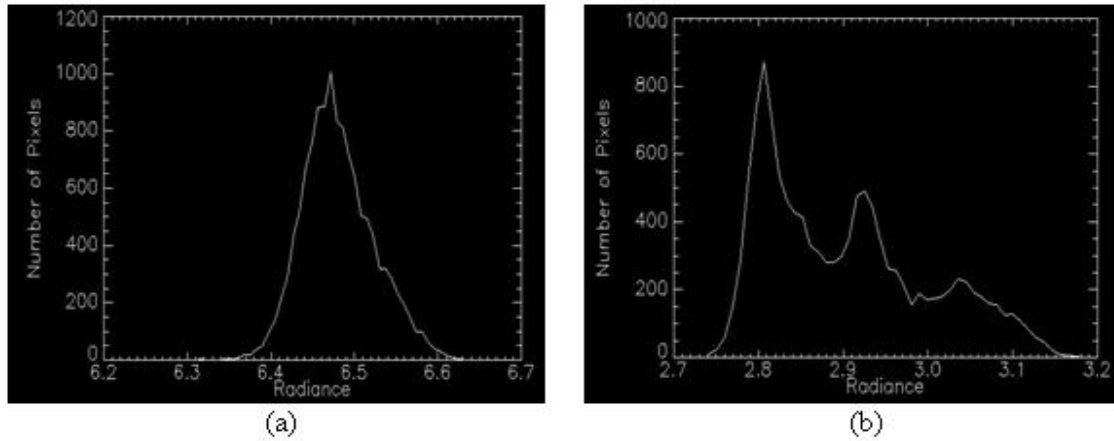


Figure 4.14: *Histograms of the pixels from the ROI described in Figure 4.13. (a) shows the histogram of band 1 from OLI which is centered at 443 nanometers. (b) shows the histogram of band 3 from OLI which is centered at 563 nanometers.*

Algorithm Details

With a qualitative methodology in place for choosing desirable bands, we can now discuss the algorithm's details. The general idea behind this method is to use forward modeling to develop a four dimensional LUT which can be used to determine the chlorophyll, suspended materials, CDOM concentrations, and atmospheric visibility contained in an imaged water pixel. A four dimensional LUT can be developed by generating a range of water types that are representative of the scene of interest, propagating their corresponding water-leaving signals through a range of MODTRAN-generated atmospheres, and spectrally sampling the sensor-reaching radiances to OLI's sensor response function. With a 4-D LUT in place, optimization can be used to search for the best (CHL, SM, CDOM, VIS) combination associated with an imaged water pixel. In this case, the MODTRAN visibility parameter controls aerosol loadings which is the dominant unknown in the atmospheric model. The details are outlined as follows:

Step 1: Develop a 3-dimensional reflectance LUT

In section 3.2.7.1, we discussed the purpose of LUTs and introduced a three dimensional space that we can use to perform constituent retrieval. The first step to this algorithm is to develop an analogous LUT, i.e., one whose axes are defined by an appropriate domain of chlorophyll, suspended sediment, and CDOM concentrations and whose range is made up of water-leaving reflectances.

Figure 4.15 illustrates the 3-D LUT that was created for this research. The domain of values used in our LUT was designed to envelop the observed range of constituent concentrations from the Rochester Embayment and Hydrolight was used to determine the water-leaving reflectances for a structured sampling of points in the LUT.

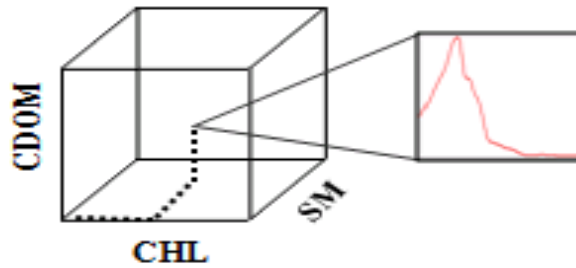


Figure 4.15: *Three dimensional LUT. Water constituent concentrations make up the domain and reflectance spectra make up the range.*

Step 2: Develop a 4-dimensional radiance LUT

With a well-structured LUT of water-leaving reflectances in place we can now add a fourth dimension to our LUT. Section 3.2.5 describes the key atmospheric parameters that must be determined to solve for sensor-reaching radiance in Equation 3.2. By running MODTRAN multiple times to envelop the domain of atmospheric conditions that we expect to observe under typical imaging conditions in Rochester, NY, a fourth dimension can be added to the LUT, i.e., the new domain of the LUT will be made up of the independent variables (chlorophyll, suspended materials, CDOM, visibility) while the range will be made up of sensor-reaching radiances, see Figure 4.16.

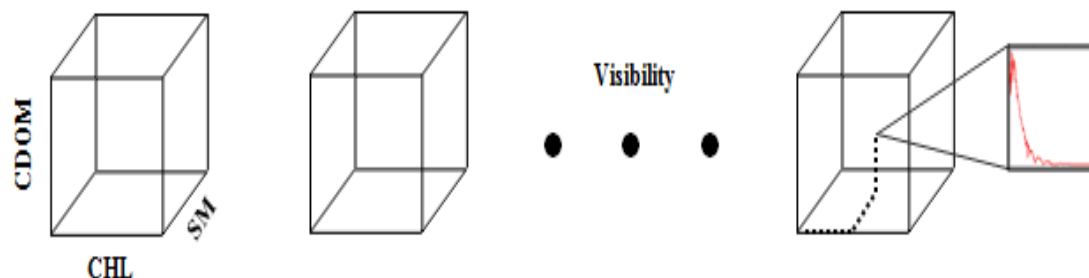


Figure 4.16: *Four dimensional LUT. Water constituent concentrations and atmospheric visibility make up the domain and radiance spectra make up the range.*

Note that this approach assumes the user has made a good estimate of the aerosol type (e.g. rural, urban, maritime, etc.). Additionally, the radiance spectra of the LUT should be spectrally sampled by the appropriate sensor (OLI in this case). With a four parameter radiance LUT in place, glint-removed radiance data can be used to determine the concentrations of constituents in the water. The following steps are performed on a pixel-by-pixel basis:

Step 3: Perform iterative search of LUT with imaged water pixel

(a) Use spectral matching and band ratios to obtain initial guess at visibility

As described at the beginning of this section, performing atmospheric compensation using forward modeling with spectral matching as a decision method fails for multispectral data. Recall in Figure 4.10 that two identical signals can result from two very different in-water and atmospheric parameters. If an educated guess at the atmosphere's visibility can be made, however, a unique solution can be found for (chlorophyll, suspended materials, CDOM). Ideally, we would prefer to take a band 1 to band 6 epsilon ratio, $\epsilon^{(1,6)}$, to determine visibility but Figure 4.17 illustrates the issues associated with this.

The red values in Figure 4.17 represent the minimum and maximum radiances associated with an arbitrary group of modeled water pixels that have been propagated to the top of an atmosphere with a 25 kilometer visibility. The blue values represent the minimum and maximum radiances of the same water pixels at the top of a 30 kilometer atmosphere. Since there is overlap, a simple epsilon ratio may result in a misrepresentation of the at-

mosphere's visibility for an imaged water pixel. Therefore, some other scheme must be employed to determine visibility.

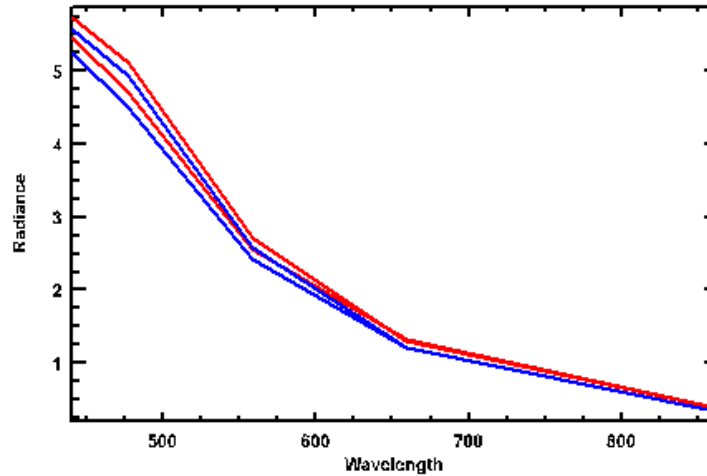


Figure 4.17: *Overlapping red and blue curves indicate issue associated with using band ratios to determine visibility with multispectral data. Red spectra show imaged values for a range of water constituents and a 25 kilometer visibility atmosphere. Blue values are for the same range of constituents and a 30 kilometer visibility.*

Figure 4.18 (Left) shows the TOA radiance for a variety of modeled water signals that have been propagated through a 25 kilometer visibility atmosphere. Spectrally, these signals exhibit a fair amount of variability. This method aims to take advantage of this variability and, in conjunction with band ratios, determine an initial estimate of the atmosphere's visibility.

The technique that we will use to estimate visibility from an imaged water pixel is a two-step process. First, we can compare an imaged spectrum to the spectra contained in the LUT developed in step 2. The constituents associated with the closest non-interpolated spectrum in the LUT (in an RMS sense) represent an estimate of the constituents associated with the imaged water pixel. Figure 4.18 (Right) shows an example of this process where the black LUT spectra are chosen from the red imaged spectrum. Now, if we fix these constituents and only work along the visibility axis, the observed epsilon ratio $\epsilon^{(1,6)}$ can be compared to the LUT ratios to determine visibility. In other words, interpolation is used to determine the visibility associated with the red spectrum in Figure 4.18 (Right). The resulting visibility value provides a sufficient initial estimate for part (b) of this search.

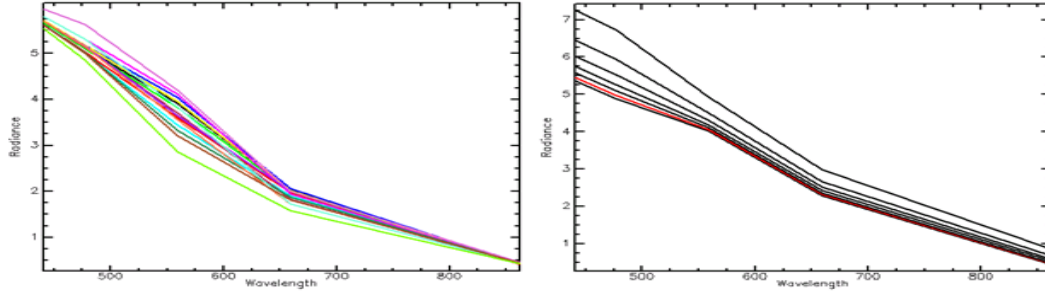


Figure 4.18: (Left) TOA radiance for various water bodies (25 kilometer visibility atmosphere). (Right) Chosen water type based on spectral shape. The red curve is an imaged water pixel and the black curves represent the closest water type.

(b) Perform iterative search using initial visibility estimate

With an initial visibility estimate in place, the Amoeba optimization routine of Section 3.2.7.3 can be used to search the four dimensional LUT developed in step 2. Since all four parameters are treated as unknowns at this point, this process tends to be computationally intensive. The end result of this stage is a (CHL, SM, CDOM, VIS) solution for the imaged pixel.

Step 4: Repeat iterative search using average visibility

It has been determined that since this method solves for visibility on a pixel-by-pixel basis, the visibility solutions obtained from step 3(b) may have significant variability. Physically, this implies that the algorithm allows neighboring pixels in an image to contain different visibilities. It is likely the case that conditions will be near ideal when performing the constituent retrieval process so the visibility should be approximately constant over the study region. Therefore, the iterative search of step 3(b) can be repeated for all water pixels but with a fixed visibility. The average of all visibility solutions obtained in 3(b) will be used to fix visibility and the LUT of step 1 used to solve for (CHL, SM, CDOM).

Summary:

Enter the algorithm with solar glint-removed data:

Step 1: Using Hydrolight, develop a 3-dimensional LUT. The domain of the LUT should

be made up of chlorophyll, suspended material, and CDOM concentrations that one expects to encounter when imaging a scene. The range is made up of water-leaving reflectances as determined by Hydrolight.

Step 2: Use MODTRAN and the existing 3-dimensional LUT to develop a 4-dimensional LUT of sensor-reaching radiances for a best-estimate aerosol type and a range of visibilities.

Step 3: Perform iterative search of LUT with imaged water pixel.

(a) Use spectral matching and epsilon ratios to obtain initial guess at visibility.

(b) Perform iterative search using initial visibility estimate.

Step 4: Repeat iterative search using average visibility.

The level of success of this algorithm depends on a few factors. Our ability to choose at least two bands where sensor-reaching radiance exhibits small variability across a scene is imperative. Therefore, sensors with poor signal-to-noise ratios, insufficient quantizers, or inadequate spectral coverage may fail with this method. Plotting histograms from representative ROI's will enable the user to determine if their sensor's bands are adequate. Other algorithms recommend using two NIR bands, as water is a significant absorber of light at these wavelengths. We will show in Chapter 5 that adequate retrieval results can be obtained using a very short blue band and a SWIR band.

Another factor which will affect this algorithm's success is our ability to characterize the aerosols in a scene. As with other methods, this algorithm uses a radiative transfer code to create atmospheres and populate a LUT. The nature of the aerosols we use to describe the atmosphere can deeply affect our ability to perform adequate atmospheric compensation. Therefore, the user must have a priori knowledge of the aerosols contained in the region that they wish to study. Any misclassification of aerosols or events such as dust storms, land breezes, and weather fronts can lead to a misrepresentation of the aerosols contained in a scene and will most likely cause the model to fail.

4.2.2.5 OLI Algorithm for Case 2 Waters (Band Ratios)

Due to the slow and iterative nature of the previous method, a second over-water atmospheric compensation algorithm has been designed specifically for the OLI instrument. The

algorithm of this section takes advantage of the concept of band ratios in its implementation. Adopting the notation of [Gordon and Wang, 1994], recall from Equation 4.11 that if

$$\epsilon^{(i,j)} = \frac{\rho_c^i}{\rho_c^j} = \frac{\rho_a^i + \rho_{ra}^i + T_v^i \rho_w^i}{\rho_a^j + \rho_{ra}^j + T_v^j \rho_w^j} \cong \text{constant}, \quad (4.12)$$

holds for some band i and band j , then a band ratio technique may be implemented to solve for ρ_w in Equation 4.2. [Gordon and Wang, 1994] use the black ocean assumption to show that Equation 4.12 holds for NIR bands 7 and 8 of SeaWiFS over case 1 waters where $\rho_w = 0$. For case 2 waters, where the black ocean assumption cannot be made, [Ruddick et al., 2000] were able to separately characterize the reflectance due to the water body of interest (ρ_w) and the reflectance due to the atmosphere ($\rho_a + \rho_{ra}$) in an effort to determine $\epsilon^{(7,8)}$ for band 7 and band 8 of SeaWiFS.

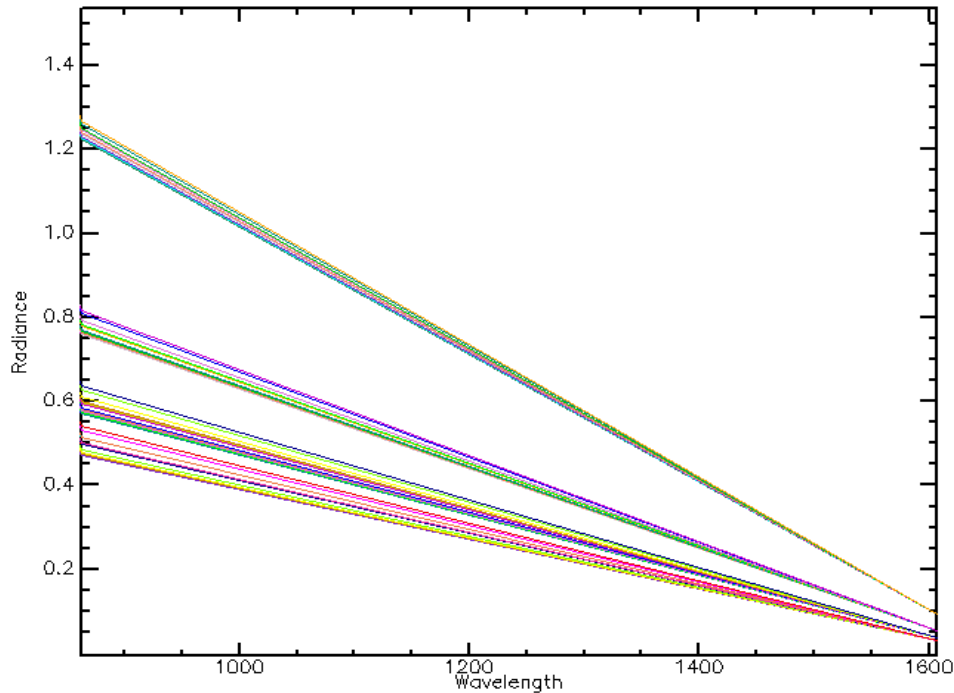


Figure 4.19: Figure showing OLI's band 5 (862 nanometers) and band 6 (1605 nanometers) radiance values for a subset of the 4-D LUT described in section 4.2.2.4. From the top family of curves to the bottom, visibility is [10,15,20,25] kilometers.

Similarly, in this algorithm we wish to use the epsilon ratio, $\epsilon^{(5,6)}$, for the NIR band and SWIR band of OLI to determine the reflectance due to the atmosphere in an image.

However, Figure 4.19 illustrates the issue associated with this practice when imaging turbid case 2 waters. This figure shows OLI's band 5 (862 nanometers) and band 6 (1605 nanometers) radiance values for a subset of the 4-D LUT described in Section 4.2.2.4. Notice for band 5 (862 nanometers) that the variability in the sensor-reaching signals is due to both the atmosphere and the water type. As a result, simply taking a band ratio $\epsilon^{(5,6)}$ will result in a misrepresentation of the atmosphere's reflectance. However, if we characterize the signal in band 5 due to darker waters and make the black ocean assumption in band 6, $\epsilon^{(5,6)}$ can be used to determine the atmosphere over dark waters in an image. This chosen atmosphere can then be removed over neighboring turbid waters in the scene, i.e., the [Ruddick et al., 2000] approach adapted to the SWIR region.

The details of this algorithm are much like those associated with the SeaWiFS algorithms of Section 4.2.2.2 and Section 4.2.2.3. Recall that, with an image that has been glint corrected, we are trying to solve for $\rho_w(\lambda)$ in

$$\rho_t(\lambda) - T_v(\lambda)\rho_g(\lambda) = \rho_r(\lambda) + \rho_a(\lambda) + \rho_{ra}(\lambda) + T_v(\lambda)\rho_w(\lambda), \quad (4.13)$$

on a pixel-by-pixel basis. To do this, we must first create a LUT of candidate atmospheric models. By varying key MODTRAN input parameters (aerosol, visibility) to solve for $\rho_r(\lambda)$, $\rho_a(\lambda)$, $\rho_{ra}(\lambda)$, and $T_v(\lambda)$, and using Hydrolight to characterize (ρ_w) for dark waters, Equation 4.13 can be solved and $\epsilon^{(5,6)}$ calculated for each model to populate the LUT.

Then, to determine the reflectance due to the atmosphere in an image, an ROI over less turbid (darker) waters can be taken and its $\epsilon^{(5,6)}$ used to choose an appropriate atmosphere from the LUT. The reflectance due to the chosen atmosphere can then be removed from Equation 4.13 to obtain (ρ_w) for each pixel in the image.

This method, of course, makes some assumptions about the scene of interest. First, we assume that there will be dark waters somewhere in the scene. Figure 4.20 shows the familiar Rochester Embayment, which represents the scene of interest for this research. Offshore Lake Ontario waters, or perhaps Cranberry pond, can be used as the dark water for this method. If non-turbid waters do not exist in the scene then (ρ_w) can possibly be modeled for a well characterized turbid water body and the same method performed.

Secondly, to use this algorithm the scene of interest must be small enough that the

atmosphere is homogeneous. As always, dust storms, weather fronts, etc. will impede our ability to accurately characterize the aerosols in the scene. Additionally, if the scene is too large, the assumption that the atmosphere is homogeneous over the entire image may not be valid. The scene that we will be working with in this research (Figure 4.20) is approximately 10×15 kilometers. Therefore, under the conditions needed to perform this type of study the atmosphere should be fairly homogeneous across the entire scene.



Figure 4.20: *RGB image of the Rochester Embayment illustrating the various lakes and ponds in the area.*

Finally, the signal-to-noise in the SWIR band (OLI band 6) must be large enough to resolve the aerosol optical thickness (visibility) in the scene. As the SNRs of the final OLI system are unknown, SNR is modeled using the half-margin noise ratios described in Appendix C.3. Experiments designed to test the efficiency of this algorithm are reported in Chapter 5. The algorithm is summarized as follows.

Summary:

Entering the algorithm with solar glint-removed data:

Step 1:

Create a LUT of candidate atmospheric models. Using MODTRAN to determine $\rho_r(\lambda)$,

$\rho_a(\lambda)$, $\rho_{ra}(\lambda)$, $T_v(\lambda)$, and Hydrolight to determine (ρ_w) for dark waters, solve Equation 4.13 and calculate $\epsilon^{(5,6)}$ for each model to populate the LUT.

Step 2:

Take ROI over dark water in the scene and determine $\epsilon^{(5,6)}$ for the region by averaging the reflectance values for that ROI.

Step 3:

Use $\epsilon^{(5,6)}$ from ROI to search LUT for the two closest modeled atmospheres and determine interpolation ratio.

Step 4:

Extrapolate the chosen model out to all wavelengths using interpolation ratio determined from two closest atmosphere models.

Step 5:

Spectrally remove atmospheric effects globally from the scene of interest.

4.2.2.6 The Empirical Line Method

In the ideal case where ground truth measurements are available, an alternative approach can be taken to compensate for the atmosphere. A simple, yet efficient method for determining water reflectances based on radiance received by the sensor is the Empirical Line Method (ELM). This method works by developing a linear relationship between the reflectances collected from in situ observations and their corresponding sensor-reaching radiances. Then, if the radiance of an unknown water pixel is collected, the reflectance associated with the pixel can be determined from the linear relationship. This process is carried out on a band-by-band basis.

Figure 4.21 shows a hypothetical example of how the method is implemented. Suppose that for *band i* of a sensor, the radiances collected for two water pixels are 6.28 and 10.47 ($\frac{W}{m^2 sr}$). At the same time, ground truth measurements have determined that the reflectances associated with the two water pixels are 0.03 and 0.31, respectively. By plotting radiance versus reflectance for the two pixels, a linear relationship can be derived for *band i*. Now, if the radiances in *band i* are known for other water pixels in the image, their corresponding reflectances can be determined by using this linear relationship. This process is carried out for all bands in the sensor and for all pixels of interest.

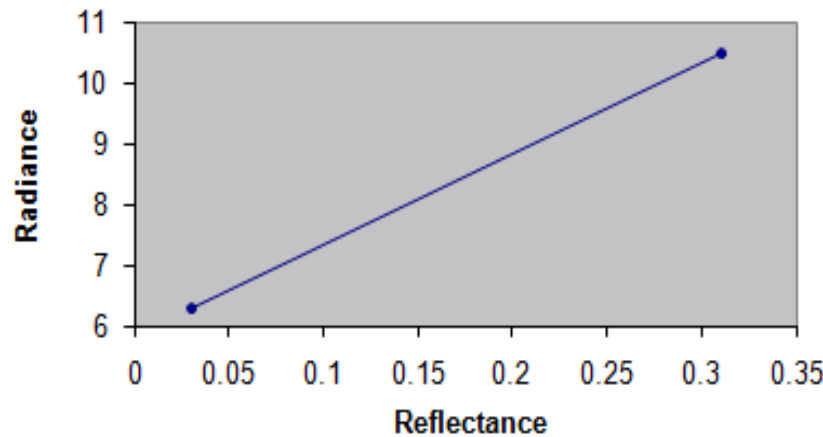


Figure 4.21: *Example of the linear relationship that can be developed when the reflectances and their associated radiances are known for an imaged water pixel.*

The popularity of this method stems from its simplicity. When adequate ground truth measurements are available the ELM is truly the desired approach for atmospheric compensation. There are a few obstacles that one must be aware of, however, when using this technique in conjunction with the constituent retrieval process. First, solar glint must still be removed. The algorithm described in Section 4.2.1 can be used in most cases to remove this effect. Secondly, the efficiency of this method hinges on our ability to collect precise ground truth measurements. Since the reflectivity of water is close to zero, we must be able to characterize how radiance changes with respect to reflectance near zero. Standard land-based ELM's fail due to the lack of dark pixels in the scene. Additionally, making the assumption that the darkest water pixel in the scene has a reflectivity of zero will also fail due to our need for precision at these lower reflectivities.

[Raqueno et al., 2000] describes a method that models the reflectance of water to be used as a dark pixel in the Empirical Line method. Using Hydrolight, if adequate in situ water measurements are collected then the water-leaving reflectances can be determined. These reflectances can be used in conjunction with bright objects in the scene (such as sand) to determine the linear relationship between radiance and reflectance. [Raqueno et al., 2000] describes this method as being quite effective but again it hinges on ones ability to collect precise ground truth measurements.

4.3 The Constituent Retrieval Algorithm

Given the water-leaving reflectance (ρ_w), we enter into the constituent retrieval algorithm. In this section we will describe how our LUT method can be used to convert ρ_w into constituent concentrations. Included in the discussion is a description of the specific Hydrolight inputs that are used in this research to build a LUT. We then discuss how Amoeba is implemented and describe modifications that were made to the existing code to improve its efficiency and accuracy.

4.3.1 Look-up Table Development

The process of building a LUT can best be described as the collecting of ground truth that is representative of a scene of interest. Theoretically, one can attempt to populate a LUT by taking thousands of in situ water samples and measuring their corresponding remote-sensing reflectances and constituent concentrations in a lab. This process is not practical, of course, so we rely on models to simulate the water samples. Hydrolight is an in-water radiative transfer code that takes inputs such as water IOPs and meteorological conditions to yield the remote-sensing reflectance of the water column as an output. Therefore, using forward modeling we can simulate various water types in a scene by providing Hydrolight with appropriate inputs and using its output to build a LUT.

The following discussion describes the common inputs used in this research to populate an arbitrary element of the table. To populate all elements of the LUT, recall that we can simply vary the concentrations of the constituents while holding all other inputs constant. In this research we assume that the water is sufficiently deep so signal from bottom reflections will not be detected. Therefore, if we recall Figure 3.7, we will be working with a four component model where we need to define the absorption and scattering properties of the three major constituents and of pure water itself.

4.3.1.1 Measuring IOP's

A first major step in developing a LUT using the forward modeling technique is to measure the IOP's from the water bodies of interest. Specifically, we need to measure the absorption coefficients for CDOM, and the absorption/scattering coefficients and scatter-

ing phase functions for chlorophyll-a, suspended materials, and pure water. Additionally, determination of the constituent concentrations is necessary in order to define the domain of values that will be specified in the LUT.

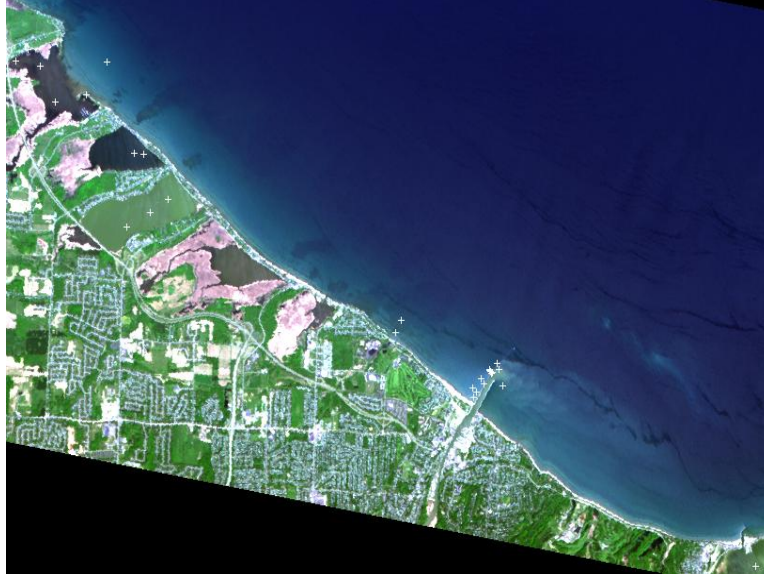


Figure 4.22: *RGB image of the Rochester Embayment. Crosses represent locations where in situ observations were made.*

Absorption/Scattering Coefficients

The absorption and scattering coefficients that we will use for pure water are defined by [Pope and Fry, 1997] and [Smith and Baker, 1981], respectively. These coefficients reflect the most recent measurements and are shown in Figure 4.23 as a function of wavelength.

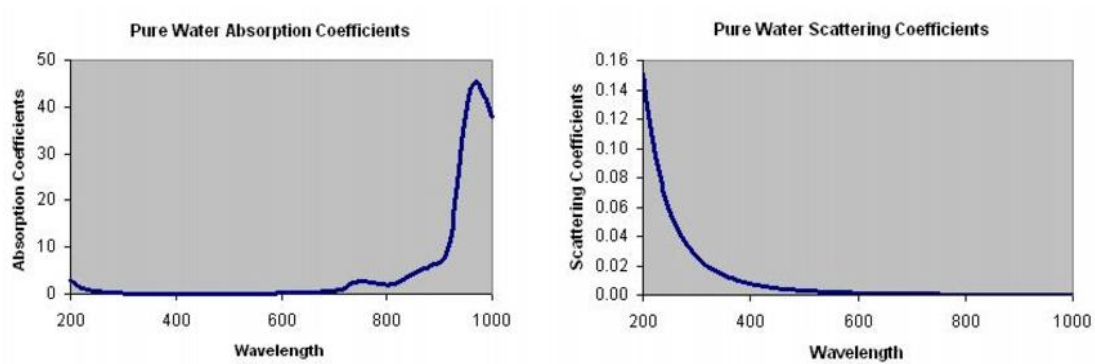


Figure 4.23: *(Left) The absorption coefficients for pure water as a function of wavelength as measured by [Pope and Fry, 1997]. (Right) The corresponding scattering coefficients as derived by [Smith and Baker, 1981].*

To determine the remaining coefficients, we refer to Figure 4.22 which shows an RGB image of the Rochester Embayment and the locations of coincident in situ ground truth measurements. Water samples were collected at the locations indicated with crosses and brought back to the lab for processing.

To measure CDOM absorption coefficients, water samples were filtered through 0.4 micron filters and the filtered liquid placed in quartz cuvettes. A dual-beam spectrophotometer was then used to determine the CDOM absorption coefficients of each sample by comparing its absorption spectra to that of distilled water blanks. Figure 4.24 shows the CDOM absorption coefficients for the various ground truth locations. A spectral average (bold, black curve) of the coefficients was taken and used as input to Hydrolight.

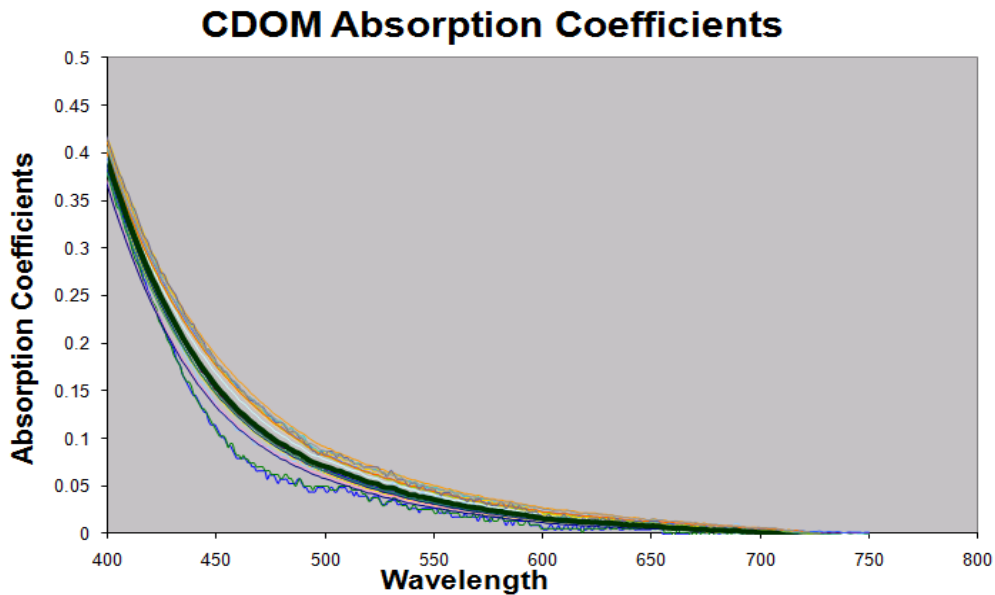


Figure 4.24: *CDOM absorption coefficients for the various ground truth locations shown in Figure 4.22. The solid black line represents the average of all coefficients.*

Figure 4.25 shows the full spectrum of the average CDOM-specific absorption coefficients that are used as input to Hydrolight. Notice that the coefficients have been normalized so that $a(350nm) = 1$ in this figure. This normalization step was performed due to the nature in which we measure CDOM concentration in this research. An indirect method for measuring relative CDOM concentrations will be discussed shortly, however, one should note that this scaling does not have an effect on the magnitude of the absorption events.

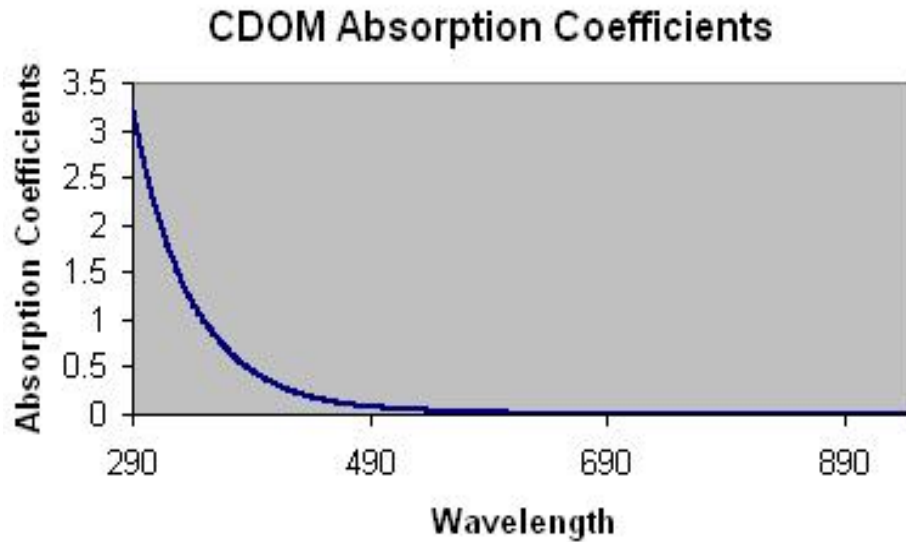


Figure 4.25: *CDOM Absorption coefficients as a function of wavelength.*

A filtering process is also used to determine the absorption coefficients of chlorophyll-a and suspended materials. Similar to the method described for CDOM, samples are filtered through a 0.4 micron pad. Again, a dual-beam spectrophotometer is used to measure the absorption properties. This process, however, requires the sample filter to be measured against a reference filter that has been wetted with distilled water. The difference in the two measurements yields a combined chlorophyll-a/suspended materials absorption coefficient.

To distinguish between the absorption coefficients for the two constituents, methanol can be used as described by [Mueller and Austin, 1995] to extract the chlorophyll pigments from the filtered sample. Using the spectrophotometer once again, the resulting curve describes the absorption coefficients due to suspended materials. Subtracting these coefficients from the coefficients obtained in the previous step allows us to calculate the absorption coefficients due to just the chlorophyll-a. As we did for CDOM, the coefficients for all samples are averaged to yield the chlorophyll-a and suspended material absorption coefficients that will be used as input to Hydrolight.

The average absorption and scattering coefficients for chlorophyll-a are shown in Figure 4.26. The absorption coefficients in Figure 4.26(a) were scaled so that $a(440nm) = 0.05$ to be consistent with Hydrolight's default absorption model which uses data derived by

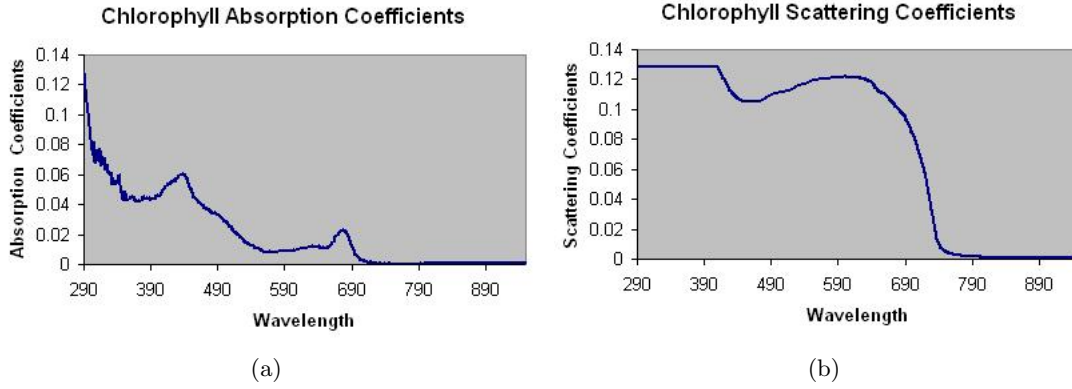


Figure 4.26: (a) shows the absorption coefficients for *Phytoplankton(Chlorophyll)* as a function of wavelength. (b) shows its corresponding scattering coefficients.

[Sathyendranath and Prieur, 1981]. Since instruments to measure scattering events were not deployed in the May 20, 1999 campaign, scattering coefficients were obtained from [Bukata et al., 1981]. Figure 4.26(b) shows the chlorophyll-a scattering coefficients as described by [Fairbanks, 1999] with an extrapolation in the NIR as suggested by [Vodacek, 2005]. Finally, Figure 4.27 shows the average absorption and scattering coefficients for suspended materials as a function of wavelength.

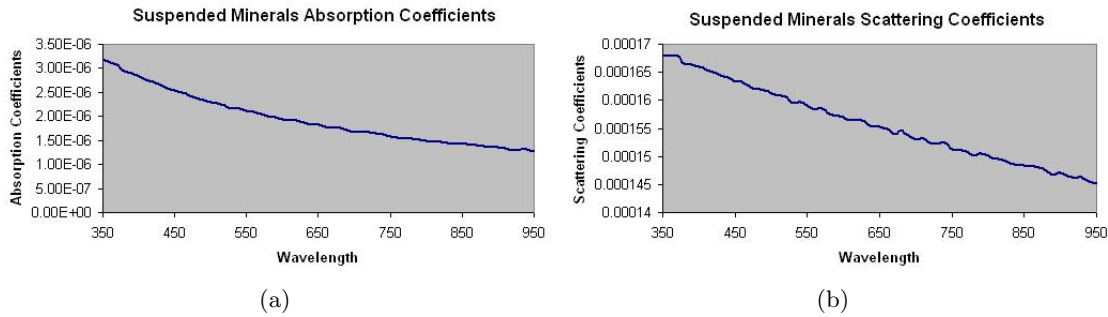


Figure 4.27: (a) shows the absorption coefficients for suspended sediments as a function of wavelength and (b) shows its corresponding scattering coefficients.

Scattering Phase Functions

Recall that the absorption and scattering coefficients only indicate the magnitude of these processes in an arbitrarily small volume of water. To perform forward modeling, we must also know the directionality of the scatter. This enables the model to predict how much

light will exit the water column in a given viewing direction. Therefore, we must model the scattering phase functions of pure water, chlorophyll, and suspended sediments (CDOM only absorbs light). These functions give us a three dimensional representation of the scatter normalized by the corresponding scattering coefficients.

Figure 4.28 shows a traditional representation of the scattering phase function for pure water, [Smith and Baker, 1981]. Since these functions are assumed to be circularly symmetric, we can sufficiently describe the function with two-dimensional plots. If zero degrees represents the forward direction for the propagation of light, one should notice that pure water is highly scattering in both the forward and backward directions. This is intuitively satisfying since water molecules are small compared to the incident VNIR light.

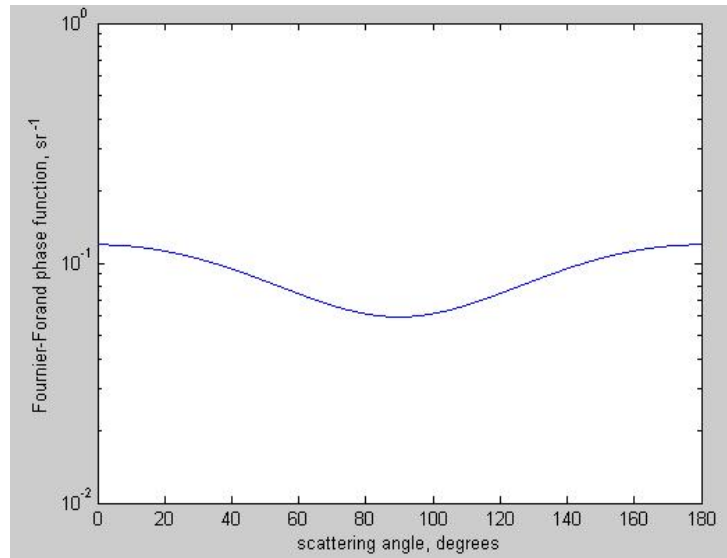


Figure 4.28: *Scattering phase function for pure water.*

The scattering phase function used in this research to model the directional scattering due to chlorophyll and suspended sediments is the highly forward scattering Fournier-Forand model. This function is attractive due to its high degree of precision and ease of calculation [Haltrin, 1998] and comes standard in the Hydrolight code. The user can choose from a library of Fournier-Forand models that are indexed based on their backscatter values. Figure 4.29 shows the Fournier-Forand phase function chosen for this research which contains a backscatter fraction of 0.025.

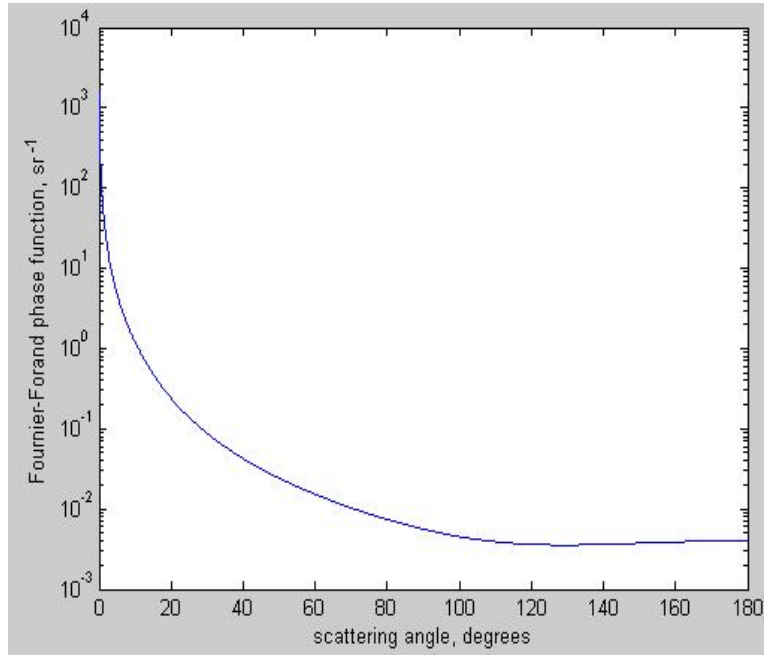


Figure 4.29: *Scattering phase function for chlorophyll and suspended sediments with a backscatter fraction of 0.025 or 2.5%. Data was obtained from a Hydrolight supplied phase-function, [Mobley, 1994].*

This fraction, which is high compared to that of case 1 waters, was determined by fitting a model to the ground truth measurements taken from Lake Ontario on May 20, 1999, [Raqueno et al., 2000]. By varying the backscatter fraction of the Fournier-Forand phase function, several LUTs were generated using Hydrolight. The constituents concentrations associated with field measured water-leaving reflectances were then determined for each of the LUTs and compared to actual measured constituent concentrations. The backscatter fraction of 2.5% provided the closest agreement between predicted concentrations and laboratory measured concentrations.

Determining Constituent Concentrations

To define the domain of values to be used in our constituent retrieval algorithm (the LUT), the constituent concentrations were measured for the various water samples collected from the Rochester Embayment. Chlorophyll concentrations, which were determined using standard spectrophotometric and fluorometric techniques ranged from $0.49 \left[\frac{\mu g}{L} \right]$ to $64.15 \left[\frac{\mu g}{L} \right]$. These measurements were in good agreement with measurements made by the Monroe

County Health Department Laboratory [Raqueno et al., 2000].

Suspended material concentrations were determined by filtering the various water samples through 0.4 micron preweighed filters. The filters were then dried and weighed again to deduce the suspended materials in the sample. Suspended material concentrations ranged from 0.13 [$\frac{mg}{L}$] to 23.33 [$\frac{mg}{L}$] for the various samples shown in Figure 4.22.

Due to a lack of proper equipment necessary to measure CDOM concentrations, an indirect metric is used in this research to describe the amount of CDOM in the water. Recalling Equation 3.8, CDOM concentrations can be determined from

$$a_{CDOM}(\lambda) = C_{CDOM} a_{CDOM}^*(\lambda), \quad (4.14)$$

where $a_{CDOM}(\lambda)$ is the observed CDOM absorption coefficients from a sample, C_{CDOM} is the unknown scalar which indicates the relative concentration of CDOM in the water and $a_{CDOM}^*(\lambda)$ is the mean, normalized CDOM-specific absorption coefficients used as input to Hydrolight (Figure 4.25). Recall that $a_{CDOM}^*(\lambda)$ has been normalized to 1 at 350 nanometers so a relative concentration of CDOM in a sample can be determined by simply observing its value of $a_{CDOM}(\lambda)$ at the reference wavelength. The observed range of CDOM scalars at 350 nanometers was 0.48 to 12.78 for the various water samples collected from the Rochester Embayment.

4.3.1.2 Other Inputs to Hydrolight

Once the IOP's of the water have been determined, we can specify a variety of other inputs to Hydrolight. We do not model any inelastic scattering or internal sources in this study. We request our data in 5 nanometer increments from 352.5 to 947.5 nanometers. A windspeed of 5 [$\frac{m}{s}$] at 12 meters above the water surface is specified to be consistent with surface conditions observed on May 20, 1999 [Raqueno et al., 2000]. MODTRAN is used to specify an atmosphere indigenous to the region and an appropriate solar-zenith angle is specified with no cloud cover.

Once the common inputs have been defined, the concentrations of the constituents are systematically varied. For example, in our LUT we varied chlorophyll between 0 and 68 [$\frac{\mu g}{L}$], suspended material between 0 and 24 [$\frac{mg}{L}$], and the CDOM scalar between 0 and 14.

These ranges reflect the in situ observations taken from that day. Next, the common inputs and combination triplets are fed into Hydrolight which outputs the associated water-leaving reflectances. This was performed for the thousand permutations of triplets shown in Table 4.1. The end result of this process is a well-populated LUT that is ready to be used for the constituent retrieval process.

Chlorophyll	Suspended Materials	CDOM
0.25	0.25	0.25
0.5	0.5	0.5
1	1	0.75
3	2	1
5	4	2
7	8	4
12	10	7
24	14	10
46	20	12
68	24	14

Table 4.1: *Constituent concentrations used to develop triplets for input into Hydrolight.*

4.3.2 Running Amoeba

The process required to run Amoeba is fairly straight forward and detailed in Section 3.2.7.4. Due to its time-consuming nature, however, a few recommendations can be made for those looking to use this optimizer. Recall that Amoeba can be used to search a LUT to determine the concentrations of constituents in a water pixel. The input to the optimizer is the retrieved (ρ_w) from Equation 4.6 while its output is the pixel’s constituent concentrations. If one has ground truth in the scene it can be used to define an error metric for the retrieval process. After some experience using Amoeba, the following observations and improvements were made.

To run Amoeba, the user supplies an initial starting point and scale factor which are used to search the LUT. The starting point fixes the initial starting position in the LUT while the scale factor indicates how far Amoeba will throw out “feelers” in which to search for our minimum. Amoeba does an extremely poor job in finding the global minimum in our LUT if an inaccurate starting point and/or scale factor is given. To combat this issue, a multiple starting point/scale factor method has been implemented which efficiently

searches the LUT in its entirety. This is done by simply looping through a variety of starting points and scale factors enabling the optimizer to test all corners of the LUT. Implementing this feature greatly reduces error but causes a significant increase in run time.

The nature of the LUT developed in this work leads to a second observation. If we look at the spectra associated with higher constituent concentrations, one can notice that a large change in concentration does not necessarily lead to a large change in spectra. In other words, as we increase the concentration of constituents in already turbid waters there is little change in color. This is shown in Figure 4.30 where four water-leaving spectra are displayed. The green and blue spectra correspond to concentrations of $(CHL, SM, CDM) = (1, 1, 4)$ and $(CHL, SM, CDM) = (3, 1, 4)$ while the black and red spectra correspond to concentrations of $(CHL, SM, CDM) = (46, 24, 14)$ and $(CHL, SM, CDM) = (68, 24, 14)$, respectively. Notice that a small change in chlorophyll of 2 units causes the significant change in spectra from the green to the blue. On the other hand, a large change in chlorophyll of 22 units has little effect on the spectra as seen from the black and red curves. Further magnifying this issue is the fact that the fluorescence peak at 700 nanometers is outside OLI's bands. Therefore it will not be detected by the OLI sensor.

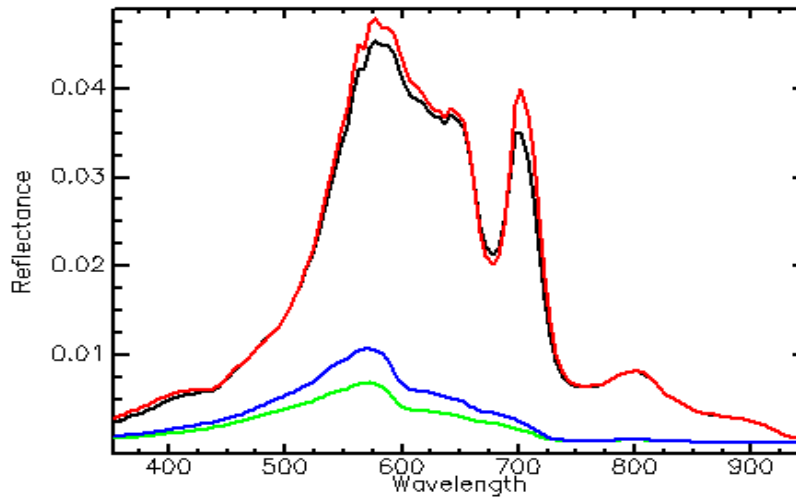


Figure 4.30: *Illustration of the variability associated with spectra in the LUT. Green is spectrum associated with $(CHL, SM, CDM) = (1, 1, 4)$. Blue is spectrum associated with $(CHL, SM, CDM) = (3, 1, 4)$. Black is spectrum associated with $(CHL, SM, CDM) = (46, 24, 14)$. Red is spectrum associated with $(CHL, SM, CDM) = (68, 24, 14)$.*

The implication of this phenomena is that, since there is little variability in the upper regions of the LUT, Amoeba will labor exhaustively to find a minimum. Figure 4.31 illustrates the issue with a two-dimensional example. The left curve resembles the sort of minimization problem we might encounter in the lower-most octant of our LUT. The minimum is clearly defined and can be found quickly. The right curve resembles the sort of minimization problem we might encounter in the upper-most octant of our LUT.



Figure 4.31: *Two-dimensional representation of an optimization issue associated with Amoeba.*

The minimum is not clearly defined so Amoeba iterates over and over searching for an answer. This is a time consuming process that actually yields inferior results. To overcome this issue, the threshold required by Amoeba should be carefully selected. Counter-intuitively, a higher threshold might actually improve results with a dramatic decrease in run-time. In this research, a threshold of 0.05 was used. This means that when the change in the RMS difference between the observed spectrum and the LUT spectrum falls below 0.05, the algorithm terminates.

4.4 Concluding Remarks

The purpose of this chapter was to introduce the techniques that one should use to perform the constituent retrieval process over case 2 waters when presented with a multispectral dataset. The improved features of the OLI sensor, which exhibits exciting potential to be used for constituent retrieval, were introduced. Techniques for removing glint and atmospheric effects from multispectral data were presented, with a particular emphasis placed on anticipated OLI data. Finally, the constituent retrieval process that will be used through-

out this research was outlined and techniques aimed at enhancing the retrieval process were discussed.

In Chapter 5, we will test the techniques of this chapter with both real and synthetic data. Naturally, we must first show that OLI is indeed a valid sensor to be used for the constituent retrieval process. A study is conducted in Section 5.1.1 which does just that. The new features of the OLI sensor are modeled and its ability to perform the constituent retrieval process is compared to that of existing sensors. Next, studies aimed at evaluating the efficiency of the OLI atmospheric compensation algorithms are conducted with synthetic data. Potential issues associated with the LUT constituent retrieval algorithm are presented and the OLI atmospheric compensation algorithms are again tested with real data. We conclude Chapter 5 with a discussion of potential issues that may exist with the AVIRIS dataset used in this work.

Chapter 5

Constituent Retrieval with the OLI Sensor: Results

In Chapter 4 we described the new features of the OLI sensor, introduced atmospheric compensation algorithms that could be used to correct OLI data, and detailed the constituent retrieval algorithm that will be used to determine the constituents in an imaged water pixel. In this chapter, experiments designed to test the methodologies of Chapter 4 are conducted on both real and synthetic data. Section 5.1.1 begins with an experiment designed to determine if OLI is a valid sensor to be used throughout this research. Next, the efficiency of the OLI over-water atmospheric compensation algorithms are tested on both synthetic and real data. In Section 5.1.2, the constituent retrieval process is performed on synthetic data followed by a synthetic image in Section 5.1.3. Section 5.2 is included in this chapter to describe some issues that may arise as we transition these methods from synthetic to real data. Finally, the constituent retrieval process is performed on real data in Section 5.3.

5.1 Synthetic Data

The purpose of using synthetic data is to evaluate the efficiency of a method or instrument under ideal conditions. It can be argued that if a method will not work under ideal conditions, then there is no hope of it working under realistic conditions. In this section, the methods of Chapter 4 are evaluated using modeled data. We begin by evaluating the

potential for OLI to be used for retrieving water quality parameters.

5.1.1 Evaluation of the OLI Sensor

To evaluate the new features of the OLI sensor and their corresponding contributions to the constituent retrieval process, a series of tests will be conducted. In the first experiment, the constituent retrieval process is performed in the absence of noise and quantization effects for the OLI sensor. A test of this nature enables us to determine how spectral coverage affects the retrieval process. Secondly, the 12-bit quantizer of OLI is modeled to determine how quantization affects a sensor's ability to retrieve water constituents. Finally, an experiment is conducted that includes sensor noise into the model. By spectrally sampling a signal, adding sensor noise, and quantizing the result we can determine how the addition of noise affects a sensor's ability to retrieve water constituents. As we wish to analyze the errors introduced to the constituent retrieval process by just the OLI sensor, all three tests are performed in the absence of atmospheric effects.

5.1.1.1 The Scene

To begin our analysis, we introduce the scene of interest. Figure 5.1 shows an image of the Rochester Embayment and its neighboring ponds. The data for this image was collected with the AVIRIS sensor on May 20, 1999 and it is with this scene that we will evaluate OLI's ability to perform the constituent retrieval process. For this experiment, image data will be simulated using Hydrolight and will reflect in situ measurements taken during the AVIRIS collect. Using simulated data allows us to work in the absence of atmospheric effects as we go through the constituent retrieval process.

5.1.1.2 Simulated Data

To simulate the scene that we have chosen in Figure 5.1 we must accurately recreate the conditions observed on May 20, 1999. From meteorological conditions, to water IOPs, to solar-zenith angle, the state of the environment must be described and used as common inputs into Hydrolight as detailed in Section 4.3.1. Furthermore, in situ water measurements were taken the day of the collect and provide us with a range of observed constituent



Figure 5.1: *RGB image of the Rochester Embayment. AVIRIS data of Rochester, NY collected on May 20, 1999.*

concentrations. Recall that the bounds of our LUT (Figure 3.14) were chosen to reflect the range of concentrations that we expect to observe in our scene. Therefore, to simulate a collect we want to randomly create water samples that appear within the bounds of this LUT.

A random number generator was written for this research that essentially creates a concentration triplet. It works by simply generating an initial random number between 0 and 68, a second random number between 0 and 24, and a third random number between 0 and 14, as these were the ranges of constituents observed from in situ measurements. These three numbers will represent the concentrations of chlorophyll, suspended materials, and CDOM that will be fed into Hydrolight, respectively. Hydrolight will then output the water-leaving signal associated with the random water sample which will represent one pixel in the scene. This process can be repeated thousands of times to simulate a scene. In this study, two thousand randomly generated pixels were created.

Once a scene is simulated, atmospheric effects can be ignored by assuming that the water-leaving reflectances obtained by Hydrolight reach the front of the sensor unscathed. Then, we can simulate a sensor's sampling process by first spectrally sampling the signals to its response function, next adding random noise, and lastly quantizing the signals with the appropriate quantizer. The end result of the sensor's sampling process is a discrete representation of the once continuous signals. We can then test how effective OLI is in

retrieving constituent concentrations by inverting these observed, discrete signals back to concentration triplets using the LUT constituent retrieval algorithm.

Figure 5.2 indicates that in addition to the OLI instrument, we have included the AVIRIS and ETM+ sensors for this study. A model of AVIRIS is included to represent an ideal sensor in regards to the constituent retrieval process. With over 60 bands in the VNIR, high SNR, and a 12-bit quantizer, its ability to perform constituent retrieval represents the best-case scenario. A model of ETM+, on the other hand, is included to show the current Landsat technology that is available to the community. With only 4 bands in the VNIR, relatively low SNR, and an 8-bit quantizer, ETM+ is not suitable for the constituent retrieval process and will serve as a baseline to measure OLI's success.

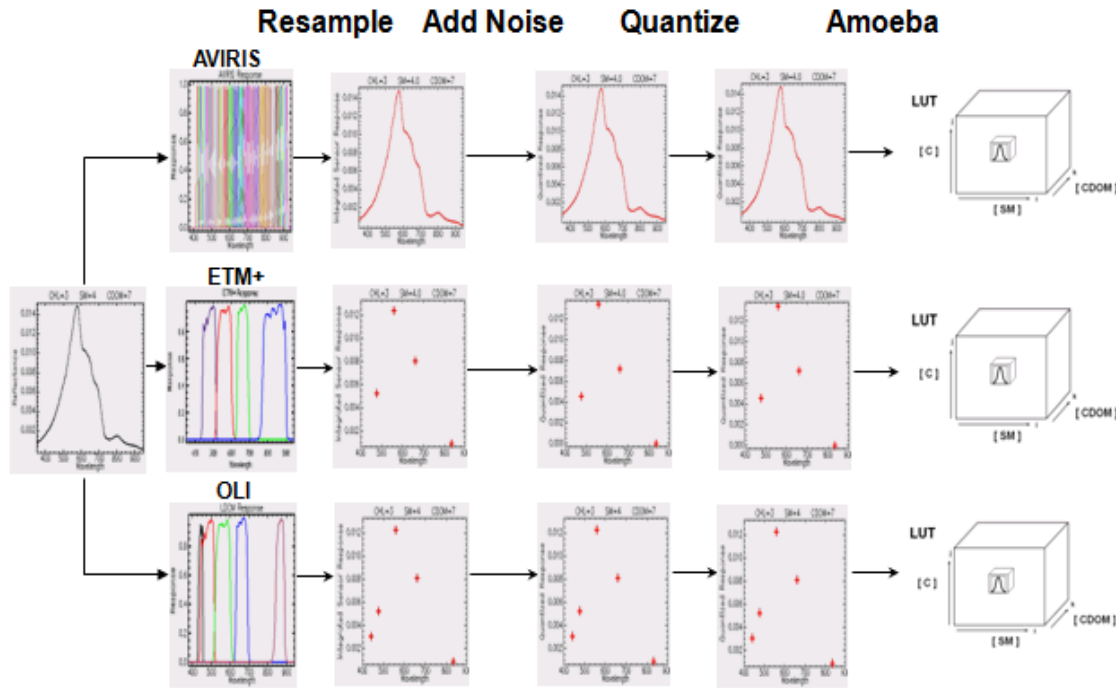


Figure 5.2: *Illustration of the constituent retrieval process when assumption of perfect atmospheric compensation is made.*

To describe the sensor modeling process, we can observe the sequence of events encountered by an arbitrary signal as it is sampled by a sensor, see Figure 5.2. Following the signal from left to right, we see how this continuous signal at the front of the sensor first gets spectrally discretized by the sampling process. In this study, the sensor-reaching signals are spectrally sampled to the sensors VNIR bands using Equation 3.12 (Recall that

water is a major absorber of light in the SWIR so we will treat the water-leaving signal past 1 micron as negligible). Therefore, ETM+ has 4 bands in the VNIR, OLI has 5 bands, and AVIRIS has 61 bands to spectrally sample the sensor-reaching signals.

In the next stage of the sensor's sampling process, a signal is further altered from the introduction of noise by the sensor. To simulate noise in this study, SNR requirements were obtained from system specifications for the ETM+ and OLI sensors, see Appendix C.2. To simply apply these signal-to-noise ratios to the reflectance signals would grossly overestimate noise levels. Since Appendix C.2 provides SNR specifications for typical radiance levels ($L_{Typical}$), equivalent reflectance noise levels can be calculated by observing the following relation.

$$\frac{N_{r_i}}{N_{L_i}} = \frac{\Delta r_i}{\Delta L_i} \Rightarrow N_{r_i} = \frac{N_{L_i} \cdot \Delta r_i}{\Delta L_i}, \quad (5.1)$$

where N_{r_i} is the desired noise in the reflectance domain for band i , N_{L_i} is the noise in the radiance domain for band i , Δr_i is an incremental change in the reflectance domain for band i that corresponds to ΔL_i , an incremental change in the radiance domain for band i . To solve for N_{r_i} (reflectance noise) in band i , we must first solve for $\frac{\Delta r_i}{\Delta L_i}$. On a band-by-band basis, simple MODTRAN runs were performed using standard inputs that reflect the conditions observed in Rochester, NY on May 20, 1999: Mid-latitude summer profile, 705 kilometer sensor height, an appropriate solar-zenith angle, rural aerosols with a 23 kilometer visibility, no multiple scattering effects, the appropriate wavelengths for band i . The difference in total integrated radiance can then be calculated for two different reflectors (albedos of 6% and 12% were used in this study) from MODTRAN's standard output of total integrated radiance and $\frac{\Delta r_i}{\Delta L_i}$ determined for each band i .

Next, Appendix C.2 can be referenced to solve for N_{L_i} for typical radiance levels ($L_{Typical}$) by observing the following relation.

$$SNR_{L_i} = \frac{S_{L_i}}{N_{L_i}} \Rightarrow N_{L_i} = \frac{S_{L_i}}{SNR_{L_i}}, \quad (5.2)$$

where N_{L_i} is the desired noise in the radiance domain for band i , S_{L_i} is the typical radiance

level for band i ($L_{Typical}$), and SNR_{L_i} is the signal-to-noise ratio at $L_{Typical}$ for band i . With all unknown terms of Equation 5.1 solved, the desired noise in the reflectance domain for band i (N_{r_i}) may be calculated. Now, noise can be added to the reflectance signals for each band by simply multiplying (N_{r_i}) by a normally-distributed, random number ($R_{(0,1)}$) with a mean of zero and a standard deviation of one and adding the result to the signal in band i (S_{r_i}) according to,

$$S_{r(w/noise)_i} = R_{(0,1)} \cdot N_{r_i} + S_{r_i}. \quad (5.3)$$

This process is repeated for all bands in the sensor and for all two thousand pixels in our simulated scene.

The final process a signal encounters as it is read in by a sensor is the quantization process. The addition of quantization effects is nearly identical to the method used to add noise to a signal. Simply dividing $\frac{1}{2^{(\#of\ bits)}}$ will grossly underestimate the quantization resolution in the reflectance domain (the quantization step size will be too large). Therefore, we must be able to relate quantization resolution in the radiance domain to quantization resolution in the reflectance domain under typical imaging conditions for the ETM+ and OLI sensors. Just as we did for noise in Equation 5.1, we can use the relationship that was developed in MODTRAN ($\frac{\Delta r_i}{\Delta L_i}$) and compute the quantization resolution in the radiance domain (L_{Q_i}) for band i to solve for the quantization resolution in the reflectance domain (r_{Q_i}) for band i according to,

$$\frac{\Delta r_i}{\Delta L_i} = \frac{r_{Q_i}}{L_{Q_i}} \quad \Rightarrow \quad r_{Q_i} = \frac{L_{Q_i} \cdot \Delta r_i}{\Delta L_i}. \quad (5.4)$$

The term L_{Q_i} can be found by simply calculating $\frac{L_{max_i}}{2^{(\#of\ bits)}}$, where L_{max_i} is the saturation radiance for band i , see Appendix C.2. Once r_{Q_i} is determined for band i , the quantization levels in the reflectance domain can be set according to,

$$r_{Q_{ij}} = j \cdot r_{Q_i} \quad for \quad j = 0, 1, \dots, n \quad and \quad 0 \leq r_{Q_{ij}} \leq 1. \quad (5.5)$$

where $r_{Q_{ij}}$ is the j^{th} quantized reflectance level in band i . Finally, with the quantization

levels set for each band, the two thousand signals may be quantized by simply rounding the signal values in each band to the closest quantized level.

The three aforementioned processes describe how a continuous sensor-reaching signal will be read in and digitized by a sensor for this study. It is with these discrete signals that we will use Amoeba to search the LUT as described in Section 4.3 to determine the constituent concentrations associated with each signal. The output to the search process will be Amoeba's best guess at the constituent concentrations associated with the signal it receives.

5.1.1.3 Results

Naturally, there will be an error associated with the retrieval process due to the way sensors degrade a signal. The beauty of the process illustrated in Figure 5.2 is that we know the concentrations of the constituents associated with each water-leaving signal since we generated them using Hydrolight. We are assuming that there is no attenuation due to the atmosphere in this study so the sensor-reaching signals are equivalent to their water-leaving form. Then, since we know the true concentrations associated with the signal at the front of the sensor and Amoeba determines the concentrations based on the signal received at the back of the sensor, the difference between the two can be defined as an error metric for the retrieval process. This error metric, shown in Equation 5.6, is simply the RMS-error between the retrieved and actual constituent concentrations,

$$RMSE_c = \sqrt{\frac{\sum_{i=1}^n (C_o(i) - C_r(i))^2}{n}}, \quad (5.6)$$

where $RMSE_c$ is the average error we can expect to observe in retrieving a constituent (c), $C_o(i)$ is the constituent concentration associated with a water-leaving signal, $C_r(i)$ is the predicted concentration resulting from the retrieval process, and $n = 2000$ for this experiment.

Recall that, to evaluate the new features of the OLI sensor and their corresponding contributions to the constituent retrieval process three tests were conducted, the results of which are reported in Figure 5.3. The first experiment is designed to determine how

spectral coverage affects the retrieval process, the second determines how spectral sampling and quantization affect the process, and the third determines how spectral sampling, quantization, and sensor noise affect constituent retrieval. The columns in Figure 5.3 show the average error in concentration one can expect to obtain for each constituent while the rows show the resulting errors for the three different experiments.

	CHL ($\mu\text{g/L}$)		SM (mg/L)		CDOM	
Spectral Coverage:						
AVIRIS	0.5	0.7%	0.1	0.4%	0.1	0.7%
ETM+	0.5	0.7%	0.6	2.5%	0.2	1.4%
OLI	0.5	0.7%	0.5	2.1%	0.1	0.7%
Quantization Included:						
ETM+	5.7	8.4%	2.8	11.7%	1.7	12.1%
OLI	1.2	1.8%	0.6	2.5%	0.2	1.4%
Noise Included:						
ETM+	7.4	10.9%	4.8	20.0%	3.2	22.8%
OLI	8.5	12.5%	1.4	5.9%	0.9	6.4%

Figure 5.3: *Black numbers show average RMS-error that we can expect to obtain from constituent retrieval process. Red numbers express these errors as a percent of the range of concentrations observed in the scene. The SNRs shown in Table C.7 are used for this experiment.*

The first group of results compares how well the three sensors perform constituent retrieval as a result of their spectral coverage. We see that OLI outperforms ETM+ in retrieving suspended materials and CDOM. This may indicate that we gain some retrieval accuracy with the addition of OLI's new blue band. The 61 bands of AVIRIS outperform the other two sensors in retrieving suspended materials but introduces the same errors as OLI for chlorophyll and CDOM. This is remarkable for OLI considering it has only 5 bands in the VNIR. The errors for all three of the sensors in this first study are relatively low so we can conclude that spectral coverage does not impair the constituent retrieval process (in the absence of atmospheric effects).

It is interesting to represent the residual errors as a percentage of the total range of observed constituent concentrations. Recall that in situ measurements across the scene indicated that chlorophyll ranged in concentrations from 0 to 68 $[\frac{\mu g}{L}]$, suspended materials ranged from 0 to 24 $[\frac{mg}{L}]$, and the CDOM scalar ranged from 0 to 14. Expressing the errors as a percentage of the total range, we see that all three sensors are well within an acceptable error-range of 10% [Raqueno et al., 2000].

The second group of results compares ETM+ and OLI when spectral coverage and quantization effects are combined in the modeling process. OLI's 12-bit quantizer should be able to preserve a signal better than ETM+'s 8-bit quantizer. Clearly this is the case as Figure 5.3 shows that the OLI sensor outperforms ETM+ in retrieving constituents when quantization effects are incorporated. The OLI sensor is starting to separate itself from ETM+ as the errors that it introduces to the constituent retrieval process are much less than 10%. ETM+, on the other hand, introduces errors of over 10% for two out of three constituents indicating that it is probably not a valid sensor for this type of research.

Finally, the third group of results illustrates how retrieval error is impacted when system noise is included in the analysis. The signal-to-noise ratios used in this study (see Appendix C.2) were obtained from [ETM Manual, 2003] for ETM+ and [LDCM Manual, 2006] for OLI. Again, referring to the red numbers in Figure 5.3 we see that OLI has an acceptable retrieval error of less than 10% for two out of three constituents and an error that is borderline for chlorophyll (12.5%). ETM+, on the other hand, shows a 20% error in constituent retrieval for two constituents and is over 10% for all three. As this study was performed in the absence of atmospheric effects, this last set of results demonstrates why, despite its attractive spatial resolution, ETM+ is ineffective for monitoring case 2 waters. OLI, on the other hand, exhibits great potential to be used for the constituent retrieval process.

It should be noted that the errors reported in Figure 5.3 reflect a worst-case scenario in regards to the constituent retrieval process. Due to the nature in which the water pixels were generated in this study, a wide range of water bodies are represented in the data. However, an actual scene will contain a much smaller range of water types. This implies that our actual scene-wide retrieval errors should be much smaller (on the average). Additionally, a handful of the randomly-generated constituent concentrations may be unrealistic

in nature. For example, it is very unlikely for a water body to contain extremely high levels of chlorophyll and low levels of CDOM and/or suspended materials. The fashion in which the water pixels were generated in this study allows for such anomalies. Therefore, one should realize that the errors reported in Figure 5.3 are most likely higher than one should expect to observe in practice.

Finally, as previously mentioned, the signal-to-noise ratios used in the OLI sensor model for this study were obtained from [LDCM Manual, 2006] and represent the minimum required SNRs for the sensor. Preliminary studies of the OLI instrument indicate that it may actually achieve significantly higher SNRs than the original required specifications. Appendix C.3 shows a bar chart of SNR margins that may potentially be achieved for each band of OLI. Given these new SNR margins, the study of this section can be extended to determine OLI's ability to perform constituent retrieval in the event that these margins are achieved. First, the OLI sensor is modeled with SNRs that reflect half the margins shown in Figure C.8 and secondly the OLI sensor is modeled with SNRs that reflect the full margins shown in Figure C.8. The constituent retrieval process is performed with the same two thousand randomly generated pixels to determine how these potentially improved SNRs will impact OLI's retrieval ability. The results of this study are shown in Figure 5.4.

	CHL ($\mu\text{g/L}$)		SM (mg/L)		CDOM	
Required SNR:						
ETM+	7.4	10.9%	4.8	20.0%	3.2	22.8%
OLI	8.5	12.5%	1.4	5.9%	0.9	6.4%
SNR at Half Margin:						
OLI	5.4	7.9%	1.0	4.2%	0.6	4.3%
SNR at Full Margin:						
OLI	4.3	6.3%	0.8	3.3%	0.5	3.6%

Figure 5.4: Comparison of RMS-errors that can be achieved from constituent retrieval process with required SNR, SNR at half margin, and SNR at full margin.

Interestingly, if just half the margins described in Figure C.8 are achieved, OLI's ability to retrieve water constituents will improve dramatically. In particular, chlorophyll retrieval will improve by 4.5% pushing retrieval errors under 10% for all three constituents. If the best-case scenario occurs and the full margins can be achieved by the OLI sensor, expected retrieval errors will be under 6.5% for all three constituents. Remarkably, the expected retrieval errors for suspended materials and CDOM will be under 4% making OLI a truly unique instrument for studying water quality. Anticipating that OLI will achieve SNR of at least half the margins described in Figure C.8, we conclude that it is a viable sensor to be used throughout this research.

5.1.2 Evaluation of the OLI Atmospheric Compensation Algorithm on Simulated Data

The experiments in the last section were designed to determine if OLI is a valid sensor to be used throughout this research. By ignoring atmospheric effects, we were able to isolate the retrieval errors introduced by just the OLI sensor. This section expands on those experiments by determining how well we can perform constituent retrieval when atmospheric effects are included. A study of this nature allows us to test the efficiency of the OLI atmospheric compensation algorithms introduced in Section 4.2.2.4 and Section 4.2.2.5.

The water samples used in this study are the same as those described in Section 5.1.1, which were randomly generated in Hydrolight to reflect in situ measurements collected on May 20, 1999 in support of the AVIRIS collect (see Figure 5.1). In this study, however, the water-leaving signals are attenuated by an atmosphere before reaching the sensor. MODTRAN was used to simulate an atmosphere that OLI may encounter over western New York during a spring collect: rural aerosols, a horizontal visibility of 23 kilometers, a mid-latitude summer profile, 15:40 GMT, with multiple scatter effects included. Using Equation 3.2, the sensor-reaching radiance was determined for each water sample.

At the sensor, each signal was spectrally sampled to OLI's response function, system noise was added, and quantization effects were included. Since the signals in this study are already in radiance units, the sensor specifications at typical radiance levels (L_{typ}) can be used directly to add noise and quantization effects. SNRs at half the margins described in Appendix C.3 were used to add system noise to the signals. These ratios reflect realistic

noise levels that one can expect to see with the final OLI system. The constituent retrieval process was then performed using the methods described in Chapter 4.

5.1.2.1 OLI Atmospheric Compensation Algorithm (Blue Band)

In this first experiment, the OLI-specific atmospheric compensation algorithm for case 2 waters (Blue Band) was used to correct for the atmosphere and determine the water constituents for all two thousand water samples. The 4-D LUT used in this experiment, shown in Figure 5.5, was generated using MODTRAN and the following common inputs: rural aerosols, a mid-latitude summer profile, 15:40 GMT, and multiple scatter effects. Additionally, visibility was varied between 5 and 60 kilometers in 5 kilometer increments in an effort to encompass (but not overlap) the imaged pixels' visibility of 23 kilometers. The constituent retrieval process for this study took approximately six hours on one core for all 2000 pixels. Figure 5.6 shows the retrieval errors that resulted from the process.

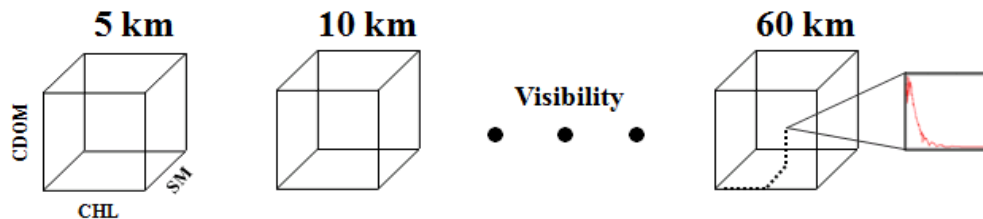


Figure 5.5: 4 parameter LUT used to perform atmospheric compensation. Visibility ranged between 5 and 60 kilometers in 5 kilometer increments.

The first row of results shows the constituent retrieval errors if the chosen atmosphere is removed on a pixel-by-pixel basis, i.e., visibility is solved for on a pixel-by-pixel basis. We see that our methods fail to adequately retrieve chlorophyll but perform well for suspended materials and CDOM. Although these results are somewhat acceptable, when the glint and in-water effects of real data are included these errors will certainly increase. Therefore, it was necessary to develop a scheme that would further drive down these errors.

Recall that step 4 of the OLI atmospheric compensation algorithm (Blue Band) suggests that we can take an average of the pixel-by-pixel retrieved visibilities and repeat the retrieval of just (Chl, SM, CDOM) by fixing this average. Since OLI has a spatial

	CHL ($\mu\text{g/L}$)		SM (mg/L)		CDOM		Average Chosen Visibility
Removal Type:							
Pixel-by-Pixel	18.4	27.1%	3.3	13.8%	1.4	10.0%	-
Global	9.0	13.2%	1.5	6.3%	1.0	7.1%	23.36

Figure 5.6: *Results of the constituent retrieval process when performed on synthetic data with atmospheric effects included. OLI's Blue Band method was used to compensate for the atmosphere. SNR's at half the margins described in Appendix C.3 were used.*

resolution of 30 meters it is valid to assume that the true visibility will not change over a small scene such as the one shown in Figure 5.1. Therefore, when compensating for the atmosphere in an image it's logical to do so globally, i.e., after averaging the pixel-by-pixel chosen visibilities.

The second row of results in Figure 5.6 shows our ability to retrieve water constituents when the average chosen atmosphere (23.36 kilometer visibility as shown in blue) is removed from all pixels. Notice that performing this averaging leads to a significant improvement in our ability to retrieve water constituents. Therefore, in the absence of glint effects, spatial effects, and in-water effects (IOP variability) this algorithm is quite successful.

Albeit slow, the OLI atmospheric compensation algorithm (Blue Band) is able to accurately retrieve constituents from a wide range of water samples (some of which, recall, may be unrealistic in nature). In this experiment, 2000 water pixels took almost six hours to process on a single core (2.1 Gigahertz processor). As we move forward to a real scene, multiple cores may be required to reduce run times. For example, the same 2000 pixels can be processed in 10 minutes if 30 cores are available.

5.1.2.2 OLI Atmospheric Compensation Algorithm (Band Ratios)

In this second experiment, the OLI-specific atmospheric compensation algorithm for case 2 waters (Band Ratios) was used to correct for the atmosphere and the constituent retrieval algorithm used to determine the water constituents for all two thousand water samples. Recall that in this method, a LUT of epsilon ratios ($\epsilon^{5,6}$), which incorporates a dark water reflectance (ρ_w), must be modeled for an appropriate range of candidate atmospheres.

To develop the LUT, the atmospheric parameters determined in the previous section were used (Recall MODTRAN was run with inputs: rural aerosols, a mid-latitude summer profile, 15:40 GMT, multiple scatter effects and visibility was varied between 5 and 60 kilometers in 5 kilometer increments). To incorporate a dark water reflectance (ρ_w), the reflectance of Lake Ontario (Figure 4.20) was simulated using Hydrolight based on in situ measurements. Finally, Equation 3.2 was used to obtain sensor-reaching radiance for the various atmospheres and their epsilon ratios ($\epsilon^{5,6}$) archived in a LUT form.

To perform the constituent retrieval process, recall that $\epsilon^{5,6}$ must be obtained from dark waters in the image. To simulate this process, the darkest 10% of the 2000 pixels values in band 5, and their corresponding values in band 6, were averaged to determine $\epsilon^{5,6}$. With an epsilon ratio in place, the corresponding atmosphere was determined and removed from each of the 2000 pixels. Finally, the constituent retrieval algorithm was applied to the resulting reflectances (ρ_w) to determine the constituent concentrations of each water pixel. The results of the constituent retrieval process using this band ratio technique are shown in Figure 5.7.

	CHL ($\mu\text{g/L}$)		SM (mg/L)		CDOM		Chosen Visibility
Blue Band Method:							
Pixel-by-Pixel	18.4	27.1%	3.3	13.8%	1.4	10.0%	-
Global	9.0	13.2%	1.5	6.3%	1.0	7.1%	23.36 (Averaged)
Band Ratio Method:							
10%	11.6	17.1%	2.2	9.2%	1.1	7.8%	23.64
5%	10.1	14.9%	1.7	7.0%	1.0	7.4%	22.97

Figure 5.7: Results of the constituent retrieval process when performed on synthetic data with atmospheric effects included. OLI's Band Ratio method was used to compensate for the atmosphere. SNR's at half the margins described in Appendix C.3 were used.

This method performs only slightly worse than OLI's Blue Band method. This could be due to the somewhat haphazard way in which the epsilon ratio was defined. In fact, Figure 5.7 shows that if only the darkest 5% of the band 5 values are used to define the epsilon ratio, the predicted visibility is much closer to 23 kilometers and the constituent retrieval errors approach those obtained in the Blue Band method. Additionally, we reiterate that

since a wide range of water types was used in this study, these errors will certainly decrease when working with more realistic water types (which will be the case in Section 5.1.3 where we process a simulated scene). Given the fact that this entire constituent retrieval process took less than 10 minutes (compared to 6 hours with the Blue Band method), the Band Ratio atmospheric compensation method is extremely attractive.

5.1.3 Evaluation of the OLI Atmospheric Compensation Algorithm on a Simulated Scene

In Section 5.1.1 the constituent retrieval process was performed in the absence of atmospheric effects and the results showed that OLI exhibits the potential to be a valuable tool for studying case 2 waters. Simulated data was used in Section 5.1.2 to demonstrate the potential of both OLI atmospheric compensation algorithms. Now, we expand on the studies of the past two sections by performing the constituent retrieval process on a simulated scene. A study of this nature will enable us to determine if an image has spatial characteristics that will impact our ability to retrieve water constituents.

5.1.3.1 Simulating A Scene

We begin this section by simulating an image that can be used to test our atmospheric compensation algorithms. Figure 5.8 shows an RGB image of the Rochester Embayment as seen from the Enhanced Thematic Mapper Plus (ETM+) sensor onboard Landsat 7. We wish to test our algorithms' capabilities on such a scene as it contains many water bodies in various trophic states. One should keep in mind throughout this discussion that the purpose in simulating a scene is to develop an image in which we have knowledge of the atmosphere and the water bodies in order to validate the OLI atmospheric compensation methods. Therefore, although we maintain the integrity of the land pixels, it is for visual purposes only.

To begin the simulation, the NIR band of ETM+ was used to determine the land/water boundaries. By setting a simple threshold in band 4, the bright land pixels naturally separate themselves from the dark water pixels. A mask can be created which sets all land pixels to 1 and all water pixels to 0. This mask can then be multiplied by the original image in Figure 5.8 to maintain the land data in the image.



Figure 5.8: *RGB image of the Rochester Embayment. Data was collected by Landsat 7 on May 16, 1999.*

Once the water pixels have been masked out, we can start implanting our own water types into the scene. The water types that we will use for our image have been selected to reflect in situ water measurements obtained from the AVIRIS collect (which were obtained four days later on May 20, 1999). Using Hydrolight, observed constituent concentrations from that collect can be converted to spectral water-leaving reflectances. Then by assuming that the constituents do not vary for a fixed water body, an image processing technique known as region filling can be used to fill in the water-leaving reflectances for the various lakes and ponds across the scene.

Next, Equation 3.2 can be used in conjunction with a MODTRAN-generated atmosphere to determine the sensor-reaching radiance for all water pixels in the scene. To be consistent with the two previous studies in this section, an atmosphere containing rural aerosols, a horizontal visibility of 23 kilometers, a mid-latitude summer profile, at 15:40 GMT, with multiple scatter effects was used. Finally, an image can be created by spectrally sampling

the signals to OLI's sensor response function, and then adding system and quantization noise. The SNRs at half the margins shown in Figure C.8 are used in this study as they reflect realistic ratios that may be achieved in the final OLI system. Figure 5.9 shows the image that results from the above procedure.



Figure 5.9: *Simulated image of Rochester Embayment. The constituent retrieval process was performed on 6 ROI's (each containing 36 pixels) using the OLI atmospheric compensation algorithms to account for the atmosphere.*

One may notice that a plume has been included in this synthetic image. The Genesee River plume was created by thresholding the water pixels using ETM+'s red band (band 3). Suspended sediment is the predominant in-water scatterer of light in the red and NIR so by observing the strength of the signal in band 3, we can predict the relative amounts of sediment contained in the river plume. Furthermore, one should notice that since care was taken in maintaining the constituent concentrations of the original scene, the colors of the simulated ponds in Figure 5.9 are similar to the colors of the real ponds in Figure 5.8.

With a simulated scene in place, we can again test the efficiency of the OLI atmospheric compensation algorithms. Performing the constituent retrieval process with an image will

differ from performing the retrieval on synthetic data in a couple of ways. First, considering the mere size of an image it is not practical in this simple test to perform constituent retrieval on every pixel when the Blue Band method is used to compensate for the atmosphere. Instead, we can take ROI's at several locations across the image and perform the constituent retrieval process at just these locations. However, as we move forward to processing actual data, the speed of the Blue Band method must be addressed.

Accordingly, OLI's Band Ratio algorithm was conceived and is particularly attractive due to its small run times. Are there limitations in this algorithm, however, that make the Blue Band algorithm a necessary alternative? If so multiple processors will be required to perform the constituent retrieval process on an image. The run time issue is one that we will be mindful of throughout this chapter. If we are able to obtain sufficient constituent retrieval results with OLI's Band Ratio algorithm then it will be the preferred compensation method for the OLI sensor.

Secondly, recall that step 4 of the OLI atmospheric compensation algorithm suggests that we fix the average of the visibility solutions and solve for (CHL, SM, CDOM) over each pixel of interest. This step was included in the algorithm based on an observation made in the previous studies. As those studies used synthetic data which included a wide variety of water types, it is unclear whether real images will contain a sufficient variety of water types to make step 4 necessary. By the end of this section, this issue will be addressed.

5.1.3.2 OLI's Blue Band Method

In this first experiment, the constituent retrieval process was performed on the synthetic image using OLI's Blue Band method to compensate for the atmosphere. Six ROI's were chosen from Figure 5.9 to perform the retrieval, each containing thirty six pixels. The atmosphere was removed both on a pixel-by-pixel basis and globally in an attempt to determine if having a limited number of water bodies affects the ability of this OLI method. The results of the retrieval process are shown in Figure 5.10.

The first row of results shows that if we solve (VIS, CHL, SM, CDOM) on a pixel-by-pixel basis, our retrieval errors for all three constituents are well under 15%. Compared to the retrieval errors found for the simulated data of Section 5.1.2 (see Figure 5.6), we

are able to obtain better results with the simulated scene. This is most certainly due to the fact that a significantly smaller variety of more realistic water types are used in our simulated scene. Figure 5.10 shows that we are able to drive down the errors even further when we account for the atmosphere globally. With retrieval errors of less than 6% for all three constituents, these results are extremely promising as we move forward to real data.

	CHL ($\mu\text{g/L}$)		SM (mg/L)		CDOM		Average Chosen Visibility
Removal Type:							
Pixel-by-Pixel	9.1	13.4%	2.6	10.9%	0.9	6.9%	-
Global	3.6	5.3%	1.3	5.6%	0.8	6.0%	23.36

Figure 5.10: *Results of the constituent retrieval process when performed on synthetic image using all 6 ROI's in Figure 5.9.*

At this point, since the constituent retrieval process was successful with only six ROIs, the question begs itself, “what is a sufficient number of water types required for this atmospheric compensation algorithm to perform adequately, i.e., can this method be used for individual water types?” It is usually the case that we have knowledge of only an individual water body in a scene or perhaps we are only interested in performing constituent retrieval over one water body. Can this algorithm still be implemented? Figure 5.11 reports the results on a experiment designed to evaluate the efficiency of our algorithm when performed on a pond-by-pond basis.

As always, the constituent retrieval errors are reported by column. The various ROI's of Figure 5.9 are grouped by row on a pond-by-pond basis. The first row of each group shows the retrieval errors we can expect when the atmosphere is considered on a pixel-by-pixel basis. The second row shows the retrieval errors we can expect when the atmosphere is considered globally, i.e., all six ROIs are used to determine an average visibility. Finally, the third row shows the retrieval errors one can expect when the atmosphere is considered pond-globally, i.e., only the visibility solutions observed over an individual water type are fixed to solve (CHL, SM, CDOM).

	CHL ($\mu\text{g/L}$)	SM (mg/L)	CDOM	Average Chosen Visibility
Lake Ontario (Red):				
Pixel-by-Pixel	0.6 1.0%	0.5 2.2%	0.2 1.7%	-
Global	0.7 1.0%	0.4 1.8%	0.3 2.0%	23.25
Pond Global	0.7 1.0%	0.4 1.8%	0.3 2.0%	23.18
***Braddocks Bay (Cyan):				
Pixel-by-Pixel	6.8 10.0%	3.4 14.2%	0.5 3.7%	-
Global	1.2 1.7%	0.9 3.6%	0.5 3.3%	23.25
Cranberry Pond (Green):				
Pixel-by-Pixel	4.5 6.6%	3.4 14.3%	2.3 16.5%	-
Global	3.6 5.3%	3.1 12.9%	2.2 15.4%	23.25
Pond Global	3.3 4.8%	2.8 11.7%	2.1 15.3%	23.32
***Long Pond (Blue):				
Pixel-by-Pixel	18.2 26.8%	1.2 4.9%	0.6 4.2%	-
Global	8.2 12.1%	1.1 4.8%	0.7 4.7%	23.25
***River Plume (Yellow):				
Pixel-by-Pixel	5.3 7.7%	3.2 13.4%	1.0 6.9%	-
Global	1.9 2.7%	1.4 6.0%	0.8 5.9%	23.25
Irondequoit Bay (Magenta):				
Pixel-by-Pixel	19.4 28.6%	4.0 16.6%	1.0 7.2%	-
Global	4.0 5.9%	0.9 3.6%	0.1 0.7%	23.25
Pond Global	6.0 8.9%	1.1 4.7%	0.6 4.4%	22.94

Figure 5.11: Results of the constituent retrieval process when performed on a pond-by-pond basis. SNRs at half the margins shown in Figure C.8 were used. (***) Could not converge to a Pond Global solution).

Two important observations should be made from the results shown in Figure 5.11. First, even with perfect knowledge of the water IOPs, our ability to accurately retrieve (VIS, CHL, SM, CDOM) is water-body dependent. For instance, in this section we were much more successful at retrieving the constituents from Irondequoit Bay than we were from Long Pond. This result perhaps explains why the retrieval errors of Figure 5.6 are higher than those of Figure 5.10, on average. In Section 5.1.2, two thousand randomly generated “water bodies” were created without regard for their validity. Each water body contained a single pixel and was used to test the constituent retrieval process. In this section, only six *realistic* water bodies were used in the constituent retrieval process, each containing thirty six pixels. Not surprisingly, the constituent retrieval algorithm performs better with realistic water types containing multiple pixels.

Secondly, it appears that the errors obtained when the atmosphere is considered pond-globally are comparable to those obtained when the atmosphere is considered globally. This is most likely due to the fact that the algorithm finds consistent visibility solutions for a fixed water type. Any variability in visibility for an individual water type can be attributed to sensor noise. Therefore, as we move forward to real data we do so with the assumption that constituent retrieval can be performed on a pond-by-pond basis. This notion will be extremely useful for a couple of scenarios. First, if ponds are spatially far apart the atmosphere may change over an image. As a result, the global solution will not be adequate. Secondly, we may only have knowledge of the optical properties for a single water body in a scene. This makes the pond-global method necessary.

On occasion, the pond global method could not converge to a solution (indicated by *** in Figure 5.11). When the average visibility parameter was fixed for Long Pond, Braddocks Bay and the Genesee River plume, Amoeba would inexplicably leave the LUT in search for the optimal (CHL, SM, CDOM) triplet. In this type of scenario, the global solution is required.

5.1.3.3 OLI's Band Ratio Method

In this second experiment, the constituent retrieval process was performed on the same six ROI's from Figure 5.9 using OLI's Band Ratio method to compensate for the atmosphere. To implement the Band Ratio method, a sizable ROI (5000 pixels) was taken over Lake Ontario to obtain the epsilon ratio for the image. The resulting visibility of 23.33 kilometers was determined and its corresponding atmosphere removed from the the six ROIs. Finally, the constituent retrieval algorithm must be implemented to ascertain the constituents associated with each pixel in the ROIs. The results of the retrieval process are shown in Figure 5.12.

Like the previous experiment, the retrieval errors for each constituent are reported by column and the various ROI's of Figure 5.9 are grouped by row on a pond-by-pond basis. Figure 5.12, however, compares the results of the OLI Band Ratio method to that of the Blue Band method. As this figure shows, the OLI Band Ratio method performs as well as the Blue Band method for most of the ponds and only slightly poorer for Irondequoit Bay. When considering that fact that the 6 ROIs took less than five minutes to process

using this method (the Blue Band method took over 2 hours), these results are extremely exciting as entire images may be processed on a single core in minutes, not days. From this experiment we can conclude that the OLI Band Ratio method is, in fact, the preferred atmospheric compensation algorithm for this work, assuming that we have a glint free, well calibrated dataset.

	CHL (µg/L)		SM (mg/L)		CDOM		Chosen Visibility
Lake Ontario (Red):							
Blue Band	0.7	1.0%	0.4	1.8%	0.3	2.0%	23.25
Band Ratios	0.7	1.0%	0.4	1.7%	0.3	2.1%	23.33
Braddocks Bay (Cyan):							
Blue Band	1.2	1.7%	0.9	3.6%	0.5	3.3%	23.25
Band Ratios	2.3	3.3%	1.1	4.8%	0.5	3.6%	23.33
Cranberry Pond (Green):							
Blue Band	3.6	5.3%	3.1	12.9%	2.2	15.4%	23.25
Band Ratios	2.9	4.3%	2.7	11.3%	2.1	14.8%	23.33
Long Pond (Blue):							
Blue Band	8.2	12.1%	1.1	4.8%	0.7	4.7%	23.25
Band Ratios	9.3	13.7%	1.1	4.6%	0.7	4.8%	23.33
River Plume (Yellow):							
Blue Band	1.9	2.7%	1.4	6.0%	0.8	5.9%	23.25
Band Ratios	2.3	3.4%	1.3	5.6%	0.7	5.1%	23.33
Irondequoit Bay (Magenta):							
Blue Band	4.0	5.9%	0.9	3.6%	0.1	0.7%	23.25
Band Ratios	5.5	8.1%	1.0	4.1%	0.5	3.7%	23.33

Figure 5.12: Results of the constituent retrieval process when OLI's Band Ratio method is used to remove the atmosphere. SNRs at half the margins shown in Figure C.8 were used in this study.

As we move forward to working with real data, we do so with the assumption that we have a robust end-to-end constituent retrieval process in place. In the experiments of this section, however, we modeled all the water types with the same IOPs and only varied their constituent concentrations. In fact, we know that different water bodies will have different IOPs and that these IOPs may change seasonally. The next section assesses the sensitivity of the retrieval process to variations in IOPs between the model and the actual water body.

5.2 Impact of Hydrolight Inputs on Constituent Retrieval

This section is included to lend insight into an additional source of errors that may occur when performing the constituent retrieval process with a constituent retrieval algorithm that uses LUTs. The studies previously mentioned in this chapter describe errors that may be introduced to the process by either the sensor or the atmospheric compensation algorithm. These studies, however, are based on the assumption that our in-water radiative transfer model behaves perfectly and does not introduce error into the process. As this will not be the case, we must now investigate errors in the constituent retrieval process that are due to poor inputs to the radiative transfer model. These errors will most certainly arise due to one's incomplete knowledge of the environmental inputs required by Hydrolight. Therefore, we now address the issue of how variability in one's knowledge of Hydrolight's inputs affects their ability to retrieve water constituents. The following studies are performed with signals that have been spectrally sampled to OLI's spectral response function, with full margin noise added (see Figure C.8), and quantization effects included.

5.2.1 CDOM Absorption Coefficients

Precise measurements of the CDOM absorption coefficients are imperative to ensure an accurate retrieval of water constituents. As described in Chapter 4.3.1, a major goal of this research is to develop a comprehensive LUT that can be used to retrieve water constituents over a wide range of water types. In developing this ideal LUT, however, the optical properties observed from various water samples in a scene must be averaged. This averaging will introduce error into the constituent retrieval process. In this section, the results of an experiment that addresses the errors introduced to the constituent process due to the averaging of *CDOM absorption coefficients* are presented.

Recall that Figure 4.24 shows the CDOM absorption coefficients measured from the various ponds in the Rochester Embayment, the average of which is used as input to Hydrolight when developing our LUT. Nine of these coefficients were chosen in a fashion such that the spread in the data was well represented, see Figure 5.13. For each of the absorption coefficients illustrated in this figure, two thousand random constituent concentration triplets were generated and supplied as input to Hydrolight in a fashion similar to that

described in Section 5.1.1. All other inputs to Hydrolight, save the CDOM absorption coefficient under investigation, are identical for the random water samples and the LUT. In the absence of atmospheric effects, the constituent retrieval process is performed on the water samples using our original LUT. The results of the constituent retrieval process are shown in Figure 5.14.

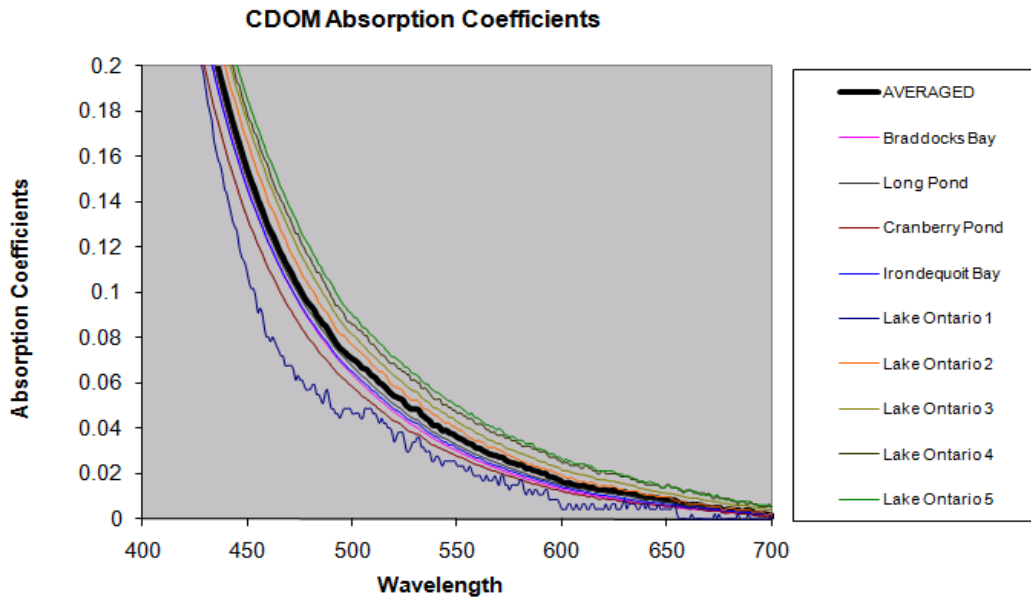


Figure 5.13: *CDOM absorption coefficients of nine water samples taken from ponds in the Rochester Embayment. The bold, black curve indicates the average absorption coefficients used to develop the LUT.*

The nine absorption coefficients are described in the first two columns of the figure. The first column describes the location from which the samples were taken while the second column describes how different the coefficients are from the average coefficients, in an RMS sense. Additionally, the coefficients are grouped in a manner such that the curves falling below the average curve are reported in the rows below the *Averaged Coefficients (LUT)* row. Likewise, the curves lying above the average coefficients are reported in the rows directly above the *Averaged Coefficients (LUT)* row. The *Averaged Coefficients (LUT)* row displays results of the retrieval process when we have perfect knowledge of the water IOPs.

Notice that when the coefficients deviate from the average (in a RMS sense), more error

is introduced into the constituent retrieval process. Particularly, our ability to accurately retrieve CDOM levels becomes impaired. This is an intuitively satisfying result as we varied the CDOM absorption coefficient IOP in this study. Interestingly, we see that our ability to retrieve chlorophyll levels becomes hindered with curves lying above the average. We can hypothesize that the reason for this is due to an increased amount of absorption in the water samples. Chlorophyll acts as an absorber of visible light so when we try to retrieve the constituents from water samples with heightened levels of absorbing IOPs, chlorophyll concentrations will be over-estimated.

	RMSE	CHL ($\mu\text{g/L}$)		SM (mg/L)		CDOM	
Sample:							
Lake Ontario 5	0.0137	14.6	21.5%	1.6	6.7%	1.5	10.7%
Lake Ontario 4	0.0056	13.9	20.4%	1.5	6.3%	1.3	9.3%
Lake Ontario 3	0.0054	9.4	13.8%	1.0	4.2%	1.0	7.1%
Lake Ontario 2	0.0028	6.5	9.6%	0.7	2.9%	0.8	5.7%
Averaged Coefficients (LUT)	0.0000	4.3	6.3%	0.8	3.3%	0.5	3.6%
Long Pond	0.0028	4.4	6.5%	0.8	3.3%	0.6	4.3%
Braddocks Bay	0.0054	5.0	7.4%	0.8	3.3%	0.7	5.0%
Irondequoit Bay	0.0056	4.4	6.5%	0.8	3.3%	0.7	5.0%
Cranberry Pond	0.0137	4.5	6.6%	0.8	3.3%	1.3	9.3%
Lake Ontario 1	0.0218	2.2	3.2%	0.3	1.3%	2.3	16.4%

Figure 5.14: *Results of CDOM absorption coefficient study. The full margin noise of Figure C.8 was used in this experiment.*

5.2.2 Chlorophyll Absorption Coefficients

A study similar to that described in the previous section was performed for varying chlorophyll absorption coefficients. Figure 5.15 shows chlorophyll absorption coefficients measured from the various ponds in the Rochester Embayment, the average of which is used as input to Hydrolight when developing our LUT. Many measurements which were noisy but overlapped the curves shown in Figure 5.15 were excluded from this study, while the

brown plot is an interpolated curve which was included to add spread to the data.

The process followed in Section 5.2.1 was repeated in this experiment. For each of the absorption coefficients illustrated in Figure 5.15, two thousand random constituent concentration triplets were generated and supplied as input to Hydrolight. Similarly, all other inputs to Hydrolight save the chlorophyll absorption coefficient under investigation are identical for both the random water samples and the LUT. Again, the constituent retrieval process is performed on the water samples using our original LUT in the absence of atmospheric effects. The results of the constituent retrieval process are shown in Figure 5.16.

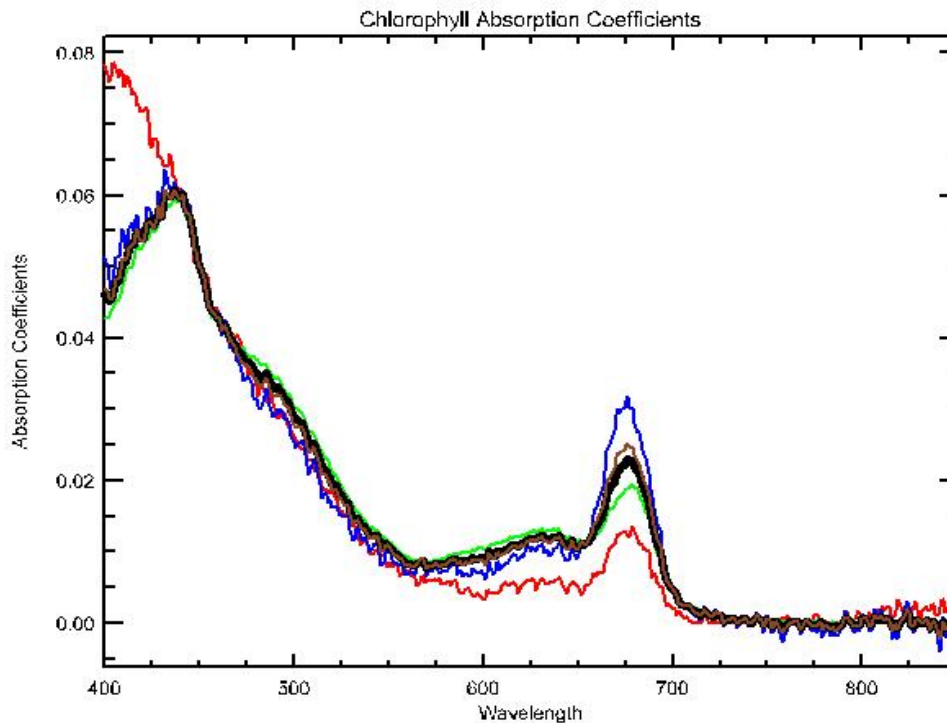


Figure 5.15: *Chlorophyll absorption coefficients of four water samples taken from ponds in the Rochester Embayment. The bold, black curve indicates the average absorption coefficients used to develop the LUT.*

Again, the first two columns of Figure 5.16 give a description of the four absorption coefficients and they are grouped in a manner such that the curves falling below the average curve are reported in the rows below the *Averaged Coefficients (LUT)* row and those lying above are reported in the rows directly above the *Averaged Coefficients (LUT)* row. Not surprisingly, as the RMS-error increases between the average coefficient and the test coeffi-

cient, one's ability to accurately retrieve water constituents decreases. What is interesting in these results, however, are the errors obtained by the Braddocks Bay sample (A5). This sample, which corresponds to the red curve in Figure 5.15, has a slightly different shape than the others (especially below 440 nanometers and between 550 nanometers and 650 nanometers). As a result the constituent retrieval errors are extremely high. This indicates that multiple LUTs may be required to study all water bodies in a scene of interest.

	RMSE	CHL ($\mu\text{g/L}$)		SM (mg/L)		CDOM	
Sample:							
A27(IB)	0.011	6.7	9.9%	2.3	9.6%	2.5	17.9%
Interpolated	0.002	4.2	6.2%	1.0	4.2%	0.8	5.7%
Averaged Coefficients (LUT)	0.000	4.3	6.3%	0.8	3.3%	0.5	3.6%
A18(LP)	0.006	9.0	13.2%	1.8	7.5%	1.6	11.4%
A5(BB)	0.027	16.2	23.8%	8.9	37.0%	2.5	17.9%

Figure 5.16: *Results of Chlorophyll absorption coefficient study. The full margin noise of Figure C.8 was used in this experiment.*

5.2.3 Chlorophyll Phase Functions

The final IOP under investigation is the scattering phase function for chlorophyll. Due to a lack of the necessary equipment needed to measure phase functions during the May 20, 1999 campaign, realistic phase function backscatter fractions for this study were determined from the literature to range from 0.005 to 0.015 with a mean of 0.010 [Whitmire et al., 2007] [Sullivan et al., 2005].

Figure 5.17(a) shows the backscatter fraction versus chlorophyll-a concentration for thousands of samples taken over a three year period. Sample locations cover a diverse range of water types and include the southern coast of California, the Mid-Atlantic Bight off the southern coast of New Jersey, and Crater lake, Oregon [Whitmire et al., 2007]. Figure 5.17(b) [Sullivan et al., 2005] shows an analogous scatterplot of backscatter fraction versus chlorophyll-a concentration for thousands of samples taken over similar sampling

locations. Notice that the general trend of both plots indicates that as chlorophyll concentration increases, the backscatter fraction decreases. Therefore, a reasonable range of backscatter fractions (0.005 to 0.015) was used for the phase functions in this study. As indicated by [Whitmire et al., 2007], the mean backscatter fraction observed from samples contained in the first optical depth is 0.010. This value was used to develop the LUT in this study.

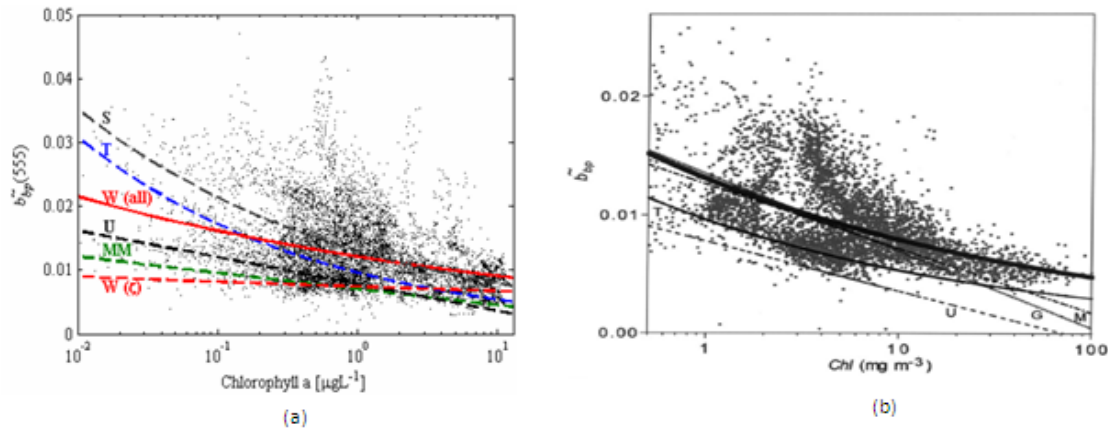


Figure 5.17: Scatterplot of backscatter fraction versus chlorophyll-*a* concentration for multiple water samples. Various models that attempt to fit the data are overlaid (a)[Whitmire et al., 2007], (b)[Sullivan et al., 2005].

The process followed in sections 5.2.1 and 5.2.2 was repeated in this experiment. For each of the backscatter fractions (0.005, 0.008, 0.010, 0.013, 0.015) two thousand random concentration triplets were generated and supplied as input to Hydrolight. All other inputs to Hydrolight, save the Fournier-Forand phase function with the backscatter fraction under investigation, are identical for both the random water samples and the LUT. The constituent retrieval process is performed on the water samples using a LUT which was generated using a Fournier-Forand phase function with a backscatter fraction of 0.01. As with the other studies, atmospheric effects were excluded. The results of the constituent retrieval process are shown in Figure 5.18. Again, the middle row with bold lettering indicates the row containing the LUT IOPs.

These results are decidedly intuitive. The more the backscatter fraction deviates from this middle row, the worse the performance in retrieving water constituents. Interestingly,

	CHL ($\mu\text{g/L}$)		SM (mg/L)		CDOM	
Fournier-Forand PF:						
Backscatter 1.5%	10.1	14.9%	3.9	16.3%	1.3	9.3%
Backscatter 1.3%	7.8	11.5%	2.0	8.3%	0.9	6.4%
Backscatter 1.0%	7.3	10.7%	0.7	2.9%	0.7	5.0%
Backscatter 0.8%	9.6	14.1%	1.7	7.1%	0.9	6.4%
Backscatter 0.5%	17.0	25.0%	3.8	15.8%	1.5	10.7%

Figure 5.18: *Results of the chlorophyll phase function study. The full margin noise of Figure C.8 was used in this experiment.*

if we observe the rows labeled *Backscatter 1.5%* and *Backscatter 0.5%* the results indicate that an equal error in backscatter fraction input does not lead to an equal error in constituent retrieval. Therefore, if one is going to err in estimating the backscatter fraction they should err on the high side since the retrieval errors are much less when the backscatter parameter is over-estimated.

5.2.4 Wind Speed and Solar Zenith Angle

Although adequate knowledge of water IOPs is necessary to the development of a functional constituent retrieval algorithm, the importance of other inputs should be investigated. Recall that a goal of the constituent retrieval process is to develop a comprehensive LUT that can be used for an extended period of time. The following discussion investigates whether or not we can use a single LUT for an entire season by exploring inputs to Hydrolight other than those describing the water. Particularly, this study determines how varying the environmental inputs of solar/zenith angle and wind speed affect our ability to retrieve water constituents.

In the previous studies described in this section, the various IOPs were provided as Hydrolight inputs to create the two thousand water samples while a base set of inputs was used to develop the LUT. This study is similar in that two thousand water samples were created for every combination of wind speed $(0, 5, 10)[\frac{\text{m}}{\text{s}}]$ and solar-zenith angle $(20^\circ, 43^\circ)$

parameters. These two solar-zenith angles were chosen to represent the Sun's position at the study site at noon on the summer solstice and the spring equinox, respectively. The LUT was created with a wind speed of $5[\frac{m}{s}]$ and a solar-zenith angle of 31° . These parameters reflect the conditions experienced during the May 20, 1999 collect. The constituent retrieval process, which was performed in the absence of atmospheric effects but included sensor effects, resulted in the errors shown in Figure 5.19.

	CHL ($\mu\text{g/L}$)		SM (mg/L)		CDOM	
Solar-zenith/wind speed:						
31/5 (Original LUT)	4.3	6.3%	0.8	3.3%	0.5	3.6%
20/0	5.9	8.7%	1.1	4.6%	0.5	3.6%
20/5	5.9	8.7%	1.1	4.6%	0.5	3.6%
20/10	5.9	8.7%	1.1	4.6%	0.5	3.6%
43/0	6.5	9.6%	1.3	5.4%	0.6	4.3%
43/5	6.4	9.4%	1.3	5.4%	0.6	4.3%
43/10	6.4	9.4%	1.3	5.4%	0.6	4.3%

Figure 5.19: *Results of solar/zenith and wind speed study. The full margin noise of Figure C.8 was used in this experiment.*

Row 1 represents the best-case scenario of where our modeled LUT inputs exactly match our modeled water sample inputs. Accordingly, for this row we get the same results as those described in Section 5.1.1. The remaining results indicate that varying solar/zenith angle has little effect on our ability to retrieve constituents while moderate variations in wind speed does not inhibit the process at all. When compared to the errors introduced to the process from insufficient knowledge of the IOPs, variations in solar/zenith angle and wind speed does not affect our ability to perform constituent retrieval. Therefore, assuming that water IOPs do not change over time, one can create a LUT with a solar/zenith angle of 31° and a wind speed of $5[\frac{m}{s}]$ to be used for a whole summer collect season.

Collectively, the results of Section 5.1 and Section 5.2 indicate that the OLI sensor has tremendous potential for water resource assessment and that its atmospheric compensation

algorithms will enable the constituent retrieval process if the IOPs of the receiving waters are well known. The sensitivity studies of this section indicate that caution in extending the method over a range of water bodies should be employed and that a different LUT is required when there is a significant change in the nature of the coloring agents, i.e., changes in the IOPs. With these studies completed, we move forward to testing our methods on real data.

5.3 Real Data

The previous sections presented results of the constituent retrieval process when performed on simulated data. The beauty of conducting such experiments is that it allows us to see errors introduced at each stage of the retrieval process. By separately evaluating errors due to the sensor, errors due to the atmospheric compensation routine, and errors due to the constituent retrieval algorithm we are able to isolate areas of concern for the entire process. Ultimately, the experiments of Section 5.2 enabled us to determine that accurate knowledge of water IOPs is essential to a successful retrieval of water constituents.

The purpose of this section is to make the transition from working with synthetic data to working with real data. To do so, we will initially perform the constituent retrieval process under the ideal case where ground truth data is available for atmospheric compensation. This enables the Empirical Line Method (ELM) to be used, the benefits of which are two-fold. First, ELM provides best-case results to measure the efficiency of the OLI-specific atmospheric compensation algorithms. Secondly, it allows us to confirm our suspicions that accurate IOP knowledge is essential to a well functioning constituent retrieval algorithm. The following sections analyze our ability to perform constituent retrieval using AVIRIS data that has been spectrally sampled to the OLI sensor response. Since OLI has not yet achieved orbit, using data from a hyperspectral sensor allows us to generate an OLI simulated scene (which is valid to do since the two instruments have similar noise and quantization characteristics).

5.3.1 Constituent Retrieval Using ELM

As described in Section 4.2.2.6 the Empirical Line Method is a simple, yet efficient technique for converting sensor-reaching signals to reflectances when ground truth is available. This section presents the results of an experiment that attempts to retrieve water constituents from simulated OLI data when ELM is used to account for the atmosphere.

To perform ELM in this research, two techniques were used to fit a line to the data. Both methods are derivations of that developed by [Raqueno et al., 2000] which uses Hydrolight to model the reflectance of water in a scene. Similar to [Raqueno et al., 2000], both methods use an ROI over Lake Ontario to serve as a dark point for the ELM. Instead of using a cloud as a bright region, however, the first method implemented in this work uses a region over Long Pond while the second method uses a sand region (see Figure 5.20).



Figure 5.20: *The locations of ground truth samples and ELM data points in the Rochester Embayment.*

In the first method, in situ observations of constituent concentrations were obtained for both the Lake Ontario and Long Pond ROIs. By submitting these observed concentrations to Hydrolight, the reflectances associated with the imaged radiances can be determined and the ELM performed on a band-by-band basis. Similarly, in the second method the

ROI over Lake Ontario is used in conjunction with Hydrolight to determine the dark point in the ELM. In this method, however, the spectral reflectance of bright sand pixels were measured using a spectrometer.

Once the line parameters have been determined for both ELM scenarios, the constituent retrieval process can be performed by first converting radiance values for each of the ROIs shown in Figure 5.20 to reflectance values. Then, on a pixel-by-pixel basis, the constituent retrieval algorithm is used to invert the reflectances to concentration triplets. These concentration triplets can be compared to actual measured values to determine the accuracy of the process, just as we did for the synthetic experiments. The results of the constituent retrieval process when Long Pond is used as a bright point in the ELM are shown in Figure 5.21.

	CHL ($\mu\text{g/L}$)		SM (mg/L)		CDOM	
Braddocks Bay:						
A3	4.2	6.2%	15.3	63.8%	0.9	6.4%
A4	4.3	6.3%	6.3	26.3%	2.3	16.4%
A5	6.7	9.9%	7.3	30.4%	1.3	9.3%
Lake Ontario:						
LO1	0.7	1.0%	0.9	3.8%	0.9	6.4%
Genesee Plume:						
A25	26.2	38.5%	13.8	57.5%	1.4	10.0%
A31	23.3	34.3%	19.4	80.8%	2.5	17.9%
Genesee	14.2	20.9%	15.7	65.4%	1.5	10.7%
Cranberry Pond:						
A19	4.3	6.3%	6.2	25.8%	1.4	10.0%
A23	3.9	5.7%	6.8	28.3%	1.5	10.7%
CP1	5.1	7.5%	1.3	5.4%	1.2	8.6%
CP2	7.6	11.2%	3.6	15.0%	1.8	12.9%
Long Pond:						
A18	11.8	17.4%	1.5	6.3%	3.1	22.1%
A20	3.9	5.7%	1.3	5.4%	0.6	4.3%
A22	22.0	32.4%	1.5	6.3%	2.3	16.4%
LP1	3.6	5.3%	1.2	5.0%	1.3	9.3%

Figure 5.21: Results of the constituent retrieval process when ELM is used to compensate for the atmosphere. Long Pond is used as the bright region in the ELM.

Figure 5.21 shows that we do an acceptable job retrieving the constituents for a few of the water bodies. Particularly, low constituent retrieval errors can be found in the glint free regions of Long Pond and Cranberry Pond (highlighted in yellow in Figure 5.21). This indicates that an adequate job has been done in characterizing the optical properties of these water bodies. Note that although the constituent retrieval errors for Lake Ontario are low, the constituent concentrations in this water body are low as well. It is natural to observe low retrieval errors in water bodies with low constituent concentrations since the IOPs resemble those of case 1 waters (recall Equations 3.8 and 3.9).

	CHL ($\mu\text{g/L}$)		SM (mg/L)		CDOM	
Braddocks Bay:						
A3	5.2	7.6%	16.8	70.0%	0.9	6.4%
A4	3.9	5.7%	9.3	38.8%	4.3	30.7%
A5	5.0	7.4%	10.3	42.9%	3.6	25.7%
Lake Ontario:						
LO1	0.4	0.6%	0.4	1.7%	0.4	2.9%
Genesee Plume:						
A25	9.4	13.8%	23.3	97.1%	0.7	5.0%
A31	13.7	20.1%	23.1	96.3%	1.3	9.3%
Genesee	8.2	12.1%	15.6	65.0%	2.0	14.3%
Cranberry Pond:						
A19	3.7	5.4%	6.5	27.1%	2.5	17.9%
A23	3.7	5.4%	7.3	30.4%	2.3	16.4%
CP1	3.7	5.4%	1.6	6.7%	2.7	19.3%
CP2	7.1	10.4%	4.1	17.1%	3.2	22.9%
Long Pond:						
A18	20.4	30.0%	1.4	5.8%	5.5	39.3%
A20	10.3	15.1%	1.4	5.8%	3.5	25.0%
A22	24.4	35.9%	1.3	5.4%	5.3	37.9%
LP1	3.1	4.6%	1.3	5.4%	2.6	18.6%

Figure 5.22: Results of the constituent retrieval process when ELM is used to compensate for the atmosphere. Ontario Beach sand is used as the bright region in the ELM.

Figure 5.22 shows the constituent retrieval errors that we obtain when a uniform region of Ontario Beach sand is used in the ELM. Again, the best results are obtained in the glint

free regions of Long Pond and Cranberry Pond (highlighted in yellow in Figure 5.22) further indicating that the IOPs have been adequately characterized in these ponds. Notice that when the two figures are compared, the Long Pond ELM outperforms the Ontario Beach sand ELM. This is due to the fact that the range of brightness values used in the Long Pond ELM is small. Therefore, the errors are minimal since the technique is tailor made for compensating water pixels.

Some significant conclusions can be made from this study. First, since large constituent retrieval errors are observed in Braddocks Bay and the Genesee river plume (see Figure 5.21), one can conclude that a poor job has been done in characterizing the IOPs for these water bodies, particularly those IOPs related to suspended materials. This further indicates that pond-specific LUTs may need to be created for the various water bodies that one may encounter across a scene. For this research in particular, although our LUT (which was generated from averaged IOPs) can be used for ponds such as Long Pond and Cranberry Pond, it should not be used universally throughout the Rochester Embayment.

Secondly, glint was a significant problem for this collect due to the high Sun and the location of the target ponds in the solar glint direction. The evidence of Sun glint is apparent in this scene as water bodies with relatively homogeneous constituent concentrations contain drastically different constituent retrieval errors. This can be seen for Cranberry Pond in Figure 5.21, where ground truth locations A19 and A23 are glint contaminated pixels. Compared to CP1 and CP2, which were hand-chosen glint-free regions, their constituent retrieval errors are significantly higher for suspended materials. Moving forward, care should be taken to remove glint from images using the algorithm described in Section 4.2.1. (Note that glint removal algorithms were not employed in this experiment).

Lastly, due to the low retrieval errors for Cranberry Pond and Long Pond we can conclude that the IOPs in these ponds are well represented in the LUT retrieval algorithm. Therefore, it is with these water bodies that we will measure the success of our atmospheric compensation algorithms. Any success in measuring the errors due to the OLI compensation routines will be had in these regions where the errors in characterizing the IOPs is at a minimum.

5.3.2 Constituent Retrieval Using OLI's Blue Band Method

With baseline errors in place, we can now test the efficiency of OLI's atmospheric compensation algorithms on real data. In this first experiment, we use the spectrally sampled AVIRIS data shown in Figure 5.20 to perform constituent retrieval over Long Pond and Cranberry Pond. Recall that these two ponds are desirable since their IOPs most resemble those contained in our LUT. The two glint-free ROIs highlighted in yellow in Figure 5.21 are chosen as test sites to avoid the need for glint removal. In this section, the OLI Blue Band method is used to compensate for the atmosphere and retrieve the constituent concentrations from each pixel in the ROIs. The resulting concentration triplets can be compared to actual measured values to determine the accuracy of the process. The errors associated with this process are shown in Figure 5.23.

	CHL ($\mu\text{g/L}$)		SM (mg/L)		CDOM	
Cranberry Pond:						
ELM:						
CP1	5.1	7.5%	1.3	5.4%	1.2	8.6%
CP2	7.6	11.2%	3.6	15.0%	1.8	12.9%
OLI Algorithm:						
CP1	3.5	5.1%	3.1	12.9%	4.6	32.9%
CP2	4.1	6.0%	3.1	12.9%	4.6	32.9%
Long Pond:						
ELM:						
LP1	3.6	5.3%	1.2	5.0%	1.3	9.3%
A20	3.9	5.7%	1.3	5.4%	0.6	4.3%
OLI Algorithm:						
LP1	3.9	5.7%	1.0	4.2%	6.0	42.9%
A20	4.4	6.5%	1.1	4.6%	5.9	42.1%

Figure 5.23: Results of the constituent retrieval process using the OLI atmospheric compensation algorithm (Blue Band).

As indicated from the studies of Section 5.1, OLI's Blue Band method does an excellent job at removing the atmosphere from the chosen water ROI's. For two out of three constituents, the OLI algorithm performs as well as the Empirical Line Method. Uncharacteristically, however, we are unable to accurately retrieve concentrations for the third constituent (CDOM). Due to our success in retrieving constituents from synthetic data in Section 5.1, and considering ELM worked reasonably well in this experiment, the source of error in CDOM retrieval may lie in the AVIRIS data. Although a multitude of issues can cause this error in CDOM retrieval, we offer the most probable explanations.

Recall that to simulate OLI imagery in this study, we spectrally sampled the AVIRIS data to the six bands of the OLI sensor. In doing so, two significant deficiencies in the AVIRIS data may have manifested themselves in the OLI data. The first is the poor SNR found in the first few bands of AVIRIS. Figure 5.24 shows a plot of the noise equivalent change in radiance versus wavelength for the four imaging spectrometers of AVIRIS, [Green and Pavri, 2001].

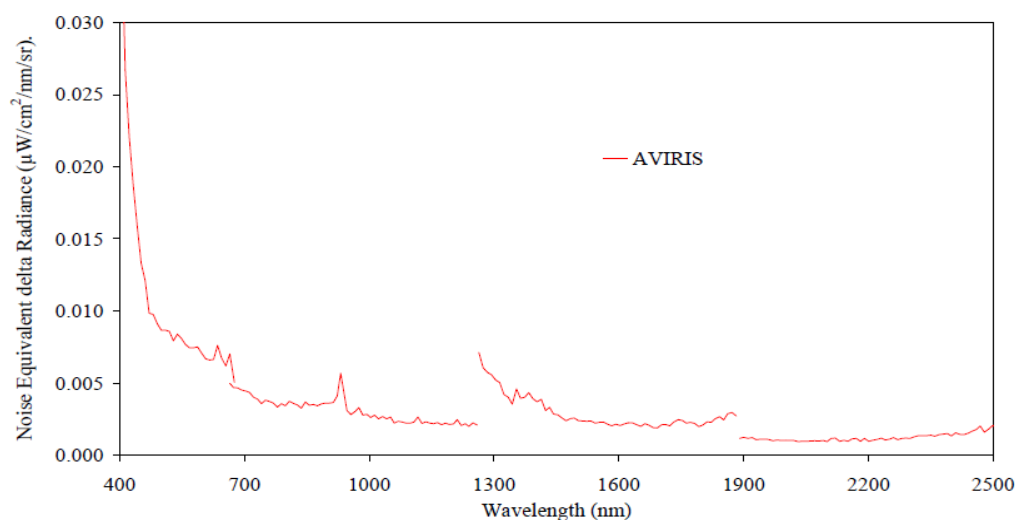


Figure 5.24: $NE\Delta L$ versus wavelength for the four imaging spectrometers of AVIRIS.

Notice in the blue region of this plot that the $NE\Delta L$ spikes. This indicates high levels of noise and it is in this region that band 1 of OLI lies. Therefore, when the AVIRIS data is spectrally sampled to band 1 of OLI, noise may be getting sampled as well. The magnitude of the impact of this noise on the constituent retrieval process is unclear. What

is for certain, however, is that the success of the OLI-specific atmospheric compensation algorithm depends on our ability to take an accurate band 1 to band 6 epsilon ratio. Noise in the first band can significantly affect this ratio which will in turn affect our ability to retrieve the visibility and water constituent parameters.

Secondly, the calibration accuracy of the AVIRIS spectrometers in this same spectral region is unclear. Error in calibration may manifest itself as an error in the retrieval process, particularly since the ELM method removes calibration error and worked reasonably well for this data set. Therefore, in an effort to determine if calibration issues exist, the gain and bias parameters determined from ELM can be compared to those from the OLI algorithm. Any difference in the two can be attributed to a calibration issue. Figure 5.25 shows the spectral bias that is applied to data when both the ELM and OLI atmospheric compensation methods are used.

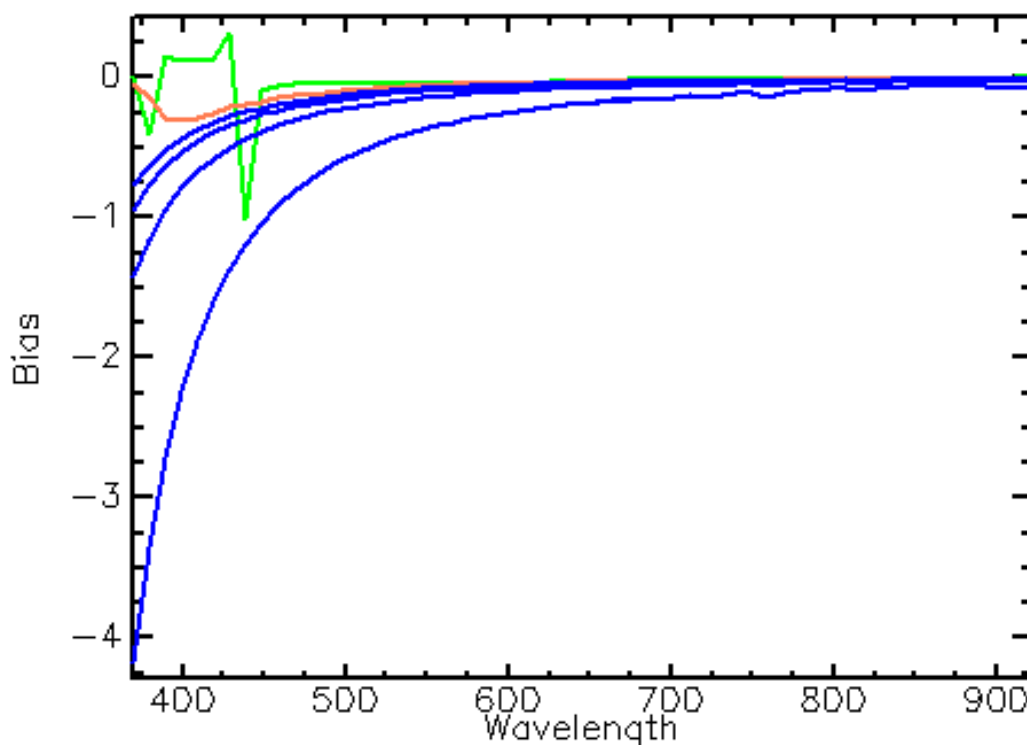


Figure 5.25: *Spectral biases that are applied to data for both the ELM and OLI atmospheric compensation methods. Blue curves are biases associated with the OLI algorithm while the green and brown curves are the biases associated with the Long Pond ELM and Ontario Beach sand ELM, respectively.*

The blue curves represent the biases associated with an atmosphere used in the OLI method. This particular atmosphere contains rural aerosols with a visibility parameter that ranges from 10 to 40 kilometers. The green and brown curves show the biases that are associated with the Long Pond ELM and Ontario Beach sand ELM, respectively. Of particular interest is the behavior of these curves below 450 nanometers. When compared to the potential bias curves that the OLI algorithm offers, we see that the ELM curves deviate in the blue end of the spectrum. Since CDOM is a major absorber of light in the blue, these retrieval errors will most likely occur with the CDOM parameter as we observed in Figure 5.23.

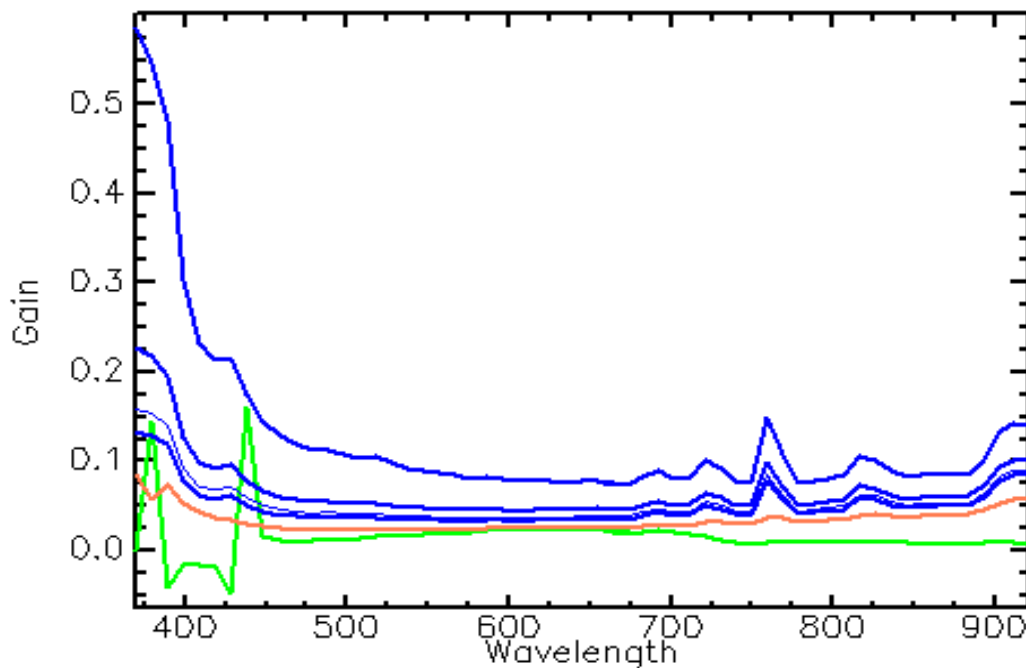


Figure 5.26: *Spectral gains that are applied to data for the ELM and OLI atmospheric compensation methods. Blue curves are the gains associated with the OLI algorithm while the green and brown curves are the gains associated with the Long Pond ELM and Ontario Beach sand ELM, respectively.*

Figure 5.26 shows the spectral gain that is applied to data when using both the ELM and OLI atmospheric compensation methods. Like Figure 5.25, the blue curves represent the gains associated with the rural atmosphere used in the OLI atmospheric compensation algorithms while the green and brown curves show the gains associated with the Long Pond

ELM and Ontario Beach sand ELM, respectively. Once again, the ELM gains deviate from the other curves below 450 nanometers. This further indicates that calibration issues may exist for the AVIRIS sensor. Coupled with the fact that AVIRIS has low SNR in the blue, it is reasonable to assume that the errors shown in Figure 5.23 are due to the AVIRIS data and not the OLI Blue Band algorithm.

5.3.3 Constituent Retrieval Using OLI's Band Ratio Method

In this second experiment, we test our ability to perform constituent retrieval when the OLI Band Ratio method is used to compensate for the atmosphere. Again, the spectrally sampled AVIRIS data of Figure 5.20 is used and the retrieval methods tested over Long Pond and Cranberry Pond. In this experiment, however, care has been taken to remove glint from the data. Unlike the previous OLI compensation method (which treats the spectral glint bias as a lower visibility atmosphere), glint will significantly affect the retrieval errors. This is due to the nature in which the Band Ratio method removes the atmosphere. Without glint removal, the retrieved reflectances that result from the atmospheric compensation process will be biased high. As a result, the constituents will be overestimated. Figure 5.27 shows Cranberry Pond and Long Pond after the deglinting algorithm of Section 4.2.1 is employed. The ROIs used in this experiment were chosen to overlap those used in the previous experiment for consistency.

To implement the OLI Band Ratio method, a procedure similar to that of Section 5.1.2.2 and Section 5.1.3.3 is followed. Two hundred of the darkest pixel values in OLI's band 5 and band 6 of the data shown in Figure 5.27 are averaged and the epsilon ratio ($\epsilon^{5,6}$) calculated to determine the atmosphere associated with the image. The atmospheric LUT used in this process is identical to that of the past sections, i.e., it was created by running MODTRAN with rural aerosols, a mid-latitude summer profile, 15:40 GMT on *May* 20, 1999, multiple scatter effects included, and the visibility parameter varied between 5 and 60 kilometers in 5 kilometer increments. When used to search the LUT, the in-scene epsilon ratio chose an atmosphere with a visibility of 23.49 kilometers. This atmosphere was then removed from the Long Pond and Cranberry Pond ROIs shown in Figure 5.27 and the constituent retrieval algorithm implemented to determine the corresponding constituent concentrations. The results of this process are shown in Figure 5.28.

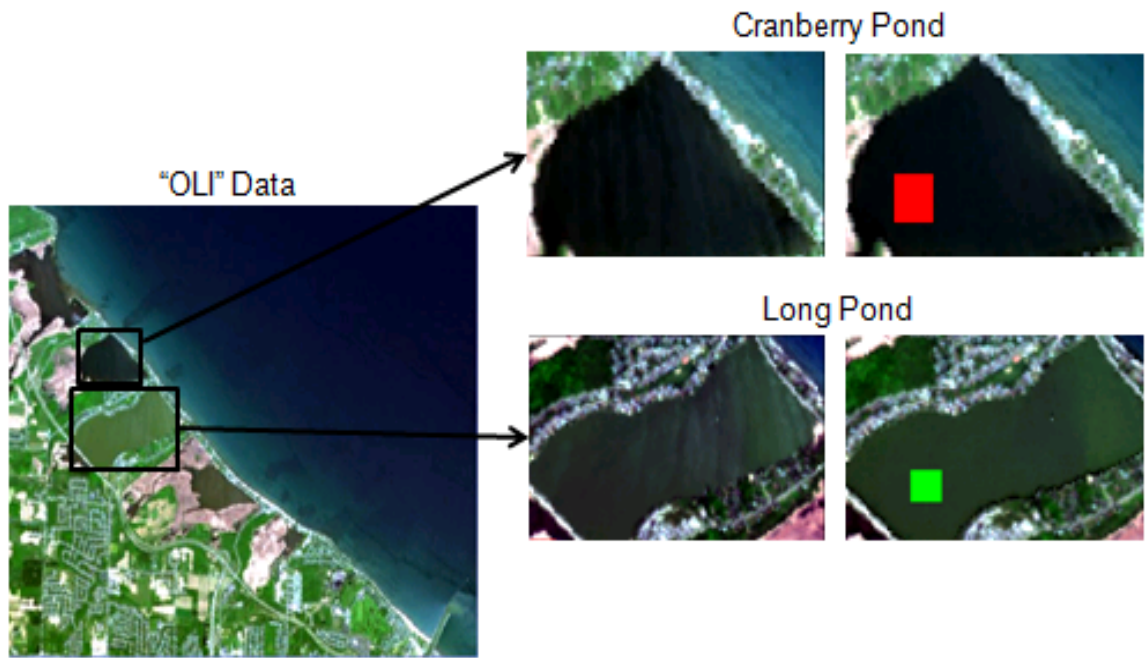


Figure 5.27: *Deglinted OLI data of Cranberry Pond and Long Pond in the Rochester Embayment. The ROIs were chosen to overlap CP1 and LP1 in Figure 5.20.*

	CHL ($\mu\text{g/L}$)		SM (mg/L)		CDOM		Chosen Visibility
Band Ratio Method:							
Cranberry Pond ROI	3.7	5.5%	3.5	14.4%	2.9	20.9%	23.49
Long Pond ROI	54.7	80.4%	1.2	5.0%	4.6	33.2%	23.49

Figure 5.28: *Results of the constituent retrieval process when the OLI Band Ratio method is used to compensate for the atmosphere.*

As one can plainly see, we did an extremely poor job in retrieving the constituent concentrations in this experiment. This was not completely unexpected, however, as we discussed that a calibration error may exist in the AVIRIS data. This experiment, provides further evidence that this may be the case.

To visualize this potential calibration error, Figure 5.29 and Figure 5.30 show the retrieved reflectances resulting from the atmospheric compensation of the ROI pixels shown in Figure 5.27 when the OLI Band Ratio method is used. The left hand side of these figures shows the atmospherically compensated pixels while the right hand side shows the

expected reflectances for the ROIs, which are modeled using Hydrolight based on in situ measurements. If we believe the modeled reflectances (which we do for these ponds) then clearly a calibration issue exists.

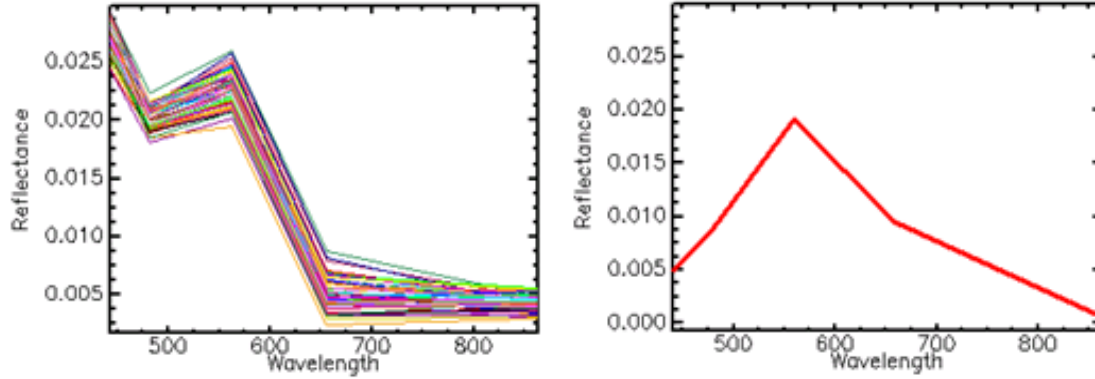


Figure 5.29: (Left) Retrieved reflectances resulting from the atmospheric compensation of the red ROI pixels shown in Figure 5.27 (Cranberry Pond) when the OLI Band Ratio method is used. (Right) Modeled reflectances of ROI based on in situ measurements.

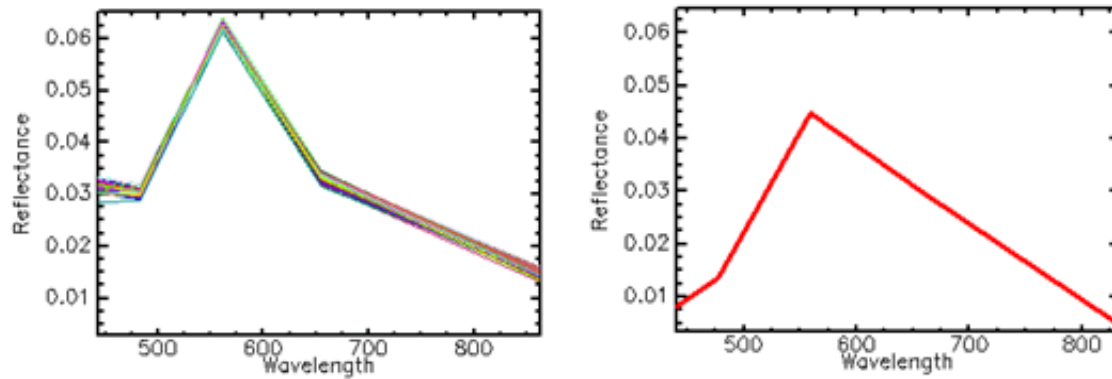


Figure 5.30: (Left) Retrieved reflectances resulting from the atmospheric compensation of the green ROI pixels shown in Figure 5.27 (Long Pond) when the OLI Band Ratio method is used. (Right) Modeled reflectances of ROI based on in situ measurements.

To investigate this potential calibration error further, ROIs were taken over both land and water pixels for the original 224 band AVIRIS data (see Figure 5.31) and a spectral slice of the data obtained in an attempt to determine if a calibration error exists. Figure 5.32(a) and Figure 5.32(b) show the resulting spectra for both ROIs over the VNIR wavelengths. Notice, as indicated by the blue circles, that there is a gap in the data (on the

digital count axis) where the first and second spectrometer of the AVIRIS sensor overlap. In both cases, the data in the first spectrometer (in the overlap region) is about 9% higher than the data in the second spectrometer. If we make the somewhat bold assumption that all the data in the first spectrometer is 9% higher than it should be, the data can be corrected over the regions of interest (Long Pond and Cranberry Pond) and the constituent retrieval process rerun. If adequate retrieval errors are obtained after this correction then perhaps the original errors can be attributed to the biased data collected from the first spectrometer.



Figure 5.31: ROIs taken from AVIRIS data over both land and water pixels in an attempt to determine if a calibration error exists in the data.

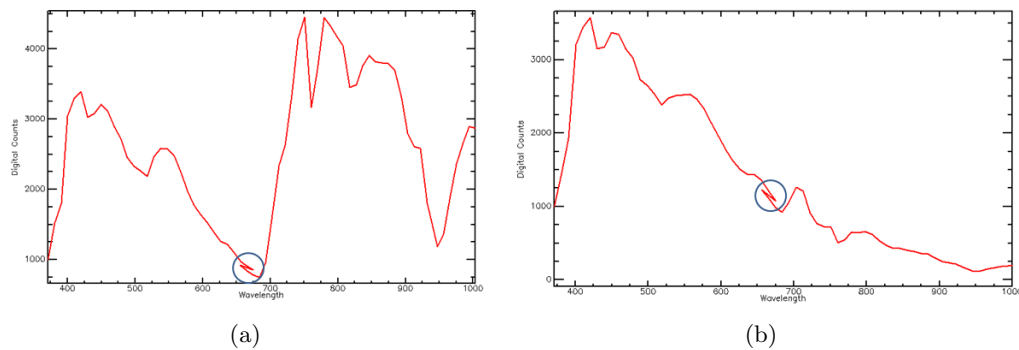


Figure 5.32: (a) Spectral slice for VNIR wavelengths of AVIRIS data for land ROI (blue) shown in Figure 5.31. (b) Spectral slice for VNIR wavelengths of AVIRIS data for water ROI (red) shown in Figure 5.31.

When the data shown in Figure 5.27 is biased down by 9% for the first 3 bands of OLI and the constituent retrieval process rerun for the ROIs, the resulting reflectance signals should represent a more accurate representation of the true water-leaving reflectances in these region. Figure 5.33 confirms that this is indeed the case.

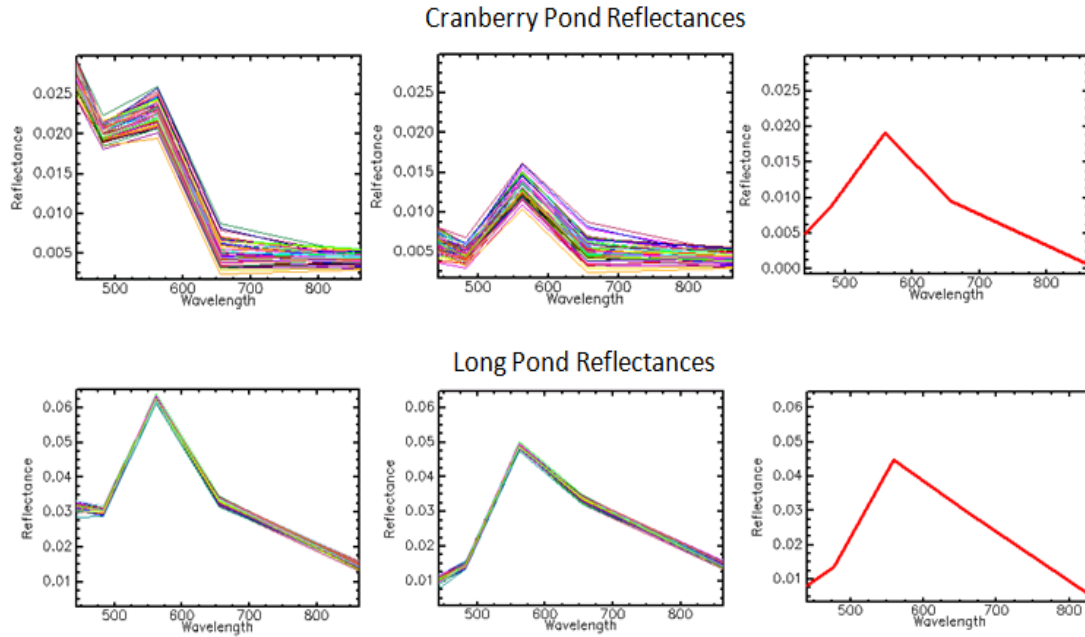


Figure 5.33: *Results of the constituent retrieval process using OLI Band Ratio method to compensate for the atmosphere. (Top) Reflectances retrieved from Cranberry Pond before 9% bias correction, after 9% bias correction, and modeled expected reflectance based on in situ observations. (Bottom) Analogous curves for Long Pond.*

The signals on the left of Figure 5.33 represent the reflectances obtained when the OLI Band Ratio method is applied to the uncorrected data for each ROI. The signals in the middle represent the reflectances obtained when the OLI Band Ratio method is applied to the 9% bias-corrected data. Finally, the signals on the right represent the expected reflectances for the ROIs, which are modeled using Hydrolight based on in situ measurements. Clearly, by inspection, the retrieved reflectances obtained from the 9% bias-corrected data are more similar to the expected reflectances than the data which is not bias-corrected.

Figure 5.33 does not show, however, how the improvement in bias-corrected reflectances equates to constituent retrieval error. Figure 5.34 shows the retrieval errors obtained when the bias-corrected reflectances are submitted to the constituent retrieval algorithm. The

retrieval errors obtained when the Empirical Line method and OLI Blue Band method are used to compensate for the atmosphere are included for reference.

	CHL ($\mu\text{g/L}$)		SM (mg/L)		CDOM		Chosen Visibility
Cranberry Pond ROI:							
Empirical Line Method	5.1	7.5%	1.3	5.4%	1.2	8.6%	-
Blue Band Method	3.5	5.1%	3.1	12.9%	4.6	32.9%	15.50
Band Ratio Method (Bias Corrected)	1.2	1.7%	4.5	18.9%	0.7	5.1%	23.49
Long Pond ROI:							
Empirical Line Method	3.6	5.3%	1.2	5.0%	1.3	9.3%	-
Blue Band Method	3.9	5.7%	1.0	4.2%	6.0	42.9%	14.50
Band Ratio Method (Bias Corrected)	8.2	12.0%	1.4	5.7%	1.4	9.8%	23.49

Figure 5.34: Results of the constituent retrieval process using OLI Band Ratio method to compensate for the atmosphere after a 9% bias correction is applied to the first 3 bands of the OLI data.

Incredibly, the errors shown in Figure 5.34 are comparable for all three processes. In particular, the retrieval results for the OLI Band Ratio method after the data is bias-corrected are almost as good as those obtained from the ELM. This is extremely exciting for future users of OLI data. Assuming a well-calibrated instrument, and that signal-to-noise ratios are sufficient (particularly in the SWIR), OLI should be a state-of-the-art technology for water quality parameter retrieval.

5.4 Concluding Remarks

This chapter contains groundbreaking material for those interested in studying case 2 waters from space. We determined that the OLI sensor exhibits the potential to be used throughout this research by evaluating its ability to perform the constituent retrieval process on simulated data. Next, to realize OLI's potential the ability of two OLI-specific atmospheric compensation algorithms were applied to simulated data which included atmospheric effects. Potential areas of concern were addressed that may impact one's ability

to perform constituent retrieval with real data. As a result, this research has determined that separate pond-specific LUTs must be developed to retrieve constituents from the various water bodies throughout a scene if the IOPs differ significantly. Finally, the OLI atmospheric compensation algorithms were successfully tested on real data and areas of concern regarding the AVIRIS dataset discussed

Now that a source for reflective data has been identified, we shift our focus to how remotely sensed data may be used to calibrate a hydrodynamic model. Chapters 4 and 5 were written in a manner such that the end-to-end process of constituent retrieval was described and potential sources of errors addressed. Chapter 6 is written in a similar fashion. The next couple of sections address the issues associated with surface temperature retrieval and describe how retrieved surface temperatures can be used to calibrate a hydrodynamic model. Section 6.2.2 details the process that one can follow to calibrate a hydrodynamic model using remotely sensed thermal data and presents the results of an experiment designed to test the methods developed in this work.

Chapter 6

Using Thermal Data to Calibrate a Hydrodynamic Model

Chapter 4 described the techniques required to perform constituent retrieval over case 2 waters with OLI reflective data. By identifying an appropriate sensor, developing an atmospheric compensation routine, and introducing a constituent retrieval algorithm we were able to describe a method which determines water constituents from imaged pixels. The format of this chapter is analogous to that of Chapter 4 but for thermal data.

We begin this chapter with a section on thermal sensors. While the constituent retrieval process of the previous sections requires a special sensor with enhanced radiometric features, determination of sea-surface temperatures does not. We will identify sensors whose thermal data can be used throughout this study if LDCM does not carry the TIRS instrument. Since thermal data typically has a lower spatial resolution than its reflective counterpart, a radiometric sharpening technique will be introduced. This method will enable lower resolution thermal data to be sharpened to the same resolution as the reflective data which will facilitate the calibration of the hydrodynamic model. Next, a section which describes how we will obtain surface temperatures from thermal data is presented for the various sensors. Finally, a comprehensive description of the inputs to the ALGE hydrodynamic model is presented and an optimization method that will enable retrieved surface temperatures to be used as a calibration tool for the model is described.

6.1 Thermal Data

The purpose of thermal data in this research is to serve as a means with which to calibrate a hydrodynamic model. Unlike the constituent retrieval process, superior radiometric fidelity is not required for sea-surface temperature retrieval. Therefore, in identifying an appropriate thermal sensor more emphasis will be placed on its temporal resolution rather than its radiometric fidelity. This section offers two alternative sensors to be used to gather thermal data in the event that TIRS is unavailable. Due to the poor spatial resolution of these instruments, a technique is introduced that radiometrically sharpens moderate resolution thermal data to the same GSD as high resolution reflective data. Finally, we close this section with a discussion of how we will obtain surface temperatures from thermal data.

6.1.1 NPOESS/MODIS

In the event that the TIRS instrument is not available, our next preference for thermal data would be to use the National Polar-Orbiting Operational Environmental Satellite System (NPOESS) sensor. In addition to providing us with the thermal bands necessary for determining surface temperatures, the NPOESS Preparatory Project aims to measure atmospheric temperatures, humidity sounding, land and ocean biological productivity, and cloud and aerosol properties from space. With the extensive suite of sensors provided on this satellite, an increased amount of environmental data can be used as input to the ALGE hydrodynamic model enabling more accurate flow estimations. The anticipated launch date for NPOESS is 2013 so although this is the preferred alternative to TIRS, we will assume that its data will not be available in time for our studies. We can, however, demonstrate the validity of our methods using MODIS data with the understanding that NPOESS is the instrument of choice if TIRS thermal data are unavailable.

The Moderate Resolution Imaging Spectroradiometer (MODIS) is an instrument on-board the Terra and Aqua satellites which has repeat coverage of the Earth's surface every 1 to 2 days. Terra is on a descending node and passes over the equator in the morning while Aqua is on an ascending node, crossing the equator in the afternoon. The MODIS instrument acquires data in 36 spectral bands and, of particular interest to us, has a number

of thermal bands in the 8-14 micron region. Figures C.6 and C.7 show the various bands of MODIS and their primary uses. Not included in these tables, however, is the spatial resolution associated with each band. Bands 1 and 2 of MODIS contain the instrument's best resolution with 125 meter GSDs while its thermal bands, bands 31 and 32, have a spatial resolution of 1 kilometer. This is a disconcerting fact for our study as we wish to resolve the detail contained in coastal waters and river plumes. TIRS's 100 meter spatial resolution would be more appropriate for this work but even if it were to achieve orbit, due to its poor temporal resolution, MODIS (NPOESS) becomes an interesting alternative when temporal resolution is important.

Although we are resigned to using moderate resolution thermal data, spatial resolution must not be sacrificed if we are to adequately calibrate the hydrodynamic model. With this in mind, we will introduce a technique that can be implemented to sharpen 1 kilometer MODIS thermal data or 100 meter TIRS data to 30 meters using the reflective bands of OLI.

6.1.2 Radiometric Sharpening

If we assume that MODIS or NPOESS will be our primary sources for thermal data, a need to perform radiometric sharpening presents itself. We would like to take advantage of the superior spatial resolution of the Landsat instruments to study river plumes so our thermal data must be similar in scale to that of the reflective data. Therefore, this section describes a simple sharpening technique that can be used to radiometrically sharpen moderate resolution thermal data to that of the high resolution reflective data.

Figure 6.1 shows Landsat 7 reflective and thermal data of the Rochester Embayment. Observing the lake's coastline, particularly at the mouth of the Genesee River, there appears to be some correlation between the color of the water and its surface temperature. [Robinson et al., 2000] describe a technique for sharpening visible data with higher resolution panchromatic data, assuming a correlation exists between the two bands. We propose to use a modified version of this method which uses higher resolution reflective bands to sharpen lower resolution thermal bands. The process is as follows:

Over the scene of interest, which should be masked to only include water pixels, per-



Figure 6.1: *Landsat 7 imagery illustrating a possible correlation between reflective data (Left) and thermal data (Right) in coastal waters.*

form a linear regression of the thermal pixel radiances versus the reflective pixel radiances by averaging the finer resolution reflective pixels contained within each thermal pixel. In other words, solve for the regression coefficients $a_0 + a_1 + \dots + a_n$ in,

$$L_{T_{obs}} = a_0 + a_1 \overline{L_1} + a_2 \overline{L_2} + \dots + a_n \overline{L_n} \quad (6.1)$$

where $L_{T_{obs}}$ is the radiance associated with an observed thermal pixel, $\overline{L_i}$ is the average radiance in *band i* of the corresponding reflective pixels contained in the observed thermal pixel, and n is the number of reflective bands. Once the regression coefficients have been determined, we can make an estimate of the “thermal” radiance associated with each subpixel by applying,

$$\hat{L}_{T_i} = a_0 + a_1 L_{1_i} + a_2 L_{2_i} + \dots + a_n L_{n_i} \quad (6.2)$$

where \hat{L}_{T_i} is the thermal estimate for *subpixel i* and L_{j_i} is the radiance value of the j^{th} band in *subpixel i* for $j = 1, 2, \dots, n$. Once the thermal estimates have been made for all subpixels in the superpixel, the radiances must be scaled using

$$L_{T_i} = \frac{\hat{L}_{T_i}}{\sum \hat{L}_{T_i}} L_{T_{obs}} \quad (6.3)$$

where L_{T_i} is the thermal radiance associated with the subpixel. This scaling ensures that the average radiance of the estimated thermal subpixel equals the original superpixel's thermal radiance.

It should be noted that mixed pixels will exist along the shoreline. These pixels should not be included in the regression calculation. However, they can still be included in the sharpening process with a minor revision. To perform the scaling shown in Equation 6.3, $L_{T_{obs}}$ from adjacent water pixels must be used. This estimate is made since the original thermal observation will be contaminated with radiance that originates over land. We now provide an illustration of the sharpening process.

Figure 6.2 shows the Rochester Embayment as seen by the 1 kilometer thermal band of MODIS (Left) and the 30 meter reflective bands of Landsat 7 (Right). Our goal is to radiometrically sharpen the MODIS data to the Landsat 7 resolution. In this process, the thermal and reflective data must be registered so Figure 6.2 (Left) was simulated using the thermal band of Landsat 7.

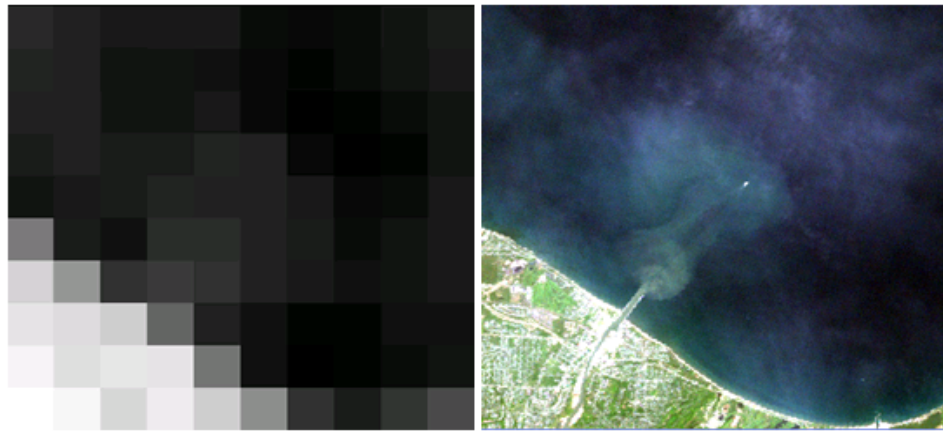


Figure 6.2: (Left) *Simulated MODIS thermal data of Rochester Embayment.* (Right) *Corresponding area as seen by the RGB reflective bands of Landsat 7.*

Following the method described above, we obtain the sharpened thermal data of Figure 6.3. This image shows that the sharpening process has maintained the detail of the reflective imagery. If we use the original Landsat thermal data as truth, the subpixel thermal data has an RMS-error of 2.79 digital counts which equates to approximately 1.5 Kelvin.

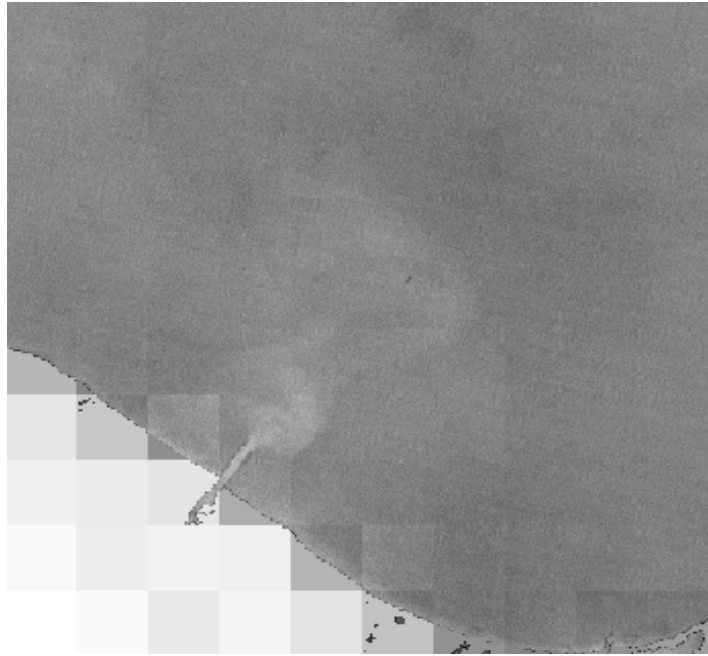


Figure 6.3: *1 kilometer MODIS thermal data that has been sharpened to 30 meter resolution using Landsat 7 reflective data.*

One must be cautious in using this sharpened thermal data, however. Although this method appears to perform well, and does so *on average*, the data may not be radiometrically accurate. In fact, the efficiency of this method hinges on the correlation between the thermal and reflective data. In this sharpening example, a correlation coefficient of $r = 0.95$ was obtained, indicating that there is in fact a strong correlation between the reflective and thermal data. Additionally, this sharpening technique does not require atmospherically compensated data. It is flexible enough to be performed in the digital count, radiance, or surface temperature domain. As we will see in the following section, this is convenient since some of the data we will work with has already been atmospherically compensated.

6.1.3 Surface Temperature Retrieval

In this section, we expand on the surface temperature retrieval process that was introduced in Section 3.3.3. A traditional algorithm that is ideal for sensors such as Landsat (which only contain one band in the thermal infrared region [10-12 microns]) is introduced. In

the event that Landsat data are unavailable, MODIS or NPOESS data can be used in conjunction with the sharpening technique of Section 6.1.2 to obtain thermal data. Although the standard MODIS product comes atmospherically compensated, the method it uses for obtaining surface temperatures is also described.

6.1.3.1 Landsat Data

In comparison to the techniques described in Chapter 4, the retrieval of sea-surface temperatures from calibrated Landsat data is straightforward. [Padula, 2008] describes a forward modeling technique that uses radiosonde data to characterize the atmosphere in an effort to model the governing equation

$$L(\lambda) = \frac{E_{de}(\lambda)r(\lambda)\tau_2(\lambda)}{\pi} + L_{ue}(\lambda) + \epsilon(\lambda)L_T(\lambda)\tau_2(\lambda). \quad (6.4)$$

With knowledge of the atmosphere, a LUT of sensor-reaching radiances can be developed as described in Section 3.3.3. Then, on a pixel-by-pixel basis, surface temperatures can be determined by comparing imaged radiance values to LUT values. The temperature of the blackbody curve in the LUT that yields the best match with the imaged water pixel is the apparent surface temperature of that pixel. The details of the process are summarized below using Figure 6.4 as a guide (which corresponds to the three terms in Equation 6.4).

In this discussion, we will assume that the shape factor (F) is equal to 1, which indicates there are no background objects in the scene. Therefore, to obtain the surface temperature of an imaged water pixel we must only account for paths E, F, and G in Figure 6.4. We do this by first modeling the atmosphere. Radiosonde data can be used to serve as a profile of the atmosphere over the scene of interest. With a lower atmosphere surface correction made to account for the temperature of the boundary layer at image acquisition time we can input the atmospheric profile into MODTRAN which, unlike other radiative transfer codes, is ideal for modeling an atmosphere's thermal properties. MODTRAN outputs spectral upwelling radiance $L_{ue}(\lambda)$, downwelling radiance $\frac{E_{de}(\lambda)}{\pi}$, and transmission $\tau_2(\lambda)$ over the thermal region defined by our sensor (10-12 microns). With these output parameters, we can now solve for sensor-reaching radiance by modeling the terms in Equation 6.4.

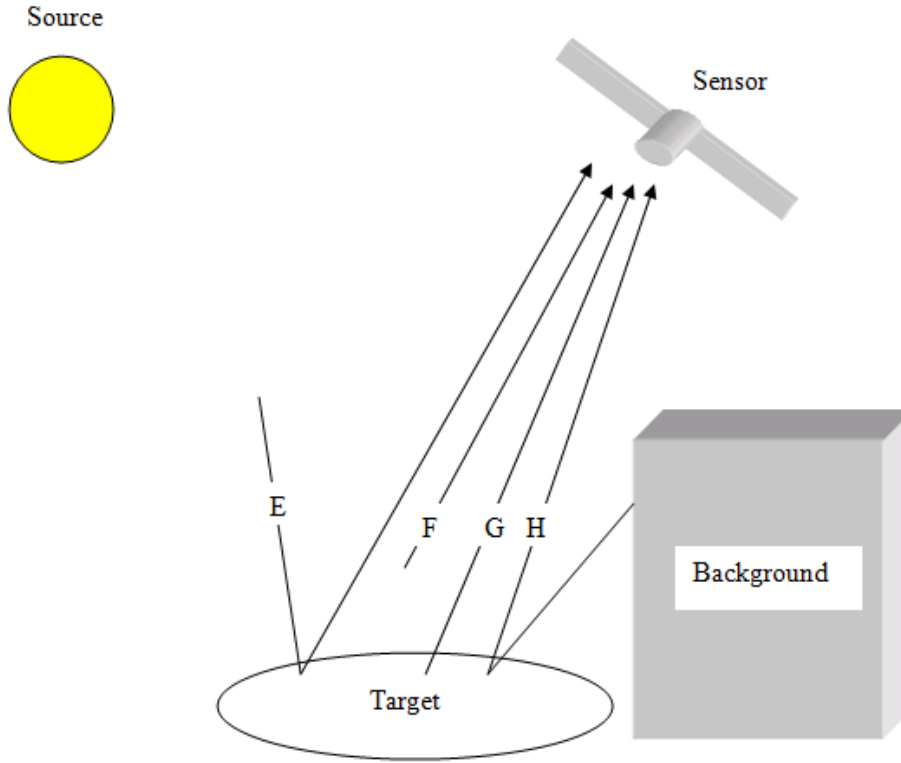


Figure 6.4: *Major self-emitted paths contributing to sensor reaching radiance.*

In this research, 31 blackbody curves are generated over the temperature range of 270.0 Kelvin to 300.0 Kelvin using Equation 3.16. This range adequately spans the temperatures that we expect to encounter when imaging water. If we assume that water has an emissivity (ϵ) of 0.986 [Padula, 2008], we can solve for path G in Figure 6.4 for all 31 curves using the transmission output from MODTRAN. Path F is also determined from MODTRAN and represents the upwelling radiance due to the surrounding atmosphere. Finally path E, or $\frac{E_{de}(\lambda)r(\lambda)\tau_2(\lambda)}{\pi}$, can be determined by multiplying MODTRAN's output for downwelling and transmission by the target's reflectivity, $r(\lambda) = 1 - \epsilon(\lambda) = 0.014$, assuming the target is Lambertian. This is a good assumption for water in the thermal if viewed near nadir [Schott, 1997]. Adding the modeled paths E, F, and G yields sensor-reaching radiance for 31 temperatures.

In order to determine the apparent temperature associated with an imaged water pixel, the 31 sensor-reaching radiances must be spectrally sampled to the sensor response of

Landsat's thermal band. Therefore, a relationship can be developed between apparent temperature and integrated radiance, as shown in Figure 6.5. Finally, this relationship can be used to convert imaged radiances to water surface temperatures using piecewise linear interpolation.

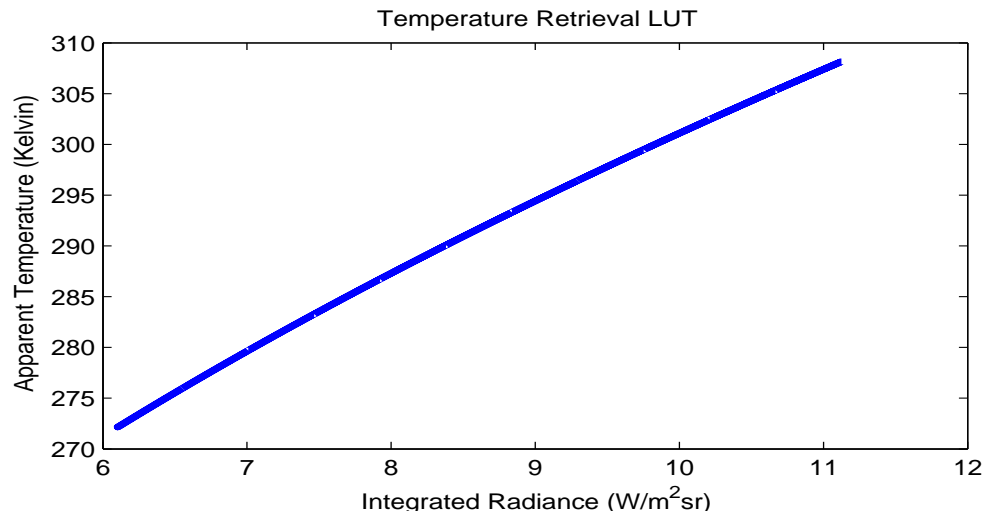


Figure 6.5: *Plot of apparent temperature versus radiance for the temperature range 270.0-300.0 Kelvin. Radiosonde data was used in MODTRAN to model the atmosphere.*

An error analysis was performed by [Padula, 2008] to test the efficiency of this surface temperature retrieval process for a wide range of atmospheres and surface temperatures. [Padula, 2008] concludes that the error associated with this process is approximately 0.6 Kelvin. Therefore, when retrieving surface temperatures with Landsat thermal instruments, we can expect to be within 0.6 Kelvin of the true surface temperature.

6.1.3.2 MODIS Data

In the event that Landsat thermal data are not available at the time of the collect, surface temperatures can be determined from MODIS thermal data. We previously mentioned that the standard level 2 MODIS products provide atmospherically compensated sea surface temperatures at 1 kilometer resolution. This data, which can be found on the MODIS website, is free and readily available for download. Assuming that the MODIS data can be adequately registered to the Landsat data, it can be used directly with the sharpening

algorithm described in Section 6.1.2 to produce the necessary high resolution surface temperature data.

Referring to Tables C.6 and C.7, daily products of sea surface temperatures (SST) are generated using the algorithm of [Brown and Minnett, 1999],

$$SST = c_1 + c_2 * T_{31} + c_3 * (T_{31} - T_{32}) * T_{src} + c_4 * (\sec(\theta) - 1) * (T_{31} - T_{32}) \quad (6.5)$$

where T_{31} and T_{32} are the brightness values from channels 31 and 32 respectively, θ is the satellite zenith angle, c_i are regression coefficients, and T_{src} is an estimate of the water surface temperatures (generated using the MultiChannel Linear (MCSST) algorithm of [McClain et al., 1985]).

6.2 The Hydrodynamic Model

With methods in place to both radiometrically sharpen and atmospherically compensate thermal data, we can now discuss the second major thrust of this work. We wish to model the Genesee River plume using the ALGE hydrodynamic model. By adequately modeling the environment in and around the mouth of the Genesee, we can begin to describe the materials transport and sedimentation process occurring within this region.

In this section, we introduce the ALGE hydrodynamic model and explain how it can be used in conjunction with thermal data to accurately describe the environment. We begin by discussing in detail the inputs required by the ALGE model. Next, a section is provided that describes how a LUT of ALGE outputs can be developed prior to a collect to serve as a calibration tool for the model. An optimization routine that can be used to search the ALGE-generated LUT is introduced, which essentially calibrates the model. Finally, we conclude this chapter with a demonstration of the calibration process. The results of an experiment in which we model the Genesee river from July 2nd to July 13th, 2009 will be provided and the calibration techniques of this section will be demonstrated using Landsat 5 thermal data.

6.2.1 ALGE Inputs

As alluded in Section 3.4, the ALGE hydrodynamic model works by accepting environmental data as inputs to yield surface temperatures, flow rates, and sediment transport as outputs. We will now describe in detail the inputs as they relate specifically to our work. For this discussion, individual input parameters can be found in a file called **param.dat** and will be printed in italics while input files will be printed in bold. For further details on the ALGE hydrodynamic model, [Garrett, 1997] should be referenced.

The inputs to ALGE begin with the user describing the scene spatially. Figure 6.6 shows a true color Landsat 5 image of the Rochester Embayment located in the Northeastern United States. It is this region that we wish to model for our research as it includes the Genesee River plume. To describe this scene for ALGE, we must create two input files called **igrid.dat** and **idepth.dat**. The file **igrid.dat** should contain a grid of land and water cells that is representative of our scene while **idepth.dat** should contain a grid of equal size, but whose cells contain depths.



Figure 6.6: *Landsat 5 true color image of the Rochester Embayment, which includes the Genesee River plume.*

Figure 6.7 illustrates how the **igrid.dat** and **idepth.dat** files are created for a region of interest. To generate an **igrid.dat** file, bathymetry data can be thresholded based on the elevation at the land/water interface. Land cells are represented with 0's for pixels whose values are greater than the threshold and water cells are represented with 1's for pixels whose values are less than the threshold. Special cells such as marsh areas, source

areas, sink areas, and boundary regions can also be defined manually with 5's for marsh cells, 7's for source cells, 6's for sink cells, and 8's or 9's for boundary cells. The *grid spacing* associated with each cell is an input that indicates its ground sample distance (GSD) and the *number of nodes* represents the number of cells in **igrid.dat** for both the x- and y-directions.

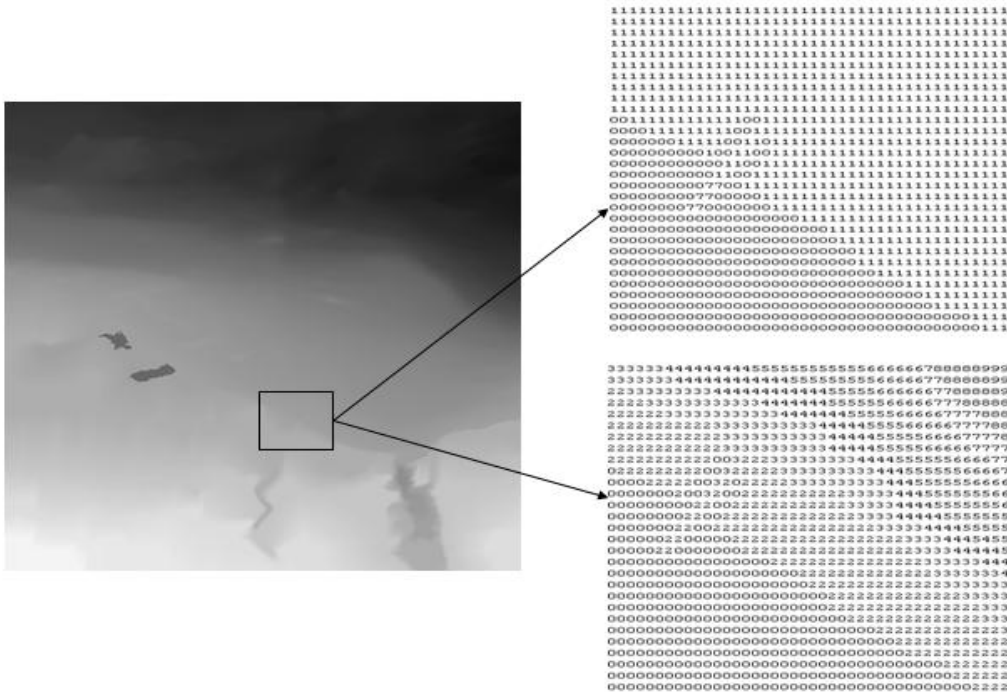


Figure 6.7: *Illustration of how bathymetry data can be used to generate the input files **igrid.dat** and **idepth.dat** for the ALGE Hydrodynamic model.*

Bathymetry data can also be used to create **idepth.dat**, see Figure 6.7. The version of ALGE code used in this research allows for 36 levels in the z-direction. By using the digits 0-9 and lowercase letters a-z, bathymetry data can be quantized into levels in order to create **idepth.dat**. The user must provide a *grid spacing* in the z-direction that represents the depth interval of each level. For our scene, the Rochester Embayment contains maximum depths of about 70 meters so our spacing for the bathymetry grid is set at 2 meters. Finally, *latitude* and *longitude* are specified to complete the description of the scene's geography.

With the scene's geography defined, we can now introduce the ALGE inputs that affect the plume's motion. Figure 6.8 shows the major energy inputs for a typical lake, [Li, 2007]. We can use this schematic as a guide to explain ALGE's remaining inputs. First ALGE requires upper air meteorological data over the area of interest. Sounding data must be provided as input in the form of temperature and precipitable water measurements in a file called **snd.dat**. This data is defined hourly at 11 different heights in the troposphere. The first input height is 100 meters above the surface. The next ten start at a height of 1 kilometer and are spaced at 1 kilometer intervals. Additionally, surface meteorological data must be provided in a file called **sfc.dat**. Wind speed and direction, dew point and temperature, barometric pressure, visibility and cloud ceiling must all be provided at hourly intervals. Depending on the accuracy of the initial inputs, many days (weeks) of meteorological data must be provided as input for the model to reach a steady state (i.e. A state in which the initial inputs are no longer driving the model).

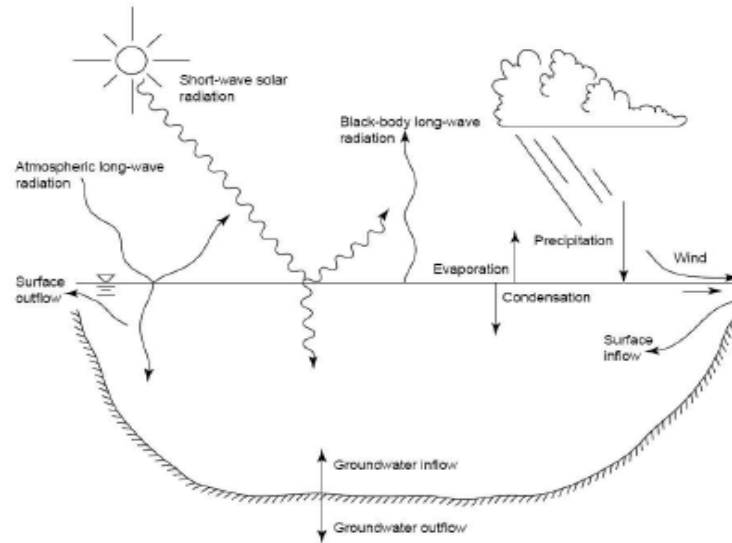


Figure 6.8: *Schematic of major energy inputs for a typical lake.*

The next group of inputs that will affect the plume's motion can be adjusted in **param.dat**. Inputs such as *Julian day*, *marsh roughness*, *surface roughness*, *boundary inflow/outflow temperatures*, and *source temperature* will all be specified to the model. In this work, the *source temperature* will be initiated using Landsat derived apparent temper-

atures obtained from the Genesee River plume. Additionally, *nudging* will be switched on for our simulations. Nudging refers to the manipulation of a small-area simulation based on large-area phenomenology. Specifically, when simulating the Genesee River plume we must account for the surface currents of Lake Ontario, which are mostly wind driven but also arise from phenomena such as tidal and/or Coriolis effects. By running a large-area model for the entire lake, we can determine its surface flow and apply these currents at the boundary of the small-area model for a more accurate representation of the plume's motion. Figure 6.9 shows the surface currents for a large-area simulation of Lake Ontario. These surface currents can be placed along the boundary of the small-area simulation and used as nudging vectors.

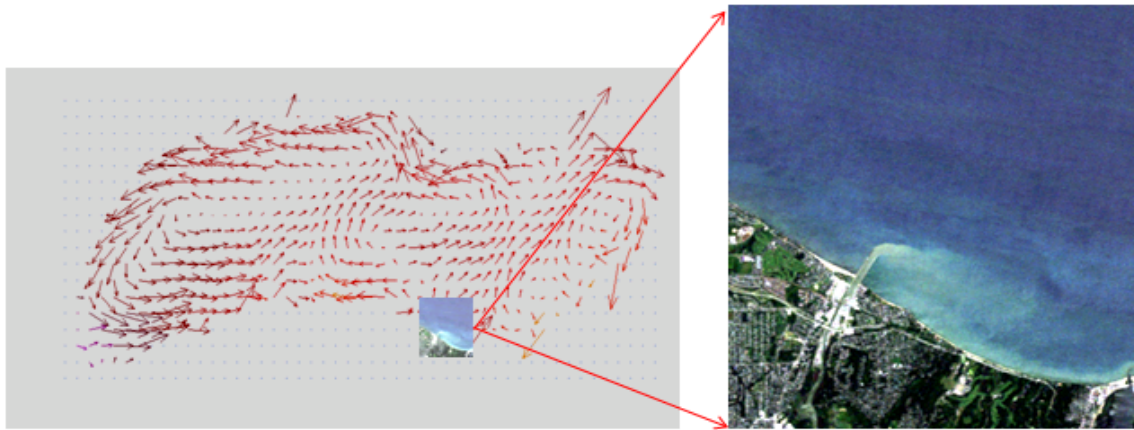


Figure 6.9: *Large-area simulation of Lake Ontario. The resulting surface currents can be used as nudging vectors for the small-area simulation.*

When *nudging* is included in a small-area simulation, two additional files must be provided as input to ALGE. First, **ndg.dat** should contain the hourly x- and y-nudging vectors for multiple points along the grid's boundary. A coarse resolution, Lake Ontario simulation was performed for this research for the summer months (5/1/09 – 8/31/09) using surface and upper-air meteorological data measured at the airport in Buffalo, NY. The cells had a GSD of 1.5 kilometers and the nudging vectors were recorded hourly.

Additionally, **wgtar.dat** is a file that contains weights for each node defined in **idepth.dat**. The idea behind nudging weights is that large scale surface currents will impact the small scale nodes differently based on the depth of the water (nudging vectors have a stronger

surface influence on deeper waters). Therefore, **wgtar.dat** is created by setting the weights equal to 0 at the shallowest grid points and increasing the weights fractionally to a value of 1 at the deepest grid points.

Next, we must be able to characterize the flow of the river. This can be done with a *mass source rate* that is *constant* or one that is *time-varying*. If the source rate is time-varying then hourly data that reflects this changing flow must be provided in a file called **flow.dat**. In this research, we collect river flow data with a sensor that is 6 miles upstream from the Genesee river mouth. By collecting data from an upstream sensor, we can avoid the effects of seiche. This enables us to obtain a more consistent representation of the river's true flow rate. Figure 6.10 shows a ten month comparison of the flow rate at the Charlotte Pump Station, which is within 1/2 mile of the river's mouth, and at the Ford Street bridge, which is six miles upstream. It appears that the overall flow rate of the two sensors are equal, especially over the summer months when a study of this nature would be conducted. This implies that the flow rate obtained at the Ford Street sensor is an adequate representation of the flow rate at the mouth of the Genesee.

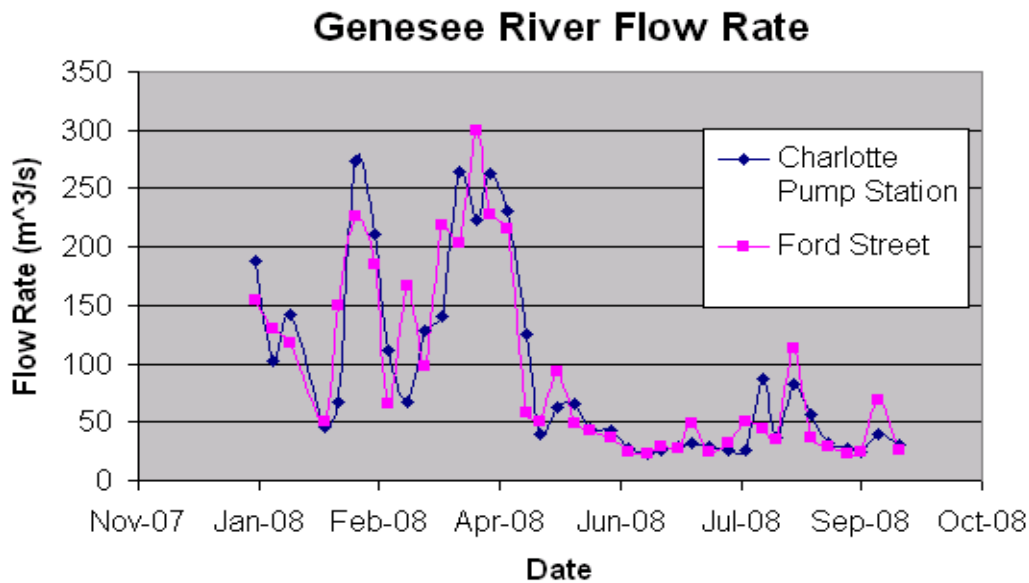


Figure 6.10: Comparison of the Genesee River's flow rate at two locations. The Charlotte Pump Station is within 1/2 mile of the river's mouth while the Ford Street sensor is six miles upstream.

Finally, ALGE allows for inputs that will affect the color of the plume such as the *particle density*, *particle diameter*, and *concentration* of river contaminants, i.e., suspended particles. These inputs can be defined based on in situ observations taken on the day of the collect or left as free parameters. In this work, we focus on the thermal properties of the plume, i.e., we want to correctly model the shape of the plume. Therefore, the color parameters are generic estimates for this study. With all inputs required by the hydrodynamic model defined, we can now run ALGE.

6.2.2 Calibrating the Hydrodynamic Model

6.2.2.1 Running ALGE

When all the inputs of the last section are defined, the ALGE hydrodynamic model can be executed. The model must be run for a sufficient number of simulation hours in order to achieve a steady state. In this application, an initial run of 200 hours seems adequate as one can observe the meteorological data take control of the model beyond this point. Figure 6.11 shows the surface temperature output from a simulation of 212 hours.

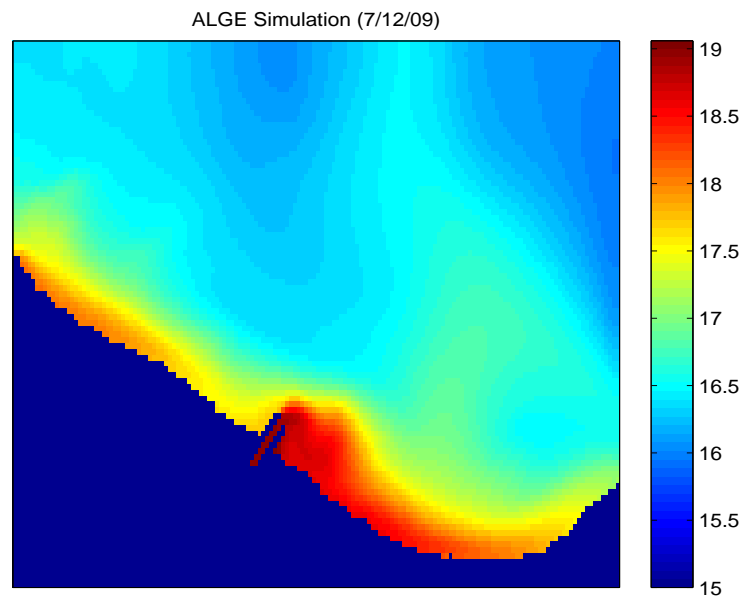


Figure 6.11: *ALGE* surface temperature output of the Rochester Embayment after 212 simulation hours. Land pixels were fixed at 15°C to show the contrast in water.

One can notice that the Genesee river plume is being pushed to the east by the westerly winds. This is a sign that the model is no longer being driven by its initial inputs but rather by the current meteorological data. Another indication that the model has reached a steady state can be observed with the use of animations. For this simulation, animations were used to view the surface temperature outputs on an hourly basis. The diurnal change in surface temperatures becomes evident as the simulation progresses, indicating that the model is being driven by the meteorological data.

6.2.2.2 Developing the Calibration LUT

Once the hydrodynamic model has reached a steady state, thermal data can be used to calibrate the model. To perform this calibration step, a LUT similar in concept to the one shown in Figure 3.14 will be generated by varying model parameters prior to a collect. Instead of three constituent parameters defining the axes of this LUT, however, the four environmental parameters that will have the greatest effect on the plume's shape (river flow rate, river temperature, wind speed, and wind direction) will define the axes. Associated with each point in this four parameter LUT will be a modeled image of the Rochester Embayment's surface temperatures, see Figure 6.12. As actual thermal data becomes available from the satellite, we can again use an optimization routine to search the LUT for the model that best matches the observed data.

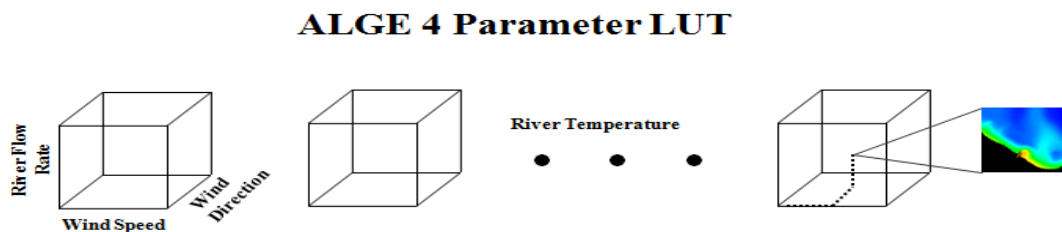


Figure 6.12: *Calibration LUT containing ALGE simulations.*

The development of the LUT in terms of running ALGE can be summarized as follows. We will run the model for at least a ten day period so the model can reach a steady state, i.e., a state in which the initial inputs are no longer influencing the model. At

least twenty four hours prior to a collect, the model will be stopped and the four input parameters described above will be adjusted. If each parameter is varied n different ways then the ALGE model must be rerun n^4 times, each run covering at least a twenty four hour simulation period. The end result of these n^4 runs will be a LUT with n^4 surface temperature images, one for each input parameter variation.

6.2.2.3 Calibrating ALGE Model Using Thermal Data

With a calibration LUT in place, thermal data that has been atmospherically compensated and registered to the simulated data can be used to calibrate the hydrodynamic model. Just as in Section 3.2.7, an optimization routine must be implemented to search the LUT for the input parameters whose modeled output most closely resembles the observed thermal data. Unlike the previous section, the cost function between the modeled and observed data is assumed to be highly nonlinear. Therefore, a nonlinear optimization routine will be used to search the LUT.

The nonlinear optimization method that we will use in this section was developed by [Coleman and Li, 1996] and is a built-in function in MATLAB. This method is a trust region approach for minimizing a nonlinear function subject to boxed bounds. At each iteration, this method approximates the cost function to a quadratic problem with the bound constraints defining the trust region size. The quadratic problem is solved using standard Newton methods.

6.2.2.4 Results

In this section, the results of an experiment that was designed to test the methods of this chapter are reported. Specifically, we wish to calibrate a hydrodynamic model through the use of remotely sensed thermal data. In doing so we will demonstrate our ability to atmospherically compensate thermal data, develop a calibration LUT, and use a nonlinear optimizer to search the LUT.

The scene that we wish to model in this study is shown in Figure 6.6. This image was collected from the Landsat 5 instrument at approximately noon on July 13, 2009. To model the Genesee River plume in this scene, the ALGE hydrodynamic model is initialized with input data from July 2nd at midnight local time and run until July 12th to achieve a

steady state. At 4am on July 12th, the model is halted and the relevant input parameters varied. Table 6.1 shows the parameters that will be adjusted for this study.

Wind Speed(%)	Wind Direction(deg.)	River Rate(%)	River Temp.(C)
20	-50	50	17
60	-30	70	19
100	-10	90	21
140	10	110	-
180	30	130	-
-	50	150	-

Table 6.1: *ALGE input parameters; variation from observed, nominal value.*

The nominal observations will be adjusted for every combination of these parameters and submitted to ALGE for a 33 hour simulation period. For example, let's consider the parameter variation (wind speed, wind direction, flow speed, flow temperature)=(60, -30, 70, 19). With this quadruplet, 60% of the observed hourly wind speeds will be used in place of the nominal hourly values in **sfc.dat**. Similarly, 30 degrees will be subtracted from each of the nominal hourly wind direction measurements that are reported in **sfc.dat**. In flow.dat, 70% of the observed nominal hourly flow measurements will be used as input. Lastly, mass source temperature will be initiated at 19°C in **param.dat**. Upon running the model for this quadruplet, the output of surface temperatures will be archived into the four-parameter LUT at the coordinate (60, -30, 70, 19). This process will be repeated for all combinations of the parameters in Table 6.1.

Finally, the observed thermal data for this scene will be atmospherically compensated and registered to the modeled data. The optimization routine can then be used to find the input parameters whose corresponding modeled surface temperatures most closely match the satellite's observed surface temperatures. In this research, we are primarily interested in determining the environmental parameters whose model most accurately characterizes the shape of the Genesee River plume. Therefore, only a 1x2 kilometer subimage which includes the plume will be registered to the modeled data and used in the optimization process. Figure 6.13 shows the atmospherically compensated Landsat 5 data and a subimage of the Genesee River plume. The subimage is displayed in color coded RGB and the land pixels have been fixed at 16°C to show the temperature contrast in the water. It is with this smaller region that we will perform the optimization.

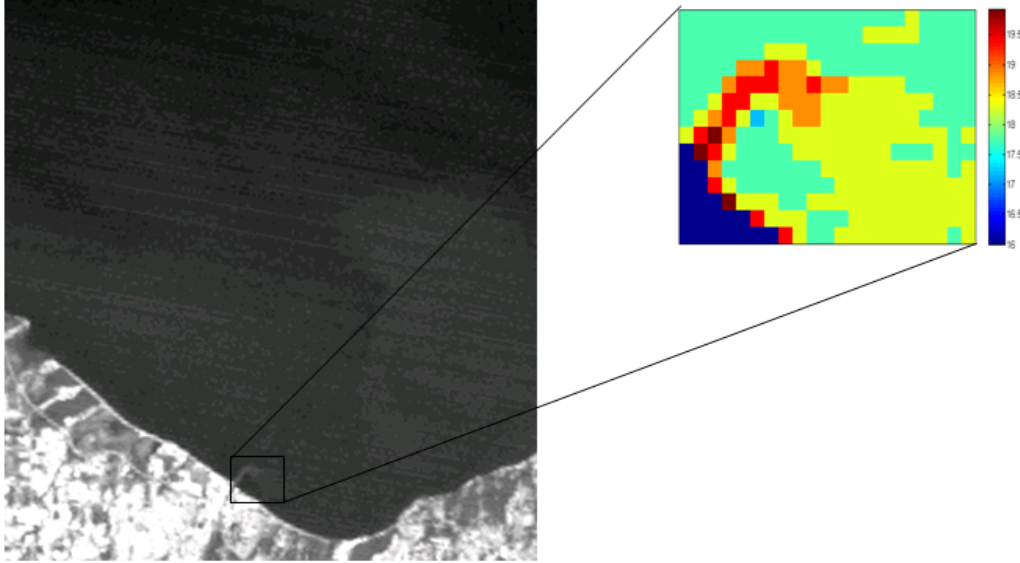


Figure 6.13: (Left) Atmosphericly compensated Landsat 5 thermal data which was collected on July 13, 2009. (Right) RGB subimage to be used in optimization process. Land pixels have been fixed at 16°C in the subimage to show the temperature contrast in the water pixels.

To perform the optimization process, the imaged data must first be registered to the modeled data. Figure 6.14 shows the imaged data and one of the model outputs of the Genesee River plume region that was arbitrarily chosen from the ALGE LUT (recall Figure 6.12).

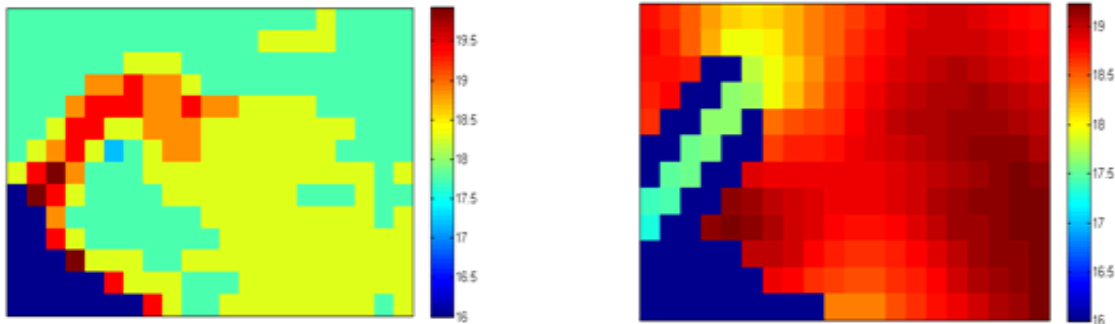


Figure 6.14: Real data (left) that is to be registered to modeled data (right).

To register the two forms of data, control points were hand selected along the pier and a simple affine transform was performed to warp the imaged data onto the modeled data. Additionally, a mask was created in an effort to block mixed pixels from being included in the optimization process. These mixed land and water pixels typically appear along the shore or up-river and must be excluded from the analysis as the atmospheric compensation method used in this process is valid for only pure water pixels. The registered and masked image data that was used to search the LUT is shown in Figure 6.15.

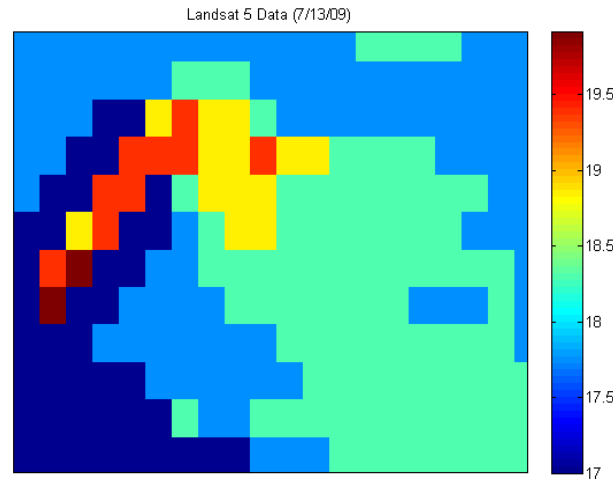


Figure 6.15: *Result of registering the two forms of data shown in Figure 6.14 and masking mixed pixels.*

With registered and masked data, the optimization routine can finally be used to determine the parameters whose corresponding modeled surface temperatures provide the closest match to the real data. Figure 6.16 shows the modeled output (Right) that was chosen from the LUT using the Landsat thermal data (Left) of Figure 6.15. Its corresponding parameter quadruplet is (wind speed, wind direction, flow speed, flow temperature)=(88.9, 6.1, 61.8, 19.5).

This quadruplet indicates that the satellite data most closely resembles the modeled data whose wind speed inputs are 88.9% of the observed nominal values, whose wind direction inputs have 6.1 degrees added to the nominal values, whose flow rate inputs are 61.8% of the observed nominal flow measurements, and whose river temperature input is initiated at 19.5°C. Considering the nominal quadruplet is approximately (100, 0, 100, 19),

with the exception of the river flow rate, the optimization process has found a model whose parameters are close to the nominal values. Additionally, the two plumes of Figure 6.16 appear to have the same shape, which is really the desired result.

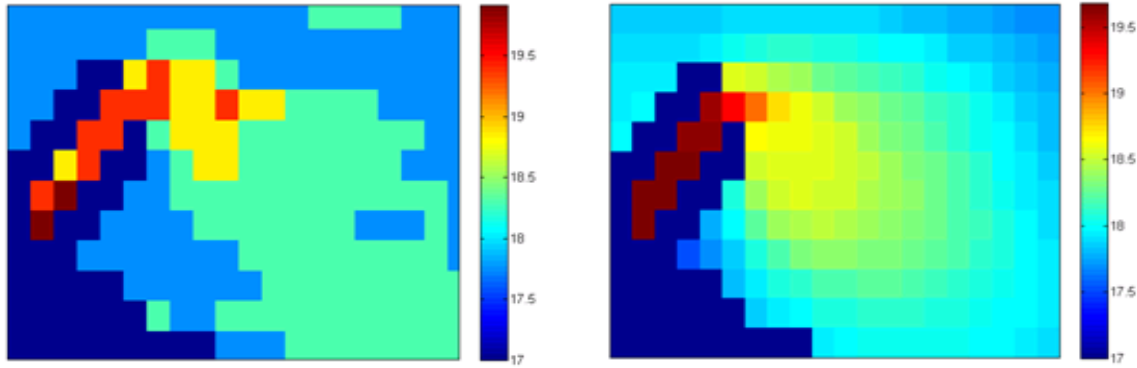


Figure 6.16: *Modeled thermal data (Right) whose surface temperatures most closely resembled the Landsat 5, satellite data (Left). The model's corresponding parameter quadruplet is (wind speed, wind direction, flow speed, flow temperature) = (88.9, 6.1, 61.8, 19.5).*

In an RMS-sense, the error between the two datasets is 0.28 Kelvin. This indicates that on a pixel-by-pixel basis we can expect an average error of about 0.28 Kelvin between the modeled data and the real data. This error can be attributed to a couple of factors. First is our ability to accurately model the region of interest. Providing ALGE with precise nominal inputs is essential to the success of the calibration process. Secondly, model calibration error will inherently exist in the observed thermal data. Referring again to Figure 6.16 one may notice that the real data (Left) is quantized while the modeled data (Right) takes on a continuous range of values. In fact, this Landsat data is quantized every 0.55 Kelvin so if we assume for a moment that the modeled pixels have temperatures that are uniformly distributed then a calibration error of 0.28 Kelvin can be attributed almost entirely to the Landsat data.

In some applications, it may be necessary to obtain surface temperatures for the entire scene. For instance, if LDCM is not equipped with the TIRS instrument then one may have to first perform the thermal calibration process with MODIS thermal data, then restart ALGE with the optimized surface temperatures, and finally run the model until LDCM's OLI data becomes available. To obtain the surface temperature input required

for an ALGE restart we can simply use the full model domain associated with the plume optimized quadruplet. Figure 6.17 shows the Landsat 5 data (Left) and the modeled data (Right) associated with the plume optimized quadruplet (88.9, 6.1, 61.8, 19.5).

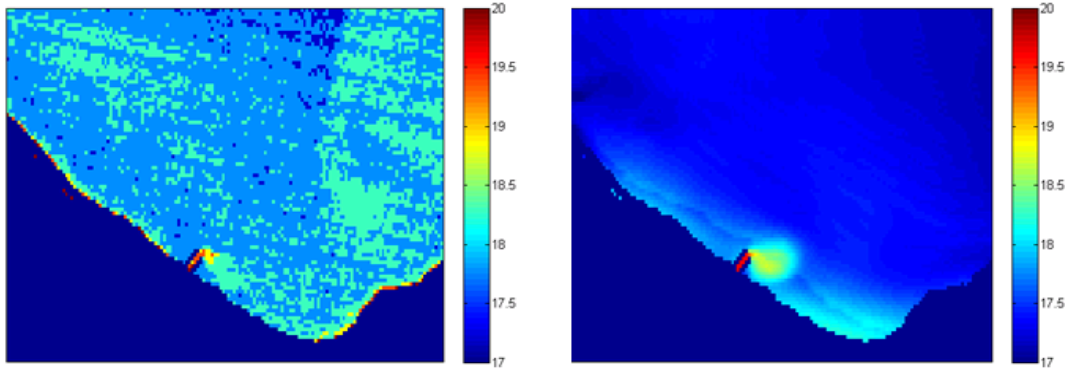


Figure 6.17: *Modeled thermal data (Right) chosen from LUT using plume optimization and Landsat 5, satellite data (Left).*

When comparing these two data on a pixel-by-pixel basis, the RMS-error increases from 0.28 Kelvin for the plume region to 0.64 Kelvin for the entire region. This indicates that, as expected, using the plume region optimization to optimize the entire region comes at a cost. To reduce this RMS-error, the ALGE calibration process may need to be done on the entire scene. However, difficulties in registration may preclude this as a possibility. To combat the registration issues encountered in this work, the **igrid.dat** and **idepth.dat** files for future runs should be created directly from the Landsat data. A simple threshold in Landsat's SWIR band can be used to create **igrid.dat**. Then, the bathymetry data shown in Figure 6.7 can be spatially resampled to **igrid.dat** to obtain **idepth.dat**. Defining these two input files in this fashion avoids the need for registration.

It should be noted that the error introduced by the optimization process does not represent the total error between actual surface temperatures and optimized surface temperatures. In fact other factors will contribute to this total error. For instance, [Padula, 2008] claims that with radiosonde data, the compensation routine described in this work is accurate to within 0.6 Kelvin. Therefore, we can expect that temperature errors will exist between actual surface temperatures and optimized surface temperatures even if the optimization process performs perfectly and our sensor is accurately calibrated.

6.3 Concluding Remarks

In this chapter, the techniques required to calibrate a hydrodynamic model using remotely sensed data were discussed. Thermal sensors that are suitable for the calibration process were introduced and a radiometric sharpening technique described which effectively increases the resolution of thermal data to the 30 meter resolution of Landsat's reflective bands. Finally, a model of the Genesee River plume was simulated for July 13, 2009 and Landsat 5 thermal data was used to calibrate the model's surface temperature output. An RMS-error of 0.28 Kelvin was obtained between the observed data and modeled data when a local area around the plume was used to perform the calibration.

The process described in this chapter illustrates how Landsat thermal data can be used to effectively calibrate a hydrodynamic model. Landsat reflective data can be used to further calibrate the model but represents a much more involved process. A summary of the work described in this dissertation as well as recommendations that will facilitate the implementation of reflective data in the calibration process are discussed in Chapter 7.

Chapter 7

Summary and Recommendations

7.1 Summary

Over thirty years ago, the remote sensing of ocean color from space began with the successful launch of NASA's Coastal Zone Color Scanner (CZCS). Expectations for this sensor were modest as it was designed to show that ocean color measurements could be used to determine chlorophyll and sediment concentrations in the open ocean (case 1 waters). Three decades later, the advancement of sensor technology has enabled the remote sensing community to push the envelope with regards to the problems that can be solved from space. Our ability to efficiently monitor optically complex case 2 waters has opened the door for a broad range of new problems to be solved with satellites. The development of the Operational Land Imager (OLI) and the Thermal InfraRed Sensor (TIRS) represents the most recent advancement in technology that should provide the water resource community with a state-of-the-art instrument which is ideal for monitoring the global water supply.

The ability to describe the sedimentation process occurring in and around the mouth of a river through the use of satellite imagery is an ongoing area of research. Remotely sensed thermal data has historically been used to describe the surface temperatures of a water body and reflective data to determine water color. Both forms of data, however, fail to describe the condition of the water at any depth and its flow over time. Hydrodynamic models are valuable tools that can be used to simulate river flow and material transport but tend to be inaccurate without precise environmental inputs. Landsat's high resolution OLI and TIRS instruments are ideal sources of data that can serve as tools to calibrate

hydrodynamic models.

Landsat instruments have traditionally been true to their name. They are ideal for land-based studies but have historically lacked the radiometric fidelity necessary for water-based research. In this work, the potential for using Landsat's new OLI instrument for the retrieval of water quality parameters was investigated. Specifically, we determined that the addition of a new aerosol blue band, a 12-bit quantizer, and improved signal-to-noise ratios enables the OLI instrument to be a state-of-the-art technology with regards to the constituent retrieval process. As a result, it was an ideal sensor to be used throughout this research.

In support of our desire to use OLI in this work, two over-water atmospheric compensation algorithms were developed for this instrument. Traditional compensation algorithms designed for multispectral sensors take advantage of 2 bands in the NIR to determine the atmospheric parameters contained within an image. Since OLI has only 1 band in the NIR, traditional algorithms are not suitable for compensating its data. Much of this research focused on the development of one compensation algorithm that uses OLI's Aerosol Blue band and another which uses a band ratio technique with the NIR/SWIR bands to determine the atmospheric parameters contained within a scene. Its ability to atmospherically compensate data was demonstrated with great success on both real and synthetic data.

Finally, our ability to calibrate a hydrodynamic model with thermal data was demonstrated. A model of the Genesee River plume in Rochester, NY was simulated for July 13, 2009. After preprocessing Landsat 5 thermal data to account for atmospheric effects and registration issues, it was successfully used to calibrate the shape of the river plume which was simulated using the ALGE hydrodynamic model.

7.2 Future Work

The ultimate goal of this research, including present and future work, is to use reflective and thermal data to calibrate a hydrodynamic model in an effort to describe the sedimentation process occurring within a river plume. The methods developed in this work facilitate the use of reflective data in the calibration process, which was developed and demonstrated using thermal data. As these methods were designed with the ultimate research goals in

mind, recommendations for the next few years of the project can be made.

First, one's ability to calibrate a hydrodynamic model using reflective data hinges on their ability to compensate for the atmosphere. Although we have demonstrated through several experiments the efficiency of OLI's atmospheric compensation algorithms in this dissertation, there may be an opportunity to further reduce retrieval errors. OLI's Blue Band method makes use of band 1 and band 6 to compensate for the atmosphere while the Band Ratio method makes use of band 5 and band 6. Perhaps all three bands can be used to obtain a more efficient and accurate compensation algorithm.

A second recommendation for future work can be made regarding the nature in which we calibrate the hydrodynamic model. In order to make a calibration LUT, a whole-lake simulation of Lake Ontario was conducted in an effort to determine the nudging vectors that would drive the flow of the small-scale simulation. Due to limitations in the current ALGE code, surface data was gathered from a single location (the airport in Buffalo, NY) and used as input for the entire lake model. Moving forward in this research, one should look into the possibility of using multiple input locations for the whole-lake simulations. Multiple surface data input nodes will most certainly ensure a more accurate representation of surface flow for the small-scale model.

Additionally, the whole-lake simulation conducted in this work used only the Niagara River as a source. Secondary sources such as the Genesee River can be included to enhance the model. As it was, adequate results were obtained with the current whole-lake simulation model so adding these recommendations can only improve one's ability to characterize surface flow.

Lastly, a suggestion regarding the calibration of the hydrodynamic model using reflective data can be made. This research tackles the issues of identifying an appropriate sensor to be used for the constituent retrieval process and developing an atmospheric compensation algorithm which enables radiance signals to be represented in the reflectance domain. We avoid the calibration of the hydrodynamic model, however, due to the nature in which it outputs data. Unlike the thermal domain where ALGE outputs surface temperatures, in the reflective domain ALGE outputs sediment profiles. In order to use satellite reflective data to calibrate the model, these sediment profiles must be converted to water-leaving reflectances. The Hydrolight in-water radiative transfer code can be used to do this for a

single profile but the ALGE outputs will consist of millions of profiles.

For example, suppose one wishes to develop a calibration LUT for reflective data that is similar to the thermal calibration LUT used in this research. To do this, approximately 500 simulations will be conducted each containing 100,000 profiles. This would require submitting 50 million profiles to Hydrolight, which is not feasible. To reduce this number, one should note that it is likely many of the profiles will contain similar levels of sediment. A quantization scheme can be developed that essentially reduces the range of sediment values allowed in each level. By performing this quantization step, identical profiles will arise (only 1 of which needs to be submitted to Hydrolight). With a reduced set of profiles, high-throughput computing, i.e., Sun-Grid Engine (SGE) can be used to greatly reduce the run times. This scheme will avoid the need to sample the plume and perform a spatial interpolation.

These recommendations are provided to facilitate the fusion of thermal and reflective data in an effort to calibrate a hydrodynamic model using remotely sensed data. This work assumes that the two forms of data are collected on the same platform and that the data are registered. If this is the case then the thermal data can be used first to calibrate the shape of the river plume while the reflective data can be used to next calibrate its color. The end result of this calibration process is a three dimensional description of a river plume.

Appendix A

Determining Exoatmospheric Irradiance

To approximate the Earth's exoatmospheric irradiance, we begin by assuming that the Sun is a perfect 5800-Kelvin blackbody. Making this assumption allows us to use the Stefan-Boltzmann equation to conclude that the total exitance from the solar surface is

$$M = \sigma T^4 = 6.42 \times 10^7 \left(\frac{w}{m^2} \right), \quad (\text{A.1})$$

where $\sigma = 5.67 \times 10^{-8} \left(\frac{w}{m^2 K^4} \right)$ is the Stefan-Boltzmann constant. By the definition of exitance, we can easily conclude that the total flux from the Sun is

$$\Phi = M \times A = M \times 4\pi r_s^2 = \left(6.42 \times 10^7 \right) \left(4\pi \left(695.5 \times 10^6 \right)^2 \right) = 3.9 \times 10^{26}(w), \quad (\text{A.2})$$

where $r_s = 695.5 \times 10^6 m$ is the radius of the Sun. Now, if we assume that this total flux originates from a point source which is located at the center of the Sun, we can use the mean Earth-Sun distance of $r_{es} = 149.5 \times 10^9 m$ to conclude that the Earth's exoatmospheric irradiance is

$$E_{ex} = \frac{3.9 \times 10^{26}}{4\pi(149.5 \times 10^9)^2} = 1390 \left(\frac{w}{m^2} \right). \quad (\text{A.3})$$

This result gives an integrated value for total energy per unit area. In fact it is the integration across all wavelengths of the curve found in Figure 3.1. Therefore, this value is of little use when we wish to confine our work to a certain portion of the EM-spectrum. When this is the case, we must use the spectral exoatmospheric irradiance in our calculations.

Appendix B

Development of Basics IOP's of Water

This treatment develops a few basic inherent optical properties (IOPs) of water. Expressing the properties of water in this form allows us to describe how light is attenuated in the medium.

We begin by observing the geometry in Figure B. If a monochromatic beam with power $\Phi_i(\lambda)$ is incident on an arbitrary volume of water, one of three events may occur. A fraction of the power may be absorbed $\Phi_a(\lambda)$ by the water. Another fraction may be scattered $\Phi_s(\lambda)$ at an angle ψ . Finally, the remaining power can be transmitted $\Phi_t(\lambda)$ through the medium.

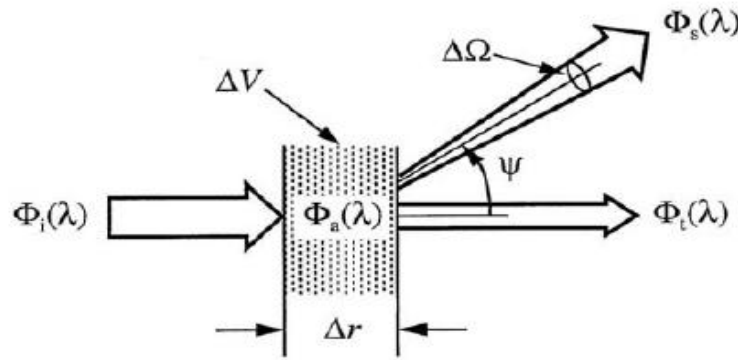


Figure B.1: *Geometry used to define inherent optical properties.*

Assuming that inelastic scattering does not occur, then by Conservation of Energy we can conclude that

$$\Phi_i(\lambda) = \Phi_a(\lambda) + \Phi_s(\lambda) + \Phi_t(\lambda). \quad (\text{B.1})$$

The fraction of incident power that undergoes each of these three processes can be quantified by noting the following definitions: The *spectral absorptance* is the fraction of the incident power that is absorbed by the water volume

$$A(\lambda) = \frac{\Phi_a(\lambda)}{\Phi_i(\lambda)}. \quad (\text{B.2})$$

The *spectral scatterance* is the fraction of the incident power that is scattered out of the beam

$$B(\lambda) = \frac{\Phi_s(\lambda)}{\Phi_i(\lambda)}. \quad (\text{B.3})$$

The *spectral transmittance* is the fraction of the incident power that is transmitted through the water volume

$$T(\lambda) = \frac{\Phi_t(\lambda)}{\Phi_i(\lambda)}. \quad (\text{B.4})$$

In the spirit of calculus, the three previous definitions are not complete until we investigate their behavior as the volume of water becomes arbitrarily small. This concept leads us to our first two IOPs. The *spectral absorption coefficient* is defined as

$$a(\lambda) = \lim_{\Delta r \rightarrow 0} \frac{A(\lambda)}{\Delta r}. \quad (\text{B.5})$$

The *spectral scattering coefficient* is defined as

$$b(\lambda) = \lim_{\Delta r \rightarrow 0} \frac{B(\lambda)}{\Delta r}. \quad (\text{B.6})$$

These two IOPs essentially place a magnitude on the absorption and scattering processes occurring within an infinitesimally small volume of water. We can note that the *total beam attenuation* is just the sum of these two coefficients,

$$c(\lambda) = a(\lambda) + b(\lambda). \quad (\text{B.7})$$

At this point, our description of absorption is complete. When monochromatic light enters a volume of water and gets absorbed, there is no need to pursue the photons any further (at least not in this analysis). If the same monochromatic light enters a volume of water and is scattered, however, simply knowing the magnitude of the scatter is an incomplete description of the process. If we, for a moment, extend the definition of spectral scatterance in Equation B.3 to include the angular distribution of the scatter, our description of the process can be completed.

Assume that a fraction of the incident power from Figure B is scattered through an angle ψ into a solid angle of $\Delta\Omega$. Then the angular scatterance per unit distance can be defined as

$$\beta(\psi; \lambda) = \lim_{\Delta r \rightarrow 0} \lim_{\Delta\Omega \rightarrow 0} \frac{B(\psi; \lambda)}{\Delta r \Delta\Omega} = \lim_{\Delta r \rightarrow 0} \lim_{\Delta\Omega \rightarrow 0} \frac{\Phi_s(\psi; \lambda)}{\Phi_i(\lambda) \Delta r \Delta\Omega} \quad (\text{B.8})$$

This definition simply describes the scattering process that occurs for light incident on an infinitesimally small volume of water that gets scattered through an infinitesimally small solid angle. If we observe all angles of ψ , a scattering function develops. Interestingly, by dividing Equation B.8 over all solid angles, we obtain the volume's scattering coefficient in Equation B.6. Finally, if we normalize Equation B.8 by Equation B.6 we observe

$$\tilde{\beta}(\psi; \lambda) \equiv \frac{\beta(\psi; \lambda)}{b(\lambda)}. \quad (\text{B.9})$$

The above equivalency describes the *spectral volume scattering phase function*. This is an important IOP that not only describes the angular distribution of the scatter but also

incorporates its magnitude. These phase functions are always circularly symmetric about their incident angles as shown in Figure B.2. A more thorough treatment of the IOPs and AOPs of water can be found in [Mobley, 1994].

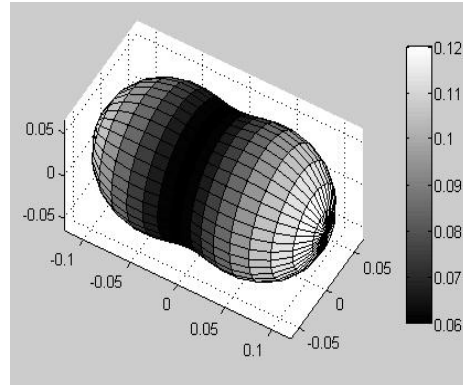


Figure B.2: *Example of scattering phase function for pure water.*

Appendix C

Sensor Characteristics

This appendix provides sensor characteristics for the various instruments used throughout this research and is specifically intended to supplement this work. Due to the nature of water, the spatial characteristics of the sensors can be ignored and a focus placed on their radiometric qualities. Accordingly, this appendix emphasizes the spectral coverage, quantization, and SNR requirements associated with the AVIRIS, ETM+, and OLI instruments. The spectral response function of the SeaWiFS sensor is also included in this appendix since atmospheric compensation techniques designed for this instrument are discussed in this research. References are provided for those requiring a more detailed treatment of the sensors' characteristics.

C.1 Spectral Response

This section describes the spectral response functions of the instruments used in this work. The complete spectral responses of ETM+ and OLI are provided in table form. Additionally, bands relevant to this work are plotted for each sensor to illustrate the spectral coverage that was included in the sensor models.

C.1.1 ETM+

Table C.1 shows the salient characteristics for the seven reflective bands and one thermal band of the ETM+ sensor [ETM Manual, 2003]. To simulate the spectral response of ETM+, text files were obtained directly from the Landsat 7 Users Guide Handbook website

[NASA, 2006] and incorporated into the model.

Band (#)	Bandpass (μm)	Spatial Resolution (Meters)	NED ρ	NEDT (K@300K)
1	0.452 – 0.514	30	0.19	-
2	0.519 – 0.601	30	0.15	-
3	0.631 – 0.692	30	0.19	-
4	0.772 – 0.898	30	0.14	-
5	1.547 – 1.748	30	0.18	-
6	10.31 – 12.36	60	-	0.22
7	2.065 – 2.346	30	0.28	-
8 (pan)	0.515 – 0.896	15	0.39	-

Table C.1: *L7 ETM+ Salient Characteristics.*

A plot of the spectral response for bands 1 through 4 of the ETM+ instrument is shown in Figure C.1. These four VNIR bands were incorporated into the ETM+ model in an effort to study the effects of spectral coverage on the constituent retrieval process, (Section 5.1.1).

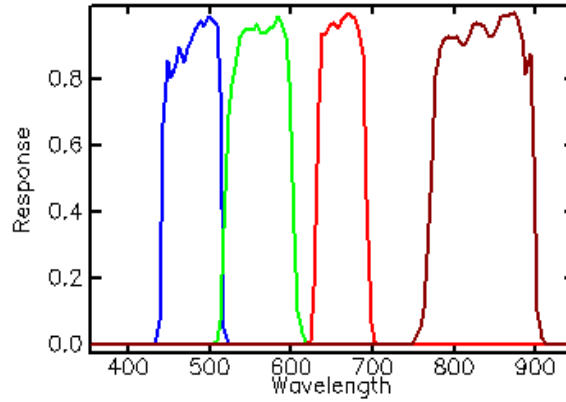


Figure C.1: *ETM+ response function vs. wavelength(nm)*

C.1.2 OLI

To incorporate the spectral response of the OLI sensor, Table C.2 was obtained from the LDCM Requirements Manual [LDCM Manual, 2006]. Although OLI's spectral response is not available in text form (as was the case with ETM+), the assumption was made that OLI's spectral response is similar to that of ETM+. This is a valid assumption for the

Blue, Green, and Red bands of OLI as can be seen by comparing Table C.1 and Table C.2. That being said, special attention was paid to the fact that OLI has a narrow Coastal Aerosol band 1, a narrow NIR band 5, and a relatively narrow SWIR band 6 (Note that bands 7, 8, and 9 were not used in this research).

#	Band	Center Wavelength (nm)	Minimum Lower Band Edge (nm)	Maximum Upper Band Edge (nm)
1	Coastal Aerosol	443	433	453
2	Blue	482	450	515
3	Green	562	525	600
4	Red	655	630	680
5	NIR	865	845	885
6	SWIR 1	1610	1560	1660
7	SWIR 2	2200	2100	2300
8	Panchromatic	590	500	680
9	Cirrus	1375	1360	1390

Table C.2: *OLI Spectral Bands.*

To create band 1, band 5, and band 6 for the OLI sensor model, values were hand selected in accordance to the requirements described in [LDCM Manual, 2006]. Figure C.2 shows the resulting spectral response of the OLI sensor in the VNIR portion of the EM-spectrum.

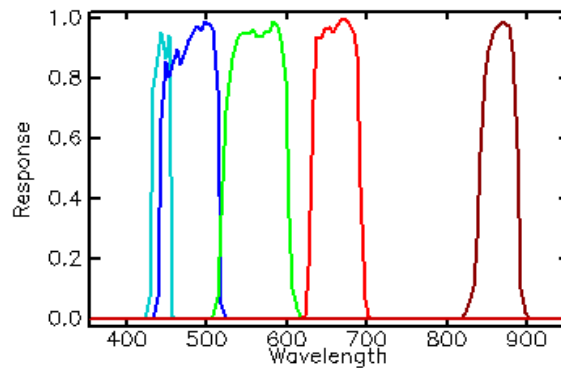


Figure C.2: *OLI VNIR response function vs. wavelength(nm).*

Notice that band 5 of OLI is much narrower than the corresponding NIR band of ETM+ shown in Figure C.1. Additionally, OLI has the narrow Aerosol Blue band centered at 443 nanometers. Figure C.3 shows the OLI spectral response with the SWIR band (band 6)

included. Although this band is excluded from the initial OLI study of Section 5.1.1, it will prove useful for the atmospheric compensation routines and glint removal techniques described in Chapter 4.

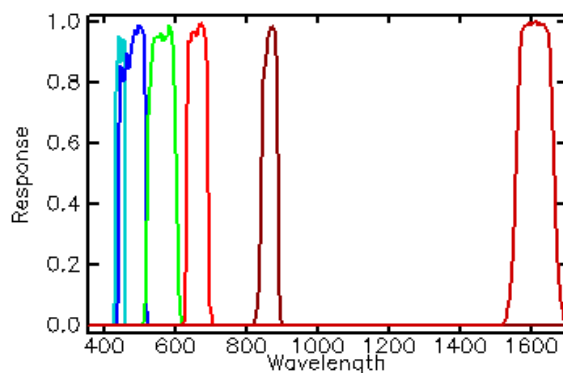


Figure C.3: *OLI VNIR/SWIR response function vs. wavelength(nm).*

C.1.3 AVIRIS

Sensor specifications for the Airborne Visible/Infrared Imaging Spectrometer (AVIRIS) can be obtained from the AVIRIS homepage [JPL, 2006]. AVIRIS is a hyperspectral sensor that uses a whiskbroom technology to collect 224 contiguous bands of data from 380 nanometers to 2500 nanometers. When flown at 20 kilometers, AVIRIS has a spatial resolution of 20 meters.

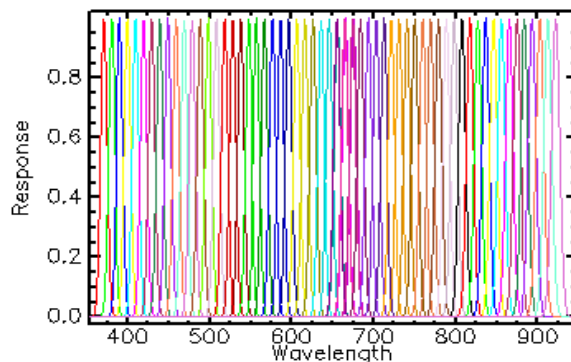


Figure C.4: *AVIRIS VNIR response function vs. wavelength(nm).*

To model the sensor response function of AVIRIS, the bands are assumed to be gaussian with a 10 nanometer bandwidth (the full width at half maximum (FWHM)). In this research, header files accompanied the *May* 20, 1999 dataset so the AVIRIS spectral response function shown in Figure C.4 was obtained by fitting a gaussian to the corresponding band center and FWHM data. This figure shows the 61 bands in the VNIR portion of the EM-spectrum that were used to model the AVIRIS spectral response. Clearly this instrument's spectral coverage is superior to that of ETM+ and OLI.

C.1.4 SeaWiFS

Section 4.2.2.2 and Section 4.2.2.3 describe over-water atmospheric compensation techniques that were designed for the SeaWiFS sensor. In support of these algorithms, Table C.3 describes the bands of SeaWiFS and their primary uses.

#	Primary use	Center Wavelength (nm)	Bandwidth (nm)
1	Dissolved organic matter	412	20
2	Chlorophyll absorption	443	20
3	Pigment absorption	490	20
4	Chlorophyll absorption	510	20
5	Sediments	555	20
6	Atmospheric correction	670	20
7	Atmospheric correction	765	40
8	Atmospheric correction	865	40

Table C.3: *SeaWiFS Spectral Bands.*

The spatial resolution of the SeaWiFS bands are 1 kilometer so this instrument is not used directly in this work. However, the methods used to atmospherically compensate its data were instrumental in the development of the techniques used in the OLI atmospheric compensation algorithms. The spectral response function of this instrument is shown in Figure C.5 for reference. Additional specifications for the SeaWiFS instrument can be obtained from [Mueller and Austin, 1995].

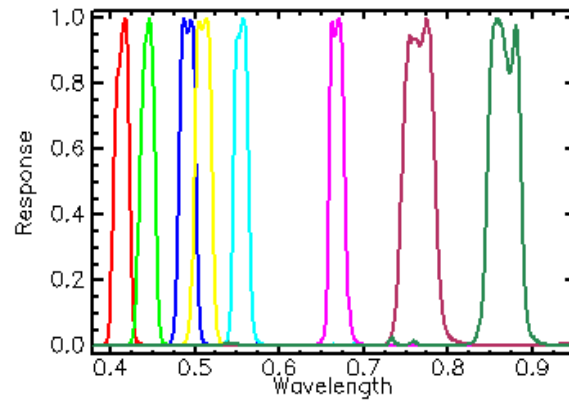


Figure C.5: *SeaWiFS VNIR response function vs. wavelength (μm).*

C.1.5 MODIS

In support of the thermal work described in Chapter 6, the spectral coverage of MODIS is shown in Figure C.6 and Figure C.7. The MODIS thermal bands (bands 31 and 32) can be used in this work as supplemental data in the event that TIRS data and NPOESS data are not available.

Primary Use	Band	Bandwidth ¹	Spectral Radiance ²	Required SNR ³
Land/Cloud/Aerosols Boundaries	1	620 - 670	21.8	128
	2	841 - 876	24.7	201
Land/Cloud/Aerosols Properties	3	459 - 479	35.3	243
	4	545 - 565	29.0	228
	5	1230 - 1250	5.4	74
	6	1628 - 1652	7.3	275
	7	2105 - 2155	1.0	110
Ocean Color/Phytoplankton/Biogeochemistry	8	405 - 420	44.9	880
	9	438 - 448	41.9	838
	10	483 - 493	32.1	802
	11	526 - 536	27.9	754
	12	546 - 556	21.0	750
	13	662 - 672	9.5	910
	14	673 - 683	8.7	1087
	15	743 - 753	10.2	586
	16	862 - 877	6.2	516
Atmospheric Water Vapor	17	890 - 920	10.0	167
	18	931 - 941	3.6	57
	19	915 - 965	15.0	250

Figure C.6: *MODIS bands with a description of their primary uses.*

Primary Use	Band	Bandwidth ¹	Spectral Radiance ²	Required NE(delta)T(K) ⁴
Surface/Cloud Temperature	20	3.660 - 3.840	0.45(300K)	0.05
	21	3.929 - 3.989	2.38(335K)	2.00
	22	3.929 - 3.989	0.67(300K)	0.07
	23	4.020 - 4.080	0.79(300K)	0.07
Atmospheric Temperature	24	4.433 - 4.498	0.17(250K)	0.25
	25	4.482 - 4.549	0.59(275K)	0.25
Cirrus Clouds Water Vapor	26	1.360 - 1.390	6.00	150(SNR)
	27	6.535 - 6.895	1.16(240K)	0.25
	28	7.175 - 7.475	2.18(250K)	0.25
Cloud Properties	29	8.400 - 8.700	9.58(300K)	0.05
Ozone	30	9.580 - 9.880	3.69(250K)	0.25
Surface/Cloud Temperature	31	10.780 - 11.280	9.55(300K)	0.05
	32	11.770 - 12.270	8.94(300K)	0.05
Cloud Top Altitude	33	13.185 - 13.485	4.52(260K)	0.25
	34	13.485 - 13.785	3.76(250K)	0.25
	35	13.785 - 14.085	3.11(240K)	0.25
	36	14.085 - 14.385	2.08(220K)	0.35
¹ Bands 1 to 19 are in nm; Bands 20 to 36 are in μm ² Spectral Radiance values are ($\text{W/m}^2 \cdot \mu\text{m} \cdot \text{sr}$) ³ SNR = Signal-to-noise ratio ⁴ NE(delta)T = Noise-equivalent temperature difference				

Figure C.7: MODIS bands with a description of their primary uses.

C.2 SNR and Quantization Requirements

This section provides the relevant information needed to model noise and quantization effects as described in Section 5.1.1. In order to determine the quantization resolution in the reflective domain (r_{Q_i} in Equation 5.4), the saturation radiances for each band must first be obtained to calculate the quantization resolution in the radiance domain (L_{Q_i}). Similarly, in order to calculate the amount of random noise that will be applied to a signal in the reflectance domain (N_{r_i} in Equation 5.1), the corresponding noise in the radiance domain (N_{L_i}) must first be calculated. This appendix provides the tables necessary to perform these calculations for the ETM+ and OLI sensors.

C.2.1 ETM+

ETM+ is equipped with an 8-bit quantizer that effectively digitizes the spectrally sampled signals. To calculate the quantization resolution in the radiance domain (L_{Q_i}), the saturation radiances for the bands of ETM+ can be obtained and divided by $2^8 = 256$ to

determine the quantization resolution. Table C.4 indicates that the ETM+ sensor contains a low gain and a high gain setting. Since this research focuses on imaging case 2 waters, the signals that we image are relatively low. Accordingly, we have assumed that the radiance levels associated with the high gain setting should be used to determine (L_{Q_i}) in this work.

Band	Low Gain Saturation Radiances ($mW/cm^2 sr \mu m$)	High Gain Saturation Radiances ($mW/cm^2 sr \mu m$)
1	28.57	19.00
2	29.13	19.37
3	22.50	14.96
4	22.50	14.96
5	4.73	3.15

Table C.4: *Saturation radiances for the first five bands of ETM+ for both the low gain and high gain settings, [ETM Manual, 2003].*

Similarly, to calculate noise in the radiance domain (N_{L_i}), the SNRs must be obtained to solve for Equation 5.2. Again, this research focuses on imaging case 2 waters so the signals that will be obtained are relatively low. Table C.5 shows the SNRs for low signal levels that were used in this work.

Band	Radiance Level for SNR, L_{low} ($W/m^2 sr \mu m$)	SNR Requirements
1	40.0	31
2	30.0	33
3	21.7	25
4	13.6	28
5	4.0	24

Table C.5: *ETM+ Signal to noise ratios at L_{low} radiance levels for the first five bands, [ETM Manual, 2003].*

C.2.2 OLI

OLI is equipped with a 12-bit quantizer that effectively digitizes the spectrally sampled signals. To calculate the quantization resolution in the radiance domain (L_{Q_i}), the saturation radiances for the bands of OLI can be obtained and divided by $2^{12} = 4096$. The OLI sensor does not have a low gain and high gain setting so the the maximum radiance levels

in Table C.6 can simply be divided by 4096 to estimate L_{Q_i} .

Band	Saturation Radiances $L_{Max} (W/m^2 sr \mu m)$
1	555
2	581
3	544
4	462
5	281
6	71.3

Table C.6: *Saturation radiances for the first six reflective bands of OLI, [LDCM Manual, 2006]*

Similarly, to calculate noise in the radiance domain (N_{L_i}), the SNRs must be obtained to solve for Equation 5.2. Table C.7 shows the SNRs that may be used for typical radiance levels and it is with these values that noise is modeled in this work.

Band	Radiance Level for SNR $L_{typical} (W/m^2 sr \mu m)$	SNR Requirements
1	40	130
2	40	130
3	30	100
4	22	90
5	14	90
6	4	100

Table C.7: *OLI Signal to noise ratios for $L_{typical}$ radiance levels in the visible and near-infrared bands, [LDCM Manual, 2006].*

C.2.3 Other Instruments

The SeaWiFS instrument is equipped with a 10-bit quantizer while the AVIRIS sensor has a 10 bit quantizer for data collected prior to 1994 and a 12 bit quantizer for data collected after 1995. Therefore, the AVIRIS data in this work used a 12 bit encoding scheme. Additionally, MODIS uses a 12 bit quantizer for its data.

C.3 OLI SNR Margins

This section provides a bar chart of SNR margins for the bands of OLI. Preliminary studies have indicated that the SNRs of the actual OLI instrument are much higher than provided in the original SNR specifications. As a result, Figure C.8 was provided to illustrate a more reasonable range of SNRs that we can expect to achieve with the final instrumentation.

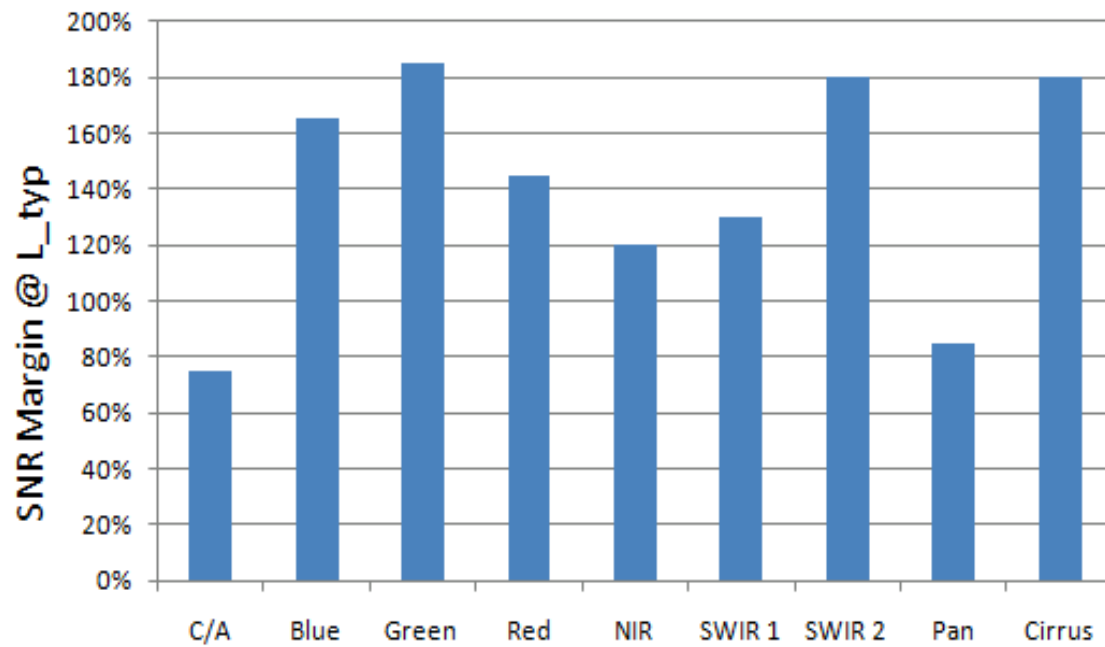


Figure C.8: *Potential SNR Margins for the OLI instrument.*

Bibliography

- [Bricaud et al., 1981] Bricaud, A., Morel, A., and Prieur, L. (1981). Absorption by dissolved organic matter of the sea (yellow substance) in the uv and visible domains. 26 (1), Limnol. Oceanogr. 43.
- [Brown and Minnett, 1999] Brown, O. and Minnett, P. (1999). *MODIS Infrared Sea Surface Temperature Algorithm*, version 2 edition.
- [Bukata et al., 1981] Bukata, R. P., Jerome, J. H., and Bruton, J. E. (1981). Validation of a five-component optical model for estimating chlorophyll a and suspended mineral concentrations in lake ontario. Technical report, Applied Optics.
- [Coleman and Li, 1996] Coleman, T. and Li, Y. (1996). An interior, trust region approach for nonlinear minimization subject to bounds. Technical report, SIAM Journal on Optimization.
- [Cox and W.Munk, 1954a] Cox, C. and W.Munk (1954a). The measurement of the roughness of the sea surface from photographs of the sun's glitter. 44, J. Opt. Soc. Am. 838-850.
- [Cox and W.Munk, 1954b] Cox, C. and W.Munk (1954b). Statistics of the sea surface derived from sun glitter. 13, J. Mar. Res. 198-227.
- [ETM Manual, 2003] ETM Manual (2003). *LANDSAT 7 IMAGE ASSESSMENT SYSTEM (IAS) RADIOMETRIC ALGORITHM THEORETICAL BASIS DOCUMENT (ATBD)*, version 1 draft edition.

-
- [Fairbanks, 1999] Fairbanks, R. R. (1999). *A CHARACTERIZATION OF THE IMPACT OF CLOUDS ON REMOTELY SENSED WATER QUALITY*. PhD thesis, Rochester Institute of Technology.
- [Garrett, 1997] Garrett, A. (1997). Alge: A 3-d thermal plume prediction code for lakes, rivers and estuaries(u). Technical report, Savannah River Technology Center. SRTC-NN-95-25 Revision 1.
- [Gordon and Brown, 1974] Gordon, H. R. and Brown, O. B. (1974). Influence of bottom depth and albedo on reflectance of a flat homogeneous ocean. 13 pp. 21532159, Appl. Opt.
- [Gordon and Wang, 1994] Gordon, H. R. and Wang, M. (1994). Retrieval of water-leaving radiance and aerosol optical thickness over oceans with seawifs: a preliminary algorithm. Volume 33 3, Optical Society of America, Univeristy of Miami.
- [Green et al., 1998] Green, R., Eastwood, M., Sarture, C., Chrien, T., Aronsson, M., Chippendale, B., Faust, J., Pavri, B., Chovit, C., Solis, J., Olah, M., and Williams (1998). Imaging spectroscopy and the airborne visible/infrared imaging spectrometer (aviris). Technical report, O. Remote Sens. Environ.
- [Green and Pavri, 2001] Green, R. and Pavri, B. (2001). Aviris inflight calibration experiment measurements, analysis, and results in 2000. Technical report, JPL AVIRIS Workshop.
- [Hale and Querry, 1973] Hale, G. and Querry, M. (1973). Optical constants of water in the 200nm to 200micron wavelength region. 12 (3), Appl. Optics. 555.
- [Haltrin, 1998] Haltrin, V. I. (1998). An analytic fournier-forand scattering phase function as an alternative to the henyeeygreenstein phase function in hydrologic optics. Technical report, IEEE.
- [Hecht, 1990] Hecht, E. (1990). *Optics*. Addison-Wesley Publishing Company, Reading, Massachusetts, second edition.

- [Hedley et al., 2005] Hedley, J., Harborne, A., and Mumby, P. (2005). Simple and robust removal of sun glint for mapping shallow-water benthos. Vol. 26, No. 10 pp. 2107-2112, International Journal of Remote Sensing.
- [Hochberg et al., 2003] Hochberg, E., Andrefouet, S., and Tyler, M. (2003). Sea surface correction of high spatial resolution ikonos images to improve bottom mapping in near-shore environments. 41 pp. 1724-1729, IEEE.
- [Jackson, 1975] Jackson, J. (1975). *Classical Electrodynamics, 2nd Edition*. John Wiley and Sons, New York, NY.
- [JPL, 2006] JPL, N. (2006). Aviris homepage. Visited November 23, 2006. <http://aviris.jpl.nasa.gov/>.
- [Kerker, 1969] Kerker, M. (1969). *The Scattering of Light and Other Electromagnetic Radiation*. Academic Press, New York, NY.
- [LDCM Manual, 2006] LDCM Manual (2006). *Operational Land Imager Requirements Document Landsat Data Continuity Mission*, draft edition.
- [Leathers and McCormick, 1999] Leathers, R. A. and McCormick, N. J. (1999). Algorithms for ocean-bottom albedo determination from in-water natural-light measurements. Volume 38 pp. 31993205, Optical Society of America. No. 15.
- [Li, 2007] Li, Y. (2007). *An Integrated Water Quality Modeling System with Dynamic Remote Sensing Feedback*. PhD thesis, Rochester Institute of Technology.
- [McClain et al., 1985] McClain, E., Pichel, W., and Walton, C. (1985). Comparative performance of avhrr-based multichannel sea surface temperatures. 90 C6, J. Geophys. Res. 11587-11601.
- [Mobley, 1994] Mobley, C. D. (1994). *Light and Water*. Academic Press, Inc.
- [Mueller and Austin, 1995] Mueller, J. and Austin, R. (1995). Ocean optics protocols for seawifs validation, revision 1. Technical report, NASA Technical Memorandum 104566.
- [NASA, 2006] NASA (2006). Landsat 7 science data users handbook. Visited November 23, 2006. <http://landsathandbook.gsfc.nasa.gov/handbook.html>.

- [Nelder and Mead, 1965] Nelder, J. and Mead, R. (1965). The downhill simplex method. Technical Report vol. 7, Computer Journal. pp 308-313.
- [Padula, 2008] Padula, F. P. (2008). Historic thermal calibration of landsat 5 tm through an improved physics based approach. Master's thesis, Rochester Institute of Technology.
- [Planck, 1901] Planck, M. (1901). On the law of distribution of energy in the normal spectrum. Technical report, Annalen der Physik.
- [Pope and Fry, 1997] Pope, R. and Fry, E. (1997). Absorption spectrum (380-700nm) of pure water. ii. integrating cavity measurements. 36 (33), Appl. Optics. 8710-8723.
- [Raqueno et al., 2000] Raqueno, R., Simmons, R., and Schott, J. (2000). A model based approach to hyperspectral analysis of water constituents.
- [Robinson et al., 2000] Robinson, G., Gross, H., and Schott, J. (2000). Evaluation of two applications of spectral mixing models to image fusion. 71, Remote Sensing of Environment. 272-281.
- [Ruddick et al., 2000] Ruddick, K. G., Ovidio, F., and Rijkeboer, M. (2000). Atmospheric correction of seawifs imagery for turbid coastal and inland waters. Technical report, Optical Society of America. k.ruddick@mum.ac.be.
- [S. Maritorena and Gentili, 1994] S. Maritorena, A. M. and Gentili, B. (1994). Diffuse reflectance of oceanic shallow waters: influence of water depth and bottom albedo. 39 pp. 1689-1703, Limnol. Oceanogr.
- [Sathyendranath and Prieur, 1981] Sathyendranath, S. and Prieur, L. (1981). An optical classification of coastal and oceanic waters based on the specific spectral absorption curves of phytoplankton pigments, dissolved organic matter, and other particulate materials. Technical report, Limnol. and Oceanogr.
- [Schott, 1997] Schott, J. R. (1997). *Remote Sensing: The Image Chain Approach*. Oxford University Press, New York, NY.
- [Sears, 1949] Sears, F. (1949). *Optics*. Addison-Wesley, Cambridge, MA. page=174.

-
- [Smith and Baker, 1981] Smith, R. and Baker, K. (1981). Optical properties of the clearest natural waters (200-800nm). 20 (2), Appl. Optics. 177-184.
- [Sullivan et al., 2005] Sullivan, J. M., Twardowski, M. S., Donaghay, P. L., and Freeman, S. A. (2005). Use of optical scattering to discriminate particle types in coastal waters. 44 9, Optical Society of America. 1667-1680.
- [Vodacek, 2005] Vodacek, A. (2005). Nir extrapolation. private communication.
- [Whitmire et al., 2007] Whitmire, A., Boss, E., Cowles, T., and W.S.Pegau (2007). Spectral variability of the particulate backscattering ratio. 15 11, Optical Society of America. 7019-7031.
- [Wilson, 2000] Wilson, N. L. (2000). Hyperspectral imaging for bottom type classification and water depth determination. Master's thesis, Rochester Institute of Technology.
- [Zoratev and Demin, 1977] Zoratev, V. and Demin, A. (1977). Optical constants of water over a broad range of wavelengths, 0.1 angstroms-1m. 43 (2), Opt. Spectrosc. 157.